Electrocatalysts for the Borohydride Oxidation Reaction : From model surfaces to non-noble fuel cell electrodes

Guillaume Braesch

THÈSE

Pour obtenir le grade de

DOCTEUR DE L'UNIVERSITE GRENOBLE ALPES

Spécialité : **Matériaux, Mécanique, Génie Civil, Électrochimie**
Arrêté ministériel : 25 mai 2016

Présentée par

Guillaume BRAESCH

Thèse dirigée par **Marian CHATENET**
et codirigée par **Antoine BONNEFONT** et **Elena SAVINOVA**,

préparée au sein du Laboratoire d'Electrochimie et de Physicochimie des Matériaux et des Interfaces (LEPMI)
dans l'École Doctorale I-MEP 2

Electrocatalyseurs pour la Réaction d'Oxydation des Borohydrures : des surfaces modèles aux électrodes non-nobles de piles à combustible

Electrocatalysts for the Borohydride Oxidation Reaction: From model surfaces to non-noble fuel cell electrodes

Thèse soutenue publiquement le **« 24 Novembre 2020 »,** devant le jury composé de :

Monsieur Christophe COUTANCEAU
Professeur, Université de Poitiers, Rapporteur (Président du jury)

Madame Elena BARANOVA
Professeure, Université d'Ottawa, Rapporteure

Madame Laëtitia DUBAU
Chargée de recherche, CNRS, Examinatrice

Monsieur Renaut MOSDALE
Docteur, Pragma Industries, Examinateur

Monsieur Gaël MARANZANA
Professeur, Université de Lorraine, Invité

Madame Elena SAVINOVA
Professeure, Université de Strasbourg, Invitée

Monsieur Marian CHATENET
Professeur, Université Grenoble-Alpes, Directeur de thèse

Monsieur Antoine BONNEFONT
Maitre de conférence, Université de Strasbourg, Co-directeur de thèse

The saddest aspect of life right now is that science gathers knowledge faster than society gathers wisdom.

Isaac Asimov

Table of contents

List of symbols and abbreviations

List of symbols:

A	Geometric Surface Area
C	Concentration ($mol.L^{-1}$)
D	Diffusion coefficient ($cm^2.s^{-1}$)
E	Potential (V *vs* Reference)
$E°$	Standard potential (V *vs* SHE)
F	Faraday constant (~96485 $C.mol^{-1}$)
I	Current (mA or A)
j	Current density ($mA.cm^{-2}$ or $A.cm^{-2}$)
l	Catalysts loading ($\mu g.cm^{-2}$)
m	Mass (g)
M	Molar mass ($g.mol^{-1}$)
n	Number of exchanged electrons
ν	Kinematic viscosity of the electrolyte ($cm^2.s^{-1}$)
P	Power density ($mW.cm^{-2}$)
S	Surface area (cm^2)
T	Temperature (°C or K)
t	Time (s or h)
V	Volume (L or m^3)
v_s	Scanning rate ($mV.s^{-1}$)
ω	Rotation rate (rpm)

List of abbreviations:

AFC	Alkaline Fuel Cell
AE	Acid Etching

AEM	Anion Exchange Membrane
AEI	Anion Exchange Ionomer
AST	Accelerated Stress Test
BOR	Borohydride Oxidation Reaction
BHR	Borohydride Hydrolysis Reaction
CCM	Catalyst Coated Membrane
CA	Chronoamperometry
CE	Counter electrode
CEM	Cation Exchange Membrane
CEI	Cation Exchange Ionomer
CV	Cyclic Voltammetry
DBFC	Direct Borohydride Fuel Cell
DEMS	Differential Electrochemical Mass Spectrometry
DFT	Density Functional Theory
DLFAFC	Direct Liquid Fed AFC
ECSA	Electrochemical Surface Area
ED	Electrodeposition / Electrodeposited
EDS	Energy Dispersive Spectroscopy
FC	Fuel Cell
FCEV	Fuel Cell Electric Vehicle
FTIRS	Fourier Transform Infra-Red Spectroscopy
GC	Glassy Carbon
GDL	Gas Diffusion Layer
GDE	Gas Diffusion Electrode
GHG	Greenhous Gas
HER	Hydrogen Evolution Reaction
HOR	Hydrogen Oxidation Reaction

KL	Koutecký-Levich (plots)
NFM	Nickel Foam
NFT	Nickel Felt
NP	Nanoparticles
OCP	Open Circuit Potential
OCV	Open Circuit Voltage
OER	Oxygen Evolution Reaction
ORR	Oxygen Reduction Reaction
PEMFC	Proton Exchange Membrane Fuel Cell
PTCFE	Polychlorotrifluoroethylene (Kel-F®)
PTFE	Polytetrafluoroethylene (Teflon®)
RDE	Rotating Disk Electrode
RHE	Reversible Hydrogen Electrode
RRDE	Rotating Ring-Disk Electrode
SEM	Scanning Electron Microscopy
TEM	Transmission Electron Microscopy
WE	Working electrode
XRD	X-Ray Diffraction

CHAPTER I: Why the Direct Borohydride Fuel Cell

The first chapter of this manuscript is devoted to a brief literature review of the current ecological and economic situation we are facing. First of all, the causes and consequences of the global warming will be identified, and a possible solution to dampen this global issue through the use of renewable energies and hydrogen as an energetic vector will be presented. Then, the Direct Borohydride Fuel Cell (DBFC) will be presented as a potential technology for portable and mobile applications. Lastly, the context and objectives of this PhD will be detailed.

.

I.1 Global warming and climate change

For several years now, each summer is accompanied with several heatwaves. Their frequency, intensity and duration noticeably increased [1], resulting in high averaged temperatures in 2019 all around the world [2](Figure I.1) and new highest historic temperature recorded in more than 35 countries since 2015. Especially alarming temperatures above T = 20°C and 38°C were recorded in Antarctica and Arctic Siberia, respectively, in the first half of 2020. In 2019, the global temperature was estimated at around + 1.29°C above the temperature of the 19th century.

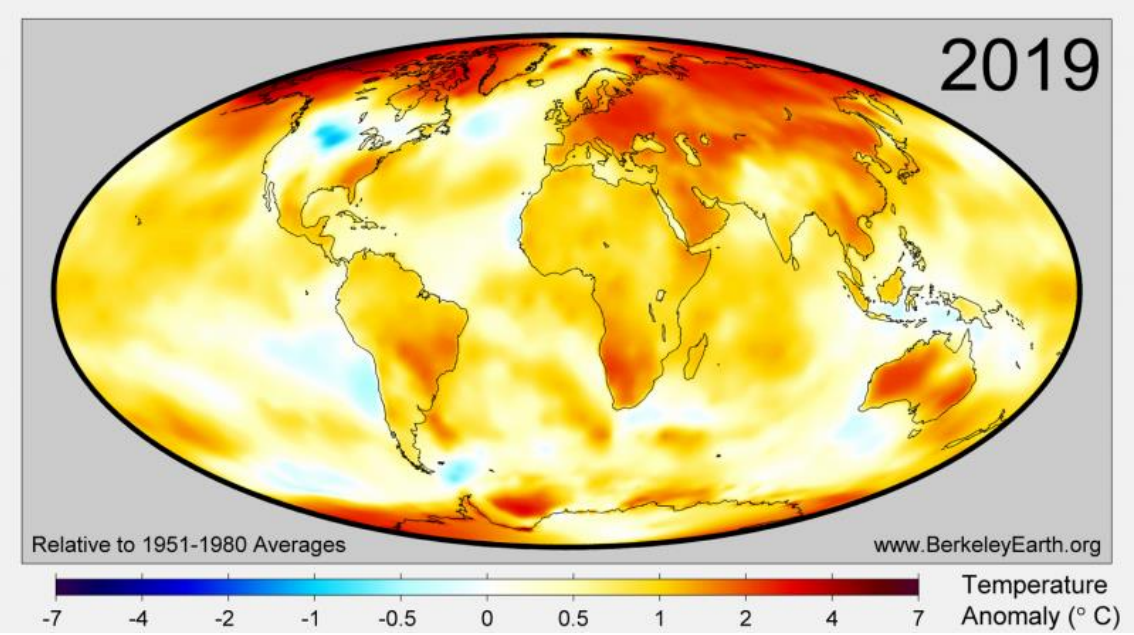

Figure I.1. Local temperatures, averaged over the whole 2019 year, recorded around the world and compared to the average temperature of 1951 – 1980. Reprinted from Ref [2]

Emission of greenhouse gases by energy and transportation sectors

Even if Earth's climate naturally cycles between colder and warmer periods, due to several effects such as small orbital variations [3], these cycles last for millennia and the transition from one to the other is often accompanied with shorter climate change period. However, the amplitude and the rate of the warming since the last century is too large to be natural and must be due to human activities, as reported by scientists for more than thirty years [4–8]

I.1.1

The increase of greenhouse gas (GHG) concentration in the atmosphere is considered as the main origin of the global warming. These gases originate from various sources and applications in different proportions (given for US emissions in 2018) [9]: carbon dioxide (81%) mainly comes from the burning of fossil fuels; methane (10%) is a by-product of fossil fuel production and transportation and is also emitted by livestock; nitrous oxides (7%) are generated by combustion of fossil fuels, solid waste and treatment of wastewater; fluorinated gases (3%) are produced by industrial processes and present the highest global warming potential [9]. Overall, the generation of GHG is mainly driven by the production of electricity (27% in 2018 in the US [10]), using fossil resources (coal, natural gas, oil), and by the transportation sector (28% [10]), mainly due to combustion of fossil fuels in thermal engines.

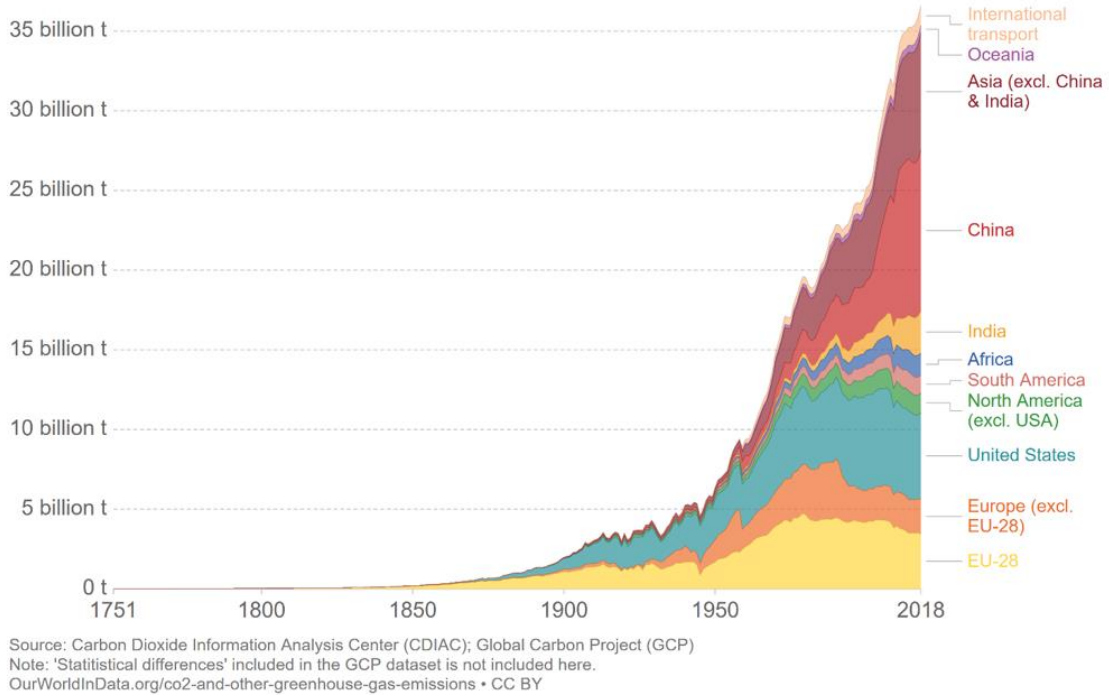

Figure I.2. Annual total CO_2 emissions by world region. Reprinted from [11].

Because of the constant growth of fossil fuel consumption, the annual CO_2 emission has been multiplied by seven since 1950 (Figure I.2). Even if warned by the scientific

community and conventions of parties (COP), gathered by the United Nations regarding the climate change since 1995 (COP1 held in Berlin), no strict actions to reduce the emissions of GHG were considered by governments so far. Because of this lack of decision, the peak emission of CO_2 was not yet reached in 2018 (Figure I.2) and will not until, at the latest, 2030 according to the Paris agreement (COP 21). Indeed, numerous countries, part of the biggest GHG emitter, ratified this agreement in 2015 with the main objective to limit the global warming to +1.5°C for the year 2100 (but such target was already proposed in 2009 [12]). Unfortunately, as shown by Figure I.3, the current policies applied to reduce the climate change impact are not sufficient to reach such goal [11]. This means that the policies voted at the COP 21 are not yet (fully) applied and are sometimes discarded, a famous example being the US government decision to withdraw from their engagement in 2019 [13] (the decision was taken in 2017 only 2 years after the ratification).

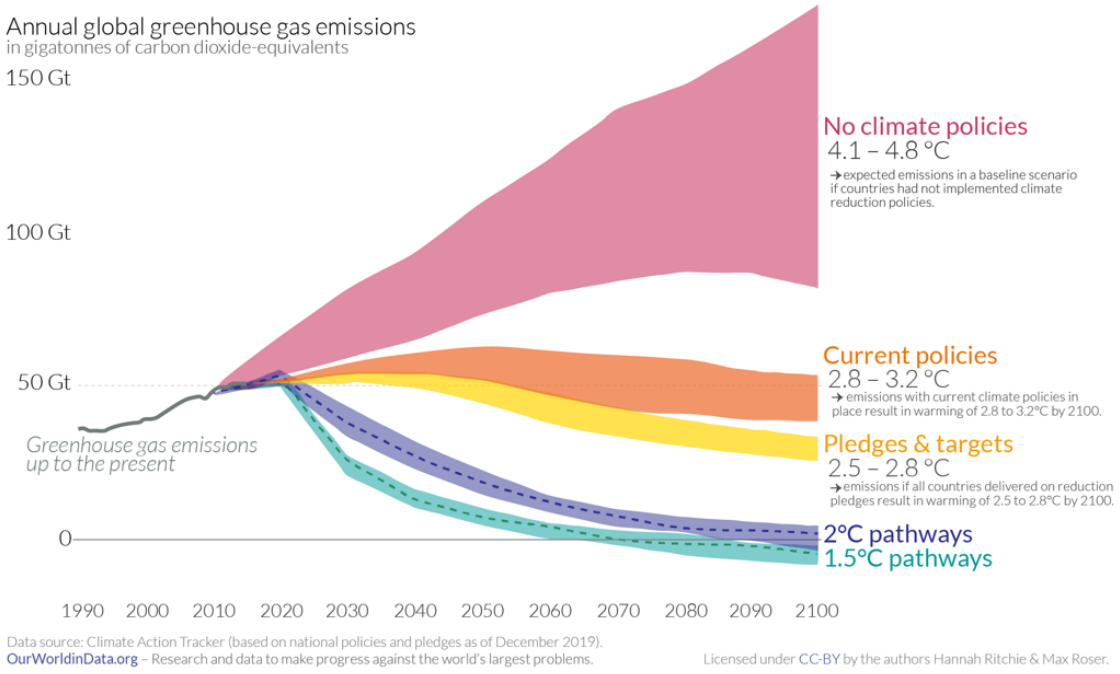

Figure I.3. Global greenhouse gas emissions and warming scenarios. Reprinted from Ref. [11].

The sanitary crisis of 2020 (SARS CoV2 pandemic) directly impacted the emission of CO_2 at the world scale: because of national lockdowns and international borders closing, transportation and energy consumption habits were modified, resulting in *ca.* 17% decrease of produced CO_2 from January to April 2020 (compared the same period in 2019) as presented by Le Quéré *et al.* [14]. Unfortunately, this habits modification was only temporary and by the time of the article publication the emission levels were already back to "normal". Another study by Zambrano-Monserrate *et al.* [15] showed that this pandemic will also have negative effects on the environment, such as the

reduced amount of waste recycled, but most importantly that decreasing GHG emissions on such short periods is not a sustainable way to reach the Paris agreement targets.

Consequences of the global warming

Going back to the pre-industrial era average temperature is not achievable with the actual development of the human society: the important population growth (1.6 billion in 1900, 7 billion in 2011, 7.7 billion in 2019 [16] requires the equivalent (or even superior) energy demand, accompanied by proportional GHG emissions as presented above. This will surely have a major impact result in direct and indirect consequences. Direct consequences are events caused by the global warming that are experienced already to this day and will aggravate in the upcoming years:

I.1.2

- Increased probability of extreme weather events

As mentioned above, the probability and frequency of heat waves is directly increased with the global warming. Ironically, this encourages the usage of air conditioning to live and work in acceptable conditions, but in return directly amplifies the global warming by generating heat [17,18]. Less intuitively, both ends of the extreme events scale are concerned, with rising minimum temperature as well as cold waves also recorded more frequently over the past decades [19–22]. Other weather events are induced by climate changes such as droughts [23,24], heavy rains and river flooding [25–27], wildfires [28,29], storms and cyclones [27,30], and will intensify depending on the amplitude of the global warming.

- Rise of the sea level

The overall increasing temperature induces melting of sea ice and glaciers [31–33] as well as a significant warming of the oceans [34,35], which all contribute to the rise of the sea level. It is possible to find small beneficial aspects from this situation, with for example new maritime routes opening that will reduce the distance of shipment between Europe and Asia [36], but its arising overall consequences will most likely be more catastrophic. According to new estimates, the sea level will rise by 1.3 meter by 2100, and more than 5 meters by 2300 if the current climate policies are maintained [37], inducing major migration crisis of coastal population (around 10% of the current total population lives below the 5 m altitude line), which already started [38]. An additional effect of the ice melting is the diminution of the ice-albedo of the planet, which will result in solar radiations being less reflected and thus more absorbed by the surface of the earth, accelerating even more its overall warming.

- Indirect consequences of climate change

The indirect consequences are the products of all the effects described previously and will affect directly our society and environment: water and hunger crisis will be amplified as a direct repercussion of more frequent droughts; important biodiversity losses will be induced by climate change [39–42]; the propagation and behavior of infectious diseases might also be modified [43–45]; what is certain is the thawing of the permafrost, which will result in resurfacing extinct diseases from past centuries [46] or even unknown ones from past eras [47,48].

In order to limit such consequences and fall in the COP 21 "+1.5°C scenario", it is of paramount importance to drastically reduce the overall GHG emissions. This means that the two main sources of GHG emissions (electricity production and transportation) must be addressed in priority.

Renewable energy and technological locks

I.1.3

The best way to decrease the energy contribution to global warming would be to produce less and diminish the overall demand by changing our consumption habits, similarly as what was observed during the sanitary crisis of 2020. However, such drastic modifications will take years or decades to be established and in the end energy would still be required. This means that a more direct approach must be taken to decrease the GHG emissions: developing new energy technologies with no or a lesser impact on the climate change. These technologies are called renewable energies and rely on principles emitting no GHG. They are regrouped in four main sources: hydropower; wind; solar; and biomass energy technologies, and as presented on Figure I.4, generate small to no GHG. They are also presented as safer energy sources, since the death rate used on this chart is calculated from air pollution and other related accidents [49].

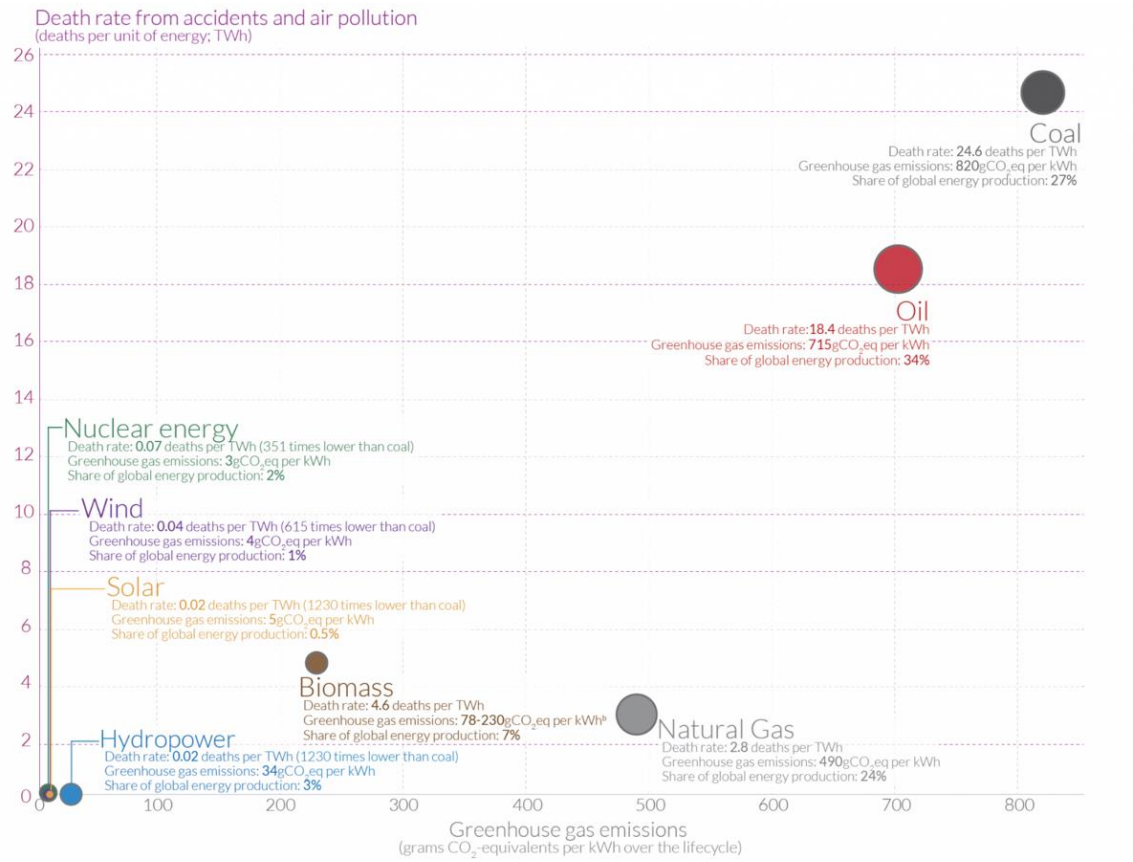

Figure I.4. The safety of the different sources of energy compared to their respective GHG emissions. Reprinted from Ref [49].

This really encourages the deployment of such technologies on a global scale. Figure I.5a shows the evolution of energy production originating from these renewable energies. Hydropower is a source well exploited since the early 1960 and the technology is pretty much mature, which explains why almost no investments are made in this sector since 2004 (Figure I.5b), and why the energy produced increases linearly: more hydropower sites are being deployed but their energy output is always the same. This is not the case for the technology exploiting other renewable resources. Biomass is slowly developed overtime but at a relatively slow pace, proportional to the dedicated small investment. On the contrary, wind and solar sources are being thoroughly investigated since the early 2000's (Figure I.5b), which directly translates into a significant energy production increase over the last decade. In 2019, wind and solar energies produced around 19% and 13% of the total renewable electricity, which corresponded itself to 11% of the global energy production [50]. This could appear as a low percentage, but they will keep increasing in future years and reach significant portion of our energy production as made in Sweden, where more than 50% of electricity was produced from renewable resources in 2018 [51].

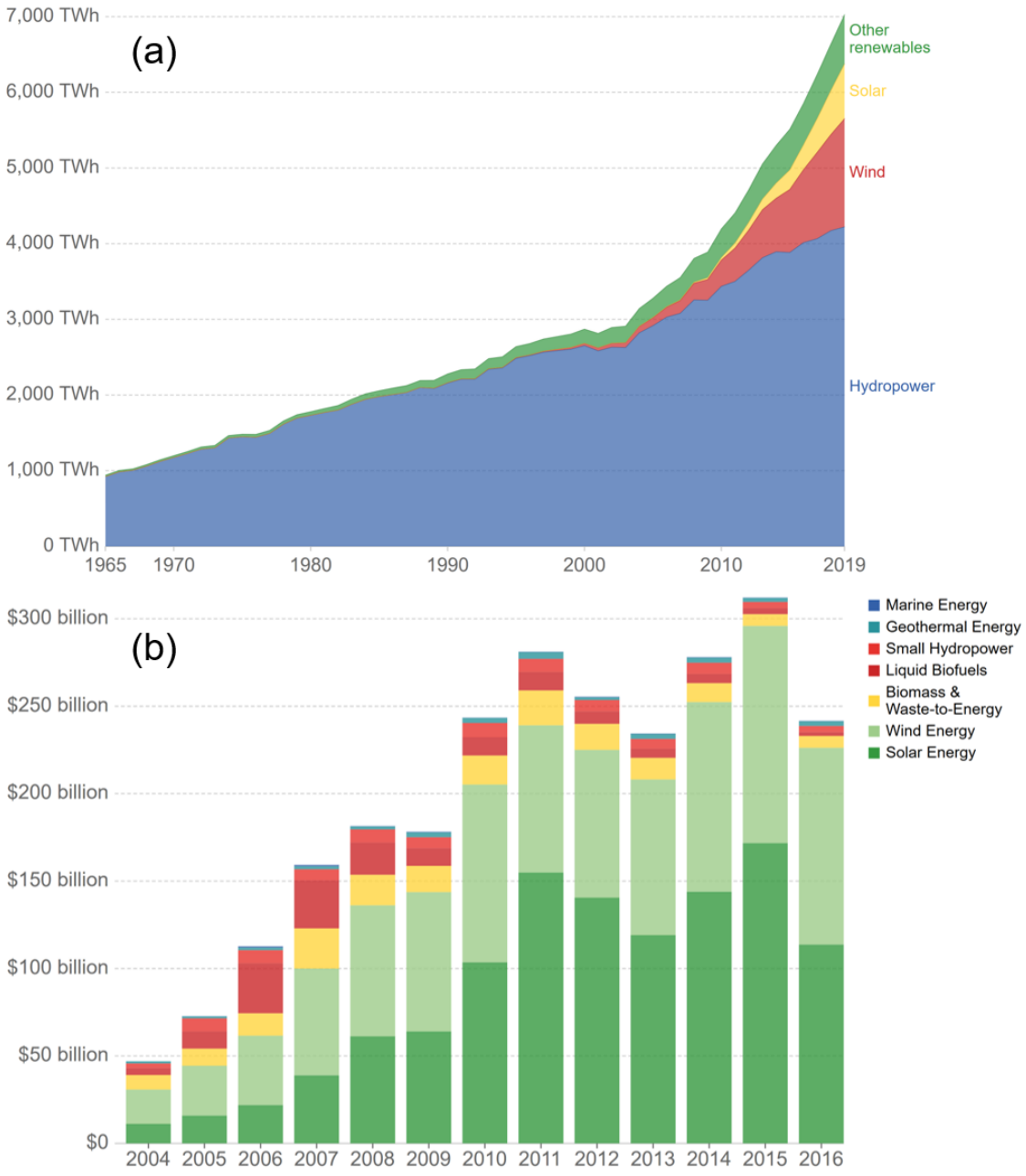

Figure I.5. (a) Global renewable energy generation by technology. Reprinted from Ref [50]. (b) Global investment in renewable energy by technology highlighting wind and solar as the main development focuses. Reprinted from Ref [49]

The nuclear energy production also proved to be an interesting source emitting no CO_2 (Figure I.4). However, because it runs on radioactive minerals, it can however not be considered as a renewable energy source. Its main issue is the important quantities of radioactive waste generated that are, for now, hardly treatable. In addition, the dismantling of nuclear plants is expensive and time consuming. Moreover, major incidents such as the Chernobyl or Fukushima events made this technology the most dangerous one by common beliefs (but is in fact much safer than GHG emitting ones [49] in terms of short term effects). It was actually estimated that the use of nuclear

energy has prevented more than 1.8 million air pollution-related deaths and the emission of 64 Gt of CO_2 [52]. The nuclear energy should therefore be used as a transition help to greatly reduce emissions until the renewables energies reach their full potential and replace it. Unfortunately, as presented by Figure I.6, all the progress made with renewable energies is only used to decrease the production part of nuclear while the GHG emitting production is almost untouched [53]. On a more hopeful and positive note, nuclear energy production could see a major milestone achieved in the next decades with the nuclear fusion technology. It should produce great amount of energy, with no GHG emission nor radioactive wastes, and is under development in France through the ITER project [54].

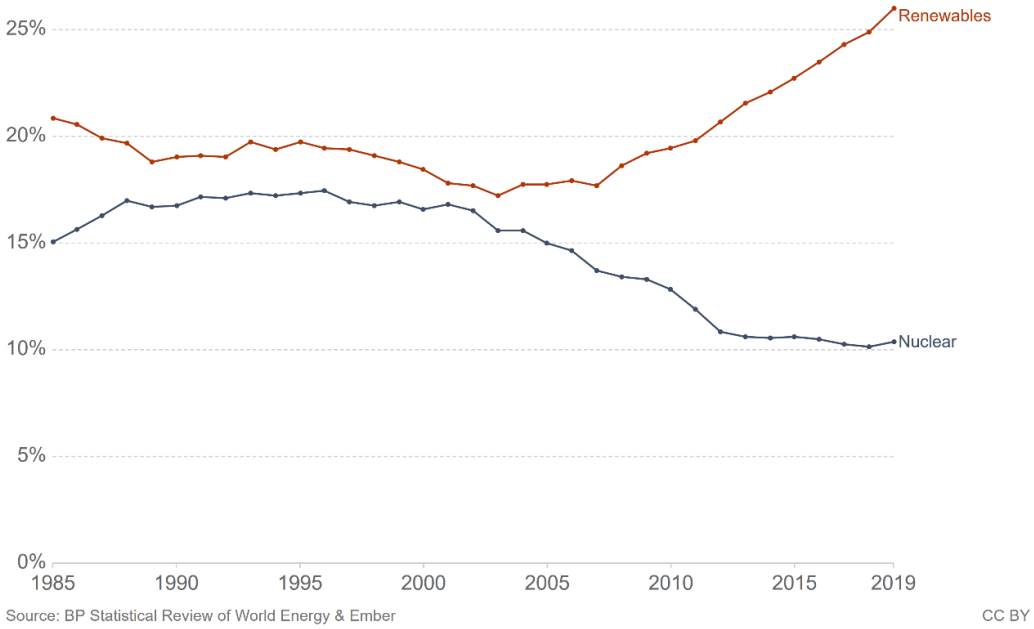

Figure I.6. The share of nuclear and renewables in total electricity production. Reprinted from Ref [53].

In addition, renewable energies are not all green and several aspects limit their development. First of all, each technology is dependent on the environment, meaning it cannot be used everywhere. This basic but really important notion means that each country must adapt its energy production at a regional scale, in function of the renewable sources available and that it is primordial to continue the developments of several technologies and not focus on one system. The development of renewable sources was also accompanied by major impact on the environment regarding local populations or biodiversity, as for the main example the important negative effects of dams over their surroundings [55–57]. The hydroelectric source is the oldest one that became practical, so more research has been conducted regarding its impacts. However, studies already reveal that wind [58,59], biomass [59] and marine [60] energy productions also have negative effects on the environment. Such effects must be

considered and minimized to avoid making renewable sources more harmful then beneficial to the environment. Solar power appears to be the less negatively impactful technology [61] but it is important to keep in mind that human-made installations will always affect their surroundings.

Moreover, by their nature, most of the renewable sources are intermittent and will thus produce energy in a discontinued manner. Such intermittency is provoked by predictable events, such as the day/night cycle for solar or the tides for marine power, and the production can therefore be adjusted in consequence. However, clouds and winds are more complex to predict and could result in unplanned production drops. This technical barrier has been used as a break to renewable energy development because of their "unreliable nature" [62]. However, it must now be addressed: the best answer to such discontinued production is to exceed to total energy demand when possible and store this surplus to be reused when needed [63,64]. The best manner to do so it to convert the exceeding electrical energy in chemical energy *via* the use of electrochemical systems. Currently the most developed technologies for stationary conversion are battery systems [64–66]. However, their closed nature and the upcoming increase of renewable energy production will require to deploy fields of battery to obtain suitable storage capacity, where other open technologies, such as redox flow batteries or fuel cell/electrolyzer systems, would only require larger storage reservoir. Redox flow batteries are promising for such applications [67] but present the inconvenience of being only devoted to management of the electrical grid.

I.2 Hydrogen: a major energy vector

In opposition to batteries, the hydrogen produced by the renewable production surplus, using water splitting electrolyzers, is not limited to be converted back to electricity in the power grid and could be instead used as a fuel in fuel cell powered portable and mobile devices and vehicles. A recent review has fully described all the different processes involved in the hydrogen energy vector, which can be summarized by Figure I.7, from the available sources, generation and storage options and the several hydrogen fueled final applications [68].

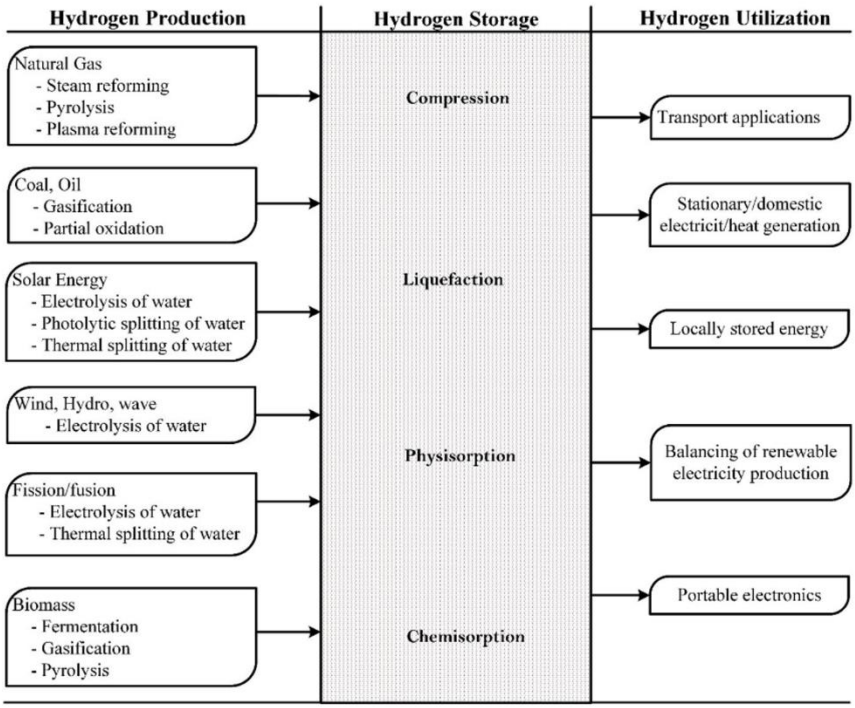

Figure I.7. The hydrogen vector: sources, generation options, storage options and end-uses. Reprinted from [68]

I.2.1 Is hydrogen really a green fuel?

In the last decade, hydrogen was often described as (near) future fuel [69–71] because of its important energy density per unit mass (three times the one of common fossil fuels). As presented on Figure I.7, the production methods can be separated in two distinct categories: fossil fuel based, and sustainable water electrolysis. Unfortunately, around 96% of the hydrogen is produced from fossil resources today (49% from natural gas, 29% from liquid hydrocarbons, and ca. 18% from coal) [68], which contribute to significant GHG and other chemicals emission in the atmosphere [70]. The main reason is obviously economic: because of the important energy demand of water electrolysis, the resulting hydrogen production cost is high (around 4 – 8 $/kg^{-1}$ *versus* 1 – 2 $.kg^{-1}$ for non-sustainable production, in 2019 [72,73]). The sustainability of hydrogen is thus still questionable nowadays, but current important investments and a real trend in the "green hydrogen production", induced by the global warming targets discussed above, can already be observed from the amount of studies published recently in this domain [74]. Such development is strongly required to reach the sustainable production target, from 0.04 $Mt.y^{-1}$ in 2010 to almost 8 $Mt.y^{-1}$ in 2030 [75] and the recent H_2 plan in France (7000 M€) goes in this direction.

The different utilization of hydrogen also shows highly disparate proportions. Indeed, most of the produced hydrogen is used in chemical refinery: more than 50% is used for

chemical reactions in Europe and over 95% for ammonia synthesis in Japan. Overall the large majority of the world hydrogen is used for petroleum refining and ammonia and methanol synthesis [68], which will also contribute to the pollution of the atmosphere with GHG or other chemicals. Again, carbon-free transportation, other mobile devices and stationary electric generation are under consequent investigations and will be presented in more detail in the following section. However, to this day, the technologies are only emerging and this energy vector is a non-negligible part of the overall GHG emissions and several years or decades will be necessary for the hydrogen vector to be fully "green".

Storage and transportation of hydrogen

I.2.2 In addition to the current issues just described, it is also necessary to store the produced hydrogen and then transport it from the production to utilization sites. The large energy density of hydrogen was mentioned previously as one of the main property to consider it as an energy carrier. However, when converted to volume, this energy density is only 5.6 $MJ.L^{-1}$ for a given pressure of 700 bar at 25°C (which is now three times lower than hydrocarbon fuels). This value obtained only at high pressure asserts the difficulty to store hydrogen compared to natural gas or other liquid fuel. Several methods were developed to such end, where the state of hydrogen varies from gaseous to liquid or even solid.

- Gaseous hydrogen

The main storage system is the compression of gaseous hydrogen, since it is relatively easy and straightforward. It allows to reach acceptable densities for several applications: 23.3 $kg.m^{-3}$ at 350 bar and 39.2 $kg.m^{-3}$ at 700 bar, which corresponds to the common pressures of fuel cell buses and commercial fuel-cell cars respectively. It is also possible to perform cryo-compression at T = 100 K to reach a density of 39.5 $kg.m^{-3}$ at relatively low pressure of 200 bar [76]. Standardized tanks are already commercialized following strict norms to limit safety issues. This storage method presents the main drawback to require an energy-consuming compression system that decreases the overall energy efficiency of the hydrogen cycle. In addition, the high pressure most often considered is too high for standard fuel cell and electrolyzer and it must be adapted. Moreover, even after compression, the volumetric energy density of pressurized hydrogen is still low compare to gasoline, thereby increasing the transportation costs [68].

- Liquid hydrogen

Another method to obtain a higher volumetric energy density is to change the state of hydrogen from gaseous to liquid (10.1 $MJ.L^{-1}$). However, this process requires even more energy than compression due to hydrogen very low density (0.089 $kg.m^{-3}$) and boiling

point (20.2 K). It was investigated for small scale storage and even considered for fueling vehicles. However, this technology is, to this day, not viable compared to pressurized hydrogen [68].

- Solid hydrogen

Because it is already complex to obtain liquid hydrogen, the methods to obtain a solid storage of hydrogen involve inserting it in other materials using physisorption or chemisorption (Figure I.7). It was proven to be an efficient method in addition to be much safer than commonly-used compressed hydrogen. Several materials can be used as insertion matrix to hydrogen such as metal hydrides [77], magnesium-based alloys [78], carbon based materials [79] or boron-based compounds [80], such as the sodium borohydride ($NaBH_4$). This specific molecule will be thoroughly discussed in the rest of the manuscript but as a fuel and not as a hydrogen storage medium. This method presents the advantage of being the easiest way to transport hydrogen.

Indeed, as briefly evoked above, the transportation of pressurized hydrogen is a real challenge. It is possible to distribute it to the user using either trucks or pipelines. It is also possible to use trucks with adapted tanks to deliver liquefied hydrogen. These three options present both advantages and disadvantages related to the delivery cost and also the deployment time required. Pipelines are more suited for very large transport capacity, but will be very expensive and difficult to deploy. The cheapest method is obviously to use a network of trucks, but it is not suited to handle a large production [68]. Because of the development of hydrogen related technologies and quantities produced in the upcoming years, it is mandatory to address this issue. In fact, it is nowadays one of the main barriers to the development of hydrogen vehicles in Europe: the hydrogen network is not sufficiently developed to motivate vehicle manufacturers to invest in the hydrogen technology and in return, governments do not develop the hydrogen distribution network because the demand is not important enough [81]. However, significant funding is now unlocked and numerous hydrogen stations are now under development [81,82].

To conclude on hydrogen, it is a really promising energy vector that would unlock low GHG energy production and transportation due to its interesting energetic properties and its possible sustainable production. However, much efforts are still required to reach such a sustainable network since the main sources and utilization of hydrogen are currently directly contributing to the atmosphere pollution by either GHG or other chemicals. Nonetheless, the recent governmental engagements and technology developments are encouraging to see the hydrogen vector potential correctly used in a near future.

I.3 Development of fuel cells

Hydrogen can be converted back to electrical energy using systems called fuel cells (FC). There exist several families of FCs which are used for different purposes ranging from homogenization of the renewable energy production, electricity and heat generator for domestic purposes, transportation applications and powering portable or mobile electronic devices (Figure I.7), that can be more generally separated in stationary and portable systems. Overall, all FCs operate with the same operation principle: a fuel (a gas or liquid) is injected in a system composed of two electrodes separated by an electrolyte. This fuel is oxidized at the anode (negative electrode), while an oxidant (O_2 in most cases) is being reduced at the cathode. In order to have an operating FC, the electrolyte, which also serves as the separator (except for liquid FC) must provide a high ionic conduction (to transport the charge carriers from one electrode to the other) but be an electronic insulator, otherwise the system will be short-circuited. The six families of FC: Proton Exchange Membrane Fuel Cell (PEMFC); Solid Oxide Fuel Cell (SOFC); Molten Carbonate Fuel Cell (MCFC); Direct FC like the Direct Methanol Fuel Cell (DMFC); Alkaline Fuel Cell (AFC); Phosphoric Acid Fuel Cell (PEFC), are operating with different characteristics. The primary ones of each FC family are regrouped in Table I.1.

Table I.1: Primary characteristics of the different FC families [83–85].

Fuel cell type	Fuel	Electrolyte	Operating temperature	Electric efficiency	Power range	Application
PEMFC	Pure H_2	Solid polymer (proton conductor)	50 – 100°C	34 – 45%	5 – 250 kW	Portable/ Stationary/ Automotive
SOFC	H_2, CO, CH_4	Solid ceramic	≈ 1000°C	> 50%	2 kW – MW	Stationary: Combine Heat and Power (CHP)
MCFC	H_2, CO, CH_4	Molten carbonate salt	≈ 650°C	> 50%	200 kW – MW	Stationary: CHP
DMFC	CH_3OH	Solid polymer (proton conductor)	20 – 90°C	≈ 50%	mW – 1 kW	Portable: electronic systems
AFC	Pure H_2	Alkaline solutions	60 – 90°C	35 – 55%	1 – 250 kW	Stationary/ Portable: marine, space
PAFC	Pure H_2	Phosphoric acid	160 – 220°C	40%	20 – 200 kW	Stationary: CHP

Stationary applications

Stationary applications are those requiring the highest power and can be separated again into three subcategories: electricity and heat generator for domestic or industrial uses; backup power sources; power generation for off-grid sites. Figure I.8 presents the evolution of large scale (P > 200 kW) stationary systems deployed worldwide in the last
I.3.1 decade. It appears that this market is largely dominated by high-temperature operating FC (MCFC, SOFC, PAFC) because of their important power density and high electric efficiency. In addition, these technologies are also used at smaller scale for domestic usage. They present the advantage of generating both heat and electricity (CHP) and are thus more practical for water heating in houses, compared to a traditional heater that will not produce any electrical energy. In 2019, 80 MW of SOFC capacity and around 100 MW of PAFC capacity, although with a lower number of systems suggesting that the technology is preferred for larger power, were deployed worldwide [85].

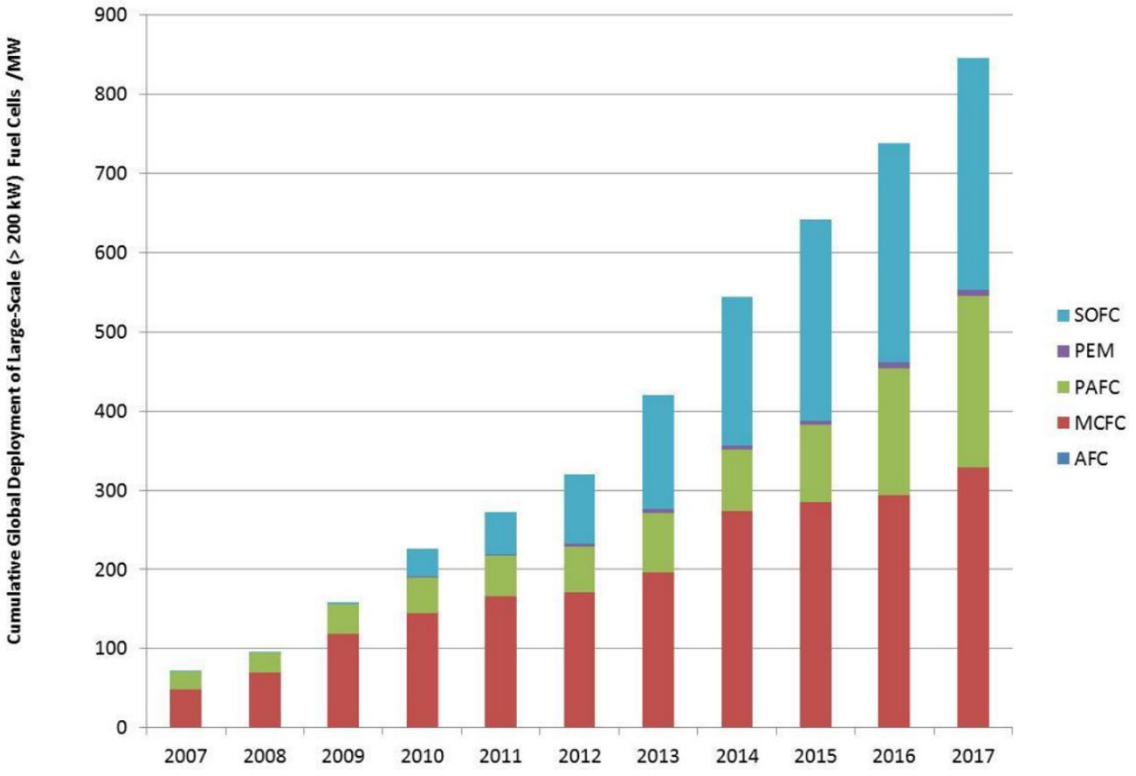

Figure I.8. Cumulative global deployment of large scale stationary fuel cells shown from 2007 onwards, displayed per technology. Reprinted from Ref [86].

Even if only few P > 200 kW PEMFC systems are deployed, this technology is actually well developed in the stationary market, especially for small power applications. It is also widely used for CHP domestic production (*i.e.* Ene-Farm) and can replace traditional power generator (fueled with fossil fuels) for supplying backup power in case of grid failure. Such systems are used in industries, hospitals or even data centers and are usually in the 1 to 10 kW range [87]. In addition, PEMFCs also cover the last

stationary application with the development of off-grid systems (*i.e.* Axane, Air Liquide's group, in France) for providing reliable electricity production in remote places (*i.e.* telecom relays) or developing countries. Overall, the PEMFC is the most developed and deployed FC technology, because of its versatility. Its stationary applications only cover a small portion of the total PEMFC capacity deployed, since the major part is dedicated to transports [85].

Transport application

Indeed, the transport applications are almost completely covered by PEM systems, with few DMFC or SOFC systems under development in 2019, with a total capacity of 900 MW in 2019 [85]. Transportation is one of the main GHG emission source, as explained in section I.1, and is a key market in our society: everyone relies on cars, public transports and shipments. It is therefore a primary focus to convert these applications to non-emitting technology. The PEMFC has played an essential role in that matter, with its emergence on every sector of the transportation spectrum.

I.3.2

- Domestic cars

There are three main vehicle constructors which commercialized Fuel Cell Electric Vehicles (FCEVs): Hyundai with the ix35 Fuel Cell and more recent NEXO SUV (2018) models, Toyota with the Mirai model and Honda with the Clarity FC model, and several other under development (Nissan, GM, Ford, Mercedez, etc.) using around 100 kW PEMFC systems. They were first commercialized in the first half of the 2010's and received continuous development with, for example, the range of the Clarity going up from 380 km upon release to 590 km with the 2016 model. In France, only few FCEV are circulating; however, Symbio (Michelin/Faurecia group) is developing a FC version of the Renault Kangoo, with 150 models delivered in 2016 [88]. The main advantages of FCEV compared to battery EV are the overall mass of the embedded power system and the refill *vs* reload time. Indeed, as Li-ion batteries progressively reach their maximum theoretical capacity [89], the only way to increase the overall energy density, and thus the range of the vehicle, is to increase the dimensions of the overall system, whereas only the hydrogen tank and/or its refill frequency must be addressed regarding FCEV. In addition, it only takes minutes to refill the hydrogen tank (generally 4-5 kg at 700 bar), where several hours are required to fully reload a car battery. The present deployment of hydrogen stations worldwide tends to facilitate the development of the overall FCEV fleet, mainly present in Asia and California today [85]. In addition, to prove their competitive aspect in comparison to other EV or even thermic vehicles, hydrogen race cars are being developed, like the Forze model or the MissionH24 project (GreenGT, Symbio).

- Shipment and handling vehicles

A large part of the transport emissions originates from merchandise transportation with cargo ships or heavy goods vehicles (HGV). The requirements for powering freighters solely by hydrogen is beyond the reach of FCs for now, but HGV are under development. Constructor like Nikola or Hyundai should deploy a fleet of several thousands of vehicles in Europe in 2020, with a 400 km range [85]. The main issue regarding hydrogen fueled trucks is the refueling of their tanks, and dedicated stations must thus be deployed: because a larger quantity of hydrogen is embedded, the hydrogen flow rates must be increased 5 to 6 times in order to limit the refueling time to 10 – 15 min and maintain a competitive cost of operation. The low refilling time, low maintenance and high energy density of PEMFC systems (compared to batteries) motivated the development of hydrogen fed forklift for materials handling: in 2013, more than 4000 PEMFC equipped forklifts were operating the USA. In France, HyPulsion and then PlugPower develop such forklift since 2012

- Passenger transport

Like other sectors, hydrogen fueled vehicles dedicated to public transports are under development and start to be deployed, like buses or even river shuttle. To prepare for the 2020 Olympics, 100 hydrogen buses were supposed to be in service in Tokyo and more than 1200 in 2023. Overall, FC-powered buses start to emerge in several countries and a significant portion of the total fleet should be fed by hydrogen by the next decade. Similarly, trains follow the same development with the priority in France to convert the remaining TER (Regional Express Trains) operating with diesel engine. Even if freighters are still out of the FC reach, small river shuttles have also been deployed with for example the Hydra, operating from 2000 to 2001 in Bonn (Germany) or the Navibus since 2018 in Nantes (France) powered by Symbio [90].

- Marine

In addition to river shuttles, other systems are developed for larger ships. To start the transition towards GHG free ships, Norway should deploy a hybrid (hydrogen/diesel) ferry with a 100 – 300 passenger capacity in 2020, as well as a first cargo with a 200 containers holding capacity fueled with diesel, batteries and hydrogen planned for 2026 using Hyon FCs. Moreover, a pusher barge will be tested in 2021 in Lyon (France) with 460 kg of hydrogen stored to fuel a 2 × 200 kW PEMFC system. The FC application in marine market is extended with Toyota announcing to power fishing ships by 2022 [85]. FC are also being investigated for submarine applications. However, because of the highly pressurized hydrogen being too dangerous for such conditions, fully liquid AFC systems will be preferred. This is true for all applications in a confined environment, like spacecraft.

Towards portable and mobile systems

I.3.3

Portable or mobile systems are defined by individual transportation or electronic devices that require smaller a power density (from hundreds of W to few kW) than other applications presented above and will focus more on a large energy density to operates for longer periods before needing refueling. For this reason, the PEMFC is not always the go to technology in this sector and DMFC are often considered. Examples of such applications bikes fueled by hydrogen such as the "αlpha" model commercialized by Pragma Industries in France (Figure I.9) powered by a 150 W PEMFC with a 150 km range and a low refueling time of 2 min (compared to hours for battery assisted bikes of the same power).

Figure I.9. The hydrogen fueled bike "αlpha" commercialized by Pragma Industries.

FC can also be used as portable power sources for military applications, such as the JENNY cell from SFC Energy, weighing from 1.7 to 3.3 kg with a corresponding energy density of 600 W.h to 1200 W.h. They operate using 25 W DMFC with fuel cartridges. However, because the focus in this sector is still turned on batteries, the development of small scale FC is more difficult and leading companies such as MyFC are forced to leave the market [85]. The next promising market might be Unmanned Aerial Vehicles (UAVs). Indeed, this market is largely growing for material handling and recreational uses, and drones present similar characteristics to forklift (where FC outperform batteries). Companies like Intelligent Energy commercialize power modules up to 2.4 kW for drones. In 2019 a drone flew for 70 min carrying a 5 kg load [85]. They also showcased in 2016 an embedded PEMFC system for powering laptops (Figure I.10). The interesting aspect of this system is the hydrogen source. Instead of standard pressurized tanks, sodium borohydride is used as the storage and hydrogen is realized to the FC through hydrolysis of the boron-based compound.

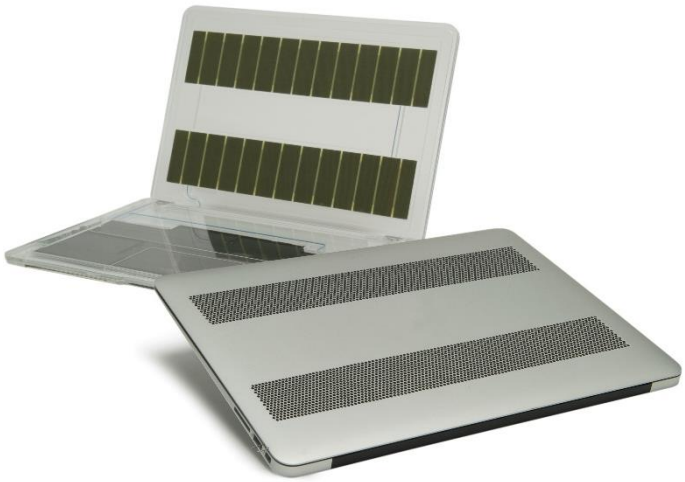

Figure I.10. Prototype of a fuel cell system for powering portable laptop developed by Intelligent Energy.

This system could be called an indirect borohydride FC, because borohydride is only used as a hydrogen carrier, in contrast to the Direct Borohydride Fuel Cell (DBFC) that will be investigated in detail throughout the whole manuscript. Such system is indeed well suited for portable applications, in particular because of its important energy density. It will be presented in more detail in the following section. It was also demonstrated with a prototype of van powered by PEMFC and sodium borohydride as hydrogen storage developed by Daimler-Chrysler in 2001 [91]

Overall, the fuel cell industry is in large expansion since the last decade and the current trend toward zero emission energy production and transportation will likely contribute to expand it even more over the next years/decades. The PEMFC is the most mature FC technology, because of its versatile characteristics and numerous advantages. However, in some applications, like high power stationary energy production, SOFC, PAFC or MCFC will often be preferred. Other technologies can present themselves more suited for niche applications such as the AFC for confined spaces (under-water or space) and the DMFC or even FC using exotic fuels (notably DBFC) for portable and mobile applications.

I.4.1

I.4 The Direct Borohydride Fuel Cell

Borohydride as a fuel

Boron-based compounds were mentioned above as a possible medium for solid hydrogen storage. However, they can also be considered as fuel in direct liquid FC, if dissolved in anolytes in the appropriate conditions. Several compounds such as

ammonia borane (NH_3BH_3), hydrazine borane ($N_2H_4BH_3$) or the sodium borohydride ($NaBH_4$) can be classified as "exotic fuels". Even if they all present interesting properties, the focus will now be placed on $NaBH_4$ and especially on its use directly as a fuel and not as a storage medium. Indeed, borohydride can be used for several applications, in particular in the chemical industry as a reducing agent, and can be electro-oxidized to generate electricity.

I.4.1.1 Production of borohydride

Borohydride in itself is not stable and must be associated to another compounds to form a salt: most commonly sodium borohydride $NaBH_4$. This molecule is not a naturally occurring material and was discovered by Schlesinger and Brown in 1940. Because their work was classified, the first study was however published in 1953 [92]. This chemical is now massively produced mainly through two different processes. The first one is the synthesis procedure developed by Schlesinger and Brown, and is still relevant. A schematic representation of the different steps involved is presented on Figure I.11. The figure is reprinted from Ref [93] with the following description of each step:

"*There are 7 steps such as: S1 as steam reforming of methane CH_4 to produce H2; S2 as electrolysis of sodium chloride NaCl to produce metallic sodium Na; S3 as refining of borax to make boric acid H_3BO_3; S4 as reaction of H3BO3with methanol CH_3OH to form trimethylborate $B(OCH_3)_3$; S5 as reaction of Na and H_2 to make sodium hydride NaH; S6 as reaction of NaH and $B(OCH_3)_3$ towards $NaBH_4$; S7 as recycling sodium methoxide $NaOCH_3$ to CH_3OH.*"

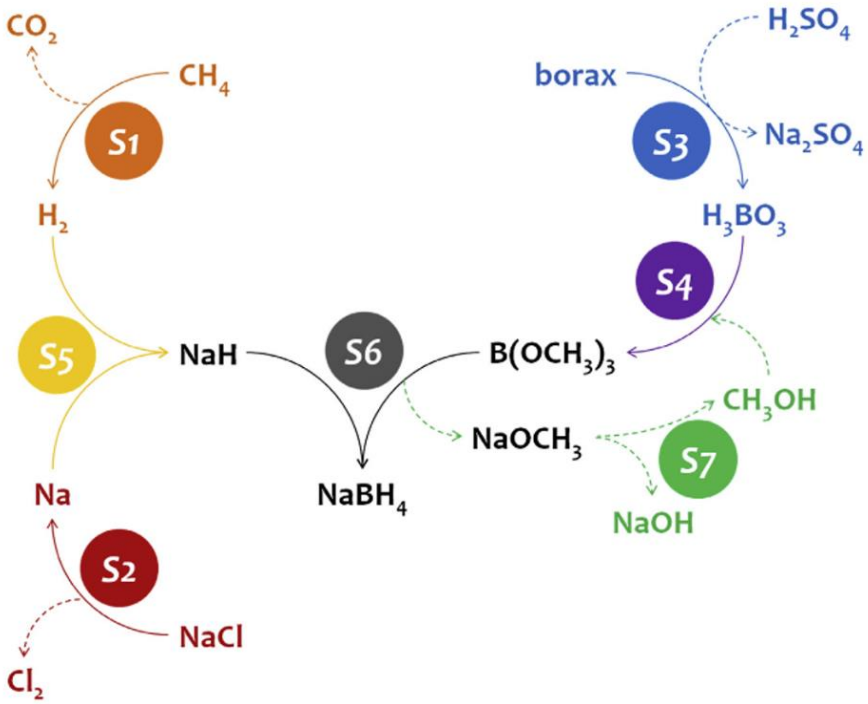

Figure I.11. Simplified scheme of the synthesis of $NaBH_4$ via the so-called Brown-Schlesinger process. Reprinted from Ref [93]

The overall reaction can be described by equation 1.1:

$$4\ NaH + B(OCH_3)_3 \rightarrow\ NaBH_4 + 3\ NaOCH_3 \qquad \text{(Brown-Schlesinger process, 1.1)}$$

This process presents the advantage of operating at atmospheric pressure and relatively low temperature (T = 250 – 270°C) Even though the reaction requires trimethylborates as precursor, it is directly obtained from borax ($Na_2B_4O_7$), a naturally occurring mineral. However, the other precursor, sodium hydride, requires the production of metallic sodium, a process highly inefficient with an electrical efficiency estimated around 50% [94]. The second main industrial process to produce borohydride was developed by Bayer and consists of a one-pot synthesis where borax, metallic sodium, hydrogen and silica are combined at high temperature (400 – 500°C) following equation 1.2:

$$Na_2B_4O_7 + 16\ Na + 8\ H_2 + 7\ SiO_2 \rightarrow\ 4\ NaBH_4 + 7\ Na_2SiO_3 \qquad \text{(Bayer process, 1.2)}$$

This one-pot method simplifies the overall production process. However, metallic sodium is still required, inducing the same inefficiency as the previous process. Moreover, the higher temperature required also reduces the overall energetic efficiency. With the increasing interest of sodium borohydride for hydrogen storage, the scientific community restarted to develop new synthesis procedures since 2000, accompanied with related patents [95]. One of the promising methods is to produce $NaBH_4$ from sodium metaborate ($NaBO_2$), via electro-synthesis [96] or using reducing agents [97,98], which would create a circular and sustainable production route since this precursor is the final product of the oxidation of borohydride (as detailed in the next sections).

Overall, these new synthesis procedures still require much work and development to become competitive to the two main industrial ones. They are both based on the restructuration of borax, which can raise the question about the sustainability of using borohydride. Borax is found in evaporate deposits produced during the evaporation of seasonal lake and salted lakes. The main deposits are localized in Turkey and California, but borax is also found all around the world, and even if the production increases every year the world reserve is still largely abundant [99].

I.4.1.2 Properties of borohydride

Sodium borohydride is a white odorless and non-toxic powder with a high melting point of T = 505°C, it will however start to decompose at T = 400°C. It presents the advantage of having the second highest gravimetric hydrogen density in the hydride family (behind $LiBH_4$), due to the low mass of the boron atom [95]. This induces an important energy density notably because of the presence of 4 hydrogen atoms per molecule. Besides the hydrogen storage application, which is rather recent [100,101], its main usage is as a reducing agent in organic reactions [102–104], and in industry for the

manufacture of pharmaceuticals, synthesis of other fine chemicals, or more recently, in synthesis of nano-scaled objects by reducing metallic salts to from nanoparticles supported on carbon [105–107], even though this property was already reported in 1956 by Brown *et al.* [108]. Such materials are the typical electrocatalysts used as active layers in a FC system. For all these applications, the borohydride is used in its ionic form (BH_4^-) and therefore must be dissolved. $NaBH_4$ is highly soluble in water (solubility limit: 550 g per 100 g of H_2O [109]), however, the BH_4^- ion is unstable in water and will decompose into a stable borate species and release its contained hydrogen atoms following the hydrolysis reaction described by equation 1.3.

$$BH_4^- + 2\,H_2O \rightarrow BO_2^- + 4\,H_2 \qquad \text{(equation 1.3)}$$

This reaction, producing gaseous hydrogen, is the main process occurring when borohydride is used as a hydrogen storage medium and its rate must thus be enhanced using metallic catalysts in order to reach significant H_2 generation [101,110]. One of the beneficial aspect of this hydrolysis reaction is that 50% of the produced hydrogen originates from water. However, for utilization as a fuel in a DBFC, borohydride must maintain the highest chemical stability possible once fed into a FC, in order to be oxidized through the Borohydride Oxidation Reaction (BOR) (equation 1.4).

$$BH_4^- + 8\,OH^- \rightarrow BO_2^- + 6\,H_2O + 8\,e^- \quad E^o_{BH_4^-/BO_2^-} = -1.24\ \text{V}\ vs\ \text{SHE} \qquad \text{(equation 1.4)}$$

This stability was determined to be dependent on both the pH of the solution and its temperature [111,112], and a strongly alkaline electrolyte will significantly slow down the rate of the hydrolysis reaction. The half-life of BH_4^- is estimated at 6.1 min, 10.2 h, 42.6 days and 426.2 days at respective pH of 9, 11, 13 and 14 [113]. It is commonly accepted that borohydride is stable for pH > 12 [114] and in general the OH^- concentration used in anolytes utilized for the BOR ranges from 0.1 M to 4 M, depending on the application (*i.e.* from laboratory to FC scale).

This anodic reaction (equation 1.4) is the core of a DBFC and what differentiates this FC from standard PEMFCs (or AFCs in this case because of the alkalinity of the electrolyte). It was first reported in 1962 by Indig and Snyder [115] that borohydride could be used as a fuel by electro-oxidizing it using metallic anodes (in their case Ni). Interestingly, they already reported that the oxidation of borohydride is accompanied by a strong hydrogen generation and that "The gassing rate increased with the electrochemical oxidation, and at a rate of 775 $mA.cm^{-2}$ much hydrogen was evolved. This indicated that hydrogen was formed as a product of the electrochemical oxidation." Olu later assigned this generation mainly to hydrolysis [113] but it will be demonstrated in detail later in this manuscript (Chapter 4 and 5) that the first intuition of Indig and Snyder was in fact correct and H_2 is a reaction product on a Ni electrode.

The BOR presents several interesting properties, such as its really low theoretical standard potential of $E^{o}_{BH_4^-/BO_2^-}$ = -1.24 V *vs* NHE at pH = 14 (or -0.41 V *vs* RHE) and 8 electrons produced per BH_4^- species fully oxidized (compared to 2 per H_2 oxidized for the Hydrogen Oxidation Reaction, HOR). However, this high number of electrons also induces a much more complex reaction, with a lot of elementary steps and intermediate species. Numerous studies have been performed to understand the mechanism of this reaction, and its current understanding by our group will be detailed later in Chapter III. The low theoretical standard potential is a promising property towards FC application, since it could provide a 400 mV increase of voltage per cell compared to standard H_2 based technologies. However, because the anolyte is aqueous, it means that for potentials below 0 V *vs* RHE, the evolution of hydrogen, a reduction reaction, will be thermodynamically favored and will result in the emergence of a mixed potential affecting the real onset of the oxidation reaction. Again, this issue will be discussed in detail in the following Chapters.

I.4.2 Operation principles of a DBFC

As mentioned above, the BOR is the main difference between an AFCs operating on H_2 and a DBFC, as it replaces the HOR as the anodic reaction. To close the circuit and generate power, the Oxygen Reduction Reaction (ORR in alkaline medium, equation 1.5) is most often considered (it is the most common cathodic reaction in conventional FCs). However, because the anode is already fueled with a liquid anolyte, it is also possible to use liquid catholyte with the Hydrogen Peroxide Reduction Reaction (HPRR, equation 1.6):

$$O_2 + 2\,H_2O + 4\,e^- \rightarrow 4\,OH^- \qquad (E^0 = 0.40\ \text{V vs. SHE, pH} = 14) \qquad \text{(equation 1.5)}$$

$$H_2O_2 + 2\,H^+ + 2\,e^- \rightarrow 2\,H_2O \qquad (E^0 = 1.76\ \text{V } \textit{vs}\text{. SHE, pH} = 0) \qquad \text{(equation 1.6)}$$

That way, a fully liquid-fed FC system is obtained, which is of great interest for applications in confined spaces such as submarines, and has been investigated for several years [116–118] because of theoretical better performance than the O_2 DBFC. Indeed, by using the HPRR a theoretical Open Circuit Voltage (OCV) of 3.01 V could be reached for a single cell compared to 1.64 V for the O_2 DBFC. This value is very impressive for a system operating in aqueous medium. However, because H_2O_2 is only stable in highly acid medium, a huge pH gradient exists between the two electrodes ($\Delta pH = pH_{anode} - pH_{cathode} \approx 14$). If this gradient is stably maintained during operation of the cell (this requires specific conditions detailed later in the paragraph dedicated to the use of different membranes), a junction voltage appears (830 mV) from water protolysis, to provide both H^+ and OH^- ions, and results in a decrease of the theoretical OCV down

to 2.18 V. The overall reaction for O_2 DBFC and H_2O_2 DBFC systems are detailed by equation 1.7 and 1.8 respectively:

$$BH_4^- + 2\,O_2 \rightarrow BO_2^- + 2\,H_2O \qquad (U_{cell}^{th} = 1.64\ V) \qquad \text{(equation 1.7)}$$

$$BH_4^- + 4\,H_2O_2 \rightarrow BO_2^- + 6\,H_2O \qquad (U_{cell}^{th} = 2.18\ V) \qquad \text{(equation 1.8)}$$

The structure of both DBFC unit cells is however the same and is schematically described by Figure I.12. The composition of the cell is actually similar to a standard PEMFC or other FC technologies and can be separated in three main layers:

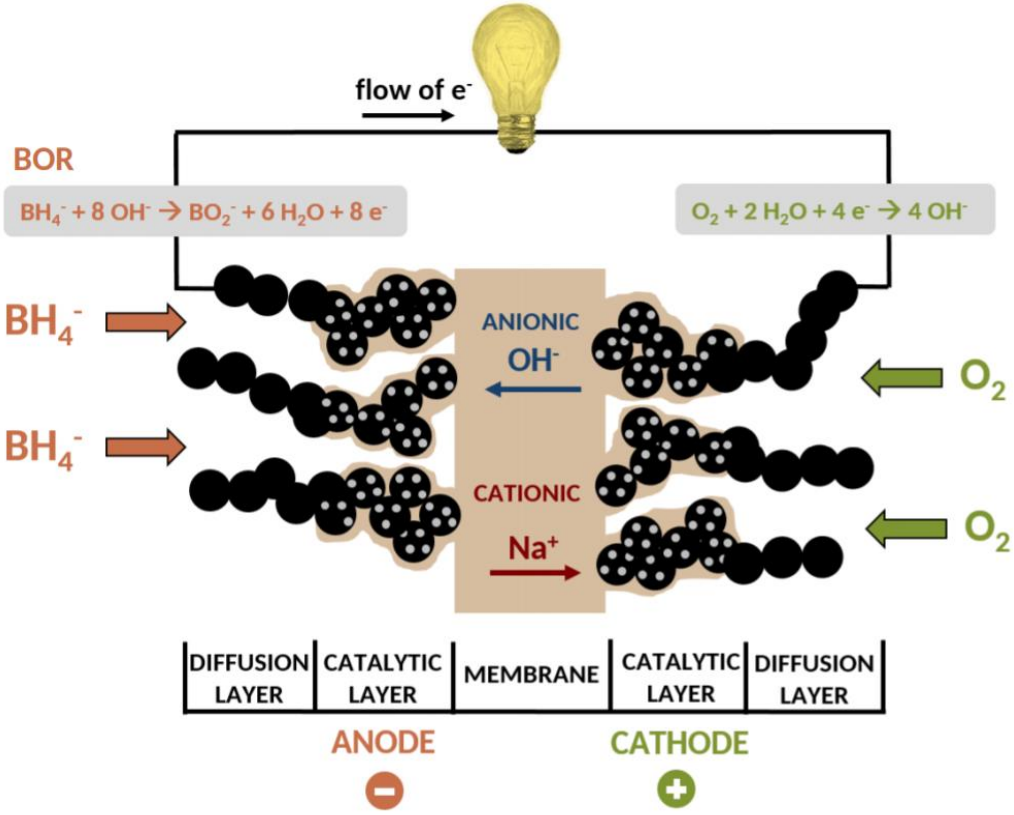

Figure I.12. Structural composition of a BH_4^-/O_2 DBFC unit cell. Reprinted from Ref [119].

- An anode that is the main seat of the anodic reaction, in this case the BOR (equation 1.4). It can itself be separated into two sub layers: the diffusion layer that serves to bring the active species to the active layer, where they are catalyzed by the electrocatalysts materials (detailed in "Anode materials" section). The produced electrons are then conducted to the current collector through the diffusion layer: it must thus be electrically conductive and present a large porosity to limit mass-transport related issues in the cell. Most commonly commercial carbon papers are used to fulfil this role.

- A cathode that is structured similarly as the previous electrode, with a diffusion layer (carbon paper) and an active layer with electrocatalysts, specifically designed for the cathodic reaction (see the "Cathode materials" section for more details).
- A membrane is used as a separator between the two electrodes and electrolytes to hinder short-circuits. However, to close the electrical circuit, it is necessary for this membrane to conduct ionic charge carriers from one electrode to the other. In a DBFC system, both Cation Exchange Membranes (CEMs) or Anion Exchange Membrane (AEMs) can be used, resulting in the conduction of Na^+ or OH^- carrier, respectively. The benefits and drawbacks of each membrane will be discussed further in the next sections and in Chapter V. Because of the liquid nature of the anolyte, no additional ionomer is required at the active layer for the ion conduction to the membrane. Nevertheless, such polymer is still used in commercial and standard anode design to bind the electrocatalyst nanoparticles to the carbon support. (This statement applies to the cathode if fed by liquid catholyte).

The different variables involved in the DBFC operation were reviewed by Olu *et al.* [120] in 2016. The geometric surface area of the anode was presented as highly affecting the overall DBFC performance with smaller electrodes displaying higher power densities in similar conditions [121,122]. It is then reported that the anolyte flow rate might contribute to largely improve the performance of the cell [123,124] or have little influence [122,125,126]. These different observations all suggest that the reactant transport conditions must be carefully studied for a given DBFC configuration in order to maximize its resulting power density, as recently confirmed by Prof. Ramani's group [127,128]. The morphology of the anodic active layer was also demonstrated by Olu *et al.* [129] to be a major variable to reach high power. This will be discussed in detail in Chapter V of this manuscript.

In 2014, the advantages and drawbacks of the DBFC were listed by Sharaf *et al.* [130], compared to other FC technologies: they are reported in Table I.2. At first sight, this list of drawbacks appears detrimental towards the development of DBFC for real applications compared to the advantages presented. However, its high OCV is not mentioned as well as its good theoretical specific energy which is 50% higher than the one of a DMFC, a commercialized system (9 $kWh.kg^{-1}$ and 6 $kWh.kg^{-1}$ respectively). In addition, several of the hindrances listed are not so true to this day: promising power densities over $P = 800$ $mW.cm^{-2}$ were reached recently with a H_2O_2 DBFC unit cell [128]; the BOR mechanism has been thoroughly investigated by Olu on Pt and Pd electrodes [113,129,131] and with the additions of this manuscript, a satisfying model of the reaction is obtained; to cover the cost of the catalysts, a global effort is made to move towards non-Platinum Group Metal (PGM) electrodes (see section III.4). Similarly, the stability of membranes, especially AEM has largely been improved in the last years (see

the "Different membrane configurations" section). The inefficiency of the cathodic reaction is enhanced by the fuel crossover and will be discussed in the section dedicated to the membranes however, this issue is present in all FC systems relying on ORR. Major progress has been made that will profit the DBFC. However, its commercialization is still hindered by the remaining issues: (i) the high cost, mainly due to the borohydride production and the use of PGM-based electrodes and (ii) the hydrogen released during operation, directly translated in an efficiency loss because electrons stored in BH_4^- are not fully valorized but partly lost in the form of molecular hydrogen.

Table I.2. Specific advantaged and drawbacks of a DBFC system compared to other FC technologies. Adapted from Ref [130].

Specific advantages	Specific drawbacks
Compact size	Fuel crossover
High fuel gravimetric hydrogen density	High cost
No CO_2 produced	Low power density
Low-toxicity and environmentally-friendly operation	Lack of analytical modelling due to unknown BOR mechanism
	Expensive catalyst
	Chemical instability of membrane and catalysts
	Inefficient Cathodic reduction reaction
	Inefficient anodic oxidation reaction due to significant hydrogen evolution

I.4.2.1 Anode materials

The electrocatalyst materials used in DBFC anodes were reviewed by Olu *et al.* [120]. What arises from this study is that noble metals are the most widely used and most active electrocatalysts towards the BOR. Non-noble electrocatalysts have been investigated with an increasing attention over the years, but with overall low performance. A more detailed description of these materials will be presented in section III.4. A brief list of the most commonly used noble metals and their respective advantages and drawbacks toward the BOR is presented below:

- Platinum

Platinum is considered as the best and most commonly used electrocatalyst for the BOR, so far. The mechanism of the reaction as it was understood at the start of this PhD will be detailed for Pt and Au surfaces in the section "III.1. Current understanding of the BOR on Pt electrodes". This noble metal is also the most active for the hydrogen reactions in alkaline medium [132–134], resulting in a good valorization of the

hydrogen formed during the BOR and thus 8 electrons produced at relatively low potentials. Such activity has also a downside since the Hydrogen Evolution Reaction (HER) will quickly become predominant at potentials below E = 0 V *vs* RHE, resulting in a BOR onset potential close to E = 0 V *vs* RHE. The 400 mV negative shift theoretically forecast by the standard potential of the BH_4^-/BO_2^- couple is thus not obtained in practice. Moreover, Pt is also a good catalyst for the heterogeneous hydrolysis of borohydride, which is detrimental for long-term operation in DBFC configuration [135,136]. Furthermore, a detrimental self-poisoning effect was reported by Finkelstein *et al.* [137]. It is still (one of) the best electrocatalysts for the BOR but the presented issues indicate that the full potential of the borohydride as a fuel cannot be exploited with a Pt-based anode. In addition, the high cost and low availability of Pt motivate the search of other BOR electrocatalysts.

- Gold

Gold is historically the second most investigated BOR catalysts. It was actually the main constituent (97% Au, 3% Pt) in the first DBFC anode reported in the literature, by Amendola *et al.* [138]. It was presented as an efficient electrocatalyst towards this reaction [125,139–141] because of its low BH_4^- heterogeneous hydrolysis activity (compared to Pt [135]). However, this metal is not an efficient electrocatalyst towards this anodic reaction, as reported by Chatenet *et al.* in 2010 [142], mainly because of too high activation potentials translating in a high onset potential (E_{onset} = 0.3 V *vs* RHE) [143]. It is now mostly studied for fundamental purposes, in particular to understand the BOR mechanism [143,144]. However, it is still common to observe new studies emerging using Au-based anodes with poor to average activity [145–147].

- Palladium

Palladium is nowadays as much investigated as Pt as an electrocatalyst for the BOR because of their similar activity in DBFC configuration [129,148,149]. Actually, the highest DBFC power densities reported were obtained using Pd-based anodes instead of Pt in both O_2 [150] and H_2O_2 configurations [128,151]. The reasons behind this good activity are yet not understood, since the behavior of the BOR on Pd surfaces appears largely different from the one occurring on Pt in a half-cell configuration [129,152]. BOR on Pd displays low onset potential (-0.2 V *vs* RHE) with a number of electron exchanged varying from 4 to 8 [152,153]. Indeed, the reaction starts with a first partial reaction wave (hence the 4 e^-). However, few mechanistic studies published so far do not provide enough information to unravel this different behavior.

I.4.2.2 Cathode materials

The most used cathode electrocatalyst for both the ORR and HPRR is platinum. Since the anodic reaction is usually the main focus in a DBFC system, cathodes are commonly highly loaded (typically 1 – 2 $mg_{Pt}.cm^{-2}$) and commercial Pt electrodes are used. They are composed of an active microporous layer (MPL) (Pt nanoparticles deposited on Vulcan XC-72 + Nafion binder) and a gas diffusion layer (GDL) (carbon paper). That way, the cathodic reaction will not be limiting and the BOR can be correctly studied. However, some studies still focus the cathodic reaction or aim to develop fully non-noble DBFC cells therefore avoiding PGM at the anode but also the cathode. In that case, several families of ORR catalysts are considered such as MnO_2-based [154–156], Co-based [157,158], Fe-based [159,160] or La-based [121,161] catalyst materials. Similarly as the anode, the cathodic efficiency also depends on additional variables such as the oxygen partial pressure, relative humidity, gas flow rate etc. that must also be optimized for each DBFC configuration in order to reach the full potential provided by the electrode materials [120].

I.4.2.3 Different membrane configurations

As mentioned above, both CEM or AEM can be used in a DBFC cell. However, CEMs are the most commonly-used due to the commercial availability of Nafion ®. This cation exchange polymer is the most developed one and is conventionally used in PEMFC to conduct H^+ charge carriers from the anode to the cathode. When used in an alkaline environment, such as the DBFC, no protons are available, so other cations are used as charge carrier instead. The large sodium hydroxide concentration of the anolyte will result in a functionalization of the Nafion membrane to conduct Na^+ ions to the cathode. This spontaneous ion exchange allows the DBFC to operates with a CEM in alkaline conditions, but also induces two major issues: (i) the overall conductivity of the membrane is divided by 4 (compared to the standard H^+ form) [162] resulting in large Ohmic losses in the cell. To limit such losses, the thickness of the membrane can be reduced, but this will also increase its permeability to BH_4^- species that will lower the cathode efficiency (by establishing mixed potential at the cathode) [163–165]. In the end, thinner membranes will still be favored to reach higher power densities. (ii) The second issue induced by the conduction of Na^+ to the cathode is the formation of solid sodium hydroxide. Indeed, Na^+ cations will react with the OH^- species produced by the ORR in alkaline medium to form crystalline NaOH (with some boron species due to BH_4^- crossover) as presented by Jamard *et al.* [166]. After long-term operation, the current collector in the cathodic compartment was largely blocked by solid crystals (Figure I.13).

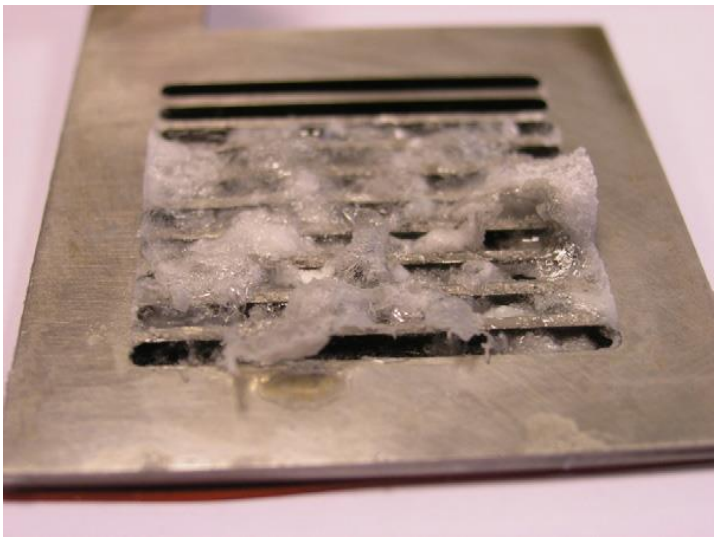

Figure I.13. Photograph of the current collector of an air cathode after prolonged operation in DBFC conditions, highlighting the formation of solid sodium hydroxide. Reprinted from Ref [166].

The use of AEM in a DBFC will prevent both issues: OH^- charge carriers are conducted from the cathode to the anode, the latter not being affected because of already large hydroxide concentration; because it is the normal conduction mode, the conductivity of the membrane will not be modified and the overall cell ohmic losses will only depend on the intrinsic conductivity of the AEM. However, in addition to OH^-, BH_4^- ions will also be conducted to the cathode in larger quantities than with a CEM (where they only cross the membrane via diffusion), resulting in lower overall OCV of the DBFC unit cell. In the past, the chemical stability of such membranes was too low for long-term operation and was thus the main lock hindering their use to spread significantly. However, the interest in developing stable AEMs largely increased in the last years [167], notably because AFCs can operate with non-PGM electrocatalysts. Several DBFC studies were presented using AEM [156,168,169], but progress is still required in this field. In addition, and following the global trend, several polymer companies such as Fumasep ®, Xergy ®, or Sustainion®, started to commercialize AEM and ionomers. Overall, the use of such membranes in DBFC is still at an early stage, but impressive results obtained in AFCs [170] suggests that the performance will keep increasing.

The H_2O_2 DBFC was mentioned to operate with an alkaline anode and acidic cathode with a pH gradient of around 14. The two different types of membranes presented above are not able to maintain such gradient between the two electrodes and this will result in an efficiency loss. To maintain such gradient, bipolar interfaces have been investigated with various application targets [171–173] and more recently for electrochemical energy converters such as redox-flow batteries [174] and DBFCs [151,175–177]. The principle of such interface is rather simple: an Anion Exchange Ionomer (AEI) is placed at the anode and a Cation Exchange Ionomer (CEI) at the

cathode. Water is dissociate into H^+ and OH^- (protolysis), inducing a 830 mV junction loss described earlier, at their interface supplying both ionomers with their respective charge carriers [178]. It was however demonstrated by Shen *et al.* [179] that in practice, the morphology of the junction greatly affects the overall performance of the bipolar interface.

I.5 Conclusion and context and objectives of the PhD

The main scientific objective of the 21st century is to limit the global warming of Earth's atmosphere to +1.5°C compared to the pre-industrial era's average temperature. This will only dampen the consequences and a significant climate change is now inevitable, and already affects our lives with more heatwaves, tropical storms, etc. To this goal, it is mandatory to decarbonize the energy production and utilization currently used all around the world. This will most likely be achieved by using emerging renewable technologies harvesting energy from sustainable resources such as the wind, solar radiations, hydraulic movements, etc. Because of the intermittent nature of renewable energies, the development of energy storage systems is required. In addition, the standard thermal engines fed by fossil fuels powering all our means of transport must also be replaced by GHG emission-free systems. Fuel cells are practical devices to convert chemical energy (mainly in the form of hydrogen) to electrical energy and can answer these two problematics. The PEMFC is dominating the market due to its high versatility and high efficiency. However, for some niche applications, such as the powering of portable and mobile devices, other technologies, such as the DBFC, could be more suited. Thanks to the solid (for storage) or liquid (for utilization) state of borohydride, all the issues of compression, purification, storage, and safety related to the use of gaseous hydrogen are avoided.

The interest in to DBFC has been constantly increasing over the years and the performance of this system keeps growing thanks to new materials created especially for this "exotic" FC. However, the core of the cell, the anodic BOR, is still not correctly understood by the scientific community due to its high complexity. In addition, the reaction mechanism can vary depending of the considered electrocatalyst nature. Mechanistic studies are thus required for each metal studied in order to understand the reaction and to be able to design materials best suited to reach high performance. Moreover, one of the primary hindrances to the commercialization of the DBFC technology is its high cost, induced by two main factors: (i) the cost of borohydride production, (ii) the utilization of Pt at both electrodes.

In that context, this PhD aims to answer three main problematics: the understanding of the BOR mechanism at noble metal electrodes and particularly in DBFC operating conditions; the search of an efficient non-noble metal BOR electrocatalyst; and the development and optimization of low-cost DBFC anodes. It is part of the MobiDiC (**Mobi**le **Di**rect Borohydride Fuel **C**ells) project funded by the French National Research Agency (ANR). This project aims to fulfil the same objectives as the PhD and to move closer to real DBFC systems with the development of a demonstrator prototype system. This project includes five institutions with different attributed tasks: (i) the Laboratoire d'Electrochimie et de Physicochime des Matériaux et des Interfaces (LEPMI, Grenoble, France), represented by Prof. Marian Chatenet, aimed to study the BOR in DBFC conditions as well as investigate non-noble metal electrocatalysts and design structured DBFC anodes; (ii) the Institut de Chimie et Procédés pour l'Energie, l'Environnement et la Santé (ICPEES, Strasbourg, France), represented by Prof. Elena Savinova and Dr. Antoine Bonnefont, focused on the mechanistic studies of the BOR in DBFC conditions on noble metal electrodes and the simulation of the reaction kinetics as well as the investigation of non-noble metal BOR electrocatalysts. The design of DBFC anodes was also investigated at ICPEES; (iii) the Laboratoire d'Energetique et de Mécanique Théorique et Appliquée (LEMTA, Nancy, France), represented by Prof. Gaël Maranzana, performed the DBFC unit cell studies with the materials tested upstream in LEPMI and ICPEES; (iv) the Institut Européen des Membranes (IEM, Montpellier, France), represented by Prof. Umit Demirci, studied the chemistry of boron species to unveil questions on hydrolysis of borohydride as well as possible reactional intermediate species.; (v) Pragma Industries (Biarritz, France), represented by Remi Succoja and Renaut Mosdale, is the industrial partner of the project and took part in developing the DBFC demonstrator prototype. Unfortunately, because of administrative issues, Pragma Industries joined the project late and its tasks could not come to fruition.

This thesis will therefore be built around the three problematic described above and structured in four additional Chapters:

Chapter II presents the materials and methods, used to obtain the results presented in this manuscript, such as the electrochemical measurements, the elaboration of nickel-based electrocatalysts, the DBFC tests, the computational methods and the characterization techniques employed.

Chapter III focuses on the BOR mechanism on noble metals (Pt, Au and Pd) in DBFC operation conditions (high borohydride concentrations): the model proposed by Olu during his PhD is updated and a particular attention is given to understand the reaction behavior on Pd.

Chapter IV deals with the elaboration of efficient non-noble metal BOR electrocatalysts, the case of Ni is presented and the effect of its state of surface is highlighted.

Chapter V closes this thesis by presenting efficient non-noble metal DBFC anodes using the Ni electrocatalysts developed in Chapter IV. The structure of the anode is then optimized and tested in various DBFC configurations with promising results.

CHAPTER II: Materials and methods

In this chapter, the experimental setup and procedures will be detailed. First the electrochemical measurements will be addressed, with description of how electrodes are prepared and how they are used in alkaline medium. The second section will focus on the preparation of metallic nickel electrodes, followed by quick descriptions of the characterization techniques and protocols used during this PhD. Two different unit DBFC setups will be detailed subsequently, with their main difference being the oxidant used at the cathode (gaseous O_2 or liquid H_2O_2). To finalize the chapter, the equations used for the micro-kinetic modelling will be quickly presented.

II.1 Electrochemical measurements

Rotating Disk Electrode in alkaline medium

II.1.1 As mentioned in the previous chapter, the borohydride ion (BH_4^-) is only stable when the pH of the solution exceeds 12. To study the BOR, and thus limit the decomposition of the fuel, it is therefore mandatory to work in strong alkaline electrolytes: 1 M or 4 M NaOH solutions are prepared from highly pure mono-hydrated sodium hydroxide crystals (99.999% purity, Merck Suprapur®) and ultrapure water (18.2 MΩ, <3 ppb total organic carbon, MiliQ-gradient + Elix, Millipore®) in order to limit the contamination by organic species. This NaOH concentration is changed from 1 M to 4 M when the concentration of borohydride is increased to the operation conditions of a DBFC unit cell: $NaBH_4$ powder (98+% purity, Merck Suprapur®) is used to obtain solutions with [$NaBH_4$] ranging from 10^{-6} M to 1.5 M.

The majority of electrochemical measurements made during this PhD are performed using a gas-tight 4-electrodes electrochemical glass cell made of Pyrex®. The cell is homemade designed and blown by Verre Equipements®. A schematic representation of the cell is presented on Figure II.1. First of all, to avoid contamination from silicates or other chemicals originating from the glass corrosion in strong alkaline solutions [180], the electrolyte is contained in a homemade polytetrafluoroethylene (PTFE, Teflon®) beaker placed in the cell. Prior to any measurement, the cell and its annexes are immersed in Caroic acid (H_2SO_5) overnight, to avoid any pollution of the electrolyte by organic species normally adsorbed on all surfaces, and then thoroughly rinsed in ultrapure water. A Rotating Disk electrode (RDE) (Origatrode®, Origalys) is used as the working electrode (WE) support in order to control the convection conditions and vary the mass-transport of the active species from the bulk of the electrolyte to the WE surface. This WE is usually a polished disk of the studied material encased in a shaft (see next section) and screwed to the RDE. A glassy carbon (GC) plate (Sigradur®) is

used as the counter electrode (CE) and the current is collected thanks to a gold wire (not immersed in the electrolyte to avoid possible contamination by Au^{x+} cations. In some cases, a Pt wire replaces the GC plate as the CE but it will be discussed in the core of the text. A homemade reversible hydrogen electrode (RHE), freshly prepared prior to each measurement to ensure its stability, is most of the time used as the reference electrode. It is sometimes replaced by a commercial mercury/mercurous oxide electrode (Hg/HgO in 1 M NaOH, IJ Cambria®). However, the potential value is always converted to the RHE scale for clarity ($E_{Hg/HgO}$ = -0.926 V *vs* RHE for 1 M NaOH [181]).

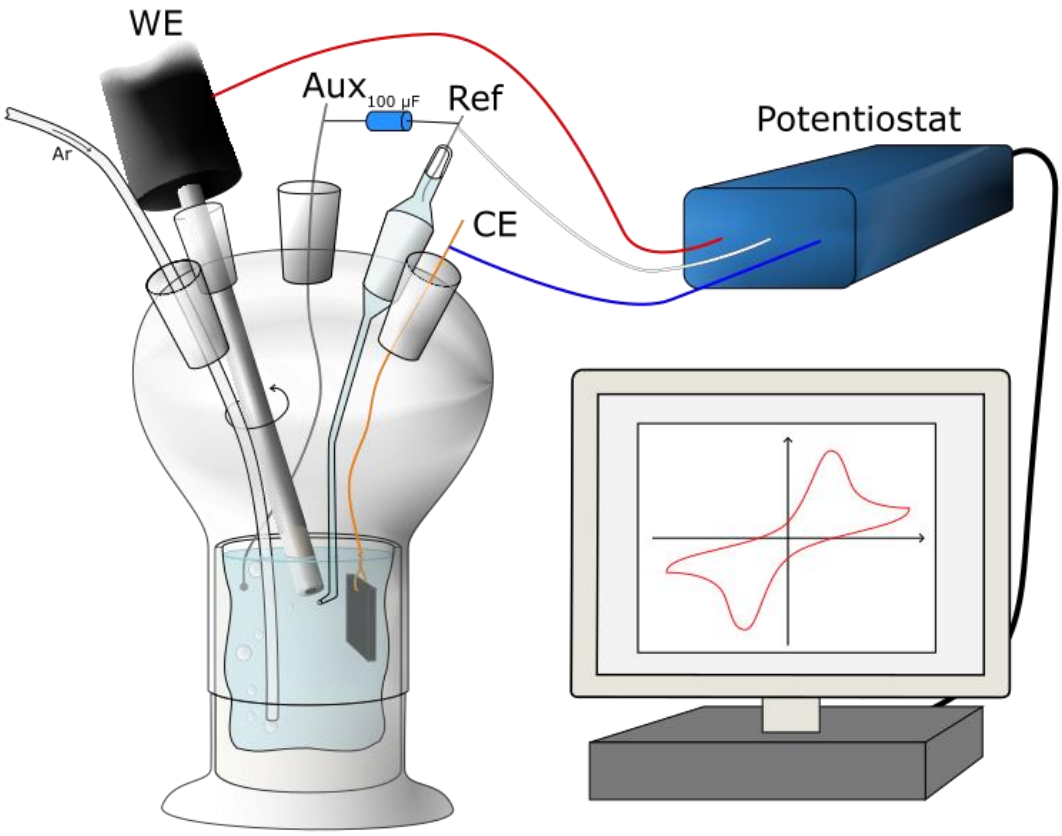

Figure II.1. Diagram of a 4-electrodes electrochemical cell connected to a potentiostat to perform electrochemical measurements.

In usual RDE configurations, only 3 electrodes are used. However, because of important perturbations caused by high-frequency (electrical) noise in LEPMI, a fourth auxiliary electrode is added in this setup. It consists of a gold or platinum wire slightly immersed in the electrolyte (to close the electrical circuit) and connected to the reference electrode through a capacitor bridge (usually 100 µF) and will act as a low-pass filter to limit such noise on the electrochemical measurements. Finally, a last entry is used to bubble inert gas (Ar or N_2, 99.999% purity, Messer®) in the electrolyte and deaerate the solution (to remove dissolved O_2) and therefore limit the contribution of the Oxygen Reduction Reaction (ORR) that occurs in the studied potential window and could modify the

overall faradic current. These 4 electrodes are connected to a computer-controlled potentiostat that applies/measures the desired potentials or currents. During this PhD several potentiostats are used: Biologic VMP-2; Biologic SP-150; Gamry REF 600; Autolab PGSTAT302F; Solartron PARSTAT. To control the temperature of the cell, a cryothermostatic bath is used and allowed characterization at T = [10, 20, 30] °C even if the temperature is mainly maintained to ambient conditions. All the electrochemical characterizations are ohmic drop compensated in dynamic mode (85%). The typical value of this ohmic drop in RDE configuration and 1 M NaOH is comprised between 5 and 10 Ω depending on the WE surfac.

In all RDE measurements presented in the core of the manuscript, two different potential regions are considered: "the full potential window -0.2 V < E < 1.5 V *vs* RHE" and "the reduced potential window -0.2 V < E < 0.4 V *vs* RHE". Prior to any electrochemical measurements, each electrode is subjected to two cyclic voltammetry (CV) pretreatment steps in supporting electrolyte (1 M NaOH) to clean the surface from adsorbates and to always start a characterization from the same initial state: 10 cycles at v_s = 100 mV.s^{-1} followed by 5 cycles at v_s = 20 mV.s^{-1} in the potential window studied. The typical CVs obtained in supporting electrolyte for Pt, Au and Pd electrode are presented in Figure II.2

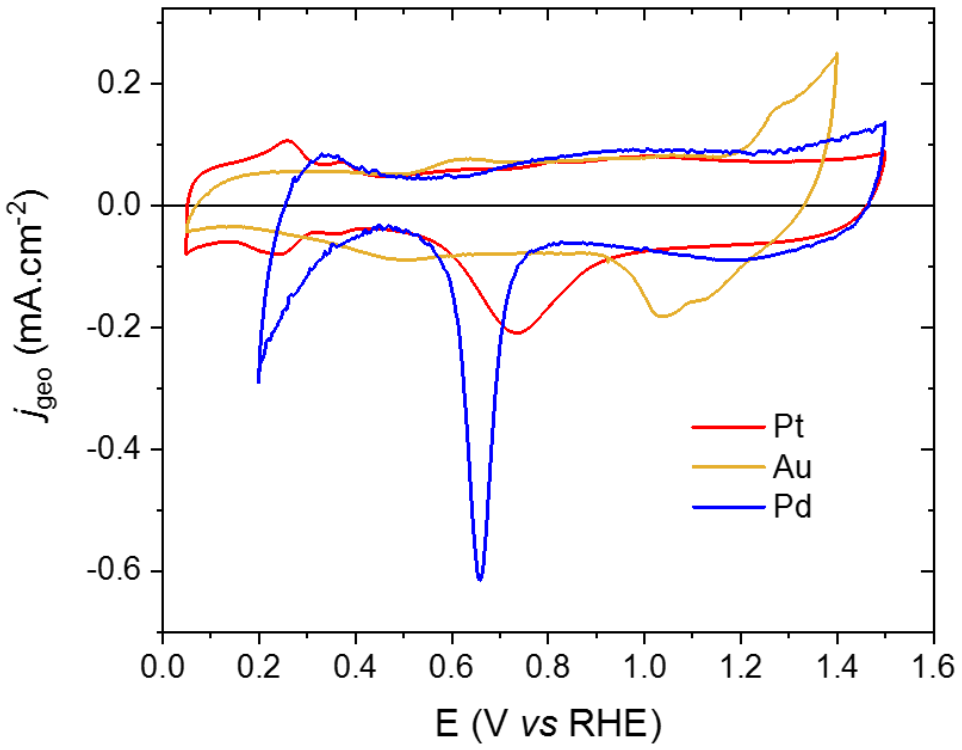

Figure II.2. CVs in supporting electrolyte (1 M NaOH) of noble mirror-polished noble metal electrodes: Pt, Au and Pd. S_{geo} = 0.031 cm², v_s = 20 mV.s^{-1}, ω = 0 rpm, T = 20°C, Ar-saturated electrolyte.

II.1.2 Electrodes and catalyst inks preparation

II.1.2.1 Bulk polycrystalline electrodes

Before studying the BOR on highly developed surface area electrodes, more fundamental measurements are performed in order to investigate the different reaction mechanisms on different electrocatalysts. To perform such study, it is important to work on a "model" surface. To do so, 2 mm wide Pt, Au, Pd (S_{geo} = 0.031 cm²) and 5 mm wide Ni (S_{geo} = 0.196 cm²) bulk polycrystalline disks (99.9%, MaTecK®) (encased in a homemade PTFE (Teflon) or PCTFE (Kel-F) shaft) are polished down to a mirror like surface using the following procedure: firstly, the electrode is polished from is rough initial state to a near mirror state using mechanical polishing machine and several silicon carbide polishing discs (Presi®) with decreasing grain size (from 1600 grains.inch^{-2} to 4000 grains.inch^{-2}) for 5 minutes per disc. The electrode is immersed in ethanol and sonicated for 5 minutes before using a disk with smaller grains. In order to reach a mirror-polished surface, the electrode is then polished by hand using diamond pastes (Presi®) with 3 different grain sizes: 6 µm, 3 µm, 1 µm. Between each grain size the electrode is immersed in acetone and sonicated for 5 minutes to remove all remaining abrasive grains from the surface. After the electrode is polished with the smaller grain size (1 µm), the electrode is cleaned using three sonication steps in acetone, ethanol and then a mix of ethanol and deionized water for 5 minutes each. The electrode is then electrochemically cleaned following the procedure described in the previous section. Prior to any electrochemical measurement, to ensure that the initial state is always the same, the electrodes are repolished but only from the second step (hand polishing using diamond paste). To avoid contamination or scratches, that will require to restart the polishing procedure from the beginning, the electrodes are stored individually in ultra-pure water (18.2 MΩ, <3 ppb total organic carbon, MiliQ-gradient + Elix, Millipore®) when not used.

II.1.2.2 Nanoparticles ink preparation and deposition

Nanoparticles supported on carbon substrates, commercially available (Premetek ®) or synthetized by collaborators, offer a highly developed surface area and are used in this PhD as potential electrocatalysts for BOR applications. However, before testing these materials in unit FC, it is important to study their activity towards this anodic reaction in RDE configuration. To do so, it is necessary to create a thin layer of electrocatalyst on the surface of the RDE tip, that will mimic the behavior of an active layer in a FC electrode. A 5 mm wide mirror-polished GC disk (S_{geo} = 0.196 cm², Sigradur®) is used as the support, because it is completely inactive in the studied potential windows. To

obtain a homogenous thin layer, the supported NPs are firstly dispersed in a mix of ultrapure water and isopropanol (IPA) using a sonication bath, to form an ink. Depending on the nature of the electrocatalyst (nature of the carbon support and metal nanoparticles considered) the proportions of IPA and water will vary in order to obtain a stable suspension and avoid agglomeration of the catalyst nanoparticles. In general, the ratio of IPA over water varies from 33% to 50%. In addition, 5 wt.% Nafion solution is added to the ink to act as a binder and provide mechanical integrity to the thin layer. The volume of Nafion added is calculated using equation 2.1 and corresponds to 30 % of the total mass of carbon dispersed in the ink.

$$V_{\mathrm{Naf}} = 0.3\frac{m_e \times l_e}{0.05 \times d_{\mathrm{Naf}}} \qquad \text{(equation 2.1)}$$

with:

V_{Naf} = volume of Nafion (µL)

m_e = mass of electrocatalyst (mg)

l_e = metal loading of the electrocatalyst (wt.%)

d_{Naf} = density of Nafion (0.874 g.mL^{-1} at T = 25°C)

After sonication a calculated volume of ink is deposited on the GC disk to obtain the desired loading of metal (40 µg.cm^{-2} or 100 µg.cm^{-2} in this work). To obtain a homogenous layer of electrocatalyst, the RDE is placed vertically, tip up, and a rotation is applied. To facilitate the drying of the ink drop, the GC tip is previously placed in a drying oven at 110°C, and a hair dryer blows hot hair at the rotating tip during the drying.

II.1.3 Rotating Ring-Disk Electrode

The Rotating ring-disk Electrode (RRDE) is a variation of the standard RDE configuration where a working electrode disk and a concentric sensor electrode ring, are used simultaneously [181]. The main use of this technique is to detect soluble species produced during an electrochemical reaction at the disk surface: once a reaction intermediate exits/desorbs from the surface and leaves the diffusion layer, it will be swept away from the disk due to the laminar flow of the electrolyte induced by the electrode rotation and will pass in front of the ring. If the correct potential is applied at the ring to oxidize/reduce this specie, its current will be modified when such species is produced at the disk. In the case of the BOR, this technique is used to determine if $BH_{3,ad}$ species are formed on Pt or Au surfaces along the reaction. It is possible to detect such species once they desorb into BH_3OH^- using a gold ring, as first demonstrated by Krishnan *et al.* [182]. Indeed, gold is capable to catalyze the oxidation of borane species at 0.2 V *vs* RHE, while remaining inactive towards the BOR [183–185]; so by

maintaining this potential at the ring when a CV is performed at the disk (Pt, Au or Ni) a detection current of BH_3OH^- can be obtained and compared to the corresponding potential applied on the disk. Figure II.3 presents a schematic representation of such measurement.

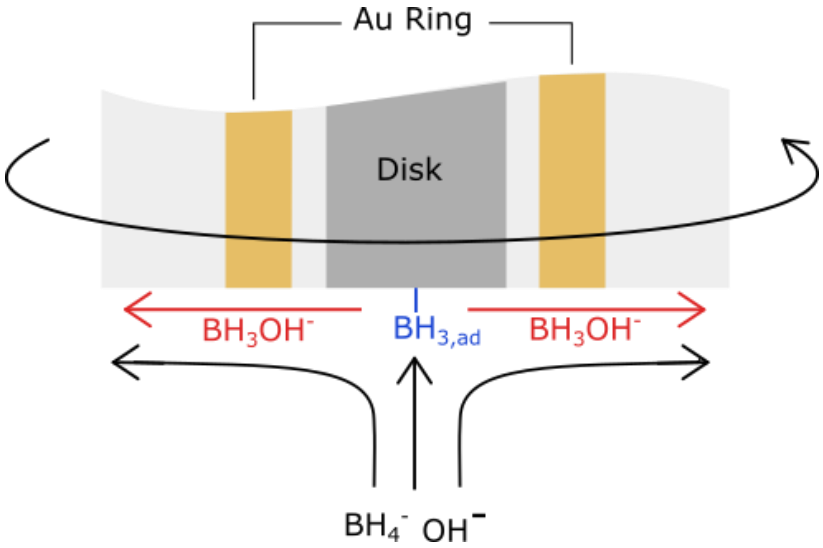

Figure II.3.Schematic representation of the detection of BH_3OH^- intermediate species of the BOR using an Au ring in RRDE configuration: a CV in the studied potential window is performed at the disk while the ring potential is maintained at E = 0.2 V *vs* RHE.

The RRDE measurements are performed using a Pine Research® rotator and two RRDE tips: a Au/Pt obtained by using at 5 mm wide mirror polished Pt disk (S_{geo} = 0.196 cm²) assembled in a "change-disk" tip from Pine Research® with a gold ring (S_{geo} = 0.110 cm²); an Au/Au "ThinGap RRDE tip" (Pine Research®) composed of a S_{geo} = 0.196 cm² disk and a S_{geo} = 0.036 cm² ring. The collection efficiency of both tips is determined, using potassium ferrocyanide as detailed on Figure II.3, to be 20.6% and 18.8% at ω = 2500 rpm for the Au/Pt and Au/Au assembly, respectively.

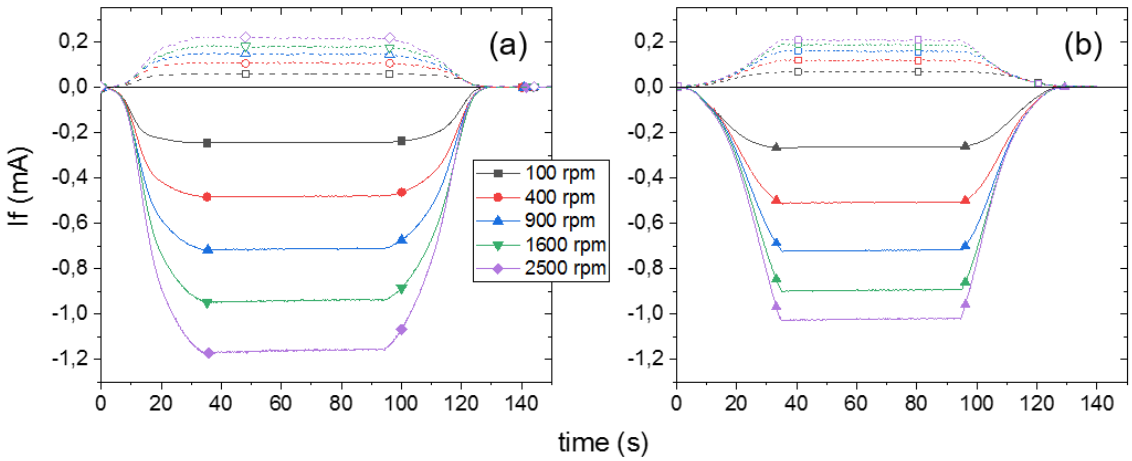

Figure II.4. Collection efficiency measurement curves for (a) Au-Au and (b) Pt-Au. Fe^{3+} is reduced on the disk and the Fe^{2+} produced is oxidized back when passing over the ring.

The oxidation current is smaller so not all species produced are detected by the ring, hence the introduction of a collection efficiency.

II.2 Metallic nickel catalyst preparation

In this PhD, one objective is to replace noble metals by non-noble Ni electrocatalyst. Because of the propensity to nickel to naturally oxidize under air, special care and techniques are required to obtain a metallic Ni surface and maintain it in this state of surface. However, synthetizing Ni nanoparticles with usual chemical procedures requires a passivation step to avoid auto-combustion of the obtained NPs. Hence, irreversibly oxidized surfaces that are rather inactive towards the BOR are usually obtained. Prior to the elaboration of DBFC anodes, a preliminary study is performed in half-cell conditions using a RDE working electrode.

Nickel nanoparticles electrodeposition on carbon support

II.2.1

The most convenient way to obtain metallic NPs is to perform an electrodeposition of Ni from an electrolyte containing nickel salt onto carbon supports, such as Vulcan XC-72R. This procedure has been developed by Oshchepkov [186,187] and is detailed here after. First, the highly developed carbon support is prepared prior to the electrodeposition: a suspension containing only Vulcan XC-72R, previously milled, is obtained using the same mixture of IPA and water described previously. The content of carbon is 1 $mg.mL^{-1}$ and the amount of Nafion used is reduced in order to reach an I/C ratio of 5 wt.%. Similarly to other nanoscale electrocatalysts, a thin layer of carbon (100 $\mu g.cm^{-2}$) is deposited on a GC (S_{geo} = 0.196 cm^2) RDE tip, previously mirror-polished and cleaned. Once the ink drop is dried, resulting in a homogenous layer, the electrode is rinsed in water and then characterized in a supporting electrolyte (1 M NaOH) to compare the CV profile before and after the electrodeposition of Ni: the conditioning CVs described previously are applied in the [-0.2 – 0.4] V *vs* RHE potential range. After another rinsing in water, to avoid contamination of the electrodeposition bath with NaOH, the electrode is transferred to the electrodeposition cell.

This independent electrochemical cell uses the same design as the one described in section II.1. The electrodeposition bath contains 0.01 M $NiSO_4 \cdot 6\ H_2O$ (99.97%, Alfa Aesar) + 0.1 M $(NH_4)_2SO_4$ (99+%, Alfa Aesar). Because its pH is neutral, the homemade RHE or Hg/HgO references are replaced by a mercury/mercurous sulfate (MSE, E_{MSE} = 0.65 V *vs* NHE in saturated K_2SO_4 at T = 25°C [181]) electrode. The CE used is a Pt wire, but no contamination by Pt redeposition has been observed on the final electrocatalyst support (see Chapter IV). Once the WE is immersed in the electrolyte,

the following electrodeposition procedure, consisting of two successive potentiostatic steps, is performed: purge the electrolyte by inert gas during 7-10 min; direct the gas flow above the solution during the deposition, apply the rotation and start electrodeposition after measuring an OCP value (for 30s): E_1 = -1.5 V *vs* MSE, t_1 = 15 s; E_2 = -1.25 V *vs* MSE, t_2= 210 s; ω = 400 rpm; in all cases, a gas flow is placed above the electrolyte (typical electrodeposition transients are shown on Figure II.5). At the end of the procedure, quickly dip the WE in water to remove any trace of the electrodeposition bath electrolyte and place it back in the characterization cell.

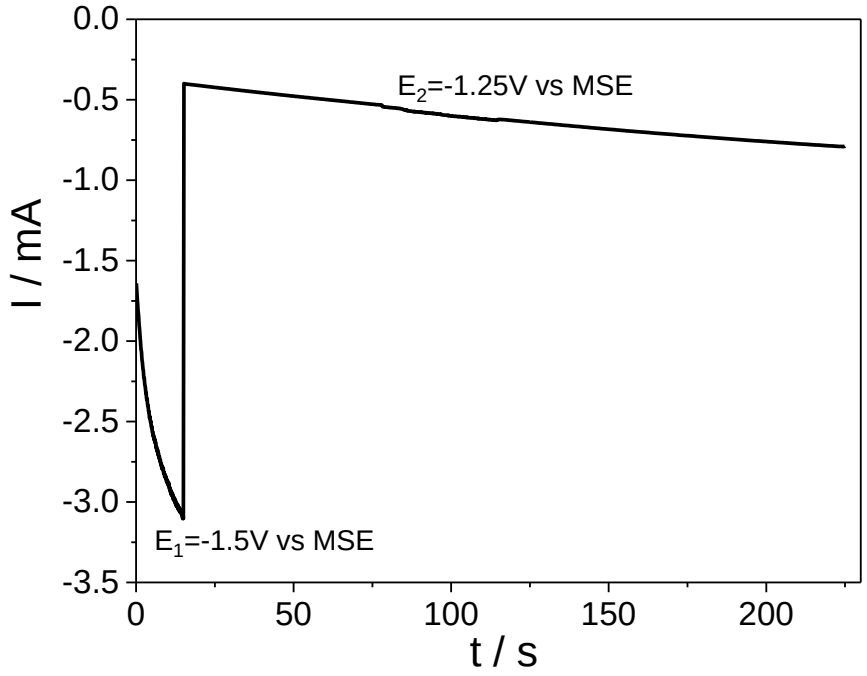

Figure II.5. Ni deposition transients obtained for Ni_{ED}/XC-72R in a deaerated 0.1 M $(NH_4)_2SO_4$ + 0.01 M $NiSO_4$ bath. The deposition parameters are as follows E_1 = -1.5 V (15 s), E_2 = -1.25 V (210 s), ω = 400 rpm, T= 25°C. Formation of gas bubbles (due to the simultaneous H_2 evolution) was observed during the deposition.

Once the deposition is done, a second characterization in supporting electrolyte (1 M NaOH) is performed to measure the surface area of Ni deposited: three CVs are measured successively, [-0.2; 0.4] V *vs* RHE, v_s = 20 mV.s^{-1}, 3 scans (stop at -0.2 V *vs* RHE); [-0.06; 0.4] V *vs* RHE, v_s = 20 mV.s^{-1}, 3 scans (stop at -0.06 V *vs* RHE); [-0.2; 0.4] V *vs* RHE, v_s = 20 mV.s^{-1}, 2 scans (stop at -0.2 V *vs* RHE).

II.2.2 Electrochemical Surface Area Determination

It is possible to determine the Electrochemical Surface Area (ECSA) of the deposited Ni NPs using the CV acquired in supporting electrolyte (as described above). Machado and Avaca demonstrated that the charge under the transition peak from Ni to surface α-

$Ni(OH)_2$ can be used to obtain the electrochemically available surface area of metallic sites using 0.514 $\mu C.cm^{-2}$ as the specific charge [188]. Other techniques are also used to determine the ECSA such as the determination of the double layer capacitance [189–193] or using oxalate salt [194]. These other techniques will give the total ECSA of the electrode while only the metallic ECSA will be obtained using Machado's method. However, the former requires cycling the Ni electrode up to high potential, resulting in an irreversible oxidation of the surface (E > 0.5 V *vs* RHE) (see Chapter IV) and should therefore be avoided to keep a metallic state of surface. The first method is therefore used in this work, but it is important to keep in mind that it also presents certain limitations. Only the metallic sites are considered for the surface determination; so if a portion of the surface is oxidized, intentionally (see the next section) or during the transfer from the electrodeposition bath to the characterization cell, the resulting ECSA will decrease; also, if adsorbed (or absorbed) hydrogen is formed at the surface, its oxidation will contribute to the overall anodic charge and thus modify the ECSA value [188].

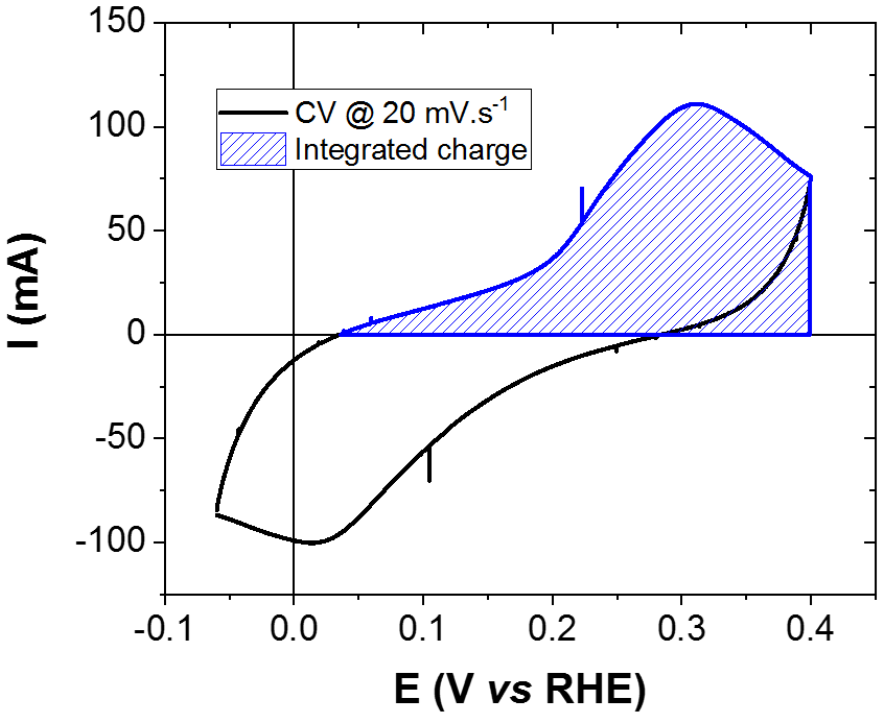

Figure II.6. CV of a Ni_{ED}/C electrode in supporting electrolyte (1 M NaOH) in the reduced potential window (-0.06 < E < 0.4 V *vs* RHE). The stripped area corresponds to the integrated charge (once corrected from the scan rate) used in the ECSA determination calculus.

To limit the influence of absorbed hydrogen, the last cycle of the second CV stopping at -0.06 V *vs* RHE measured in supporting electrolyte (1 M NaOH, v_s = 20 $mV.s^{-1}$) is used. This low potential limit is chosen to avoid formation of absorbed hydrogen and to

fully reduce the α-Ni(OH)$_2$ layer formed in the anodic sweep [187]. The anodic current is integrated (hatched area in Figure II.6) and the resulting area is divided by the scan rate and the specific charge to give the metallic ECSA of the Ni electrode.

II.2.3 Intentional oxidation of Ni surfaces

To modify the electrochemical behavior of Ni surfaces, intentional oxidation procedures are performed at two different degrees, resulting in partially and strongly oxidized electrodes. These oxidation procedures are based on the irreversible transition from the α-Ni(OH)$_2$ phase to the β-Ni(OH)$_2$ one when the applied potential exceeds E = 0.5 V *vs* RHE (see Chapter IV).

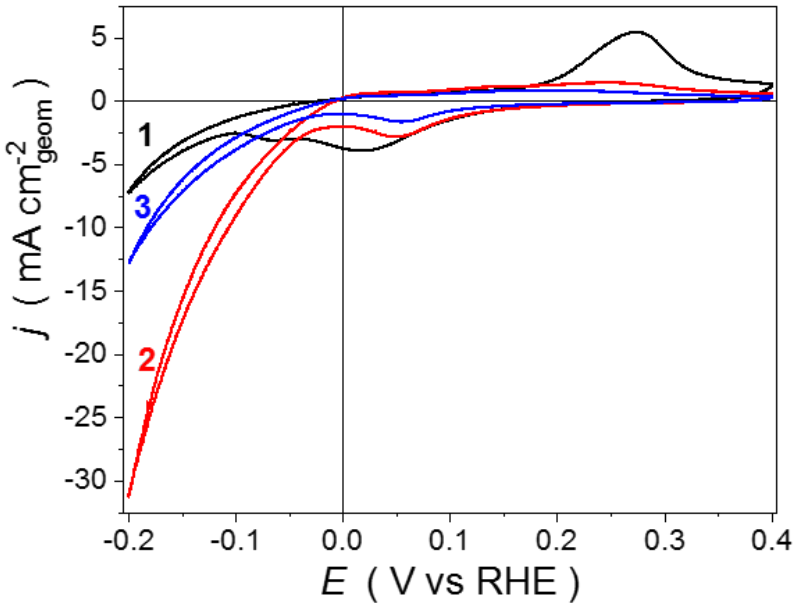

Figure II.7. CVs of Ni$_{ED}$/C electrode in supporting electrolyte (1 M NaOH) at the three different oxidation states: (1) metallic; (1) partially oxidized; (3) strongly oxidized. N_2-saturated electrolyte, v_s = 20 mV.s^{-1}, ω = 0 rpm, T = 25 °C.

The partially oxidized electrodes are obtained by applying one cycle up to E = 1.2 V *vs* RHE at v_s = 50 mV.s^{-1} in supporting electrolyte, which results in a surface significantly more active towards the hydrogen reactions (see Chapter IV). The typical CV in supporting electrolyte of such state of surface is represented on Figure II.7, where the Ni/α-Ni(OH)$_2$ transition peak is drastically reduced compared to the initial metallic state, confirming an important state of surface modification. The same anodic peak is even smaller on strongly oxidized electrodes, obtained after either prolonged storage under air atmosphere or by cycling 10 times up to E = 1.2 V *vs* RHE at v_s = 50 mV.s^{-1} in supporting electrolyte. Some metallic sites are however still present at the electrode surface, as demonstrated by the cathodic peak monitored at E = 0.05 V *vs* RHE. Figure

II.7 presents CVs obtained on Ni_{ED}/C electrodes but such oxidation procedure can be performed on any metallic nickel surface.

Surface treatments on 3D structured Ni supports

II.2.4

In order to replace carbon supported electrodes usually used in fuel cells, two different 3D nickel structures are investigated. The first one is a commercial nickel foam from T-Max Battery Equipment®, with a thickness of 1.5 mm (later mentioned as NFM). The second one is a commercial nickel felt from Sorapec®, with a thickness of 0.5 mm and composed of randomly dispersed 20 µm thick wires (later mentioned as NFT). Two different electrode sizes are considered in this study: 0.196 cm² samples (5 mm diameter disks) are utilized for the RDE configuration and 8 cm² (2 x 4 cm) ones for DBFC anodes. These disks are cut and then tucked in the RDE tip where the GC cylinder is pushed back inside the PTFE shaft to compensate the thickness of the nickel sample (the typical Ohmic resistance with this configuration is between 4 and 8 Ω, ensuring a good electrical contact between the GC and Ni). Different surface treatments, aiming to remove oxides from the initially strongly-oxidized surface of the two nickel materials are presented.

II.2.4.1 Hydrogen reduction treatment

At first, a heat treatment under hydrogen atmosphere are considered to reduce the oxide layer and obtain metallic surfaces. The procedure used is inspired by Serov's group [195–197], and is performed in the following conditions: the samples are heated up to 400°C with a 20 $K.min^{-1}$ ramp under a 10% H_2 in N_2 atmosphere flowing at 100 $mL.min^{-1}$ for 60 min. After natural cooling at room temperature the oven is purged with N_2 for 15 min followed by a flow of 3% O_2 in N_2 at 100 $mL.min^{-1}$ to slowly passivate the sample and avoid metallic Ni to burst into flames upon contact with the ambient atmosphere.

II.2.4.2 Acid Etching procedures

The second approach to obtain a metallic surface on the Ni support is to physically remove the top oxidized layers of the material and reveal the underlying metallic sites. To do so, several etching procedures in acidic media are performed on both 3D Ni structures.

- Acid etching in concentrated weak acid

An acid etching (AE) bath, composed of ascorbic acid (2 M $C_6H_8O_6$ 99.9%, Sigma Aldrich®) in ultrapure water, is contained in an independent electrochemical glass cell of the same design as shown in Figure II.1. Such a cell is used to purge oxygen from the bath and to enable rotating the RDE. The weak ascorbic acid is chosen as the etchant so that the Ni structures are not completely dissolved in a short amount of time. The Ni structures are first characterized in supporting electrolyte (1 M NaOH) then quickly

rinsed in ultrapure water and transferred in the AE cell, previously purged from O_2 using Ar or N_2 for at least 10 min, and thermostated at T = 25 °C. The rotation of the RDE is set to ω = 400 rpm, to ensure a good supply of species throughout the whole sample thickness. After 2 hours, the electrode is rinsed again in water and transferred back to the electrochemical cell to characterize the state of the surface post AE.

- Electro-assisted acid etching in weak acid

The second treatment is an electro-assisted AE. A potential is now applied to reduce the time of etching. To ensure a good conductivity, 0.1 M $(NH)_2SO_4$ (99+%, Alfa Aesar®) is added to the 2 M $C_6H_8O_6$ solution. A Pt wire is used as the CE and a saturated calomel electrode (SCE) is used as the reference. After the same conditioning in supporting electrolyte (1 M NaOH), the RDE tip is immersed in the electro-etching bath and 1 min potentiostatic measurements at E = 0.75 V *vs* RHE are applied for t = 1 min. Such step can be reproduced up to 10 times to vary the amount of Ni etched from the electrode. A linear relation is observed between the etching time and the Ni mass removed, until a critical time where the integrity of the structure is compromised. The electrode is then rinsed in water and characterized post AE in supporting electrolyte.

- Acid etching in concentrated strong acids

The third AE treatment is reproduced from Jerkiewicz's group [189] and consists in immersing the samples in a mixture of strong acids: 50% of CH_3COOH (glacial, Carl Roth®), 30% HNO_3 (>65%, Carl Roth®), 10% H_2SO_4 (96%, Carl Roth®), 10% H_3PO_4 (>85%, Sigma Aldrich®). The immersion time varies depending on the Ni structure used: t = 90 s for the NFM and only t = 30 s for NFT. If the NFT is etched for a longer time, too much Ni is dissolved and the mechanical strength of the electrode is significantly reduced (Figure II.8), the electrode is completely dissolved after around t = 50 s.

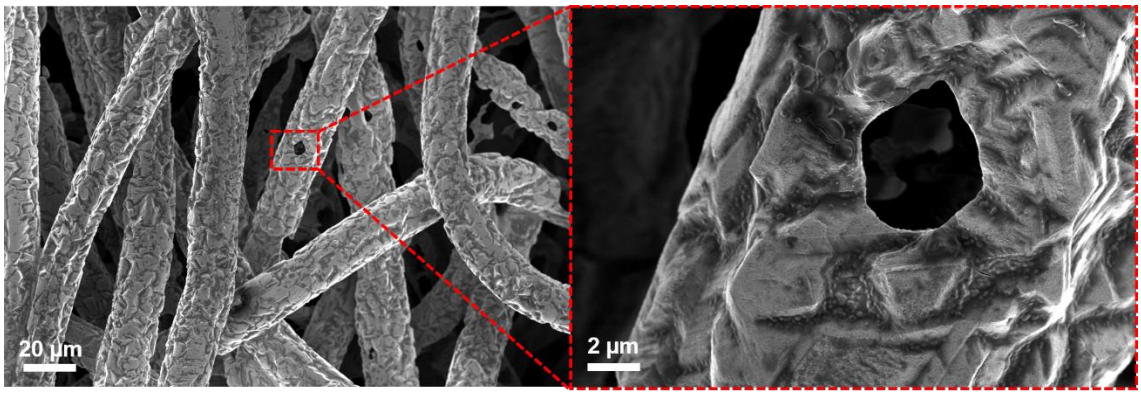

Figure II.8. SEM images of etched NFT for too long at ×500 and ×5k magnification. Grain boundaries are severely attacked, weakening the overall NFT structure. The Ni wires composing the felt are pierced and reveal a hollow structure.

II.2.4.3 Ni electrodeposition on etched Ni support

Once the 3D Ni substrates are in the right state of surface (after AE), they can be used as support to electrodeposit Ni NPs. The electrodeposition procedure is thus reproduced in the same conditions using the Ni structure tucked in the RDE instead of the standard XC-72R thin layer deposited on GC. The typical deposition transient obtained using the NFT support is presented on Figure II.9.

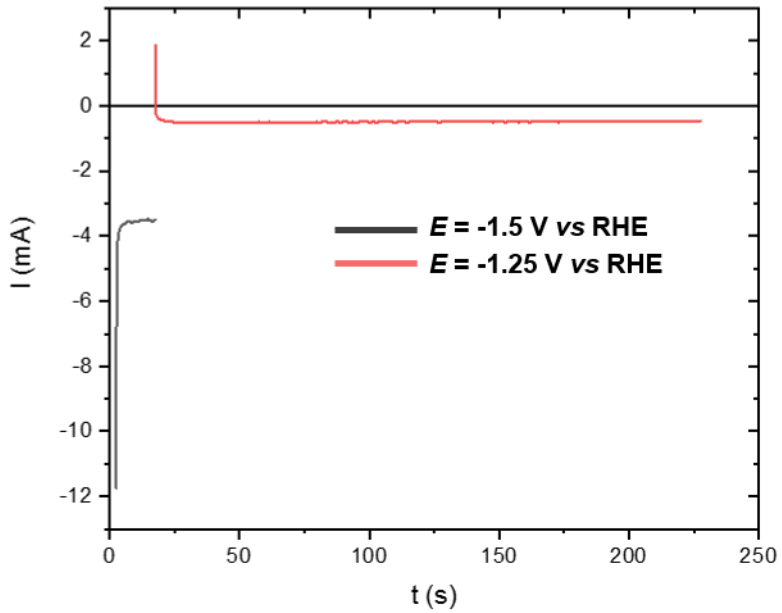

Figure II.9. CA transients obtained during the electrodeposition of nickel NPs on the nickel foam in a 0.01 M NiSO4 + 0.1 M $(NH_4)_2SO_4$ electrolyte. The electrode is agitated at 400 rpm to ensure no electrolyte replenishment in the pores of the material during the deposition. The reference used in this medium is a Mercury/Mercurous Sulfate (MSE) electrode.

II.3.1

II.3 Characterization techniques

Microscopy methods

II.3.1.1 Transmission Electron Microscopy

Transmission Electron Microscopy (TEM) is used to observe the surface and morphology of nanoscale objects such as the NPs supported on carbon used as BOR electrocatalysts in this work. Ni_xM materials synthetized either by Prof. Atanassov's group at University of New Mexico (now at University of California, Irvine) or by Prof. Dekel's group from Technion, Israel Institute of Technology, are characterized by M. Chatenet in the "Laboratoire des Matériaux et du Génie Physique" (LMGP Grenoble-

INP, Grenoble, France) using a LaB6 Jeol 2010 TEM, operating at 200 kV with a 0.19 nm resolution.

Electrodeposited Ni_{ED}/C electrocatalysts are also characterized by TEM: the thin layer of a Ni_{ED}/C sample, prepared upstream, is gently scratched from the GC support and deposited on a Cu TEM grid. Microstructure analysis of this sample is performed using a JEOL 2100F microscope operating at 200 kV by C. Ulhaq-Bouillet in the Institut de Physique et Chimie des Materiaux de Strasbourg (IPCMS, Strasbourg, France).

II.3.1.2 Scanning Electron Microscopy

Scanning Electron Microscopy (SEM) is used to observe samples too large for TEM or too thick to allow the electron beam to be detected in transmission mode. This microscopy technique also allows better imaging of the topography of the surface of a sample by capturing low-energy secondary electrons (SE). The acceleration tension of the beam is thus smaller than a TEM: typically, 3 kV for SE imaging). Chemical contrast can also be observed using backscattered electrons (BSE), allowing to easily observe samples presenting different local compositions. The composition itself can then be determined using X-Ray Energy Dispersive Spectroscopy (X-EDS) (see next section).

The morphology of Ni_{ED}/C electrodes was observed by T. Dintzer in Institut de Chimie et Procédés pour l'Energie, l'Environnement et la Santé (ICPEES, Strasbourg, France) using a JEOL JSM-6700F at an accelerating voltage of 6 kV. The same observation was done on Ni_{ED}/GDE samples for both low and high loading of Ni, revealing formation of agglomerates.

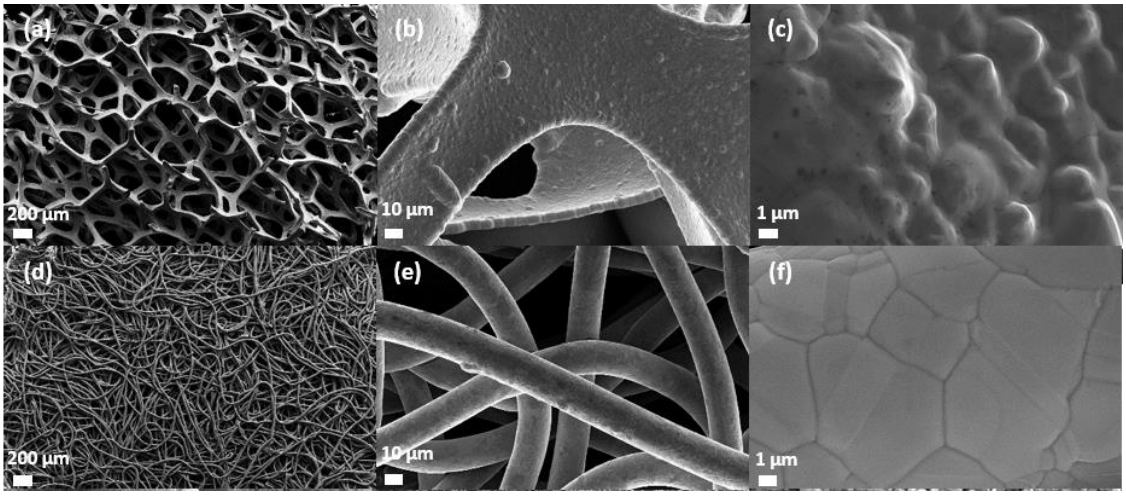

Figure II.10. SEM images of (a, b, c) sintered polycrystalline nickel foam (NFM), (d, e, f) nickel felt (NFT) composed of 20 µm thick polycrystalline wires at different magnifications: (a, d) ×30; (b, e) ×x500; (c, f) ×5000.

The 3D Ni structures are characterized by SEM at every stage of their elaboration: pristine, after AE, after electrodeposition of Ni NPs and after deposition of anion

exchange ionomer. They are imaged by R. Martin in Consortium des Moyens Technologiques Communs (CMTC Grenoble-INP, Grenoble, France) using a Zeiss ® Gemini SEM-500 operating at 3 kV or 15 kV for SE and BSE mode respectively. The initial morphology of both structures can be observed in Figure II.9.

Pt/GDL samples synthetized in Université de Technologie de Troyes (UTT, Troyes, France) were characterized using a Hitachi UHR FEG-SEM SU8030 microscope operating at 5 or 10 kV with a work-distance < 6 mm.

Structural and compositional characterization

II.3.2.1 X-Ray Energy Dispersive Spectroscopy

II.3.2

X-EDS is a complementary tool to the SEM and allows to determine the chemical composition of a sample as mentioned previously. X-EDS analysis of both Ni structures are performed by R. Martin using an EDAX ® OCTANE ELITE 25 spectrometer incorporated in the Zeiss ® Gemini SEM-500 chamber, operating at 15 kV, in CMTC (Grenoble, France). The X-EDS spectra of the pristine NFM and NFT can be found on Figure II.12 and II.13, respectively. Performing quantitative analysis of the composition requires specific conditions and is often used improperly. In this case the analysis will be limited to a qualitative observation of the samples composition: NFM only presents Ni, while NFT is mainly composed of Ni, but impurities such as Fe, Mo or Cr are also detected.

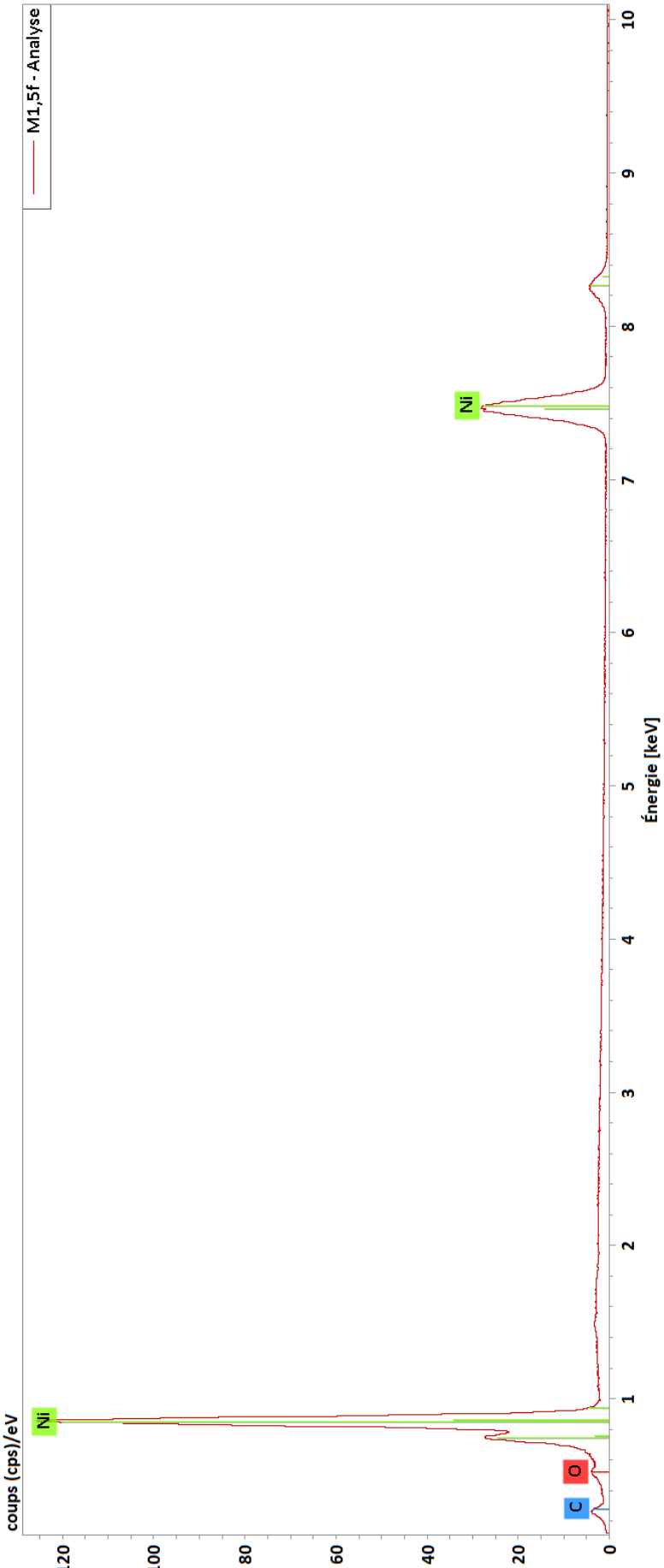

Figure II.11. X-EDS spectrum of nickel foam (M1.5) obtained using EDAX ® OCTANE ELITE 25 EDS sensor in a Zeiss ® Gemini SEM-500 at 15 kV. Only Ni is detected on this material. A small peak around 1.5 keV can be seen but is attributed to aluminium from the SEM support.

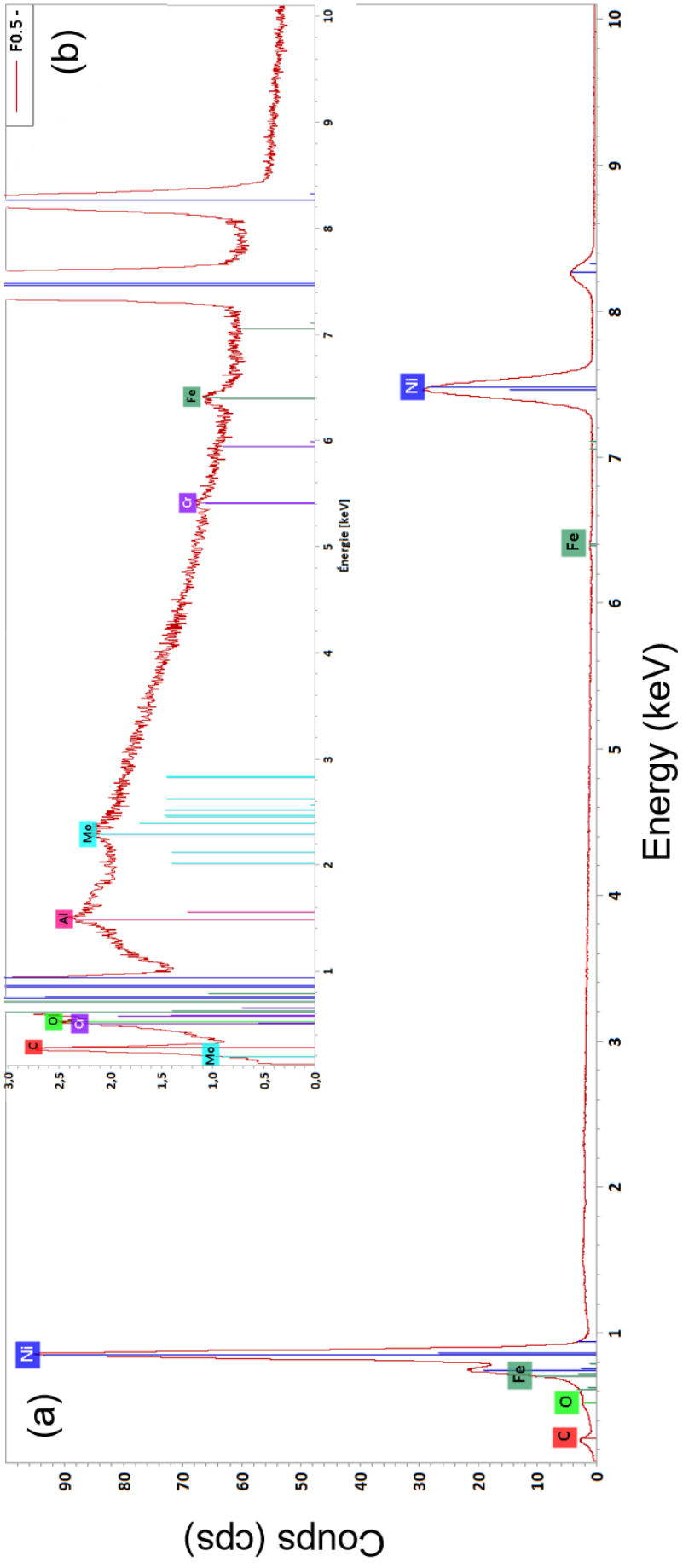

Figure II.12. (a) X-EDS spectrum of nickel felt (0.5) obtained using EDAX ® OCTANE ELITE 25 EDS sensor in a Zeiss ® Gemini SEM-500 at 15 kV. Small peaks can be detected and are shown in more details on the inset (b): traces of iron, molybdenum and chromium are detected on the material. The aluminium peak is attributed to the SEM support.

II.3.2.2 X-Ray Diffraction Spectroscopy

The crystallographic structure of both Ni structures (NFM and NFT) have been analyzed by T. Encinas in CMTC (Grenoble, France) using a Bruker ® D8 ADVANCE Diffractometer using a Cu radiation source. The resulting 2 θ diffraction patterns (Figure II.11) are compared to reference X-ray patterns for Ni (cubic Fm-3m (225)). Because of the very open porosity of the NFM structure, a small asymmetry on the left side of each peak is detected (Figure II.11a) and assigned to the diffraction of lattices in depth compared to the surface of the sample. A small shift to the left of each peak is detected on the NFT XRD pattern (Figure II.11b) and assigned to the contribution of possible impurities in the lattice, slightly modifying the lattice parameters of the material.

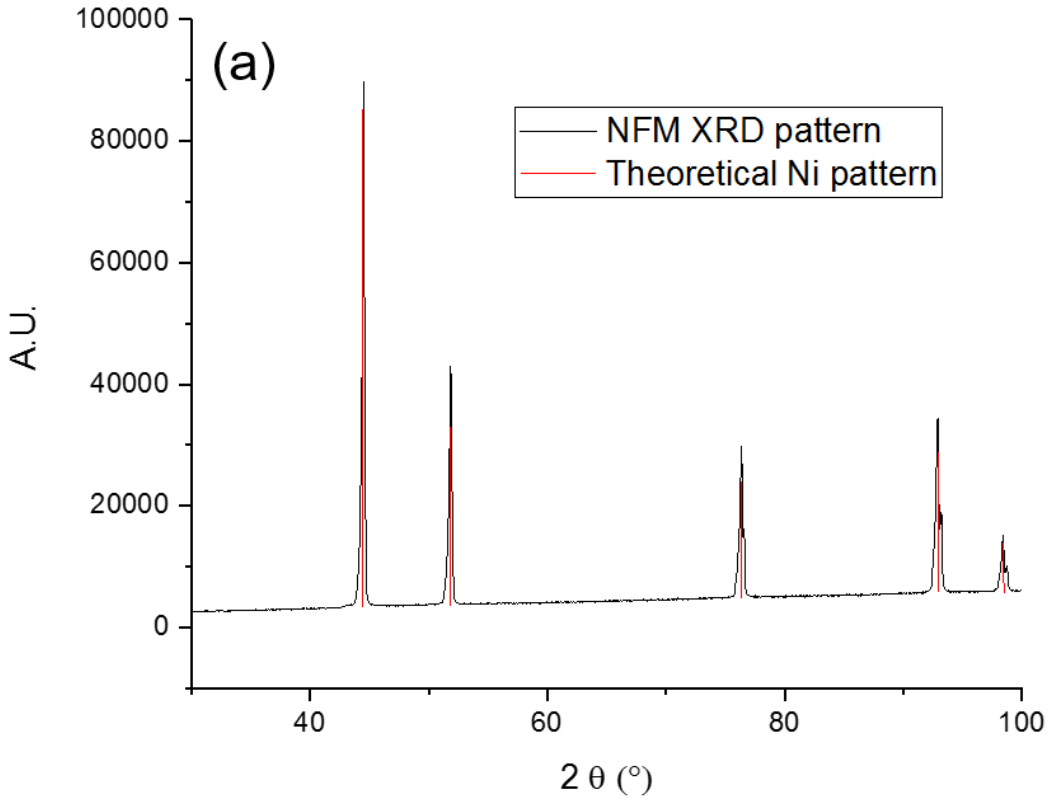

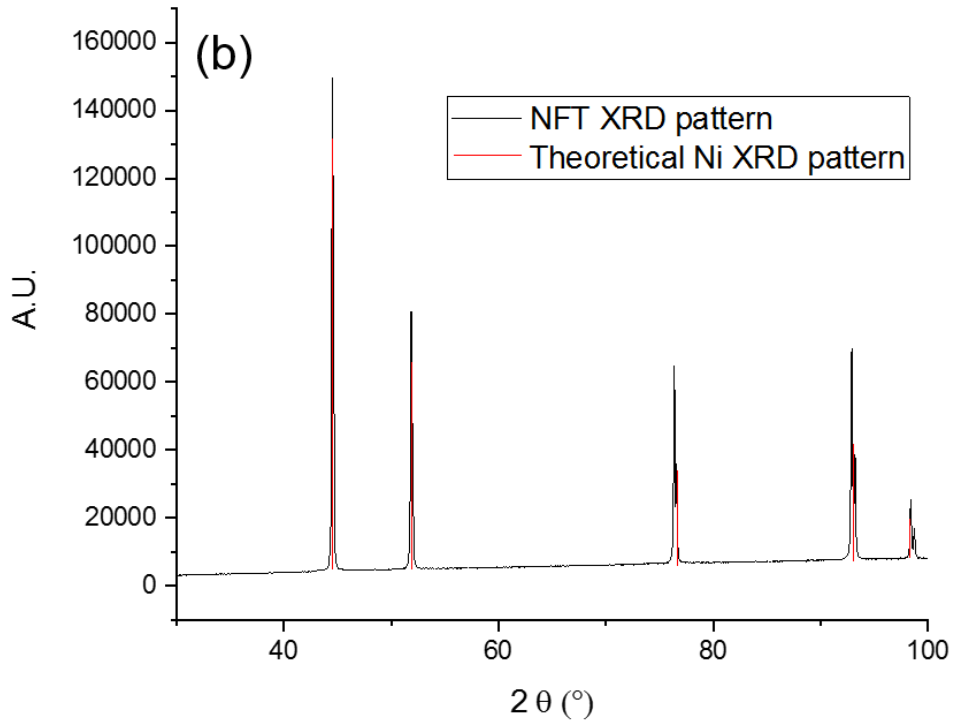

Figure II.13.XRD pattern of (a) the NFM and (b) the NFT, compared to the theoretical pattern of Ni (cubic Fm-3m (225)) (red lines).

II.3.2.3 Inductively coupled plasma atomic emission spectrometry

Inductively coupled plasma atomic emission spectrometry (ICP-AES) is used to determine the average mass of Ni deposited during the elaboration of Ni_{ED} samples. Because this analysis is destructive, several dedicated samples are prepared upstream according to the following procedure:

Electrodeposited samples are prepared according to the usual procedure and characterized in supporting electrolyte to be able to correlate the ECSA to the measured Ni mass. ICP-AES requires liquid samples, so it is necessary to dissolve the Ni catalyst layer in 30% HNO_3 solution from either the top surface of GC cylinder or the surface of SGL paper (for DBFC anodes, see next section). To that goal, the whole surface covered by Ni NP is immersed in a glass jar, placed under a stove, containing 2 mL of 30% HNO_3 (Fisher Scientific) solution for t = 60 min at $T \approx$ 50 °C. The solution is agitated during the whole dissolution procedure using a magnetic bar. When operating with Ni/GDE, a special attention is given to cover the tweezer holding the sample by Teflon tape to avoid contamination of the analyzed solution with other metallic species.

A part of the solution may be evaporated during the heating. In order to consider this, one should check the volume of the solution after the heating and add some amount of

ultrapure water if necessary. The total volume should be less than 3 mL for dissolved Ni_{ED}/XC-72R samples in order to not be inferior of the detection limit of ICP-AES. For the reference sample, a solution with 20-30 µg of Ni is prepared by adding the calculated amount of 0.01 M NiSO4 electrolyte to the jar with 30% HNO_3 solution.

The ICP-AES analysis was performed by A. Boos at Institut pluridisciplinaire Hubert Curien (IPHC - UMR 7178, Strasbourg, France).

II.3.3 Coupled spectroscopic methods

To obtain precise information of reaction products of the BOR on different electrocatalysts, the use of coupled spectroscopic methods is required to detect *in situ* the intermediate species and products at a given applied potential.

II.3.3.1 Differential Electrochemical Mass Spectrometry

The Differential Electrochemical Mass Spectrometry (DEMS) is a technique used to identify the gaseous or volatile species produced at the interface of an electrode during an electrochemical reaction: such species are sucked and accelerated towards the mass spectrometer by a vacuum cascade. The experimental setup developed at LEPMI by M. Chatenet and V. Martin is directly inspired by Refs. [198–200] and a schematic representation is given by Figure II.14: a homemade RHE is freshly prepared prior to each experiment, a Pt wire is used as the CE and an RDE is placed vertically. A bare GC disk is used and the electrode is not connected to the potentiostat, it only serves to agitate the solution and induce a “controlled” mass-transport at the WE. However, the exact flow of electrolyte brought to the WE is not perfectly defined, so no calculation involving mass-transport dependencies can be performed using this setup. Indeed, the WE is placed at the bottom of the cell and pressed against three piled Teflon membranes positioned on a steel frit for mechanical support. This way, the volatile species produced at the electrode can pass through these porous membranes, while a good water tightness is maintained. This configuration also requires the WE to be highly porous, otherwise no species could be detected by the MS. To that goal, sputtering deposition of Pt, Au or Pd is performed on a PTFE membrane to obtain a 50 nm thick porous structure used as the WE. Because it is placed at the bottom of the cell, a gold ring is pressed against the electrode and used as the current collector. For the DEMS study of Ni, the etched NFT is used as the WE and the gold ring is replaced by a strongly oxidized (in order to decrease its BOR activity) Ni one.

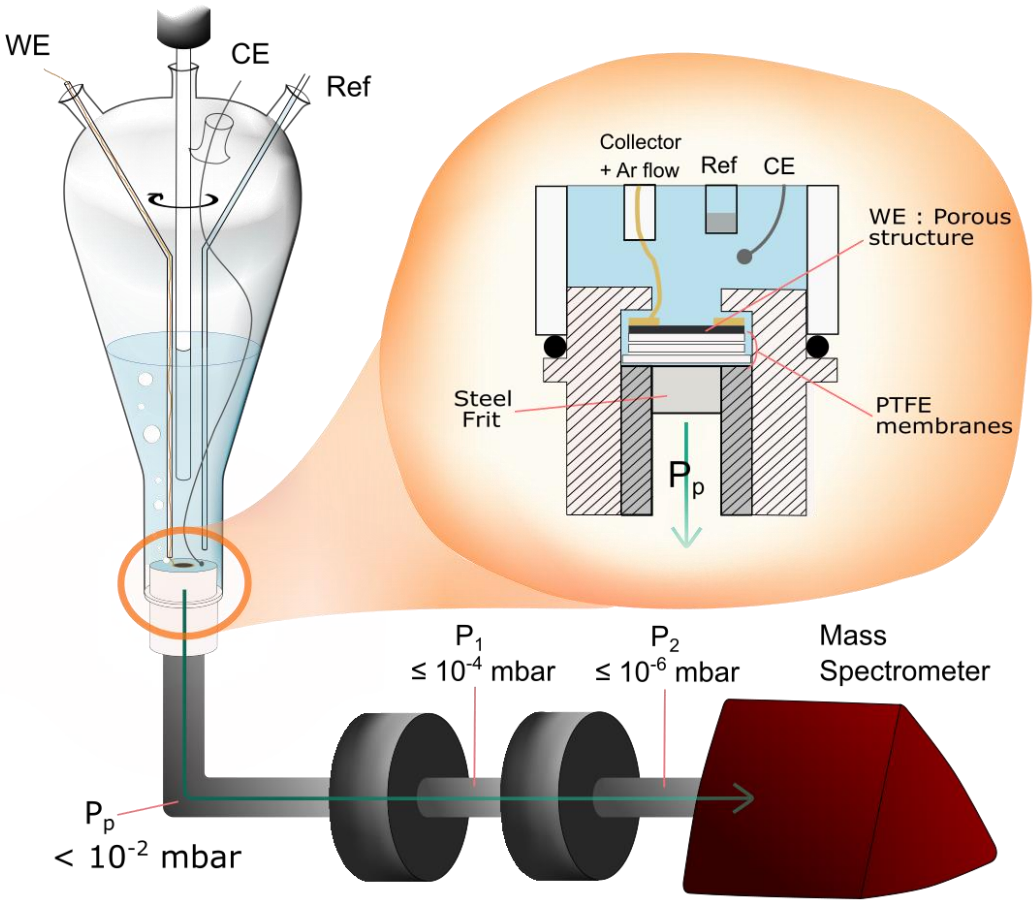

Figure II.14. Schematic representation of a Differential Electrochemical Mass Spectrometer cell. A cut view of the interface between the electrolyte and the vacuum is detailed in the insert.

In this work, DEMS measurements are used to detect the release of H_2 during the BOR. To do so, usual BOR CVs in 1 M NaOH + 5, 50, or 500 mM $NaBH_4$ in the desired potential window, [-0.2, 1.3] V *vs* RHE for noble surfaces and [-0.2, 0.4] V *vs* RHE for Ni, are performed at v_s = 10 mV.s^{-1}, to allow a better detection of species with the MS. It is possible to convert an ionic current, measured by the MS, to the faradic one, measured by the potentiostat if a calibration step has been performed for this specific current. In the present case the H_2 production is calibrated for each experiment using a CV in the HER region in supporting electrolyte (1 M NaOH). Because the detected H_2 in this region is only produced by the faradic HER (before addition of borohydride), the measured $I_{m/z=2}$ current (corresponding to H_2) can be converted to the maximum faradic current, giving a calibration constant $K_{calibration}$ and the corresponding H_2 equivalent current $I_{H2,eq}$. The calibration curves as well as their calibration constants for the 4 different electrodes are presented in Figure II.15.

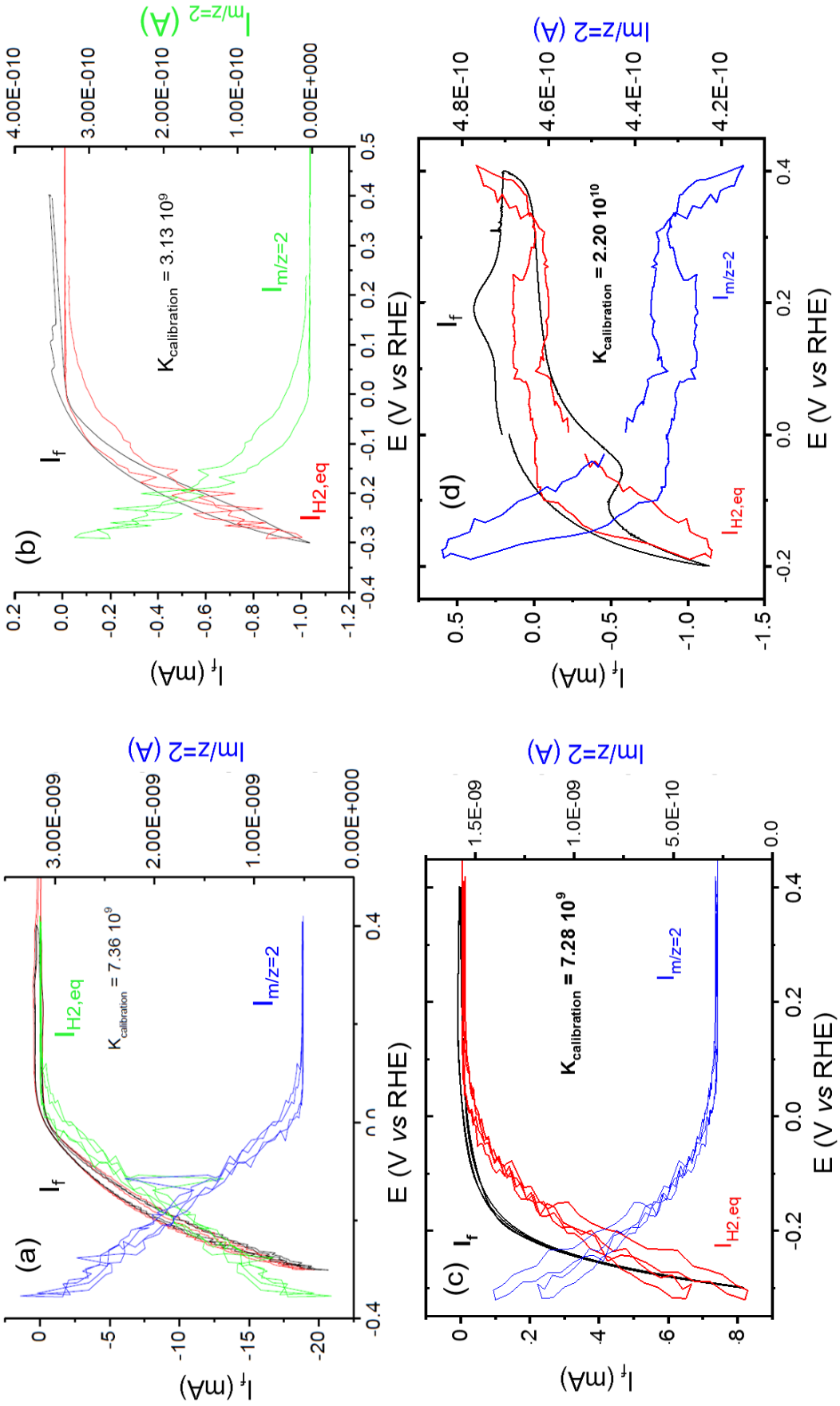

Figure II.15. Hydrogen escape current calibration for (a) Pt, (b) Au, (c) Pd sputtering electrodes and (d) etched Ni felt. HER faradic current (IR-corrected, v_b = 10 mV.s^{-1}) and corresponding DEMS current $I_{m/z=2}$. The $H_{2,\,eq}$ current is obtained with the calibration constant $K_{calibration}$ in order to obtain $I_{H2,\,eq}$ = - $K_{calibration}$ * $I_{m/z=2}$.

The H_2 contributions from the supporting electrolyte (from the HER) or from the BOR (or the hydrolysis of BH_4^-) cannot be distinguished using standard $NaBH_4$ electrolyte. To go beyond this uncertainty, deuterium-substituted $NaBD_4$ (98% purity, Sigma Aldrich) can be used in the same concentrations in NaOH, H_2O. That way, $I_{m/z=3}$ and $I_{m/z=4}$, corresponding to the detection of HD and D_2 species respectively originating from the BD_4^- reaction, are now detected and differentiated from the $I_{m/z=2}$ contribution from water reduction. Using isotopic borodeuteride species for DEMS measurements has been performed firstly by Jusys *et al.* [201].

II.3.3.2 In situ Fourier Transform Infra-Red spectroscopy

In situ Fourier Transform Infra-Red spectroscopy (FTIRS) has been performed to detect intermediate species and products produced during the BOR on Ni electrodes. This part of the experimental work is made by A. Oshchepkov and A. Bonnefont using a Bruker IFS 66v/S FTIR spectrometer (ICPEES UMR7515, Strasbourg, France). The experimental setup used in thin layer configuration, described by Figure II.16 and, is composed of an electrochemical glass cell with a similar design as the DEMS one (the bottom of the cell is open). A Ni disk, freshly polished to be in metallic state, is used as the WE and pressed against a ZnSe prism in thin film mode; a Pt wire is used as the CE and a homemade RHE freshly prepared before each experiment as the reference. The spectrometer chamber is continuously purged with N_2 and the IR spectra are acquired with a N_2 cooled MCT detector (double-sided acquisition) with 3 mm diaphragm at 40 kHz in the [4000, 700] cm^{-1} wavenumber range with a 4 cm^{-1} resolution. Every spectrum recorded is averaged based on 256 individual measurements.

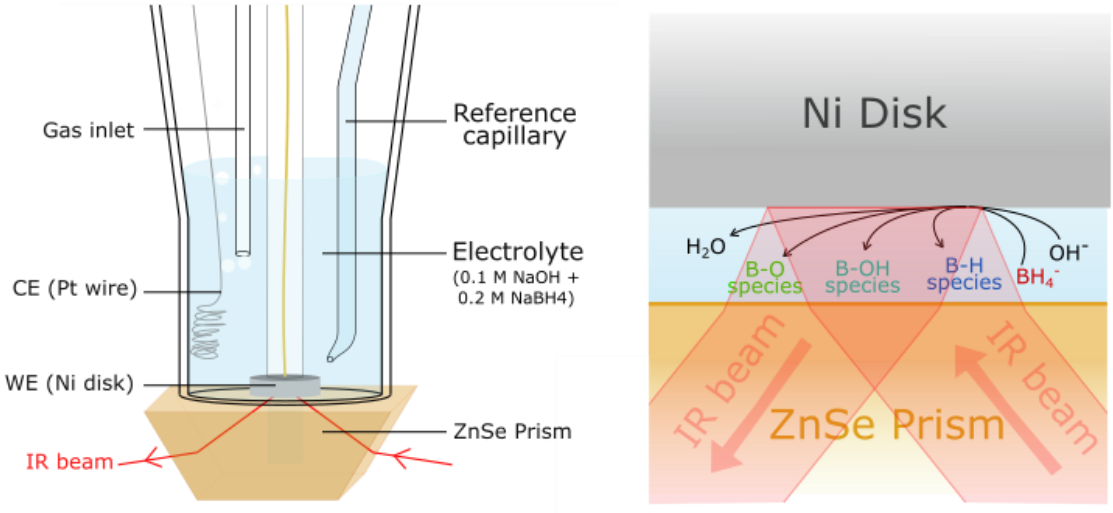

Figure II.16. Schematic representation of the *in situ* FTIRS setup using a ZnSe prism. The thin layer is detailed on the right-hand side with the expected intermediates or final products of the BOR.

The following procedure is used to acquire a spectrum in BOR conditions every 100 mV from E_{oc} to E = 0.4 V *vs* RHE: (i) polish the Ni disk down to a mirror surface (using 0.3 µm Al_2O_3) to reveal metallic sites, (ii) record 3 consecutive CVs in 0.1 M NaOH: from -0.2 to 0.4 V *vs* RHE at v_s = 100 mV.s^{-1}; from -0.06 to 0.4 V *vs* RHE at v_s = 20 mV.s^{-1}: from -0.2 to 0.4 V *vs* RHE at v_s = 20 mV.s^{-1}, (iii) add 0.2 M $NaBH_4$ in the electrolyte, (iv) record a BOR CV from -0.2 to 0.3 V *vs* RHE at v_s = 20 mV.s^{-1}, (v) apply $E = E_{oc}$ then press the disk against the prism and record the background spectrum at E_{oc}, (vi) apply 100 mV steps from E_{oc} to E = 0.4 V *vs* RHE and record 11 consecutive spectra at each potential step.

Similarly as the DEMS study, the measurements are also performed using deuterated species such as $NaBD_4$ or even NaOD (in deuterated water) to differentiate the contributions originating from the fuel or the solvent. Reference spectra are recorded at E_{oc} using various boron-based species: $NaBH_4$, $NaBD_4$, NH_3BH_3 (97% purity, Sigma Aldrich), $NaBO_2$ (99+ purity, Sigma Aldrich), $Na_2B_4O_7$ (99.5+% purity, Sigma Aldrich) to measure several B-based bonds (Figure II.17). Each peak is attributed to a bond using Refs [202–205].

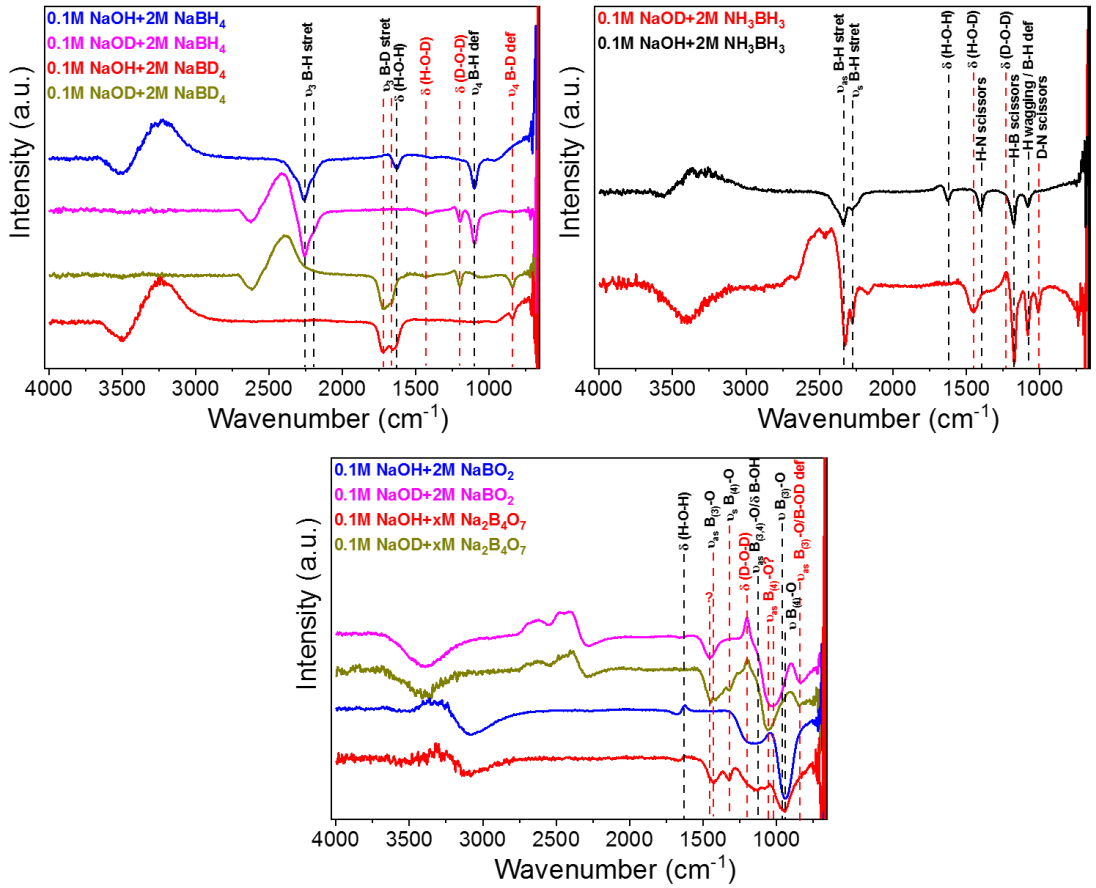

Figure II.17. Reference FTIR spectra in thin layer configuration using a freshly polished Ni electrode and various boron-based species: $NaBH_4$, $NaBD_4$, NH_3BH_3, $NaBO_2$, $Na_2B_4O_7$, in either 0.1 M NaOH or 0.1 M NaOD (in deuterated water).

II.4 Fuel Cell tests

Different anodes are elaborated using the Ni_{ED} electrocatalysts previously described at the RDE scale. Collaborators from Université de Technologie de Troyes (UTT, Troyes, France) developed an elaboration procedure to deposit Pt NP directly in the pores of a gas diffusion electrode (GDE). DBFC unit cells are tested in two different configurations: a BH_4^-/O_2 setup in Laboratoire d'Energétique et de Mécanique Théorique et Appliquée (LEMTA, Nancy, France), and a fully liquid BH_4^-/H_2O_2 setup in Washington University in Saint Louis (Saint Louis, United-States).

Anode preparation

II.4.1 *II.4.1.1 Ni_{ED}/GDE anode elaboration procedure*

At first, the electrodeposition procedure of metallic Ni NPs is adapted to create the 8 cm^2 (4 × 2 cm) anode fitting in the DBFC setup of LEMTA (see next section). The adopted procedure is used to deposit NP directly in the pores of a carbon paper (SGL Sigracet® 25AA), usually used as a gas diffusion layer (GDL).

The SGL carbon paper is first conditioned in HNO_3 prior to ED to decrease the hydrophobicity of the carbon and allow the electrolytes to penetrate all the pores. The same electrodeposition bath and cell as the first deposition procedure are used for this upscaled one but with an increased concentration of active species: 0.1 M NiSO4 + 0.1 M $(NH_4)_2SO_4$; RE = MSE (0.96 V *vs* RHE); CE = Pt wire; Glass Cell with one compartment at room temperature as described in section II.1.1. The electrodeposition step is modified to one repeatable step now called pulse consisting of 3 successively applied potentials: E_1 = 0.03 V *vs* RHE (conditioning step to avoid current overloads) for t_1 = 10 s for the first pulse and 5 s for the following ones. E_2 = -0.74 V *vs* RHE for t_2 = 10 s; E_3 = -0.54 V *vs* RHE for t_3 = 120 s without IR compensation.

Two differently loaded Ni_{ED}/GDE electrodes are obtained using this procedure: Ni_{ED}/GDE-L after one pulse, Ni_{ED}/GDE-H after 6 pulses. The typical ED transients of these two samples are represented in Figure II.18.a. and b, respectively.

- Procedure to elaborate Ni_{ED}/GDE electrode

1) Soak in conc. HNO_3 solution during t = 5 min to improve the hydrophobicity;
2) Sonicate in water for t = 5 min;
3) Put in the cell with 1 M NaOH and record CVs with IR compensation (80% of Ru);

4) Sonicate in water for 3 min;
5) Sonicate in 0.1 M $NiSO_4$ + 0.1 M $(NH_4)_2SO_4$ for t = 5 min;
6) Electrodeposition step: applied n pulses depending on the loading required (1: low loading - L; 6: high loading -H);
7) Rinse in water to avoid transfer of Ni_2SO_4 in the supporting electrolyte;
8) Move the electrode in the characterization cell with 1 M NaOH and record CVs: [-0.2; 0.4] V *vs* RHE, v_s = 20 mV.s^{-1}, 3 scans.

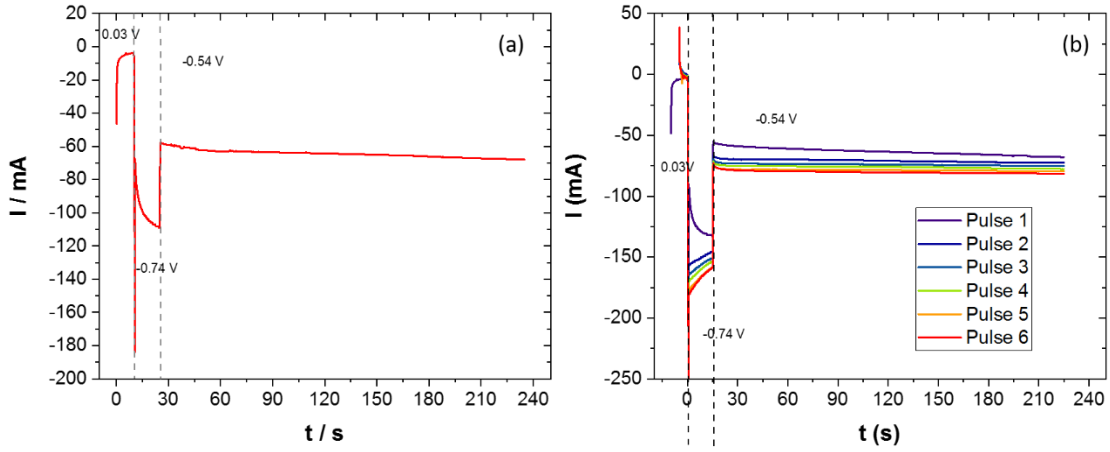

Figure II.18. Ni electrodeposition transients obtained with the upscaled procedure.to create (a) Ni_{ED}/GDE-L with a single pulse and (b) Ni_{ED}/GDE-H with 6 pulses in N_2 saturated 0.1 M $NiSO_4$ + 0.1 M $(NH_4)_2SO_4$.

II.4.1.2 Ni_{ED}-based anodes elaboration using Ni support

Similarly as the RDE samples, this upscaled electrodeposition procedure is applied to the 3D Ni structures. At this stage of the study, NFT samples proved superior performance towards the BOR and a more suited morphology as anode support than NFM; so the latter is no longer considered. First, the AE step is performed to the 8 cm² NFT samples. Electro-assisted AE is no longer possible because of this large surface area; the applied currents exceeded the potentiostat limits. To save time, the 30 seconds AE in strong acids is preferred over the 2 hours AE in ascorbic acid: the 8 cm² samples are fully immersed in the AE bath for t = 30 s then rinsed in ultrapure water before characterization in supporting electrolyte (1 M NaOH) in the electrochemical cell. To facilitate the manipulation of the electrode, the samples are cut with a 1 cm² annex at one side. The current is collected using a Ni wire (1 mm thick, 99.9% purity, MaTecK) attached to this annex. Next, the same upscaled ED procedure presented above is applied to the etched NFT (6 pulses) producing Ni_{ED}/eNFT anodes. After a last characterization in 1 M NaOH, the annex is removed before installation in the DBFC cell. Because the nature of the support and the NP is similar no ICP-AES analysis could be performed and thus the loading of deposited Ni cannot be obtained.

II.4.1.3 Pt/GDL anode elaboration

In order to compare fairly the Ni-based electrodes to Pt electrocatalysts, Pt nanoparticles are (chemically) deposited directly in the volume of a carbon GDL (Pt/GDL) from SGL Carbon (Sigracet® - 25AA) not bearing any microporous layer (no Vulcan XC72 carbon + PTFE added). Prior to this deposition, the GDL substrate is cleaned firstly with a Caroic acid solution to remove all organic residues from the substrate, then with demineralized water and dried in air stream. The Pt nanoparticles average size (between 5 and 6 nm) and size distribution are measured from SEM images (Figure II.19); the total loading is 0.16 $mg_{Pt}.cm^{-2}$. This procedure has been developed and performed by F. Asonkeng and T. Maurer in Université de Technologie de Troyes (UTT, Troyes, France) and no additional details can be given at this stage (proprietary).

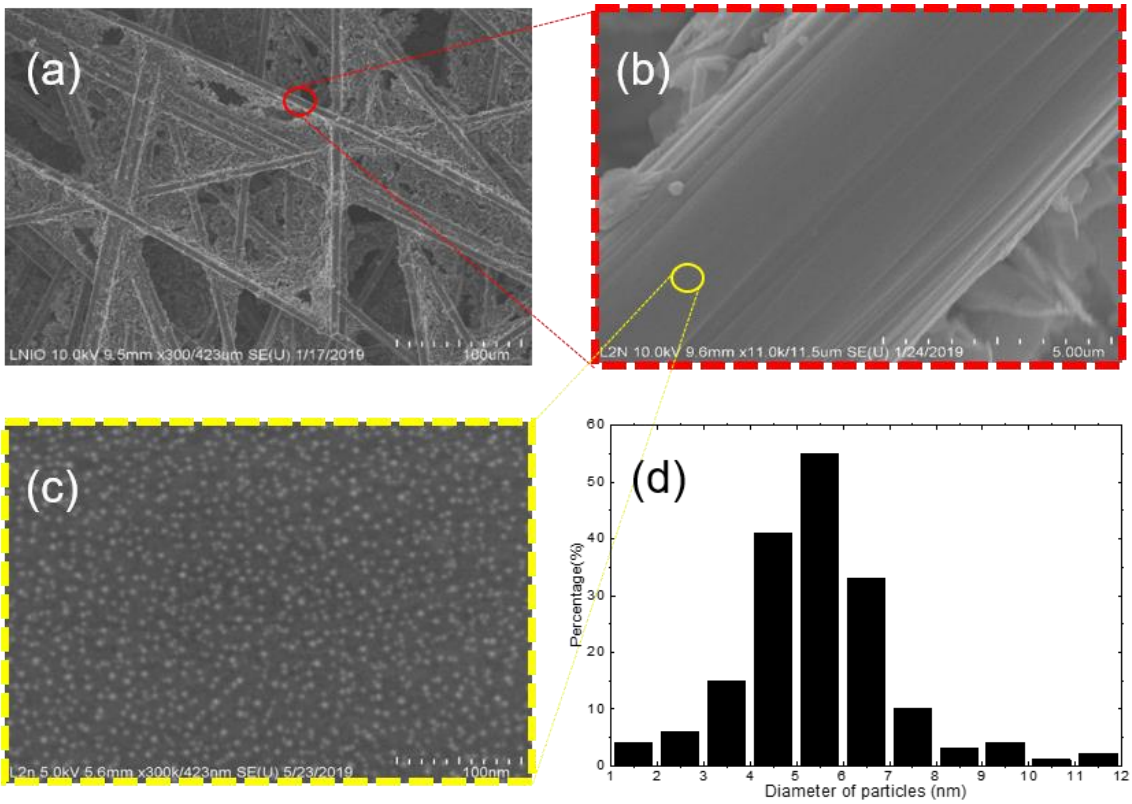

Figure II.19.SEM images of (a, b, c) Pt nanoparticles deposed in the volume of a carbon GDL (Pt/GDL) at different magnification. a) Inside the volume of a GDL made of carbon fibers at x300k; b) carbon fiber of 6µm in diameter supported of Pt nanoparticles at x11k; c) Pt nanoparticles distributed on the surface of carbon fiber. d) Particle size distribution of Pt/GDL electrodes (imageJ software).

II.4.1.4 Preparation of the SEBS55 polymer and deposition on Ni-based anodes.

The preparation of the Styrene-ethylene-butylene-styrene (SEBS) polymer has been reported in Refs [151,169] and is reproduced with the help of Z. Wang and S.

Sankarasubramanian. The solution of chloromethylated SEBS55 (55:45 molar ratio of styrene to rubber) in chlorobenzene is used to coat the Ni_{ED}/eNFT anodes by two methods. The first one is directly adapted from the coating technique used by Wang *et al.* [151] and consists of spraying the SEBS solution directly onto the previously-prepared Ni_{ED}/eNFT electrode using an air brush (Badger model 150) fed by nitrogen (N_2, 99.999% purity). The sample is placed on a heating plate (70°C) to evaporate remaining water present in the thickness of the felt and also to evaporate the chlorobenzene, producing a layer of SEBS-55 on the Ni_{ED} NPs. Once the polymer sprayed on the surface, the sample is immersed in a solution of 1-methyl-2-pyrrolidinone (NMP) (20 mL) and trimethylamine (TMA, 31–35 wt.% in ethanol) (5 mL) at 50°C for 24 hours to functionalize it and yield the AEI (SEBS55-TMA). The second method consists of immersing the prepared Ni_{ED}/eNFT electrode in the solution of chloromethylated SEBS55 + chlorobenzene for 10 min. The chlorobenzene has to be removed from the pores prior to the functionalization step in NMP + TMA. To that goal, a drying step of 1 h in a vacuum oven at 60°C is added after the immersion. The vacuum is mandatory in order to avoid heating the metallic Ni electrode in presence of O_2 and therefore its irreversible oxidation. Once the sample is dry, the same functionalization step described previously is performed. Prior to the installation of the anode in the cell, it is cleaned with deionized water and then immersed in 1 M KOH for 1 h at room temperature to replace the Cl^- anions by OH^-.

II.4.2 Unit Direct Borohydride Fuel Cell characteristics

II.4.2.1 BH_4^-/O_2 DBFC setup

As mentioned previously, an 8 cm² DBFC unit cell developed at LEMTA is used to perform tests in BH4-/O2 configurations, with the help of J. Dillet and G. Maranzana. A schematic representation of the full setup is detailed on Figure II.20. Anodic and cathodic flow fields are single-serpentine channels (1 mm width, 0.7 mm deep) machined in a brass block and coated with gold. The membrane electrode assembly constituted of (i) an anodic active layer made of either a commercial Pt-black/GDE with a loading of 2 $mg_{Pt}.cm^{-2}$ (Fuel Cells Etc), a NiED/GDE with a loading of 0.60 ± 0.05 or 3.6 ± 0.1 $mg_{Ni}.cm^{-2}$ for NiED/GDE-L or NiED/GDE- H, respectively (according to ICP-AES) or Ni_{ED}/eNFT, (ii) a commercial Nafion NRE-212 membrane exchanged to the Na+ form, and (iii) a commercial air cathode Pt-black/GDE (2 $mg_{Pt}.cm^{-2}$). PTFE seals are used to adjust the thickness of the electrodes to get 20% compression of the initial thickness. The anodic feed is composed of 0.5 M $NaBH_4$ in 4.0 M NaOH (VMR Analar Normapur). Pure oxygen (Messer, 99.99%) is used at the cathode. No sensitivity to oxygen flow rate is noticed. Temperature regulation is provided thanks to a circulating bath driven by a

Pt (100) probe inserted in the anodic plate. Before entering the cell, the cooling water passes through a heat exchanger, the function of which is to preheat the borohydride solution so it enters the cell already at a desired temperature. An in-line half PEMFC using a commercial Pt black/GDE electrode operating in hydrogen pump mode is used to measure (live) the amount of H_2 escaping the DBFC cell on-line.

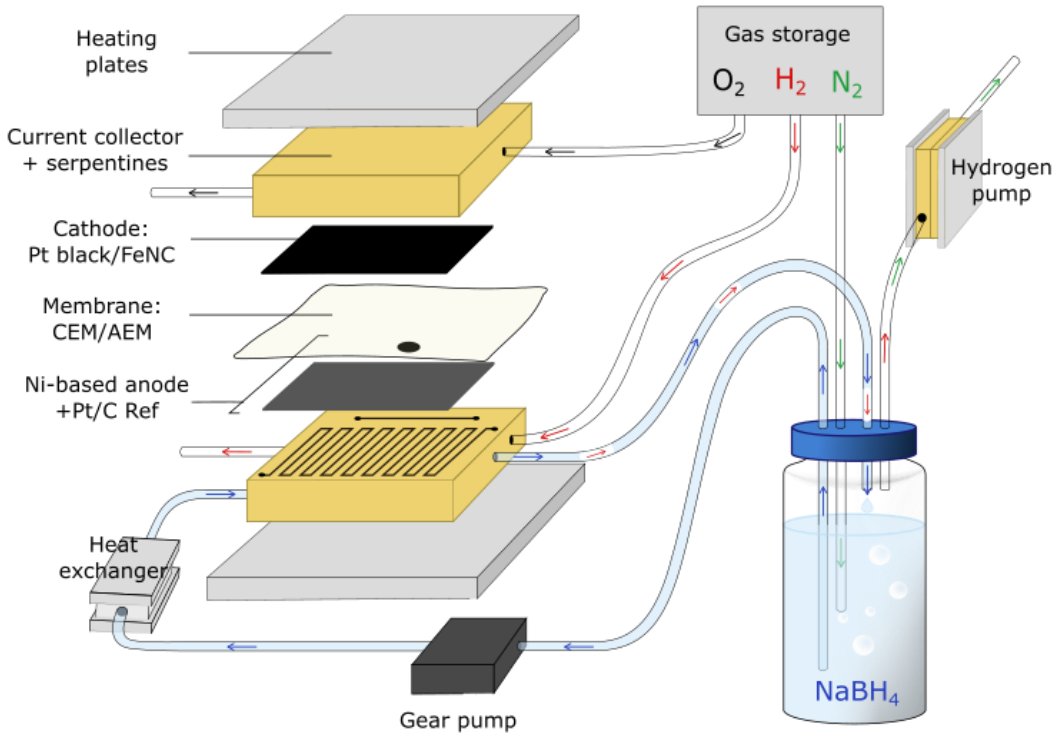

Figure II.20. Schematic representation of the BH_4^-/O_2 DBFC setup. The anolyte is recirculated in the system and its flow is ensured by a gear pump. The amount of H_2 escaping the cell is measured *in situ* using an in-line half PEMFC cell in the hydrogen pump mode.

II.4.2.2 $BH4^-/H_2O_2$ DBFC setup

The DBFC measurements performed at Washington University, with the help of Z. Wang and S. Sankarasubramanian are performed at 70°C in a corrosion-resistant cell (Fuel Cell Technologies, Inc.) composed of squared 5 cm² electrodes (2.24 x 2.24 cm) with interdigitated channels. The anode support dimensions are thus reduced from 8 to 5 cm² before any elaboration step. The optimum temperature of T = 70°C is chosen as it resulted in the best balance between DBFC performance and minimization of unwanted side reactions. The anodes used are the Ni_{ED}/eNFT + AEI samples described above and the cathode is made of a carbon-supported Pt catalyst (46 wt.% Pt/C, Tanaka K. K.) sprayed on porous carbon paper (GDL 24AA diffusion media, Ion Power) resulting in a catalyst loading of 1 mg.cm^{-2}. A commercial Nafion-117 (175 µm thick) membrane is used to separate the two electrodes and ensure H^+ conduction. The anolyte is made of 3 M KOH + 1.5 M $NaBH_4$ and the catholyte of 15 wt.% H_2O_2 in 1.5 M H_2SO_4 and both

are flown through the cell using peristaltic pumps with a flow rate of 5 mL.min^{-1}. The flowrate has also been previously optimized [128]. The measurements are performed using a Solartron® potentiostat with a 4 A limitation. 0.1 V decreasing steps are applied and maintained for 2 min from the OCV value to 0.05 V or until the current limitation is reached. A 400 µm-thick seal is used at the anode, compressing it by 25%.

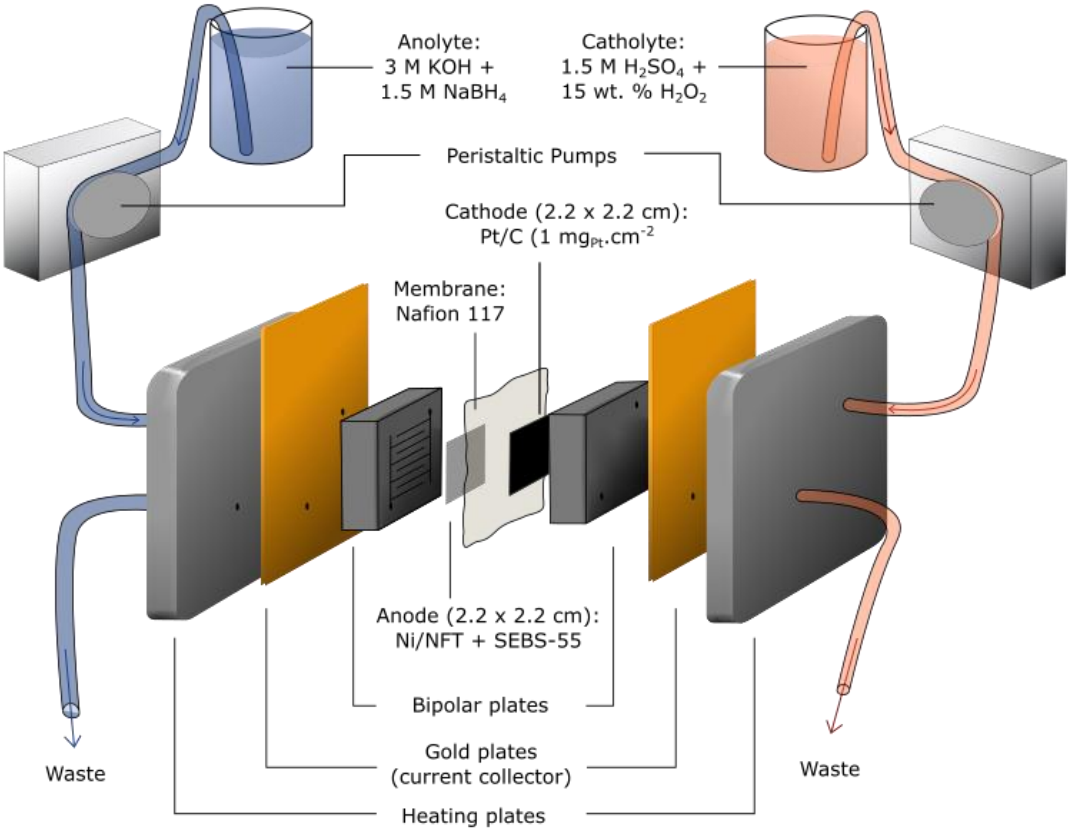

Figure II.21. Schematic representation of the BH_4^-/H_2O_2 DBFC setup. The flow rate of both electrolytes are controlled by two peristaltic pumps. Interdigitated channels were used to ensure the electrolytes passing through the electrodes.

II.5 Computational methods

Density Functional Theory calculations

Density functional Theory calculations (DFT) are performed by G. Rostamikia and M. J. Janik in Pennsylvania State University (State College, United States). All calculations are performed using the *ab initio* total energy and molecular dynamics Vienna *ab initio* simulation program (VASP) developed at the Institute for Material Physics at the University of Vienna [206,207]. The projector augmented wave method, Perdew–Wang [208] form of the generalized gradient approximation (GGA) and a cut-off energy of 450 eV are used to represent the electronic structure. A 5 × 5 × 1 Monkhorst–Pack k-point grid [209] and spin-polarized calculations are used during structural optimizations. Structural optimization minimized the forces on all atoms to less than 0.02 eV $Å^{-1}$. Harmonic vibrational modes are calculated to determine the zero-point vibrational energy (ZPVE) corrections to the total energy of adsorbed species and isolated molecules. The Ni (111) surface is modelled using a 3 × 3, four-layer slab with the bottom two layers constrained to the Ni face-centered cubic (fcc) lattice positions. A vacuum region of 15 Å is inserted between the slabs.

II.5.1

II.5.2

Microkinetic model calculations

The microkinetic modelling and simulations are performed by A. Bonnefont in the Institut de Chimie de Strasbourg (Strasbourg, France). The aim of the microkinetic modelling is to provide a semi-quantitative description of the BOR on Ni, using a simplified model able to reproduce the main features obtained from the DEMS, FTIR, DFT and electrochemical studies. For the HOR/HER on pure metallic Ni surfaces, the Heyrovsky-Volmer mechanism is considered [187,210] :

$H_{ad} + OH^- \rightleftarrows * + H_2O + e^-$ (1) (equation 2.2)

$H_2 + * + OH^- \rightleftarrows H_{ad} + + H_2O + e^-$ (2) (equation 2.3)

where * denotes a free Ni surface site.

The proper description of the HOR and BOR on Ni requires also the consideration of the surface Ni hydroxide formation, which is described by a two-step process:

$OH^- + * \rightleftarrows OH_{ad} + e^-$ (3) (equation 2.4)

$OH_{ad} + OH^- \rightleftarrows (OH)_{2,ad} + e^-$ (4) (equation 2.5)

The first step of the BOR is assumed to be the non-dissociative adsorption of BH_4^-:

$BH_4^- + x^* \rightleftarrows BH_{4,ad} + e^-$ (5) (equation 2.6)

followed by the hydrolysis of $BH_{4,ad}$:

$BH_{4,ad} + OH^- \rightarrow BOH_{ad} + 2\,H_2 + e^-$ (6) (equation 2.7)

The BOH_{ad} oxidation is assumed to be the rate determining step of the BOR on Ni:

$BOH_{ad} + 2\,OH^- \rightarrow B(OH)_{3,ad} + 2e^-$ (7) (equation 2.8)

while the desorption of the $B(OH)_{3,ad}$ species is fast process:

$B(OH)_{3,ad} \rightarrow B(OH)_3 + x^*$ (8) (equation 2.9)

The rate equations associated to these reactions steps can be formulated as:

$$\nu_1 = k_1 S_t\left(\theta_H e^{(1-\alpha_1)f(E-E_1)} - \theta_V e^{-\alpha_1 f(E-E_1)}\right)$$

$$\nu_2 = k_2 S_t\left(C_{H2}\theta_V e^{(1-\alpha_2)f(E-E_2)} - \theta_H e^{-\alpha_2 f(E-E_2)}\right)$$

$$\nu_3 = k_3 S_t\left(\theta_V e^{(1-\alpha_3)f(E-E_3)} - \theta_{OH} e^{-\alpha_3 f(E-E_3)}\right)$$

$$\nu_4 = k_4 S_t\left(\theta_{OH} e^{(1-\alpha_4)f(E-E_4)} - \theta_{(OH)2} e^{-\alpha_4 f(E-E_4)}\right)$$

$$\nu_5 = k_5 S_t\left(C_{BH4}\theta_V^x e^{(1-\alpha_5)f(E-E_5)} - \theta_{BH4} e^{-\alpha_5 f(E-E_5)}\right)$$

$$\nu_6 = k_6 S_t \theta_{BH4} e^{(1-\alpha_6)fE}$$

$$\nu_7 = k_7 S_t \theta_{BOH} e^{(1-\alpha_7)fE}$$

$$\nu_8 = k_8 S_t \theta_{B(OH)3}$$

with

$$\theta_V = 1 - \theta_H - \theta_{OH} - \theta_{(OH)2} - x\left(\theta_{BH4} - \theta_{BOH} - \theta_{B(OH)3}\right)$$

and

$$f = \frac{F}{RT}$$

S_t is the number of Ni active sites per geometric surface area and k_i, α_i, and E_i are the rate constants the charge transfer coefficient and the potential of step (i) respectively. F = 96485 C mol^{-1} is the Faraday constant, R = 8.314 $J.K^{-1}mol^{-1}$ is the ideal gas constant, T = 298 K is the temperature, E is the electrode potential.

The Faradic current is given by:

$$I_F = F(\nu_1 + \nu_2 + \nu_3 + \nu_4 + \nu_5 + \nu_6 + 2\nu_7)$$

The current-potential curves can be simulated by solving the following set of equations giving the time evolution of the electrode potential *E*, the BH_4^- and the H_2 concentrations at the electrode surface, C_{BH4} and C_{H2}, the H_{ad}, OH_{ad}, $(OH)_{2,ad}$, $BH_{4,ad}$, BOH_{ad}, and $B(OH)_{3,ad}$ coverages, θ_H, θ_{OH}, $\theta_{(OH)2}$, θ_{BH4}, θ_{BOH}, $\theta_{B(OH)3}$:

$$C\frac{\mathrm{d}E}{\mathrm{d}t} = \frac{U-E}{R_e} - I_\mathrm{F}$$

where C is the double layer capacitance, U the applied potential and R_e the sum of the electrolyte and the external resistance.

During, a linear potential sweep at a scan rate v, U is given by:

$$\frac{\mathrm{d}U}{\mathrm{dt}} = v$$

Assuming a linear concentration profile for the species in solution, the time evolution of C_{BH4} and C_{H2}, at the electrode surface are given by:

$$\frac{\mathrm{d}C_{BH4}}{\mathrm{d}t} = \frac{2.4674 D_{BH4}}{\delta_{\mathrm{BH4}}^2}(C_{\mathrm{BH4}}^0 - C_{\mathrm{BH4}}) - \frac{2.4674}{\delta_{\mathrm{BH4}}}\nu_5$$

$$\frac{dC_{\mathrm{H2}}}{d\mathrm{t}} = \frac{-2.4674 D_{\mathrm{H2}}}{\delta_{\mathrm{H2}}^2} C_{\mathrm{H2}} - \frac{2.4674}{\delta_{\mathrm{H2}}}\nu_1$$

D_{BH4} and D_{H2} are the BH_4^- and H_2 diffusion coefficients respectively, $C_{BH4}{}^0$ is the BH_4^- bulk concentration and δ_{H2} and δ_{BH4} are the H_2 and BH_4^- diffusion layer thicknesses.

The time evolutions of the surface coverages of the intermediate reaction species depend on the reaction rates:

$$S_\mathrm{t}\frac{\mathrm{d}\theta_\mathrm{H}}{\mathrm{d}t} = \nu_2 - \nu_1$$

$$S_\mathrm{t}\frac{\mathrm{d}\theta_\mathrm{OH}}{\mathrm{d}t} = \nu_3 - \nu_4$$

$$S_\mathrm{t}\frac{\mathrm{d}\theta_{(\mathrm{OH})2}}{\mathrm{d}t} = \nu_4$$

$$S_\mathrm{t}\frac{\mathrm{d}\theta_{\mathrm{BH4}}}{\mathrm{d}t} = \nu_5 - \nu_6$$

$$S_\mathrm{t}\frac{\mathrm{d}\theta_{\mathrm{BOH}}}{\mathrm{d}t} = \nu_6 - \nu_7$$

$$S_\mathrm{t}\frac{\mathrm{d}\theta_{\mathrm{B(OH)3}}}{\mathrm{d}t} = \nu_7 - \nu_8$$

Finally, the H_2 escape current can be calculated using the equation:

$$I_{H2} = 2F\frac{D_{H2}}{\delta_{H2}}C_{H2}$$

Table II.1: Values of the variables involved in the tentative BOR mechanism.

Constant	Definition	Units	Value
S_t	Ni site density	mol cm^{-2}	4.4 10^{-9}/4.4 10^{-8}
D_{BH4-}	BH_4^- diffusion coefficient	cm^2 s^{-1}	1.6 10^{-5}
D_{H2}	H_2 diffusion coefficient	cm^2 s^{-1}	10^{-4}
k_1	Volmer rate constant	s^{-1}	0.1
E_1	Volmer step equilibrium potential	V *vs.* RHE	0.15
k_2	Heyrovsky H_2 rate constant	s^{-1}	250
E_2	Heyrovsky step potential	V	-0.51
k_3	OH^- adsorption/desorption rate constant	s^{-1}	100
E_3	OH^- adsorption equilibrium potential	V *vs.* RHE	0.02
k_4	$(OH)_{2,ad}$ formation rate constant	s^{-1}	0.1
E_4	$(OH)_{2,ad}$ equilibrium potential	V *vs.* RHE	0.2
k_5	BH_4^- adsorption rate constant	cm^3 mol^{-1} s^{-1}	2 10^4
E_5	BH_4^- adsorption potential	V	-0.8
k_6	BOH_{ad} formation rate constant	s^{-1}	100
k_7	$B(OH)_{3,ad}$ formation rate constant	s^{-1}	10
k_8	$B(OH)_{3,ad}$ desorption rate constant	s^{-1}	500
k_6	BOH_{ad} oxidation rate constant	s^{-1}	10

α_{1-6}	Charge transfer coefficients of steps (1) to (6)		0.5
α_7	Charge transfer coefficient step (7)		0.9
δ_{BH4}	BH_4^- diffusion layer thickness	µm	14.5
δ_{H2}	H_2 diffusion layer thickness	µm	26.7
Scan rate	Potential sweep rate	$V\ s^{-1}$	2×10^{-2}
*R*e	Ohmic drop	Ω	10^{-2}
C	Double layer capacity	F	10^{-4}

CHAPTER III: BOR mechanism on noble and model surfaces

Although the BOR mechanism has been studied in many papers so far, the knowledge of this reaction is essentially limited to (i) noble metals (Pt and Au, mostly) and (ii) very mild experimental conditions (low borohydride concentration, typically < 50 mM $NaBH_4$, room temperature) that are far from those experienced in practical DBFC anodes. As a result, one can still not predict what the behavior of electrocatalysts different from Pt and Au will be in real operating conditions. This chapter aims at going beyond these insufficiencies. It is based on two articles addressing the BOR mechanisms on noble metal bulk electrodes [211,212] presenting several detrimental effects when the borohydride concentration is increased from the fundamental to the application scale. Parts of the data presented in this chapter were obtained by P.Y. Olu or M. Chatenet prior to this PhD work. First, the understanding of the Borohydride Oxidation Reaction (BOR) at the start of this PhD will be presented as a reference mark; it mostly concerns the behavior of Pt electrodes at low concentration of $NaBH_4$. From this point, the borohydride concentration will be increased to match more realistic conditions and the resulting effects will be presented. The proposed model will then be detailed to include these new insights for Pt as well as the mechanism of the reaction on Au electrodes. Next, Pd will be investigated as a potential substitute to Pt towards the BOR. The differences observed between these noble metals will be pointed out and then a tentative mechanism will be proposed for the reaction on Pd electrodes. To conclude this chapter, a brief review of the literature will guide us towards the use of non-noble metal electrocatalysts for the BOR, which will be discussed in the following chapters.

III.1 Current understanding of the BOR on Pt electrodes

As mentioned previously, the borohydride oxidation reaction (BOR) is a really complex electrochemical reaction, because 8 electrons are (theoretically) generated per BH_4^- species oxidized, which means that it must proceed in several elementary steps and involve intermediate species. One of the interesting properties of the BOR, described by equation 3.1, is its impressively low standard potential (E^o = -0.41 V *vs* RHE) that could, theoretically, significantly increase the voltage of the DBFC (in comparison with a conventional PEMFC or AEMFC).

$$BH_4^- + 8\,OH^- \rightarrow BO_2^- + 6\,H_2O + 8\,e^- \qquad \text{(equation 3.1)}$$

However, this potential is difficult to reach in practice, not only because of slow BOR kinetics but also because the reaction enters in competition with the hydrogen evolution reaction (HER) when E < 0 V *vs* RHE. These competitive reactions will induce a mixed potential and the activity of the electrocatalysts used towards the BOR and the HER will

determine the actual onset potential. The HER is a rather well understood reaction (very well in acidic medium, much less in alkaline medium), where H_{ad} species are adsorbed at the surface of the catalyst *via* the Volmer step (equation 3.2) and then combined either with another H_{ad}, *via* the Tafel step (equation 3.3), or a water molecule, *via* the Heyrovsky step (equation 3.4), to form molecular hydrogen, H_2, which will be dissolved in the electrolyte until it reaches the solubility limit, and then goes into the gas phase [134,213]. Because of the activity of Pt towards the HER, H_2 will be favorably evolved at negative potentials on the RHE scale, resulting in a positive shift of the onset potential of the BOR towards higher values (typically -50 mV *vs* RHE for 5 mM $NaBH_4$); this strongly limits the advantages of the BOR on Pt (one would like the reaction to proceed at potential close to -0.41 V *vs* RHE).

Volmer : $H_2O + e^- \rightleftarrows H_{ad} + OH^-$ (equation 3.2)

Tafel : $2\,H_{ad} \rightleftarrows H_2 + 2\,s$ (equation 3.3)

Heyrovsky : $H_{ad} + H_2O + e^- \rightleftarrows H_2 + OH^-$ (equation 3.4)

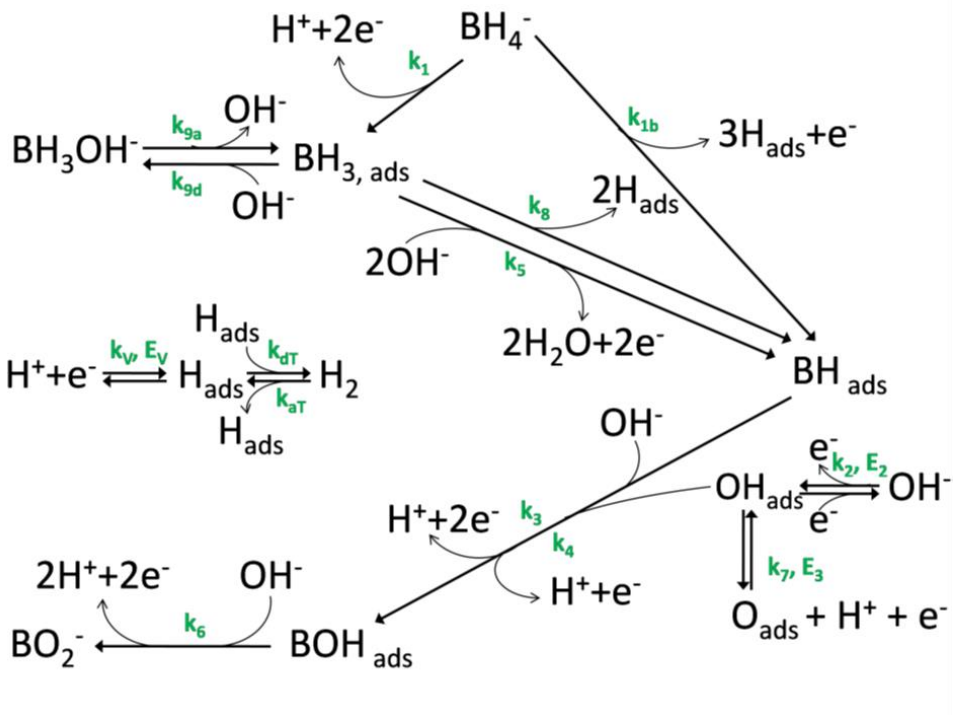

Figure III.1. Tentative BOR mechanism on Pt electrodes proposed by Olu in his PhD manuscript [113]. Note that the partial reactions are presented in their acidic form for brevity, but they obviously occur in alkaline form in practice.

Moreover, other parasitic reactions affect the efficiency of the BOR, such as the heterogeneous hydrolysis of BH_4^-. Indeed, when dissolved in water, the fuel suffers significant decomposition (catalyzed by Pt and other noble metal electrodes) into a H_2

molecule and the intermediate BH_3OH^- species, as described by equation 3.5. This anion can undergo a second chain hydrolysis reaction to form 3 other H_2 molecules and the final, and stable, BO_2^- product. This purely chemical process is quite detrimental to the valorization of BH_4^-, since the fuel is consumed without generating any electrons, which is directly translated into an energy loss of the DBFC system (at least if the produced H_2 molecules are not valorized, i.e. further oxidized). Overall, a significant amount of gaseous hydrogen is produced through this process (4 H_2 produced per BH_4^- consumed), which is in opposition with the first principle of the DBFC, being to use liquid fuel to avoid the issues encountered when using H_2 in PEMFC, as mentioned in Chapter I. This hydrolysis process is activated by the temperature and a low pH of the solution [110,114,214]. It is therefore possible to slow down the kinetics of reaction of the two hydrolysis steps by working at low temperature and high pH (typically T = 20°C and pH = 14 in a 1 M NaOH supporting electrolyte). The nature and morphology of the catalyst used will also impact the rate of the hydrolysis and could be modified accordingly to decrease it.

$$BH_4^- + H_2O \rightarrow BH_3OH^- + H_2 \qquad \text{(equation 3.5)}$$

$$BH_3OH^- + H_2O \rightarrow BO_2^- + 3\,H_2 \qquad \text{(equation 3.6)}$$

The BOR has been studied in LEPMI for more than 10 years, in particular through the PhD of Belen Molina Concha (2009) [144] and Pierre-Yves Olu (2015) [113], where numerous measurements and calculations, performed mainly on Pt and Au model electrodes, allowed to unveil the different pathways of the reaction and the intermediate species they produce. Based on these experiments and data gathered from the literature, especially from Density Functional Theory (DFT) calculations [215–219], Olu developed a tentative model of the BOR on a Pt electrode (Figure III.1) using micro-kinetic simulations. From this model, the complete reaction can be separated into several steps involving the intermediate specie that had been detected and predicted by modelling in the above-cited references.

The first step of the BOR is the adsorption of BH_4^- anions onto the electrocatalyst surface. This adsorption will already determine the reaction pathway since it could result in different produced species depending on the studied electrocatalysts. For a gold surface, DFT calculations suggest that borohydride adsorbs molecularly [216], following the reaction described by equation 3.7, producing one $BH_{3,ad}$ adsorbate. On the contrary, for platinum surface, BH_4^- anions adsorb in a dissociative manner [216], producing one BH_{ad} and three H_{ad} species as well as one electron (equation 3.8).These adsorbed hydrogen species will be very quickly valorized on a Pt electrode once a positive potential (*vs* the reversible hydrogen electrode scale) is reached, because of the well-

known HOR activity of Pt. So, for Pt, large current generation is possible at low overpotential (as soon as $E > 0$ V *vs* RHE) *via* the production of three additional electrons due to ionization of 3 H_{ad} species.

Molecular adsorption: $BH_4^- + s + OH^- \rightarrow BH_{3,ad} + H_2O + 2e^-$ (equation 3.7)

Dissociative adsorption: $BH_4^- + 4\,s \rightarrow BH_{ad} + 3\,H_{ad} + e^-$ (equation 3.8)

However, according to DFT calculations, the BH_{ad} species produced by this first step of the reaction on Pt are the most stable amongst all possible species taken into account. This means that their oxidation following an Eley-Rideal (E-R) mechanism involving OH- from solution (equation 3.9, k_3 on Figure III.1) can be assumed to be the rate determining step. It produces two additional electrons and BOH_{ad} species that will undergo a second E-R oxidation reaction (equation 3.10, k_6 on Figure III.1) leading to the final 2 electrons and product of reaction BO_2^-.

BH_{ad} oxidation (E-R): $BH_{ad} + 2OH^- \rightarrow BOH_{ad} + H_2O + 2e^-$ (equation 3.9)

BOH_{ad} oxidation (E-R): $BOH_{ad} + 2OH^- \rightarrow BO_2^- + H_2O + 2e^-$ (equation 3.10)

With this pathway, the reaction is correctly completed with 8 electrons produced. It was demonstrated by Finkelstein *et al.* [137] that a significant self-poisoning occurs on both Pt and Au electrodes, decreasing the efficiency of the BOR. This is explained within the proposed model by the slow oxidation of BH_{ad} species on Pt electrode in step 3.9. Indeed, these intermediate species require several neighboring active sites to be formed *via* the dissociative adsorption (equation 3.8). Because they are the most slowly-oxidized adsorbates (equation 3.9, rate determining step), they can accumulate on the surface until it is covered and no configuration with several adjacent active (free) sites can be found. This results in a large current decrease, since no H_{ad} species are formed anymore. When this state is reached, a switch in the adsorption mechanism from dissociative to molecular occurs (molecular adsorption does not require as many adjacent free active sites). Because the $BH_{3,ad}$ adsorbates formed by equation 3.7 are not as stable on the Pt surface as BH_{ad}, they can easily desorb into BH_3OH^- species (equation 3.11, k_9 on Figure III.1) if not transformed quickly enough. These ions are detected using Rotating Ring-Disk Electrode (RRDE) on Pt electrodes [131]. The $BH_{3,ad}$ species that indeed desorb and escape from the diffusion layer induce a significant loss of six electrons. However, if not desorbed, the $BH_{3,ad}$ adsorbate can itself be dissociated into 2 H_{ad} and a BH_{ad} specie (equation 3.12, k_8). Two additional neighboring sites are however necessary. When no sites are available anymore $BH_{3,ad}$ could be oxidized following equation 3.13 (k_5 on Figure III.1), but because of the slow nature of the E-R process they will more likely desorb (or poison the electrode surface).

$BH_{3,ad}$ desorption: $BH_{3,ad} + OH^- \rightleftarrows BH_3OH^- + s$ (equation 3.11)

$BH_{3,d}$ dissociation: $BH_{3,ad} + 2\,s \rightarrow BH_{ad} + 2\,H_{ad}$ (equation 3.12)

$BH_{3,ad}$ oxidation (E-R): $BH_{3,ad} + 2OH^- \rightarrow BH_{ad} + 2\,H_2O + 2e^-$ (equation 3.13)

From this point, the reaction rate on Pt is determined by the oxidation of BH_{ad} until a higher potential is reached. Indeed, for E > 0.6 V *vs* RHE, OH_{ad} adsorbates start to form at the surface (k_2 on Figure III.1) allowing a new BH_{ad} oxidation pathway following a Langmuir-Hinshelwood (L-H) mechanism (equation 3.14, k_4 on Figure III.1). The resulting oxidation occurs at a much faster rate than the initial E-R one, since it is potential-activated. This results in a fast regeneration of the surface and a large current increase with 8 electrons produced per BH_4^- once again (see the high potential region, E > 0.8 V *vs* RHE on Figure III.3a for illustration of the phenomenon).

BH_{ad} oxidation (L-H): $BH_{ad} + OH_{ad} + OH^- \rightarrow BOH_{ad} + H_2O + e^-$ (equation 3.14)

These proposed reaction pathways for the BOR on Pt surfaces, and the corresponding kinetic simulations correctly fit the experimental data [113] for a concentration of borohydride in the range of mM (typically 5 mM $NaBH_4$ in laboratory experiments). However, in a real DBFC system, the concentration of $NaBH_4$ is much greater in order to generate more current and not to be limited by the consumption of the fuel during operation. The typical DBFC concentration varies between 0.5 M $NaBH_4$ and 2 M $NaBH_4$ [120,151,220], which results in large (theoretical) limiting current density but might also raise some issues regarding the self-poisoning of the electrode and change the reaction mechanism. Such high operating concentrations will be investigated on both Pt and Au model surfaces in order to observe if detrimental effects appear and adapt the BOR model to gold electrodes.

III.2.1

III.2 Influence of the $NaBH_4$ concentration on the reactions pathway

Poisoning effects of surface at different borohydride concentration

In this section, mirror-polished electrodes 2 mm in diameter (S_{geo} = 0.031 cm²) of pure Pt and Au were used in a Rotating Disk Electrode (RDE) configuration, in a 4-electrodes electrochemical cell, to measure the different limiting currents in various borohydride concentrations, from [$NaBH_4$] = [10^{-6}; 1.5] M. More details about the electrochemical cell configuration and the preparation of the electrolytes are given in sections "II.1.1 Rotating Disk Electrode in alkaline medium". The preparation of the noble-metal RDE

electrodes is detailed in the section "II.1.2 Electrodes and catalyst ink preparation". For clarity, 3 concentrations were chosen to represent the laboratory scale, intermediate conditions, and (DBFC) operation conditions: [$NaBH_4$] = [5; 50; 500] mM respectively. All measurements were performed using dynamic Ohmic-drop corrections, which is particularly necessary at high concentration, where high currents are reached.

Before this study, Open Circuit Potential (OCP) measurements were performed on both electrodes for the whole concentration window. The obtained OCP values are presented in Figure III.2 (OCP in supporting electrolyte ([$NaBH_4$] = 0 M) are not presented in the logarithmic scale) versus the concentration represented both linearly and logarithmically for clarity reasons. The OCP is the potential value taken by the electrode at zero current. It might result from the occurrence of several simultaneous redox reactions at the interface of the WE material and the species in the electrolyte. In the case of the supporting electrolyte (1 M NaOH), only hydroxides and oxides (OH_{ad} and O_{ad}) are formed and reduced at the metal surfaces. The formation of OH_{ad} occurs for E > 0.6 V *vs* RHE at pH = 14 for a platinum electrode however, the recorded OCP is higher (E_{Pt} = 0.86 V vs RHE), probably owing to an equilibrium between OH_{ad} and O_{ad}. Au oxides should form at a higher potential (E = 1.1 V *vs* RHE), but the recorded OCP is this time lower (E_{Au} = 0.93 V *vs* RHE). For [$NaBH_4$] = 10^{-6} and 10^{-5} M, the OCP of the two electrodes stays unmodified versus the case in supporting electrolyte, because the amount of borohydride species at their interface is too low to have an impact on the presence of metal (hydr)oxides and therefore on the mixed potential. Then for higher $NaBH_4$ concentrations, the "steady-state" is completely modified and the OCP significantly decreases as a result of the occurrence of concomitant reactions. On platinum, the potential drops to a value near E = 0 V *vs* RHE for [$NaBH_4$] = 10^{-4} M and further slowly and gradually decreases to values approaching E = -0.1 V *vs* RHE at the highest $NaBH_4$ concentrations studied here. The OCP on Pt drops this fast because H_2 is generated through the hydrolysis of the fuel (equations 3.5 and 3.6) and is therefore driven by the fast HOR kinetics. Because as soon as the potential becomes negative *vs* RHE, the HER (equations 3.2, 3.3 and 3.4) is triggered, so the OCP value will not decrease significantly more. This value thus results from the competition between the HER/HOR and the BOR.

On gold, a drop of 450 mV is first observed between 10^{-5} M and 10^{-4} M $NaBH_4$, and then tends to stabilize around E = 0.25 V *vs* RHE until 10^{-2} M $NaBH_4$. Because of the slow charge transfer kinetics of the HER and BOR on Au, its oxidation current in this potential range can be compensated by the oxygen reduction reaction (ORR) coming from the residual oxygen in the electrolyte, before the BOR contribution becomes too large (≥ 10^{-2} M $NaBH_4$). For those higher concentrations, the OCP reaches lower values on Au than on Pt, because hydrogen evolution (and oxidation as well) reaction kinetics

is slower on Au, and thus the compensation of the BOR current by the HER occurs at lower mixed potential than on Pt.

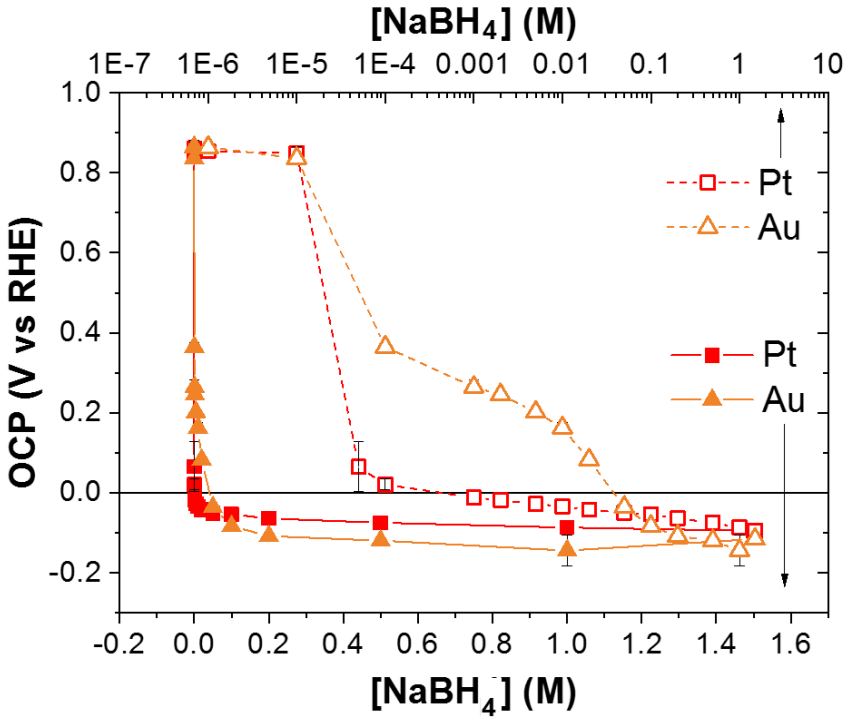

Figure III.2. Open Circuit Potential (OCP) measured on polycrystalline gold and platinum electrodes (S_{geo} = 0.031 cm²) for sodium borohydride concentration varying from 10^{-6} M to 1.5 M in Ar-saturated 1 M NaOH at T = 20°C and ω = 1600 rpm. Full lines and symbols correspond to the linear concentration scale and dashed-lines to the logarithmic one.

Cyclic voltammograms were recorded on both Pt and Au electrodes while varying the rotation rate of the electrode (Figure III.3 and III.4). The values for the rotation rate were chosen to observe a constant current increase between each cycle if the reaction is mass-transport limited, following Levich's law (equation 3.15). The second 400 rpm cycle is used to observe if the state of the surface changed during the measurement.

Levich's Law: $$I_L = 0.620\, n.F.A.D^{2/3}.\omega^{1/2}.\nu^{1/6}.C \qquad \text{(equation 3.15)}$$

with:

n the number of exchanged electrons

F the Faraday constant (C mol^{-1})

C the concentration of $NaBH_4$ (mol cm^{-3})

D the diffusion coefficient of BH_4^- (cm^2 s^{-1})

ν the kinematic viscosity of the electrolyte (cm^2 s^{-1})

ω the rotation rate of the RDE (rad s^{-1})

The CVs recorded using the Pt electrode (Figure III.3a) at low concentration (5 mM $NaBH_4$) can be separated in two distinct zones when ω = 400 rpm: first, a well-defined

plateau is observed for $E < 0.8$ V *vs* RHE; once this potential is reached, a small decrease is observed before the appearance of a second plateau, however less defined (the measured current is not strictly constant). The first region corresponds to a mass-transport limited plateau, because the current increase is linearly proportional to the square root of the rotation rate. However, the plateau's stability decreases when more species are brought to the electrode. The cycle measured at ω = 2500 rpm shows that, as soon as the maximum current is reached, it starts to decrease until, at the end of the plateau, it becomes similar to the initial current measured at ω = 1600 rpm ($j_{E=0.8V,2500rpm} \approx j_{E=0.3V,1600rpm} \approx 40$ mA.cm^{-2}). This current decrease is explained by the surface poisoning by BH_{ad} species and OH_{ad}, starting to appear from $E = 0.6$ V *vs* RHE, described in the previous section. Indeed, to make the parallel with the proposed model, the onset of reaction is slightly below 0 V *vs* RHE; positive current is measured once this potential is reached (however the reaction starts earlier but is masked by the HER contribution) via the oxidation of H_{ad} (originating from BH_4^- dissociative adsorption, equation 3.8), a fast reaction on Pt, accounting for the fast kinetics observed. When the rotation rate is relatively low, the reaction is stable; however, when more species are brought to the surface, it gets covered faster by the adsorbed BH_{ad}, resulting in a current loss. Quickly the current increases again to form the second plateau; however, because of charge-transfer kinetics still too slow, the limiting current of the first plateau is hardly reached, especially at high rotating rates, where the surface starts to completely passivate with the continuous formation of surface oxides and gets possibly blocked by borate species. The second cycle at ω = 400 rpm is well superimposed with the first one, meaning that the surface is essentially regenerated from its poisons when cycled to high potentials, as described by Finkelstein *et al.* [137].

When the borohydride concentration is increased to the intermediate value (Figure III.3b, 50 mM $NaBH_4$), the two potential-separated regions can be observed again. However, the first one does not correspond to a mass-transport limited plateau anymore. Indeed, even at ω = 400 rpm, the current starts to decrease above $E = 0.5$ V *vs* RHE and for higher rotation rates, the current increase is not proportional to the square root of the rotation rate anymore. Because more active species are present at the electrode interface, it takes longer to reach a mass-transport limited state and as soon as the reaction kinetics is not the limiting process, the current drops significantly due to a lack of available active sites. A second peak is observed once OH_{ad} species start to form ($E = 0.6$ V *vs* RHE), which is not explained by the proposed BOR mechanism: the L-H oxidation of BH_{ad} is activated for $E > 0.8$ V *vs* RHE. A possible explanation for this peak is the appearance of a dual behavior of the electrode. For a poisoned electrocatalytic reaction, if Omhic-drop compensation is applied, it is possible to observe the formation of auto-organized domains on the surface of the electrode: one part will be in a mass-transport limitation state, while the other is still in the poisoned

state [221,222]. This will result in the emergence of a shoulder or peak as seen on Figure III.3b. After ω = 900 rpm, mass-transport does not appear to influence the reaction in the low potential region, suggesting once again that the reaction is limited, most probably by the small amount of available active sites. The current measured in the second potential region (E > 0.9 V *vs* RHE) is also limited for ω ≥ 900 rpm, again suggesting that the L-H mechanism (equation 3.14), even if it is faster than the E-R one, is still a rather slow reaction and the surface gets passivated before the mass-transport limitation is reached. The reaction is overall limited by the poisoning of the surface at this concentration, but the second 400 rpm cycle still corresponds to the first one, meaning that the surface is still able to regenerate with the formation of oxides at E = 1.5 V *vs* RHE.

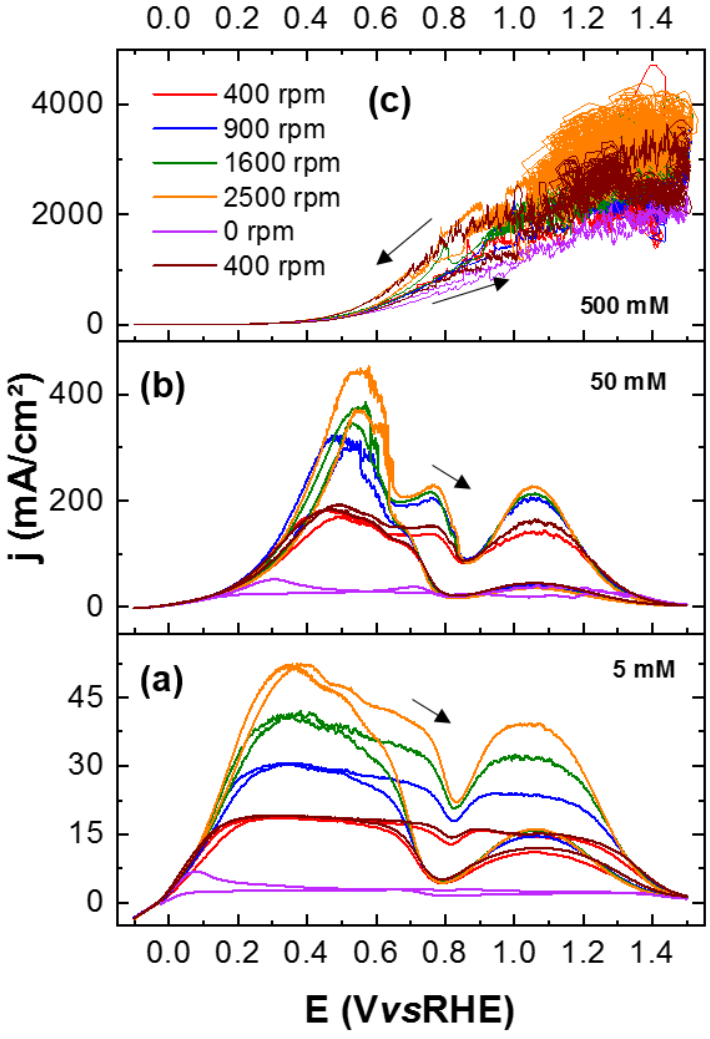

Figure III.3. Ohmic-drop corrected CVs measured on Pt mirror-polished polycrystalline electrodes (S_{geo} = 0.031 cm²) in RDE configuration at three different borohydride concentrations: 1 M NaOH + (a) 5 mM, (b) 50 mM, (c) 500 mM $NaBH_4$ and various rotating rate of the electrode following this cycle: [400; 900; 1600; 2500; 0; 400] rpm. Ar-saturated electrolytes, v_s = 20 mV.s^{-1}, T = 20°C

The two distinct regions are not detected anymore for the high $NaBH_4$ concentration, corresponding to the DBFC operation condition (Figure III.3c, 500 mM $NaBH_4$). At such concentration, significant amounts of bubbles are generated, resulting in a very noisy signal. Those bubbles are also problematic regarding the Ohmic drop correction. Indeed, they grow to a certain size before being ejected from the surface, which results in significant parts of the electrode being covered by bubbles during the reaction and a decreased active surface area. Therefore, the Ohmic resistance is also modified and, because of the dynamic correction used, a noise appears in the abscissa direction, resulting in a spooled signal when combined to the normal y-axis noise. This noise is significantly amplified when the oxide region is scanned (E > 0.9 V *vs* RHE), because the H_2 produced cannot be valorized on Pt oxides and therefore significant amounts escape the interface, as it was discovered by Olu during his PhD [113]. This will be detailed at several concentrations later in this chapter. Regarding the reaction itself, only small mass-transport contributions are observed: the current measured at ω = 2500 rpm and E = 1.5 V *vs* RHE is only around 1.6 time higher than the one measured without forced convection (ω = 0 rpm) at the same potential. This could indicate that the reaction is mostly limited by charge-transfer kinetics. In addition, the backward scan on the second 400 rpm cycle is significantly higher than the onward scan in the 0.5 V *vs* RHE < E < 1.1 V *vs* RHE region. This effect is also observed on other cycles but not as clearly. It indicates again that the formation of oxides allowed the surface to regenerate some of its poisoned active sites, and that as soon as these oxides are reduced, new BH_4^- and intermediate species (*e.g.* H_{ad}) can be formed, increasing the current generation.

The same measurements were conducted using the Au electrode (Figure III.4) and once again two distinct regions can be discerned (at low and intermediate concentration). However, they do not correspond to the same phenomena. First of all, the reaction onset on a gold surface (0.3 V *vs* RHE at 5 mM $NaBH_4$) is significantly higher than on platinum (0 V *vs* RHE at the same $NaBH_4$ concentration). This major difference originates from the inability of Au to adsorb dissociatively BH_4^- ions, as mentioned previously. This detrimental aspect already rules Au out of the potential catalysts for high energy DBFC systems, since around 0.7 V is lost in activation overpotential (compared to the standard potential of the reaction $E°_{BH4-/BO2}$ = -0.41 V *vs* RHE). The BOR on Au electrode will nonetheless be investigated to understand how it occurs and compares with the mechanism proposed on Pt. The two regions correspond to two waves of reaction, the first one starting at E = 0.3 V *vs* RHE followed by the second around E = 0.8 V *vs* RHE at 5 mM $NaBH_4$ (Figure III.4a). Olu already made some preliminary RRDE studies [113] and detected the formation of BH_3OH^- species during the first wave, confirming the presence of $BH_{3,ad}$ intermediate species at the electrode surface at the start of the reaction. This study will be completed in the next section. An important observation is that the current density reached at the first plateau corresponds to half of the second

one. Moreover, this second plateau displays similar current density values to the one observed on Pt at the same concentration (Figure III.3a) (*ca.* 40 mA.cm^{-2} for ω = 2500 rpm). If 8 electrons are assumed to be produced on Pt, this could mean that the BOR on Au follows a pathway involving 4 electrons in the first wave and requires higher potential to reach 8 electrons produced (complete BOR). These two plateaus correctly follow the Levich's law, with the current proportional to the square root of the rotation rate (at 5 mM and 50 mM $NaBH_4$).

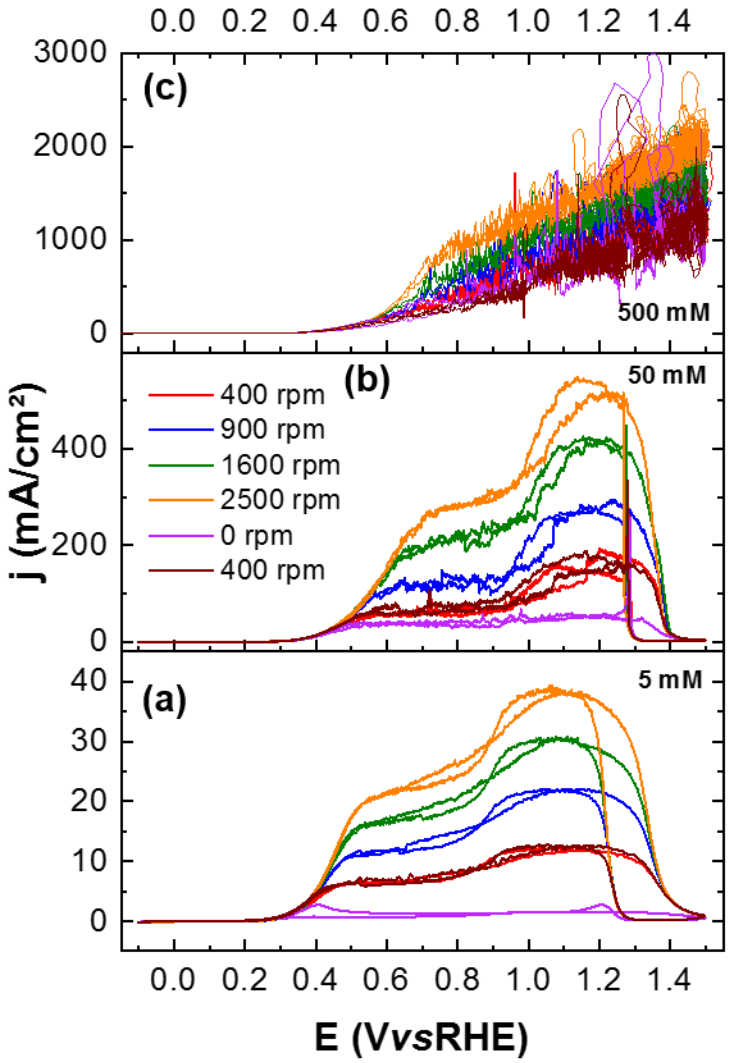

Figure III.4. Ohmic-drop corrected CVs measured on Au mirror-polished polycrystalline electrodes (S_{geo} = 0.031 cm²) in RDE configuration at three different borohydride concentrations: 1 M NaOH + (a) 5 mM, (b) 50 mM, (c) 500 mM $NaBH_4$ and various rotating rate of the electrode following this cycle: [400; 900; 1600; 2500; 0; 400] rpm. Ar-saturated electrolytes, v_s = 20 mV.s^{-1}, T = 20°C

For the intermediate concentration (Figure III.4b), the same behavior is observed, however slightly delayed in potential, due to the slow charge-transfer kinetics. This time, the current density measured on the second plateau is greater than the maximum current density recorded on the Pt electrode (Figure III.3b), confirming that the latter

suffers from important poisoning and H_2 escape, resulting in a loss of faradic efficiency already at E = 0.5 V *vs* RHE. From this observation, the poisoning of the surface on Au electrodes appears less important than on Pt. For the operation concentration (Figure III.4c), the maximum current density reached is now smaller than for Pt (*ca.* 2000 $mA.cm^{-2}$ and 3000 $mA.cm^{-2}$, respectively). This could be explained by the slower charge-transfer kinetics of the pathway contributing to the first wave, resulting in smaller current at higher concentrations. However, some mass-transport dependence can be observed for high rotation rate of the electrode (ω = 1600 and 2500 rpm). It is observed on both forward scans with quite defined "plateaus", unlike for Pt, where the current of the backward scan appeared noticeably greater. Moreover, the same current was measured for ω = 400 rpm and 2500 rpm on Pt. By comparing these two different behaviors, one could propose that the reaction is mostly limited by the charge-transfer kinetics on Au electrodes at 500 mM $NaBH_4$, where BOR on Pt appears to be mostly limited by surface poisoning. Overall, the BOR seems to follow a simpler pathway on the Au electrode, with only two mass-transport limited reaction waves and smaller propensity to poisoning.

CVs at complementary concentrations were performed on the Pt electrode to confirm that its driving limiting process occurring at high concentration is indeed the surface poisoning and observe its effect on the start of the reaction. The positive scans of each CV are presented on Figure III.5a: increasing the concentration indeed has an important effect on the reaction. Until 100 mM $NaBH_4$, the onset of the reaction is correctly described by the charge-transfer limitation; however, for higher concentrations, the reaction is delayed. When too many BH_4^- species are brought to the surface, even before the start of the reaction, the active sites start to be blocked by intermediate $BH_{x,ad}$ species, forcing the reaction to go through the alternative "partially dissociative" pathway. This is obviously not a binary process since the current density is already delayed at 200 mM $NaBH_4$ (Figure III.5a), but keeps falling down when the concentration is further increased, meaning that the pathway switch occurs gradually with the amount of species brought to the surface. To observe in more details this behavior at the onset of the reaction, potentials were retrieved at an arbitrary current density value, corresponding to *ca.* 1/3 of the diffusion-limited faradic current of the lowest concentration considered (1 mM $NaBH_4$) (Figure III.5b). This potential decreases from 1 mM to 100 mM $NaBH_4$, which can be correlated to the OCP decrease when the concentrations increases. It shows that the reaction efficiency actually increases until this concentration, since a smaller overpotential is required to reach the same current density. However, similarly as the full CVs, as soon as [$NaBH_4$] is increased above 100 mM, the potential increases. It seems to stabilize at 1 M $NaBH_4$ and above, suggesting that a steady state between the two reaction pathways is reached.

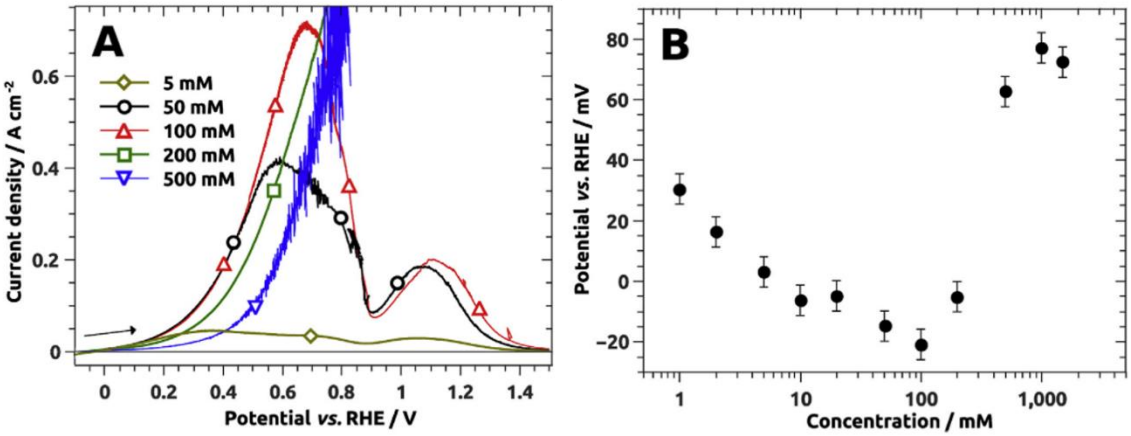

Figure III.5. Selection of a few positive sweep scans of BOR CVs performed at v_s = 20 mV.s^{-1} on a polycrystalline Pt electrode in RDE configuration (ω = 1600 rpm) for 5, 50, 100, 200 and 500 mM $NaBH_4$ in 1 M NaOH (T = 25°C). (b) Dependence of the potential value measured at a current density of j_{geo} = 3.1 mA.cm^{-2} ($E_{j=3.1\ mA\ cm-2}$) versus [BH_4^-]. Reprinted from Ref. [211].

It is important to mention that the poisoning effects described in this section are dependent on the density of active sites. In the present case, the 0.031 cm² mirror-polished electrodes exhibit a rather limited surface (roughness factor ≈ 2 – 3, determined with H_{UPD} on the Pt electrode) and therefore these poisoning effects appear enhanced. In application, materials with much more developed surface areas, such as nanoparticles supported on carbon supports, are used and poisoning should only occur for larger $NaBH_4$ concentrations. This means that the key concentration to minimize the effects of poisoning will be increased in a real system. However, some recent DBFC studies using a relatively low $NaBH_4$ concentration (100 mM $NaBH_4$) presented rather promising performance [149].

Overall, the Pt electrode displays interesting performance towards the BOR, mainly thanks to the fast oxidation of the H_{ad} through the HOR at potentials close to 0 V *vs.* RHE; it explains why Pt is the most used catalyst for this reaction. However, it was demonstrated that Pt does not utilize the advantages of borohydrides fully. Its onset potential is really high compared to the standard potential of the BOR, because Pt promotes fast HER/HOR and the electrons generated during the BOR are mainly produced through the HOR. In application, it does not really matter since energy is still produced (at least if the generated H_2 is fully oxidized). However, this indirect aspect of the reaction can be translated to poor ability of Pt surfaces to oxidize the boron-based species, resulting in their important and detrimental poisoning and H_2 escape. In application, the poisoning could be limited by performing a "cleaning" step by increasing the potential of the anode to potentials required to form Pt-oxides. However, this could induce drastic degradation of the anode and most importantly the cathode [223,224] and should be avoided. Despite its lower OCP and smaller surface poisoning,

Au is not an efficient catalyst for the BOR and should only be used for fundamental and mechanistic studies.

Existence of additional reaction pathways

III.2.2.1 Hydrogen escape at different borohydride concentrations

To complement the DFT calculations and RDE measurements, and confirm the predicted intermediate species and reaction pathways, it is important to perform spectroscopic characterizations, preferably *in situ*. Those could enable to correlate directly the detection of BOR intermediates with the applied potential. It is possible to measure precisely the amount of H_2 escaping the electrode during the BOR using Differential Electrochemical Mass Spectrometry (DEMS). In this technique, a porous electrode (most commonly obtained by sputtering deposition) of the studied metal is pressed against PTFE membranes at the bottom of the spectro-electrochemical cell. On the other side of the membrane vacuum is generated by vacuum pumps that will suck the gaseous or volatile species produced at the interface of the electrode and electrolyte. Those will be accelerated in a cascade of vacuum (via two compartments separated by a small diaphragm and each connected to turbomolecular pumps) towards a mass spectrometer, and these species can be detected in function of the potential of the working electrode. If the cell is correctly calibrated, it is also possible to quantify the amounts of each species detected and directly compare them to the faradic current measured by electrochemistry. Details about the setup and the calibration are given in section "II.3.3 Coupled spectroscopic methods".

III.2.2

Both platinum and gold electrodes were tested by Chatenet to observe at which potential H_2 is escaping the electrode at 5 mM $NaBH_4$ (Figure III.6). The faradic current measured on the sputtered electrode (Figure III.6a) is already different from the RDE measurements. Indeed, the number of active sites is greater in this configuration, because of a more developed surface area (S_{geo} = 0.785 cm²) and especially the porous morphology of the structure, that significantly limits the surface poisoning at this low concentration. Because of the contribution from the current collector (ring + wire pressed against the WE, see section II.3.3) the determination of the ECSA using H_{UPD} or oxide formation/reduction is not possible, thus no roughness factor was obtained. This results in a one wave BOR on the Au electrode and no important current decrease on Pt around E = 0.8 V *vs* RHE. Here the advantages of Pt are clearly highlighted, since the same limiting current is reached for both electrodes but once again, the onset of the reaction on Au is delayed by 0.3 V compared to Pt. Two different behaviors are observed regarding the current of H_2 escape (Figure III.6b). First, on the Pt electrode, H_2 is

detected in two distinct potential regions. For potentials $E < 0$ V *vs* RHE, hydrogen is produced at the WE through the HER; however, H_2 is detected up until $E = 0.2$ V *vs* RHE, where BOR current is already detected. Jusys *et al.* [201] demonstrated by using isotopic $NaBD_4$ that this "low potential hydrogen" mainly originates from the decomposition of water and not from the dissociative adsorption of BH_4^- (only $I_{m/z=2}$ current is consequent) suggesting that bubbles of H_2 produced during the HER are trapped in the pores and are gradually oxidized once the potential is increased above $E = 0$ V *vs* RHE. No H_2 is detected up until the second potential region ($E > 0.8$ V *vs* RHE), where Pt surface oxides form. It was demonstrated in the previous section and by previous DEMS and Rotating Ring-Disk Electrode (RRDE) measurements [131,201,225,226], and DFT calculations [216], that the BOR requires a fully available Pt surface in order to occur in the fully dissociative pathway. However, the OH_{ad}/O_{ad} formed at this potential start to cover a significant part of the surface, forcing the reaction to proceed through the partial dissociation, leading to $BH_{3,ad}$ species. Once formed, they can desorb, combine with OH^- to form BH_3OH^- (equation 3.11) and be detected by RRDE, as detailed later in this section. It was also proposed that they could undergo a second dissociation to form $BH_{ad} + 2\,H_{ad}$ (equation 3.12). It appears that when the surface becomes covered by oxides, these $2\,H_{ad}$ species are no longer valorized and escape the interface, suggesting a new "dehydrogenation" pathway for the $BH_{3,ad}$ species: $BH_{3,ad} \rightarrow BH_{ad} + H_2$. This "high potential H_2" was confirmed to originate from borohydride species thanks to the isotopic study of Jusys [201] (detection of $I_{m/z=4}$ during BD_4^- oxidation).

The Au electrode presents the same escaping H_2 features at potentials below and around $E = 0$ V *vs* RHE; the currents are smaller though, because of the lower HER activity of Au versus Pt. As for Pt, a slight H_2 current is detected in the oxide formation region ($E > 1.3$ V *vs* RHE); however, because of the fast passivation, this contribution is rather limited. Unlike Pt, a significant peak of escaping H_2 is detected around $E = 0.4$ V *vs* RHE. This peak corresponds to the BOR onset and fades off once the limiting current is reached (kinetics-controlled region). This H_2 valorization above $E = 0.4$ V could arise either from a faster HOR rate on the Au electrode (because of the increased potential), or a faster $BH_{3,ad}$ oxidation, becoming faster than the dehydrogenation. This supports the DFT calculations suggesting that Au surfaces are unable to dissociatively adsorb BH_4^- (at least at low overpotential), forcing the BOR through the partial dissociation pathway with the formation of $BH_{3,ad}$ species. Contrary to the Pt electrode, this dehydrogenation pathway seems unavoidable on Au since it appears as soon as the BOR proceeds.

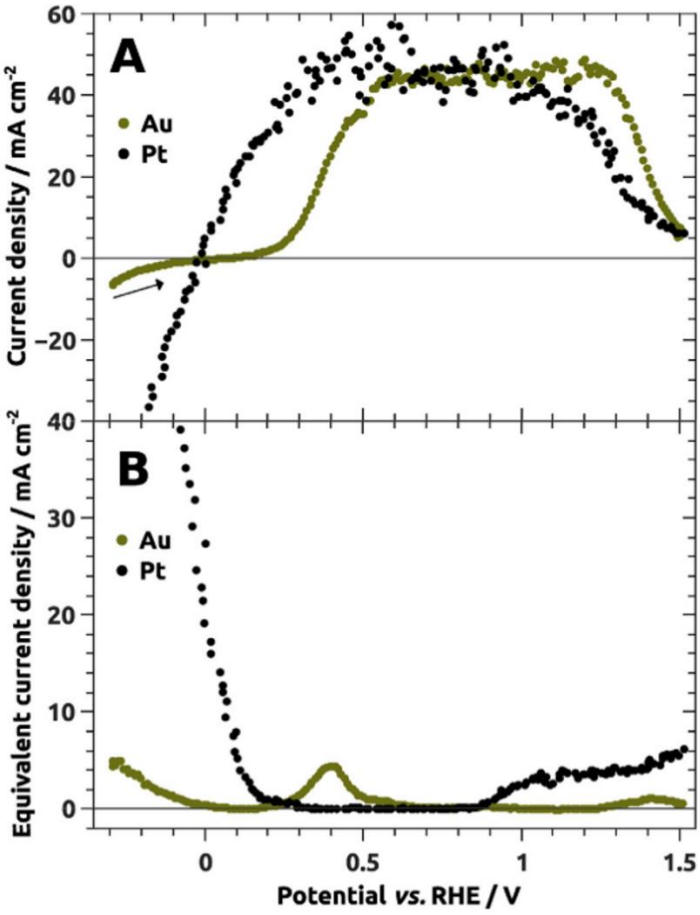

Figure III.6. Ohmic drop corrected (in dynamic mode) faradic current monitored during the positive-going scan of the second CV cycle (v_s = 10 mV s^{-1}), during electrooxidation of $NaBH_4$ in 1 M NaOH + 5 mM $NaBH_4$ electrolyte at T = 25°C on a sputtered Pt or Au electrode. (b) Corresponding equivalent HER current ($I_{H2,eq}$) calculated from the $I_{m/z=2}$ signal and the DEMS calibration constant. The convection was controlled during the whole measurements, by using a PTFE rotator in the DEMS cell. Reprinted from Ref [211]

The concentration of $NaBH_4$ was increased from 5 mM to 50 mM and then 500 mM to observe the behavior of the gold (Figure III.7a, b) and platinum (Figure III.7c, d) porous electrodes. The Au electrode presents the same behavior, but with larger currents when the concentration is increased. One could notice a slight poisoning of the surface with the appearance of the previously described two waves of reaction at 50 mM $NaBH_4$. The H_2 escape current follows (again) the kinetic region of the first wave and decays completely only near the start of the second wave, around E = 0.85 V *vs* RHE. At the highest concentration, only increasing currents are measured, because of the too high amount of active species (the BOR kinetics is too slow to enable reaching mass-transfer limitation in the explored potential range). Besides, the H_2 current still follows the faradic one: no limitation plateau is reached. Calculations of the number of electrons valorized per BH_4^- species are detailed in Ref [211] and confirm that the Au electrode is a poor BOR catalyst: this number only approaches the theoretical value of 8 at *ca.*

E = 0.6 V *vs* RHE for [BH_4^-] = 5 mM, at 0.85 V *vs.* RHE for [BH_4^-] = 50 mM and only reaches 7.5 at E =0.85 V *vs* RHE for [BH_4^-] = 500 mM.

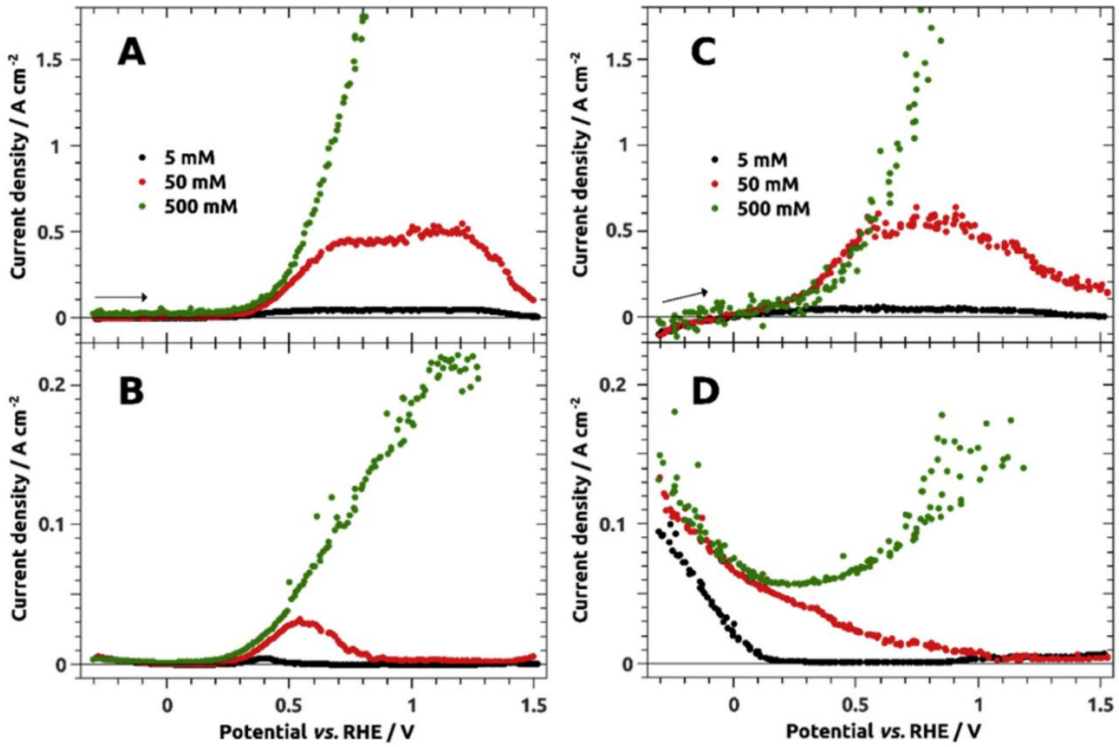

Figure III.7. Ohmic drop-corrected (in dynamic mode) faradic current monitored during the positive-going scan of the second CV cycle (v_s = 10 mV s^{-1}), during $NaBH_4$ electrooxidation in 1 M NaOH + 5, 50 or 500 mM $NaBH_4$ electrolyte at T = 25°C on a sputtered (a) Au or (c) Pt electrode. Corresponding equivalent HER current ($I_{H2,eq}$) calculated from the $I_{m/z=2}$ signal and the DEMS calibration constant on a sputtered (b) Au or (d) Pt electrode. The convection was controlled during the whole measurements, by using a PTFE rotator in the DEMS cell. Reprinted from Ref [211].

The behavior of the Pt electrode (Figure III.7c, d) significantly changed with the increase of the concentration. Indeed, already at 50 mM $NaBH_4$, only a small faradic current is measured for E < 0.3 V *vs* RHE and the CV is pretty similar to the one of Au (Figure III.7a). This denotes a loss of faradic efficiency until E = 0.6 V *vs* RHE, where the mass-transport limitation plateau is finally reached. These results suggest that the BOR mechanism changed from the dissociative adsorption to partial (or molecular) one, only by increasing the concentration and therefore limiting the quantity of available Pt sites. This is supported by the H_2 escape detected (Figure III.7d) originating from the dehydrogenation of $BH_{3,ad}$ species: in contrast to the behavior at low concentration, no distinct low and high potential regions are observed and H_2 is detected throughout the whole potential interval. The intensity of the $I_{H2,eq}$ current decreases once the limitation plateau is reached, suggesting once again that the behavior of a poisoned Pt surface approaches the one of Au. At 500 mM $NaBH_4$, the faradic current is more delayed, as presented previously on the RDE measurements, suggesting once again a larger

propensity of platinum to poisoning. Similarly to Au, the number of electrons valorized per BH_4^- species was calculated for the three concentrations [211]: around 8 electrons are reached at *ca.* E = 0.3 V vs. RHE for [BH_4^-] = 5 mM. The change of reaction pathway results in number of electrons reaching 7.5 at E = 0.6 V vs. RHE and 8 at E = 0.9 V *vs* RHE for [BH_4^-] = 50 mM and only 7.5 at E = 0.7 V *vs* RHE for [BH_4^-] = 500 mM. The BOR activity of Pt is thus significantly impacted by a large borohydride concentration, but is still better than Au (lower onset potential and better H_2 valorization are measured on Pt, even when the partial dissociation mechanism proceeds at high BH_4^- concentration).

III.2.2.2 Detection of BH_3OH^- species using RRDE

In order to confirm the $BH_{3,ads}$ oxidation pathway on Au and on poisoned Pt, it is possible to perform RRDE measurements [182]. In that case, the BOR is conducted on a polycrystalline disk of either Au or Pt, while a polarized Au ring is used as a sensor to detect any hydroxyborane species (BH_3OH^-) formed at the disk. At a potential of E = 0.2 V *vs* RHE, gold is indeed able to oxidize BH_3OH^- species, which are formed upon desorption of $BH_{3,ads}$ [129,182,183,185], while it is rather inactive for BH_4^- oxidation. Figure III.6a shows such RRDE measurements for the BOR on an Au/Au electrode at 5 mM, 50 mM and 500 mM $NaBH_4$ in 1 M NaOH at T= [10, 20, 30] °C and ω = 2500 rpm. The ring current, measured at a constant ring potential E = 0.2 V *vs* RHE during the BOR on the disk, is plotted as a function of the disk potential. Because some $BH_{3,ad}$ species can also adsorb on the ring and will contribute to the oxidation current (especially for the largest $NaBH_4$ concentrations), the ring current is corrected from its baseline.

At 5 mM $NaBH_4$, as soon as the BOR current is detected on the Au disk (Figure III.8a), the current on the ring increases, suggesting that some BH_3OH^- species are produced at the disk during the BOR. During the first wave, three simultaneous reactions occur in competition with each other: the oxidation of $BH_{3,ads}$ its desorption into BH_3OH^- and dehydrogenation into BH_{ad} [211]. This dehydrogenation generates gaseous H_2 that perturbs the ring current by modifying its active surface (coverage by bubbles). When the second wave of oxidation starts (at E = 0.8 V *vs* RHE), the ring current is modified, and in particular has a tendency to decrease, and even reach negative values. This unexpected behavior could mean that another soluble and reducible species is produced at the disk and can be reduced at the ring at E = 0.2 V *vs* RHE. This peculiar behavior will be reproduced for larger $NaBH_4$ concentrations and further discussed below. When the passivation occurs at E = 1.1 V *vs* RHE, a peak is observed on the ring, corresponding to the desorption of all previously-adsorbed species on the disk (these species being

expelled and replaced by gold oxides), or that BH_3OH^- species cannot re-adsorb on Au-oxides surface. Increasing the cell temperature enhances the BOR charge-transfer kinetics (at the disk), but these variations are not detected on the ring, except potentially the production of the reducible species at T = 30°C.

At 50 mM $NaBH_4$ (Figure III.8a) a small negative current is observed on the ring below the start of the BOR at the disk. A likely explanation comes from the conjunction of two processes: (i) BH_3OH^- species are formed at the disk at OCP (by partial heterogeneous hydrolysis on Au, (equation 3.5)) and can be oxidized on the gold ring (which is always polarized to enable such detection); (ii) this production of BH_3OH^- stops (or slows down) as soon as the Au disk is polarized positive of its OCP (and/or the Au disk becomes capable to oxidize (some of) the BH_3OH^- it generates), therefore lowering some of the ring current baseline contribution. This was not detected at 5 mM $NaBH_4$, because the BH_3OH^- concentration at the Au disk at OCP was too small, likely owing to a rather quantitative heterogeneous hydrolysis at the Au electrode (leading to H_2 and BO_2^- via the sequence of equations 3.5 and 3.6). The picture changes at larger BH_4^- concentrations: more Au active sites are occupied, thereby favoring the partial heterogeneous hydrolysis. Once again, when the BOR onset potential is reached (at *ca.* E = 0.3 V *vs* RHE), a production of BH_3OH^- is detected on the ring, confirming the $BH_{3,ad}$ oxidation pathway. Then, noise induced by hydrogen bubbles formation appears, and the ring current starts to decrease once again when the second wave of the BOR initiates, leading to a reduction in the level of noise.

For [$NaBH_4$] = 500 mM (Figure III.8a), the same negative ring current is observed, before the BOR starts. Then, it rises in the same manner as for the two previous concentrations. However, at E = 0.6 V *vs* RHE, this current starts to decrease and reaches negative values. At E = 1.1 V *vs* RHE, this diminution speeds up and reducing currents on the order of -3 mA are observed on the ring (*i.e. ca.* 1% of the disk current in absolute value). At T = 30°C, the BOR kinetics is faster, and the slope of the disk current is greater than at T = 10 and 20°C. However, this is accompanied by larger H_2 generation, and because Au is not good to valorize H_2 and the electrode shaft is vertically positioned, bubbles likely formed at E = 0.9 V *vs* RHE, stabilize on the PTFE ring separating the Au disk from the Au ring and prevent the proper detection of BH_3OH^- at the ring. Then, these bubbles further grow until both surfaces (that of the disk and of the ring electrode) are completely covered and the contact between the electrodes and the electrolyte is lost. This behavior has been found reproducible for multiple replicates: although all the experimental traces do not necessarily superpose to those of Figure III.8a, they all show the same type of behavior, thereby revealing the difficulty to make "fine" measurements in the practical conditions of a running DBFC (*e.g.* $NaBH_4$ concentrations above 100 mM).

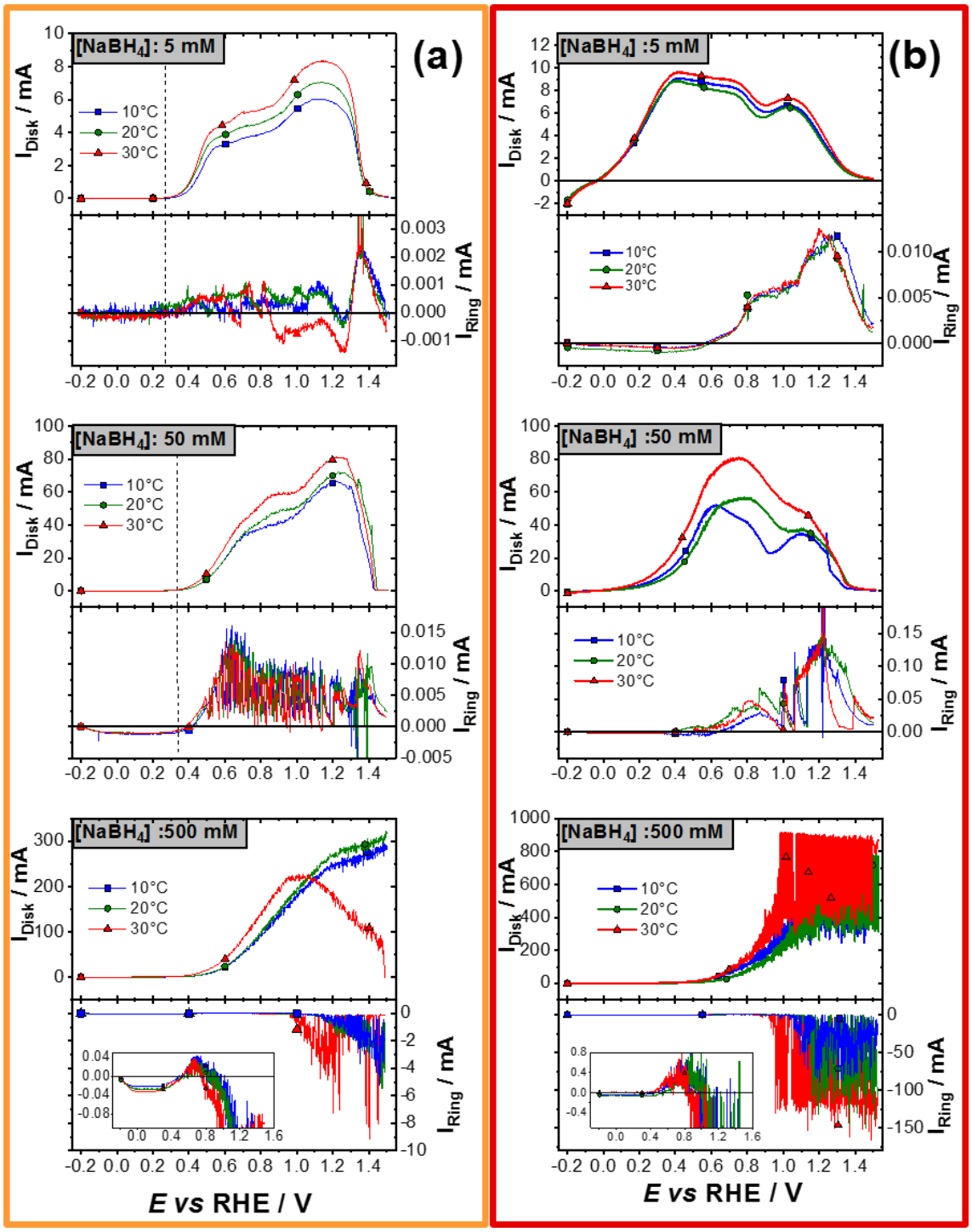

Figure III.8. Ohmic drop-corrected (in dynamic mode) positive scans of the BOR on (a, yellow border) Au and (b, red border) Pt disk electrode for 5, 50 and 500 mM $NaBH_4$ in 1 M NaOH, and their corresponding current measured on a Au ring at T = [10, 20, 30] °C and ω = 2500 rpm. Ring currents were initially measured with a chronoamperometry at a potential of E = 0.2 V *vs* RHE and subsequently corrected to fit the potential during the BOR. An inset corresponding to a focus on the low ring currents is presented for 500 mM $NaBH_4$. Reprinted from Ref. [212].

Figure III.8b is the equivalent of Figure III.8a with a Pt/Au RRDE electrode (Pt disk, Au ring). This time, at 5 mM $NaBH_4$, the BOR starts on the Pt disk while the current on the

Au ring stays null until the disk potential reaches E = 0.6 V *vs* RHE, which corresponds to the beginning of the surface poisoning of the Pt disk and the formation of OH_{ad} species. Above that potential value, BH_4^- complete dissociation is no longer possible due to a lack of free neighboring Pt active sites (the number of free sites is also decreased by the fact that Pt surface oxides form) and the partial dissociation into $BH_{3,ad}$ begins [211]. This new mechanism triggers the formation of BH_3OH^- species, which are directly detected on the ring electrode. The ring current nevertheless stabilizes when the L-H oxidation of BH_{ad} species is activated (E = 0.8 V *vs* RHE), regenerating active sites for $BH_{3,ad}$ to dissociate. Thus a steady-state between consumption and desorption of $BH_{3,ad}$ is more or less established. For higher disk potential values, the Pt surface is passivated by complete oxides coverage. In the same manner as observed on the Au/Au RRDE (Au disk, Au ring), other adsorbates are forced to desorb and so the ring current increases. This peak is broader than for the Pt/Au system because the passivation happens at a slower rate.

The mechanism on the Pt disk at 50 mM $NaBH_4$ is again modified with the delayed onset of the reaction. Oxidation currents are measured on the ring in the kinetics-controlled region, confirming the partial dissociation pathways alleged from RDE measurements and supported by the DEMS characterization. Concerning the fuel cell-like concentration of 500 mM (Figure III.8b), because the Pt surface is strongly poisoned (as discussed previously), the $BH_{3,ad}$ pathway becomes predominant. Thus, the BOR starts on Pt in the same manner as on Au, and the ring current follows the same trend as well: a production of BH_3OH^- is detected at the onset of the BOR. When the disk potential reaches E = 0.8 V *vs* RHE, the same phenomenon appears: rather slow diminution of the ring current until E = 1.0 V *vs* RHE at T = 30°C or E = 1.1 V *vs* RHE at T = 10 and 20°C. Then this diminution of the relative value of the ring current accelerates drastically and the current reaches negative values way more important than on Au/Au, on the order of -40 mA, -60 mA and -80 mA at T = 10°C, 20°C and 30°C respectively. This reduction signal is also much noisier, so these values are only rough estimates; anyhow, this current is *ca.* 10 to 20 times more important than the one detected on the Au/Au electrode, when the disk current is only 2 times greater (300 mA on Au disk, and 600 mA on Pt disk), suggesting a much larger proportion of formation of the incriminated "reducible species", assuming they exist.

The reduction current observed on the ring of the Au/Au electrode could also be explained by a modification of the local pH at the interface of the electrode. During the first BOR wave, 3 OH^- ions are consumed to form a BH_{ad} species and then 5 more OH^- ions are consumed to complete the BOR and obtain the final BO_2^- product [211]. Moreover, the ratio of hydroxide anions concentration to fuel concentration, $[OH^-]/[BH_4^-]$, is only 2 in these conditions, meaning that the reaction could become limited

by the OH^- concentration, and therefore that the local pH could drastically drop at the disk | electrolyte interface, provided all the BH_4^- species were consumed at the interface. In such case, the electrolyte leaving the disk in direction of the ring would have a lower concentration of OH^- and the equilibrium potential of the reactions (e.g. the HER/HOR) could be modified at the ring. For example, if the pH of the electrolyte at the ring interface drops from pH 14 to 7, the hydrogen electrode equilibrium potential would be shifted by *ca.* 0.4 V towards positive values, such shift being sufficient to promote the HER at the ring. In that scenario, the larger the disk current, the higher the OH^- consumption, leading to larger pH drops at the ring interface and increasing HER current at the ring. This hypothesis could also explain the increasing noise on the ring signal all along the potential scan on the disk; it will be tested hereafter. Concerning the Pt/Au system, the noise is greatly accentuated at high potential values, because of the larger H_2 escape on Pt-oxides discussed previously.

Table III.1. Estimation of the mass-transport-limited current densities if BH4- transport limits the BOR (j_L (BH_4^-)) or if OH^- transport limits the BOR (j_L (OH^-)), calculated for [$NaBH_4$] = 500 mM in 1 M and 4 M NaOH on Au/Au RRDE. Values for DBH_4^- and ν have been determined by Chatenet et al. [227] with experimental conditions approaching the ones used in this study. Values for DOH^- were estimated from Refs [228,229] . The mass-transport-limited current densities were calculated using the Levich (equation 3.15)

T = 20°C, ω = 2500 rpm	500 mM $NaBH_4$	
	1 M NaOH	4 M NaOH
ν ($cm^2.s^{-1}$)	0.015	0.03
D_{BH4-} ($cm^2.s^{-1}$)	$2.5x10^{-5}$	10^{-5}
D_{OH-} ($cm^2.s^{-1}$)	$3x10^{-5}$	10^{-5}
n_{BH4-}	8	8
n_{OH-}	1	1
$j_L(BH_4^-)$ calculated ($A.cm^{-2}$)	6.7	3.2
$j_L(OH^-)$ calculated ($A.cm^{-2}$)	1.9-	3.6
Maximum experimental value of j, measured at 1.5 V *vs* RHE: $j_{1.5V}$ ($A.cm^{-2}$)	1.5	3

To test this pH modification hypothesis, the expected BOR limiting current values, calculated from the Levich theory (equation 3.15), were compared to the maximum current values monitored experimentally at E = 1.5 V *vs* RHE, considering either a mass-transport limitation by BH_4^- species ($j_L(BH_4^-)$) or by OH^- species ($j_L(OH^-)$). For the 1 M NaOH + 500 mM $NaBH_4$ electrolyte solution, Table III.1 firstly shows that $j_L(BH_4^-)$ exceeds $j_L(OH^-)$; this means that the BOR could likely be limited by the mass-transport of OH^- anions and not by that of BH_4^- anions in these conditions. As $j_{1.5V}$ is of the same order of magnitude as $j_L(OH^-)$ ($j_{1.5V}$ = 1.5 A cm^{-2} versus $j_L(OH^-)$ = 1.9 A cm^{-2}), significant depletion of OH^- species at the electrode | electrolyte interface could become possible

when the experimentally monitored BOR current approaches its maximum value, which could affect (and in particular decrease) the interfacial pH. As an attempt to mitigate this effect, the experiment at 500 mM $NaBH_4$ has been reproduced with a higher concentration (4 M) of NaOH on both Au/Au (Figure III.9a, c) and Pt/Au (Figure III.9b, d) RRDEs.

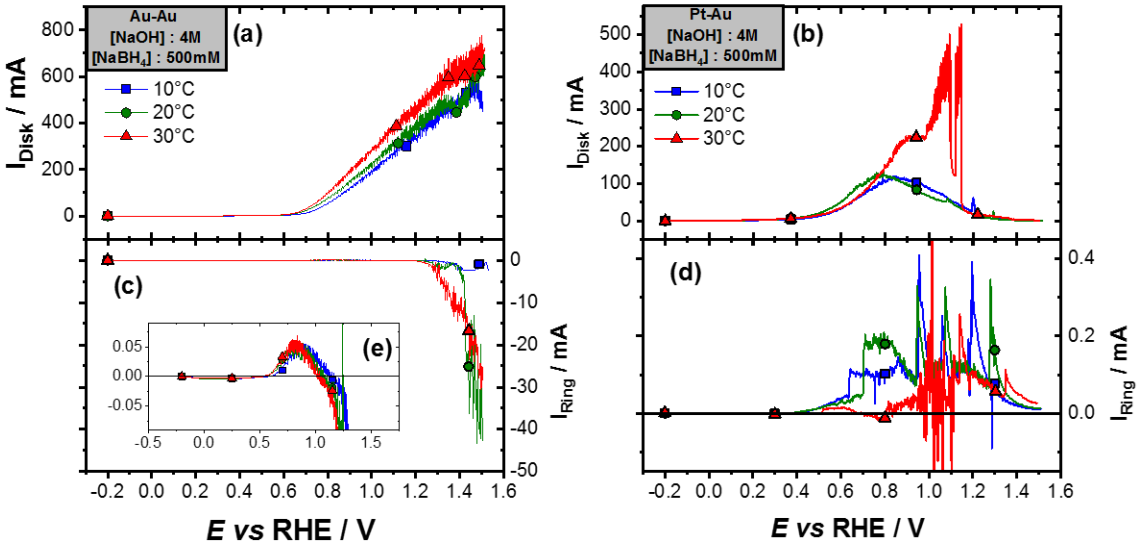

Figure III.9. Ohmic-drop corrected (in dynamic mode) positive scans of the BOR on (a) Au and (b) Pt disk electrode for 500 mM $NaBH_4$ in 4 M NaOH, and their corresponding current measured on the Au ring (c) (d), at T = [10, 20, 30] °C and ω = 2500 rpm. Ring currents were initially measured with a chronoamperometry for a set potential of E = 0.2 V *vs* RHE and subsequently corrected to fit the potential during the BOR. (e) corresponds to a focus on the low ring current at 500 mM $NaBH_4$. The ring current measured at T = 10°C on Au/Au (c) is limited because of a mistake in the settings of the max current range during the measurement. Reprinted from Ref [212].

The first thing to notice is that the BOR current on Au is no longer limited by the mass-transport but only by the charge-transfer kinetics (Figure III.9a); as a result, a current two times higher is obtained with the four times higher OH^- concentration. This confirms that the BOR currents might have been limited by the low concentration and slow transport of OH^- at the interface with a [NaOH] = 1 M solution, again highlighting the possibility of modification of the local pH at the interface. However, the current observed on the ring follows the same pattern as previously (for 1 M NaOH supporting electrolyte), negative values being monitored; more precisely, the monitored reduction currents at the ring are roughly 10 times greater. As the local pH variation should be less important in the case of the 4 M NaOH electrolyte, this reduction current cannot (at least not fully) be associated with a change of the local pH at the ring/electrolyte interface. In the case of the 4 M NaOH electrolyte, the calculations of Table III.1 rule out a complete depletion of OH^- at the electrode | electrolyte interface: $j_{1.5V}$ is always inferior to $j_L(OH^-)$ (3 A cm^{-2} versus 3.6 A cm^{-2}), which is itself superior to $j_L(BH_4^-)$ (3.2

A cm^{-2}); this means that mass-transport limitations in this electrolyte shall mostly concern BH_4^- species and not OH^- species, thereby ruling out severe interfacial pH decrease. Moreover, the potential necessary to obtain such HER current on a Au electrode, because of its poor charge transfer kinetics, would be way too low (Au is not a good HER catalyst). As a result, the measurement of negative ring currents likely has another explanation than the interfacial pH change. Here we postulate that a soluble reducible intermediate species is produced at the disk in the potential region of the "second BOR wave".

So the hypothesis that another reducible species is produced during the BOR on Pt is now also appropriate on Au. We propose that the soluble reducible intermediate species formed at the Au and Pt disk in the "high-potential BOR wave" could be BH_2-like species. Such species have already been detected during the BOR by Molina *et al.*, using FTIR spectroscopy [205,230]. DFT calculations [217] also predict the formation of BH_2-like species (namely BH_2OH_{ads}, but these species can likely desorb, *e.g.* in the form of $BH_2(OH)_2^-$) at similar potential values. It is therefore believed that such BH_2-hydroxide species could explain why their production is favored when the concentration of OH^- is increased. Unfortunately, the results obtained on Pt/Au at 4 M NaOH (Figure III.9b) do not give more information on this BH_x reducible intermediate, because no negative current is measured anymore. Indeed, at the potential of Pt-oxides formation, the BOR current starts to decrease until complete passivation at the end of the potential scan. Unlike for the BOR on Au/Au for 500 mM $NaBH_4$ in 1 M NaOH at T = 30°C (Figure III.8a), this decrease cannot be ascribed to H_2 bubbles formation, because the current goes back up in the return scan (not displayed here), which means that the electrode/electrolyte contact is maintained. A hypothesis is that most of the OH^- brought to the interface at 500 mM $NaBH_4$ in 1 M NaOH (Figure III.8b) were consumed for the BOR, thereby preventing quantitative formation of Pt-oxides. With the higher NaOH concentration, some OH^- are now available for the Pt oxides formation, so the surface passivates in the same manner as for lower $NaBH_4$ concentrations. This confirms important role of OH^- in the BOR, in particular when the $NaBH_4$ concentration is large (*i.e.* in the conditions of DBFC operation).

III.2.2.3 Adapting the proposed BOR model

The BOR model proposed by Olu was modified to include the findings described above, *i.e.* the pathways of the reaction on Au and the dehydrogenation of $BH_{3,ad}$ species. Figure III.10 represents all the different pathways the reaction can take (from our current understanding) either on Pt or on Au; it is also updated with the correct partial reactions in alkaline medium. The reactions represented by the red arrows are only

possible on Pt surfaces, since they represent the dissociation of BH_4^- and $BH_{3,ad}$ and producing BH_{ad} and several H_{ad} species. The reactions of OH^- adsorption are presented in red as well, since on gold they occur at too high potentials, where the slower E-R oxidation of BH_{ad} is already activated. The dehydrogenation step is represented by the loss of a H_2 molecule to pass from BH_{3ad} to BH_{ad}; this process was observed as soon as some BH_{3ad} species were detected on any of the studied surfaces. This model was constructed in a similar way as the previous one (Ref. [113,131]) and its elaboration, performed mainly by Olu and Bonnefont, is detailed in Ref [211].

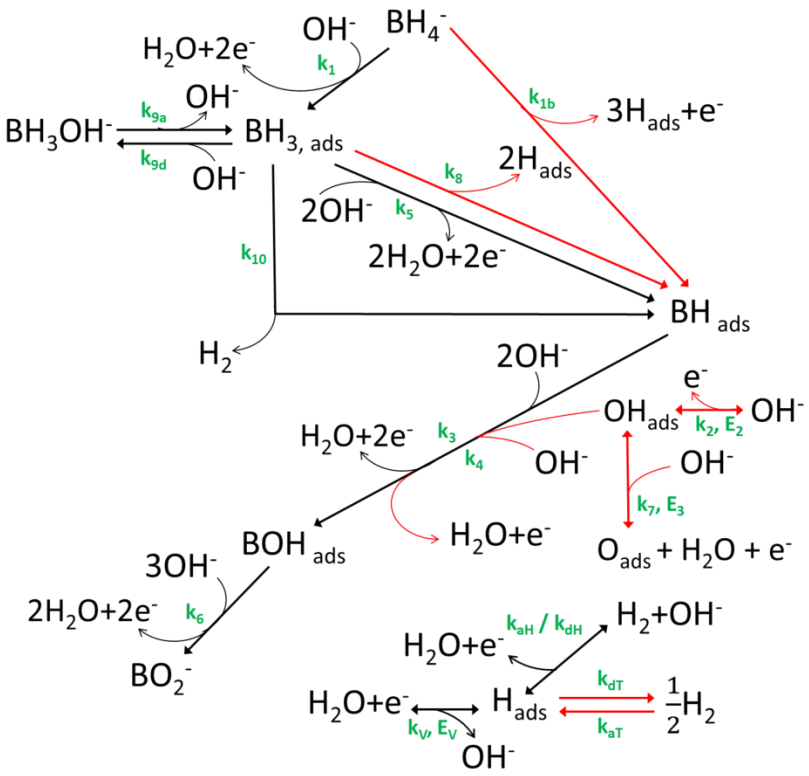

Figure III.10. Updated version of the proposed BOR model integrating the new findings about dehydrogenation of the $BH_{3,ad}$ species observed with DEMS measurements and the overall Au mechanism. Reprinted from Ref [211].

Using Figure III.10 as a basis for the calculations, new simulations of the BOR on both Au and Pt surface at 50 mM and 500 mM $NaBH_4$ were done by Olu and Bonnefont (Figure III.11). The calculated BOR current on Au electrode reproduces the trends measured experimentally previously: the BOR onset is higher than for Pt, but is not impacted by the increase of concentration to 500 mM $NaBH_4$, sign of a low influence of surface poisoning; H_2 generation occurs at soon as the BOR proceeds, supporting the BH_{3ad} dehydrogenation (k_{10} from Figure III.10); it is correctly reproduced (Figure III.11b) at 50 mM $NaBH_4$: the I_{H2} peak decreases when the limiting plateau is reached; as soon as the BOR is limited by mass-transport of BH_4^- species, the coverage of BH_{3ad} species decreases. For 500 mM $NaBH_4$, this current is also calculated to decrease, where it kept

increasing in a linear way on the DEMS measurement (Figure III.7b). It is important to mention that the current model is not able to reproduce the "two-wave" mechanism, with corresponding 4 and 8 electrons valorized, observed on Au RDE electrodes (Figure III.4), since the model only takes into account production of one H_2 molecule per BH_4^- ion oxidized. As mentioned previously, the hydrolysis of the fuel might influence the electrode by generating additional H_2 and BH_3OH^- that could interact with the surface. It is also possible that BH_4^- dehydrogenize into two H_2 to form a "4 electron process" proposed by Wang *et al.* [231]. This first model could thus still be refined to include these steps and to reproduce the 2 waves of oxidation observed in the experiment.

The model does not take into account the formation of bubbles in the pores of the electrode during the cathodic cycling (which was experimentally measured by DEMS) and therefore H_2 production above 0 V *vs* RHE is not reproduced by the model. According to the kinetic simulations, the reaction is only limited by the reaction charge-transfer kinetics up to 0.4 V *vs* RHE, similarly to the RDE experimental data (Figure III.3b). In the simulations, H_2 appears again in the high potential region, where the surface starts to be significantly covered by oxide species (E > 0.7 V *vs* RHE). In the DEMS measurement, this second H_2 contribution is not observed (Figure III.7d) for 50 mM $NaBH_4$. One tentative explanation of this inconsistency is that the OH_{ad} and O_{ad} blocking of the Pt surface likely depends on the conditions of the experiments, especially concerning the Ohmic resistance of the system (and its dynamic correction, which was made here). The morphology of the surface (roughness) can also influence this phenomenon. During the BOR, poisoning of the Pt surface (by its oxides or by the products of the BOR, *e.g.* boron oxides, even if these latter species have not been considered in the present simplified model), results in the surface blocking, so that an apparent negative resistance is observed (see the BOR CVs in RDE configuration of Figure III.3), this phenomenon being accentuated by the Ohmic drop (electrolyte resistance, for instance). Thus, the Pt poisoning from (hydr)oxides is not as "severe" as when no correction is applied, and the formation of $BH_{3,ad}$ over BH_{ad} is not favored (thus corresponding to the absence of H_2 escape). When no IR-correction is applied, H_2 escape is experimentally observed on Pt at 50 mM $NaBH_4$ in the high-potential region (see Ref [211]); this observation reinforces the latter explanation.

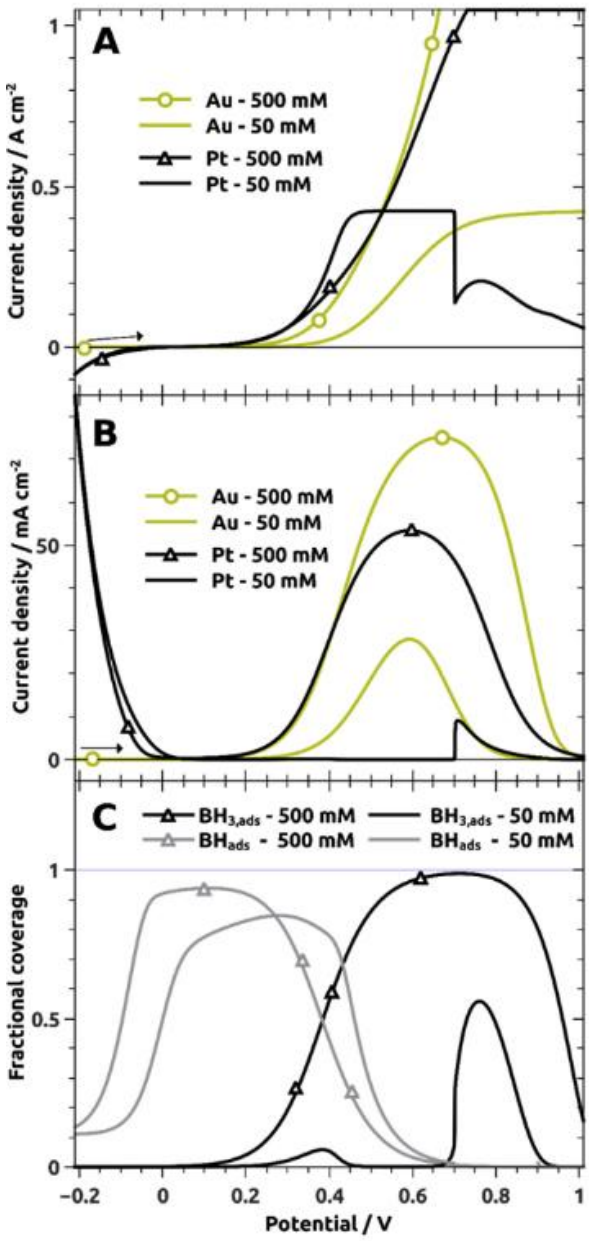

Figure III.11. Simulated plots of the BOR on Au and Pt electrodes using the tentative BOR mechanism of Figure III.10. The $NaBH_4$ concentrations taken into account are 50 and 500 mM. (a) Faradic current, (b) H_2 escape current and (c) $BH_{3,ad}$ and BH_{ad} fractional coverage for the Pt electrode. Reprinted from Ref [211].

For the fuel cell operation concentration (500 mM $NaBH_4$), the model captures the surface poisoning and the associated "partial dissociation pathway", as expected from the experimental data. Indeed, the surface is initially mostly covered by BH_{ad}. However, if mass-transfer limitation (interfacial $[BH_4^-]$ close to 0) is not reached before a critical coverage of BH_{ad} (which is likely with high flux of $[BH_4^-]$, *i.e.* typically the case for the 500 mM $NaBH_4$ electrolyte with convection), then the surface of Pt cannot accommodate all the BH_4^- species arriving at the surface and becomes poisoned by the BH_{ad} species. Thus, $BH_{3,ad}$ coverage quickly increases at the expense of BH_{ad}, for $E > 0$ V *vs* RHE

(Figure III.11c), which is directly accompanied by important H_2 generation that follows the BOR faradic current. Again the contribution from residual H_2 originating from the HER and stored in pores is not taken into account by the model. Because the reaction through $BH_{3,ad}$ species is slower, the simulated faradic current is delayed compared to the case at a lower concentration (Figure III.11a), in agreement with the experimental data.

To summarize, the only reaction pathway for the BOR on Au surfaces is assumed to proceed through the formation of $BH_{3,ad}$ intermediate species, because Au cannot fully dissociate BH_4^- ions. This pathway induces important drawbacks in terms of faradic efficiency: (i) the intermediate species can desorb in the form of BH_3OH^- or self-dehydrogenate releasing gaseous H_2 in the electrolyte, directly leading to significant loss of 6 and 2 electrons, respectively (because Au cannot efficiently oxidize H_2); (ii) because of the inability of Au to form H_{ad} species, the reaction must proceed through the slow E-R oxidation of $BH_{3,ad}$, resulting in a very high reaction onset potential. However, because this reaction is the only possible way, no significant poisoning of the surface is observed and the apparent BOR activity of Au seems directly correlated to the borohydride concentration. The BOR mechanism on Pt surface is much more complex with a dual behavior appearing at low potential (below the Pt-oxide formation region), that triggers both reaction pathways (their respective proportion depending on the surface roughness/BH4- concentration ratio). The reaction mechanism is dictated by the borohydride concentration and the active site density of the electrode, both affecting the BH_{ad} coverage. At low concentration and/or high active site density, the reaction is mainly driven by the "fully dissociative" pathway and the formation of BH_{ad} species; it switches to the "partially-dissociative" one once the concentration is increased enough (with respect to the active site density) to saturate the available active area by BH_{ad} species. The reaction then proceeds through the formation of $BH_{3,ad}$ species and a mechanism resembling the one predicted on Au (but complemented by the ability of Pt to form H_{ad}). For higher potentials, the oxide formation plays a dual role: on the one hand, OHad/Oad species regenerate the surface by recombining with BH_{ad} species through a L-H mechanism, thus allowing faster oxidation of the latter and avoiding surface poisoning. On the other hand, because the coverage of OHad/Oad species increases with the potential, they also poison the electrode (reduce the amount of Pt free sites), forcing the "partially-dissociative" pathway for all concentrations, before completely passivating the surface at higher potentials. It is important to note that an optimal borohydride concentration exists when using Pt electrodes for the BOR and that it depends on the parameters of the setup used. Optimizing the active surface area and the morphology of the surface (porosity, thickness) as well as the mass-transport conditions of the system used shall allow to maximize the BOR efficiency at low potentials as well as minimize the detrimental H_2 generation/escape.

III.3 Towards a kinetic model of the BOR on Pd surfaces

The great activity of platinum surfaces was demonstrated to be strongly dependent on the conditions of operation and suffers from non-negligible surface poisoning. Moreover, the use of Pt electrocatalysts prevents reaching the promising energy density of the BOR in a DBFC system, because of the "high" reaction onset (*ca.* 0 V *vs* RHE) due to parasitic HER. Au surfaces present a lower OCP, but cannot reach high power densities because of the slow kinetics of reaction at low overpotential induced by a partially dissociative pathway in every conditions, resulting in large activation potentials. Palladium has been investigated as a potential substitute to Pt for the BOR for more than a decade [232–236] and very promising (or even superior) performances have been reported in the past few years using Pd-based catalysts in both RDE and FC conditions [129,149,151,237–239].

III.3.1 BOR on Pd: Differences with Pt and Au

The same RDE measurements, presented in the previous section on Au and Pt surfaces, were reproduced using a mirror-polished polycrystalline Pd electrode (S_{geo} = 0.031 cm²) to analyze its behavior towards the BOR. The OCP of the electrode in presence of borohydride was measured in the same [$NaBH_4$] concentration window and compared to that of the Pt surface (Figure III.12). With a borohydride concentration almost null, the OCP on Pd is slightly lower than on Pt, because of its more oxophilic nature. It is also more sensitive to BH_4^-, since a noticeable OCP decrease is already observed at [$NaBH_4$] = 5.10^{-5} M, where the potential remained stable on Pt. Because it is less active towards the HER, the decrease is less abrupt than for Pt and a negative OCP is reached around 5 mM $NaBH_4$ (*vs* < 1 mM for Pt). This lesser ability of Pd to evolve hydrogen allows the OCP to decrease further towards the standard potential of the reaction: for [$NaBH_4$] > 50 mM, the OCP on Pd becomes lower than on Pt and keeps decreasing until reaching around -250 mV *vs* RHE at 1.5 M $NaBH_4$. Interestingly, such negative values are not reached even on Au, whereas the HER activity of the former metal is way worse than the one of Pd. This suggests that the evolution of hydrogen on Pd might be reduced in presence of BH_4^-, this effect being exacerbated for the highest [$NaBH_4$] and that the BOR kinetics is faster on Pd compared to Au electrode. Nonetheless, this first observation of the BOR behavior on Pd is promising, but should also be considered with care since a low OCP does not necessarily translates into good BOR activity, as was observed on Au.

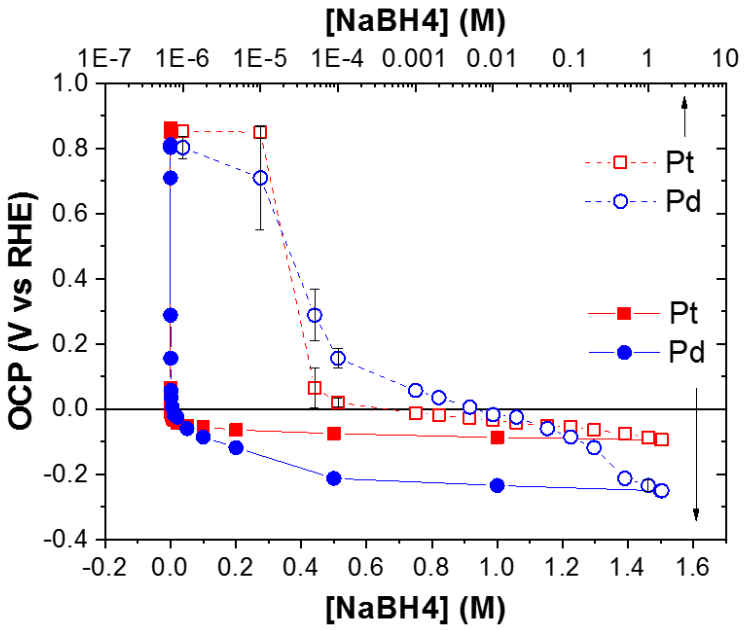

Figure III.12. OCP measured on platinum and palladium polycrystalline electrodes (S_{geo} = 0.031 cm²) for sodium borohydride concentration varying from 10^{-6} M to 1.5 M in Ar-saturated 1 M NaOH at T = 20°C and ω = 1600 rpm. Full lines and symbols correspond to the linear concentration scale and dashed-lines to the logarithmic one.

It is important to mention that BH_4^- ions are expected to adsorb on Pd surfaces following the dissociative pathway (equation 3.8) and producing BH_{ad} and H_{ad} species, as predicted by Rostamikia *et al.* [216] using DFT. Unfortunately, no further DFT calculations were performed to this date for the BOR on Pd surfaces to the author's knowledge. However, the adsorption mechanism already suggests a reaction pathway similar to the one of Pt. Indeed, Pd is a good HOR catalyst [240–243] (even if its HOR/HER activity is lower than that of Pt) and should therefore be able to valorize the produced H_{ad}. A fast reaction is thus expected for potentials E > 0 V *vs* RHE. The recorded CVs on the polycrystalline Pd electrode demonstrate, however, a different reaction behavior (Figure III.13). Despite a low OCP value, the BOR current on Pd stays very low until the electrode potential reaches *ca.* E = 0.1 V *vs* RHE. Moreover, a limitation plateau is reached at a lower current density than expected for an 8 e- process. This first observation suggests that the BOR does not proceed through a "fully dissociative" pathway on the mirror-polished electrode and a behavior comparable to the one of the gold electrodes at low potentials is observed, even at 5 mM $NaBH_4$. The "partial dissociation" pathway might therefore be favored, leading to the formation of $BH_{3,ad}$ species. It was demonstrated by Olu *et al.* that Pd is a good catalyst for the oxidation of BH_3OH^- [129], meaning that this pathway is indeed possible.

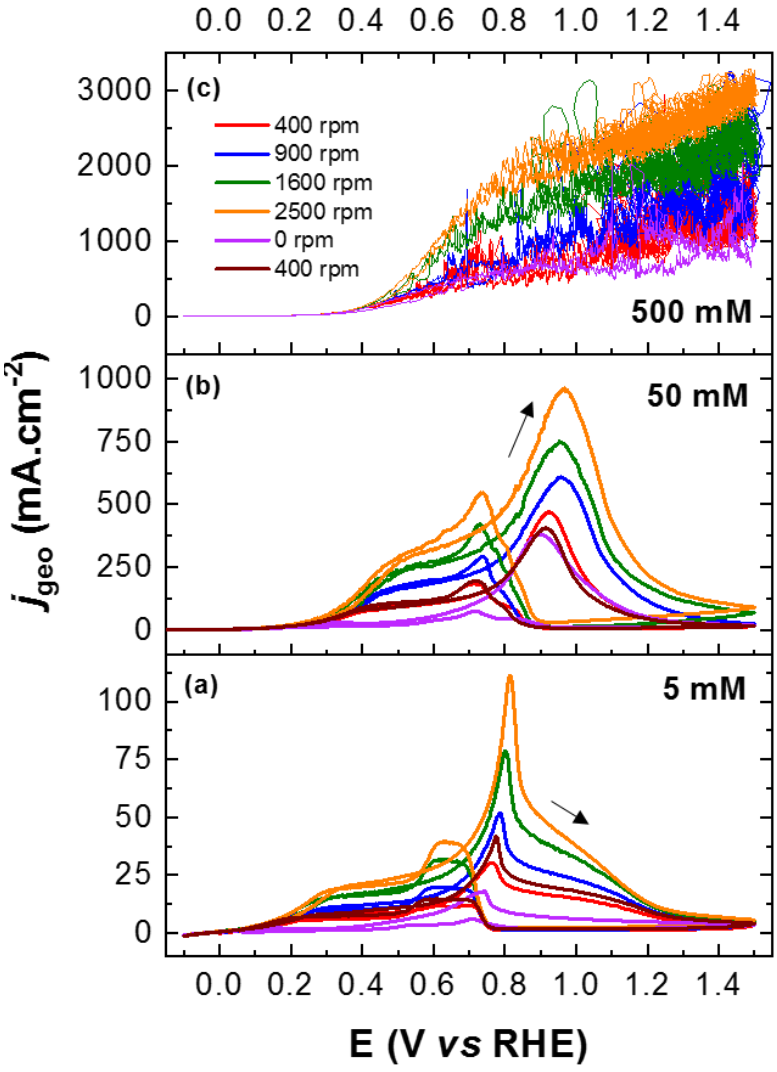

Figure III.13. Ohmic-drop corrected CVs measured on Pd mirror-polished polycrystalline electrode (S_{geo} = 0.031 cm²) in RDE configuration at three different borohydride concentrations: 1 M NaOH + (a) 5 mM, (b) 50 mM, (c) 500 mM $NaBH_4$ and various rotating rate of the electrode following this cycle: [400; 900; 1600; 2500; 0; 400] rpm. Ar-saturated electrolytes, v_s = 20 mV.s^{-1}, T = 20°C.

The CVs of Figure III.13 present, however, a completely different behavior for E > 0.6 V *vs* RHE: a new reaction is activated, resulting in a sharp and very intense current density peak followed by a slow passivation for E > 0.9 V *vs* RHE. This type of CV is typical of a large accumulation of blocking species being suddenly stripped because of a potential activation (like a CO-stripping), followed by a "steady state", controlled by mass-transport. In the present case, the surface is not blocked before the stripping occurs, since the first limitation plateau is controlled by mass-transport and consistently increase with both the rotation rate of the electrode and the concentration (50 mM $NaBH_4$, Figure III.13b). The peak maximum current density also increases following the same conditions, meaning that a mass-transport limited reaction is involved. However, this peak is also observed without forced convection, especially at 50 mM $NaBH_4$ (Figure

III.13b); its intensity is similar to the one at ω = 400 rpm, where the initial BOR current is significantly lower. This part of the reaction therefore involves several processes and will be discussed in detail later in order to understand better the full BOR process on Pd. Regarding the surface poisoning, the Pd electrode appears significantly less affected than the Pt electrode: increasing the concentration to 50 mM and then 500 mM seems only to delay the reaction because of the rather slow charge-transfer kinetics. This, again, recalls the behavior of Au and its single possible BOR pathway, suggesting once again that the "partially dissociative" pathway is favored on Pd against prediction of the DFT calculations. At 500 mM (Figure III.13c), a clear mass-transport dependence is observed, meaning that, if $BH_{3,ad}$ species are indeed the only possible adsorption product, their oxidation step is faster on Pd than on Au, as already pointed by the onset potential of the reaction at lower concentration.

Now that the behavior of Pd towards the BOR has been observed, it can be compared with the two other noble metals in Figure III.14, where the current corresponding to 8 electrons produced was calculated using the Levich's law (equation 3.15). The values used for the calculations were taken from Ref. [227]. At low concentration (Figure III.14a), the difference between Pt and Pd is clearly demonstrated: slower charge-transfer kinetic, higher onset potential and most importantly, smaller current density value at low potential on the Pd electrode. It is confirmed that the first plateau is similar to the one observed on Au, but is reached at a significantly lower potential. Increasing the concentration also confirms the lesser propensity of Pd to surface poisoning. Indeed, while for Pt increasing the $NaBH_4$ concentration from 5 to 50 mM results in a positive shift of the cyclic voltammogram (Figure III.14b), minor changes are observed for Pd. This effect is even more highlighted at 500 mM $NaBH_4$ (Figure III.14c), where the Pt surface is completely blocked by BH_{ad} poisons and the reaction proceeds via $BH_{3,ad}$ species, whereas the reaction is now faster on Pd with a current density of 1 $A.cm^{-2}$ reached almost 0.2 V before Pt. This "resistance" to poisoning might explain why Pd displayed better performances than Pt in certain DBFC conditions.

The sharp peak observed on Pd for $E > 0.6$ V *vs* RHE largely surpasses the "8 electrons per BH_4^- current density" line for both 5 mM and 50 mM, suggesting that an additional reaction is contributing to the current on palladium in this potential region. To understand in more detail how the reaction proceeds during this current peak, further characterizations are necessary.

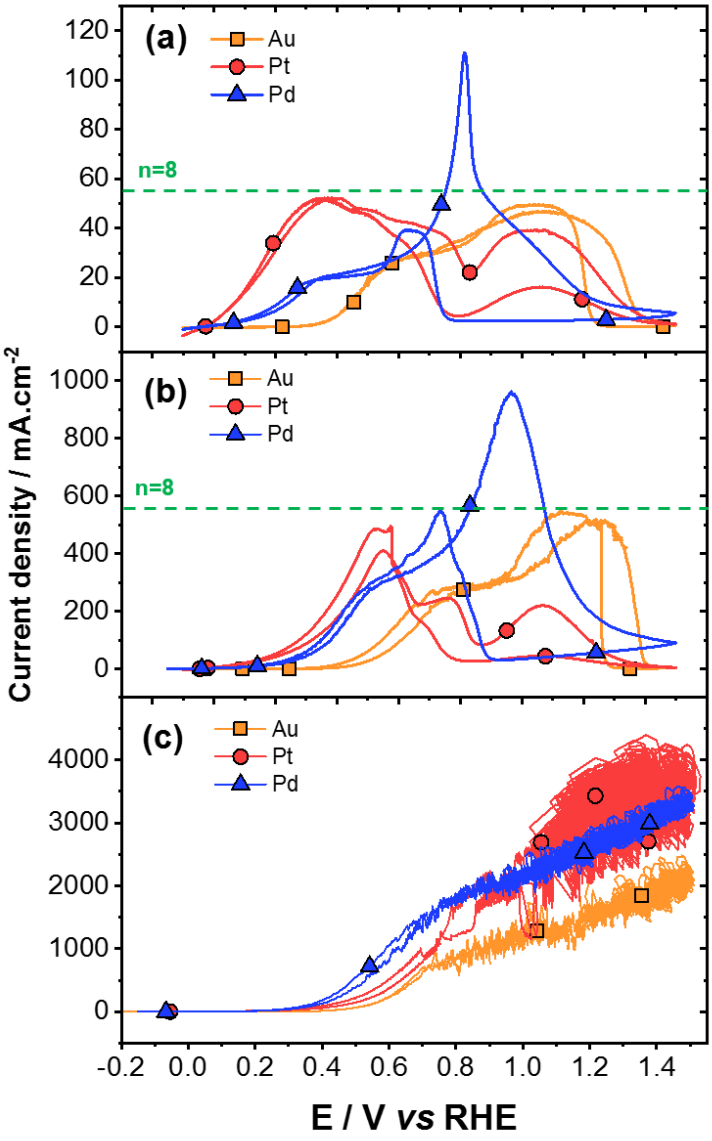

Figure III.14 Comparison of CVs measured on Au, Pt and Pd polycrystalline electrodes (S_{geo} = 0.031 cm²) in RDE configuration at three different borohydride concentrations: 1 M NaOH + (a) 5 mM, (b) 50 mM, (c) 500 mM $NaBH_4$. Ar-saturated electrolytes, ω = 2500 rpm, v_s = 20 mV.s^{-1}, T = 20°C. Green-dashed line correspond to 8 electrons generation calculated using the Levich's law. Adapted from [212].

To investigate the hydrogen escape during the BOR, DEMS measurements were reproduced using a Pd sputtered electrode. The spectro-electrochemical cell was calibrated in order to compare directly the faradic current of HER and the hydrogen ionic current ($I_{m/z=2}$): a calibration constant enables transforming $I_{m/z=2}$ into an equivalent hydrogen current ($I_{H2,eq}$), as detailed in section "II.3.3.1 Differential Electrochemical Mass Spectrometry". The BOR current and the corresponding hydrogen escape were measured for the three borohydride concentrations (Figure III.15) and the HER contribution has been cropped at 5 mM and 50 mM $NaBH_4$ to observe more clearly the oxidation currents. The first thing to notice on Figure III.15 is that the

absolute value of the faradic current of the HER is greater than the H_2 escape current detected, meaning that the calibration constant is overestimated for Pd; as such, quantitative interpretations such as the number of electrons produced during the BOR are not possible for the Pd electrode (in the DEMS cell). It also means that the hydrogen escape over the faradic current ratio decreased in presence of borohydride (since the calibration is performed in supporting electrolyte).

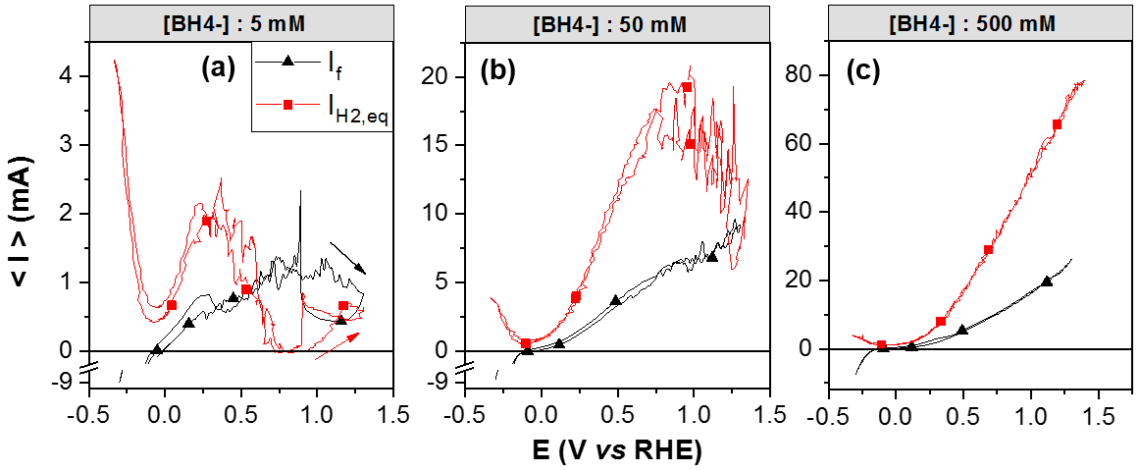

Figure III.15. Faradic current of the BOR on sputtered Pd (*ca.* 50 nm thick) and corresponding H_2 escape current ($I_{H2,eq}$) obtained from the $I_{m/z=2}$ signal and the DEMS calibration (see section II.3.3.1) for (a) 5 mM, (b) 50 mM and (c) 500 mM in 1 M NaOH. (note the presence of a break in the faradic current axis of the HER, for 5 mM and 50 mM $NaBH_4$, to observe the oxidation currents more easily). Reprinted from [212].

Regarding the BOR for [$NaBH_4$] = 5 mM (Figure III.15a), the current obtained is smaller than during previous RDE studies (Figures III.13 and III.14), because the mass-transport of electrolyte to the static sputtered Pd electrode is ensured by a simple PTFE rotator at the top of the cell (in practice a classical RDE equipped with a pure PTFE tip) generating some convection at the WE surface (at the bottom of the cell); this convective flux is not as strong and well-controlled as when a Pd RDE is used. However, this setup is sufficient to observe that the BOR starts rapidly at E = 0 V *vs* RHE, at variance to the case of a planar Pd surface, where it was kinetically slow (the sputtered Pd electrode has much more Pd active sites than a planar Pd electrode, resulting in larger "kinetic" current at lower potential). Besides, H_2 is generated until a potential of E = 0.3 V *vs* RHE is reached, suggesting a slow dissociation of BH_4^- and/or $BH_{3,ad}$ allowing the molecule to dehydrogenate. Above this potential, the H_2 produced is completely valorized. In addition, the intense current peak observed on bulk Pd at E = 0.8 V *vs* RHE is no longer present on sputtered Pd. This originates from the morphology of the electrode and more precisely of the larger number of active sites, as detailed in the following section of this chapter. H_2 is detected once again at high potentials, once the formation of oxides starts on the Pd surface. On the backward scan, H_2 is not valorized until these oxides are

reduced at E = 0.9 V *vs* RHE. For [$NaBH_4$] = 50 mM (Figure III.15b), both $I_{H2,eq}$ and I_f are *ca.* 10 times greater than for [$NaBH_4$] = 5 mM, which suggests that these two currents are linked to the same process. One may also note that the peak of activity occurs later, probably owing to the sluggish BOR charge-transfer kinetics. Likewise, at 500 mM $NaBH_4$, the slow kinetics and poisoning of the surface by adsorbates limit the two currents measured and in this case the potential at which H_2 is valorized is no more reached. Pt was behaving in a near-similar manner at large $NaBH_4$ concentration (Figure III.7).

Tentative explanation of the BOR mechanism on Pd

III.3.2 With the results gathered so far and the literature, a tentative BOR mechanism on palladium surfaces can now be proposed. It was demonstrated that the BOR on Pd surfaces does not occur according to the mechanism predicted by DFT calculations and cannot be fully described even by the updated model proposed by Olu *et al.* (Figure III.10). One phenomenon that can account for such difference is the formation of palladium hydrides (PdH) on the electrode in the presence of borohydrides. Indeed, when BH_4^- is adsorbed onto the surface, its full dissociation into BH_{ad} and H_{ad} may trigger, at least for E < 0.3 V *vs* RHE, hydrogen insertion into the Pd lattice and related formation of palladium hydrides [244,245]. Such modification of the Pd bulk structure is well-known [246–248] and Pd is often used as a storage material for hydrogen [246,249–252]. By comparison to Figure III.12, it is at this potential that the OCP starts to stabilize, so the BOR is likely compensated by the formation of PdH at intermediate concentrations of $NaBH_4$. For higher $NaBH_4$ concentrations, the sub-surface of the electrode is saturated in PdH, so the HER takes over, but it is slower on PdH than on Pd, and the OCP can reach a lower value (typically as low as E = -0.24 V *vs* RHE in Figure III.12). If the formation of palladium hydride is spontaneous at low potential values, so is the desorption of hydrogen, under usual conditions, when the potential is swept back towards more positive values. However, while PdH formation occurs in the bulk of the Pd electrode, other species may adsorb during the insertion period (typically intermediates of the BOR: BH_{ad} and $BH_{3,ad}$), thereby covering the whole available surface. Thus, no (or very few) active sites are available for the desorption of hydrides and the BOR starts on a PdH surface fully covered by BH_{ad} and $BH_{3,ad}$. Then, the reaction follows the $BH_{3,ad}$ oxidation pathway. As it has been shown that the oxidation of BH_3OH^- occurs on Pd at significantly lower potential values than on Au [129,185], the first oxidation wave is observed at smaller potential on Pd than on Au. Going positive in potential, the desorption of hydride/oxidation of H_{ad} may account for (some of) the large peak current monitored on Pd RDE (Figures III.13 and III.14). As noted above, this

intense peak is observed with a current greater than the maximal faradic current of the BOR (Figure III.14); more specifically, it occurs at a potential corresponding to the beginning of the hydroxides and oxides formation on palladium. Indeed, once they form, the oxidation of the poisoning BH_{ad} (and $BH_{3,\,ads}$) species occurs through a Langmuir-Hinshelwood mechanism, as on Pt, but at the same time, free active sites are regenerated on the electrode surface and the palladium hydrides can now be desorbed leaving behind metallic Pd. This abrupt modification of the structure and related oxidation of the adsorbates explains, to some extent, the intense current peak: the PdH oxidation concomitant to the BOR generates more current than theoretically possible only with the (stationary) mass transport-limited BOR contribution. The fact that the capacitive PdH desorption occurs in parallel to the BOR in the region of the current peak explains why the latter is, to some extent, depending on the rotation rate of the RDE for 5 and 50 mM $NaBH_4$ as measured at *ca.* E = 0.8-0.9 V *vs* RHE in Figure III.13. Going further up in potential after the current peak, oxides continue to form and a slow passivation of the surface, similar to the one on Pt, is observed.

The palladium hydrides are also the cause of the calibration overestimation in DEMS configuration (Figure III.15). Indeed, a large fraction of adsorbed hydrogen produced during the HER inserts into the Pd lattice rather than desorbs to form H_2, and is thus not detected by the DEMS. Although they seem completely different from RDE measurements, DEMS results on Pd corroborate this hypothesis. The active area of the porous Pd structure is much greater than the planar polycrystalline disk, which means that a much higher number of active sites per geometric surface area is available, the concentration of $NaBH_4$ being kept similar for the RDE and DEMS studies. Thus, at low concentration of $NaBH_4$ (5 mM and 50 mM), the surface is not completely covered by $BH_{x,ad}$ species, and the palladium hydrides can be released at lower potentials simultaneously with the BOR oxidation; therefore, an oxidation current is observed at E = 0 V *vs* RHE. The structural modification ends at E = 0.3 V *vs* RHE, where a small peak can be observed on the faradic current (Figure III.15a). The surface is then composed of metallic Pd and the H_2 produced can now be quantitatively valorized, leading to the decrease of $I_{H2,eq}$ down to zero. In the meantime, the BOR continues, and no peak current is observed, because all hydrides have already been oxidized; overall, the reaction proceeds in a more continuous manner. As soon as palladium oxides form, a H_2 escape current re-appears, corresponding to the mechanism observed on Pt.

To conclude on these DEMS measurements, the behavior of Pd towards hydrogen generation and escape during the BOR is a combination between the behavior of Au, at low potential ($BH_{3,ad}$ oxidation on PdH), and of Pt, as soon as the structure is free of PdH and back to metallic Pd.

The effect of Pd structure modification

III.3.3

Further RDE end DEMS experiments were performed in order to confirm this formation of structural PdH. The two main goals of the following measurements were first, to observe how the reaction evolved when the amount of PdH was deliberately increased and secondly, to try to strip these hydrides from the matrix of the electrode and observe how the BOR proceeds on purely metallic Pd. It was mentioned in the tentative explanation of the BOR that if this behavior in really originating from PdH formation, it seems linked to the oxidation of the electrode: once the formation of oxides starts, the surface is stripped from its adsorbates and active sites are freed to release the hydrides. This link can be more clearly observed on Figure III.16a were both CV in supporting electrolyte and in presence of borohydride are superposed. During the cathodic scan, the BOR is reactivated only once the oxides start to reduce (E < 0.8 V *vs* RHE) and a mass transport-limitation plateau, approaching the 8 electrons limit (Figure III.14), is reached on this PdH-free surface. As soon as the oxides are fully reduced, the current drops back to the initial plateau corresponding to roughly 4 electrons, suggesting a mechanism switch because the L-H oxidation of BH_{ad} is not possible anymore. The influence of the amount of active sites is also demonstrated on Figure III.16b, where the same electrode was re-used after a first set of characterization without being re-polished to its mirror state. It results in a 4 times rougher surface (calculated from the oxide reduction peak in supporting electrolyte), which translated into a modification of the BOR CV: the first plateau is not as well defined, the peak of desorption of PdH is broader and a new small peak starts to appear around E = 0.9 V *vs* RHE, at the start of the surface passivation. The current produced on the oxidized surface is greater, because of the higher number of active sites; nonetheless, the kinetics of reaction at low potential did not improve, suggesting (again) that the reaction is limited by the surface coverage of intermediate species and/or the presence of PdH in the lattice of the electrode at 5 mM $NaBH_4$, even with the increased surface area. The overall shape of the CV, and particularly the broadness of the peak at E = 0.8 V *vs* RHE, indicates however that the PdH might start to leave the electrode as soon as the first plateau is reached. These findings on the rougher Pd electrode agree with those obtained with the sputtered Pd electrode in DEMS, and show the non-negligible impact of the electrode surface site density on its BOR activity (as was noted for Pt as well).

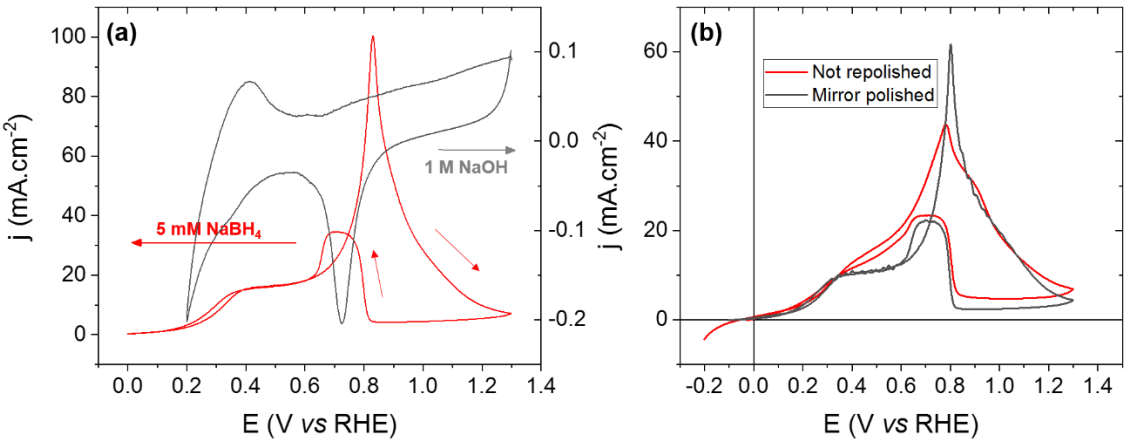

Figure III.16. (a) CV of polycrystalline Pd electrode (S_{geo} = 0.031 cm²) in supporting electrolyte (grey line) and in presence of 5 mM $NaBH_4$ (red line) at ω = 1600 rpm. (b) Comparison of the BOR at 5 mM $NaBH_4$ on a polycrystalline Pd mirror-polished prior the measurement (grey line) or the same electrode used after several BOR characterization, without being re-polished (red line) at ω = 1600 rpm. Ar-saturated electrolytes, T = 20°C, v_s = 20 mV.s^{-1}.

To study the effect of the hydride formation inside the Pd electrode along the BOR, a protocol, referred to as "PdH insertion procedure" thereafter, has been established: a series of CVs of 2 cycles between a lower potential limit varying from -0.2 < E < 0.7 V *vs* RHE and E = 1.3 V *vs* RHE (the upper potential limit) at v_s = 20 mV s^{-1} are alternated by CA in the PdH insertion region. The time of the CAs increases between each CV to also increase the amount of PdH inserted in the Pd. The second cycle of the CV is used as a probe of the state of the surface: it is expected to be similar every time if all PdH inserted during the stationary step are entirely removed during the first cycle. For clarity, all the first cycles will be represented together and separated from the second ones. Figure III.17 presents the results obtained using this procedure on the "rough" (not re-polished) electrode at 1 mM $NaBH_4$ for rather short insertion times (Figure III.17a) and 5 mM $NaBH_4$ for long insertion times (Figure III.17b).

At a very low concentration (Figure III.17a), the peak of PdH desorption is rather small and occurs at a lower potential (E ≈ 0.6 V *vs* RHE) in the initial state and a second oxidation plateau can be discerned before the passivation. This could be explained by the fact that few PdH are present in the electrode and, because of its higher surface area, they can be released at lower potential revealing the "real" second part of the BOR with a plateau similar to the BOR on Au. After 30 s of PdH insertion at E = 0 V *vs* RHE (≈ E_{oc}) the intensity of the peak increased but the second cycle remained similar to the initial state, meaning that all additional PdH inserted during this period were removed. The intensity of the peak follows the time spent at 0 V *vs* RHE, confirming that more hydrides are inserted. However, from $t_{E=0V}$ = 2 min, the second cycle does not reach the initial state back. It could mean that either that too much PdH were inserted and could

not be released in one cycle, or that the surface area of the electrode increased because of deformations created by the insertion/desorption of hydrogen atoms. Because the peak reaches its maximum current value at a similar potential for all insertion times and that the second plateau is always discerned, the morphology change proposition appears more likely. It is also important to observe how the reaction changes at low potentials. The more hydrides are present in the surface, the later the reaction starts, supporting the BOR mechanism presented previously: no oxidation was observed at 0 V *vs* RHE, owing to the presence of PdH in the electrode. Because the surface is more developed (and keeps developing along the cycles), the first plateau cannot be discerned and the PdH desorption starts as soon as $BH_{3,ad}$ species are oxidized, freeing active sites.

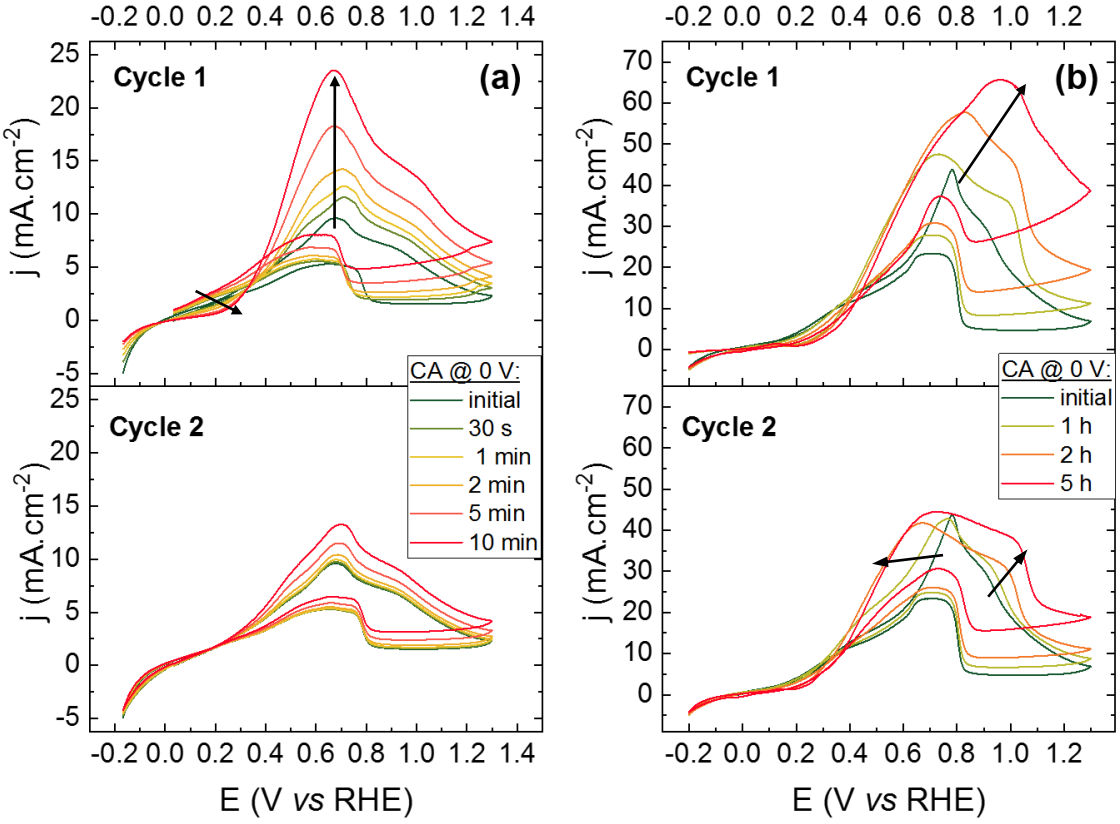

Figure III.17.PdH insertion procedure on the not re-polished Pd electrode: 2 cycle CVs alternated with increasing time at E = 0 V *vs* RHE in 1 M NaOH + (a) 1 mM or (b) 5 mM $NaBH_4$. ω = 1600 rpm. Ar-saturated electrolytes, T = 20°C, v_s = 20 mV.s^{-1}.

The same experiment was reproduced at 5 mM $NaBH_4$ with longer insertion time (Figure III.17b). Because more species are brought to the electrode, the peak is sharper and now appears at E = 0.8 V *vs* RHE. After 1 hour at E = 0 V *vs* RHE, the kinetics at low potentials changed and the peak is now really broad. All the hydrides can be desorbed at rather low potential (as soon as the reaction starts), and the second plateau is now well defined on the first cycle. In addition, the shape of the second cycle is

different from the one observed for the initial state and the peak remained broader, meaning a surface area increase. For longer insertion time, the same observation can be made, especially for $t_{E=0V}$ = 5 h, where the desorption peak on the first cycle is still broad; it also extends to E = 1 V *vs* RHE, because it takes more time to free the electrode from all the additionally-inserted hydrides. The second cycle asserts that the morphology of the surface completely changed from its initial state. The desorption occurs simultaneously with the BOR: almost no peak is observed and the second plateau is now well defined before the passivation of the electrode. The fact that this passivation occurs at higher potential and that the BOR current on the oxidized surface is also greater is another sign of the surface area increase. This surface distortion under hydride formation/desorption might look interesting because it increases the performance of the electrode over time; however, when applied to supported electrocatalysts nanoparticle, this might result in severe particle restructuring and eventually detachment leading to irreversible loss of activity.

The PdH insertion procedure was reproduced on a mirror-polished electrode to observe how the electrode behaves when the surface area is small and is strongly blocked by adsorbed species. To avoid forming additional PdH when cycling at low potential, the lower potential limit was firstly increased to E = 0.2 V *vs* RHE (Figure III.18a). Even without scanning below this potential, the intensity of the peak at E = 0.8 V *vs* RHE remained the same in the initial state (compared to previous measurement, Figure III.14a), suggesting that the same amount of PdH is present in the electrode. Even more surprising, when the electrode is maintained at E = 0 V *vs* RHE, the intensity of the peak does not increase, and even slightly diminishes. This unexpected result can be explained by the fact that the surface is already completely blocked by adsorbed species and that no additional hydrogen atoms can be inserted in the Pd structure. The shape of the CV still changes with the increased "insertion" time, especially for $t_{E=0V}$ = 10 min, where the signal starts to look like the one from the not re-polished electrode on Figure III.16b: the BOR onset is slightly delayed, the desorption starts as soon as the first plateau is reached, which results in a smaller peak and the slight apparition of the second plateau in the passivation region. This is thus typical of the surface area increase just detailed. However, the second cycle is always identical, meaning that the initial state of the surface is reached back. One hypothesis could be that during the time at E = 0 V *vs* RHE, a small amount of hydrides is inserted/desorbed, slightly modifying the structure of the electrode, but the formation of the oxide layer at high potential allows to reorganize it so that the initial state is regained. In fact, this can be observed on the cathodic scan of the first cycles, where an identical reactivation plateau is reached although it should increase for a larger amount of active sites. Increasing the potential limit to E = 0.4 V *vs* RHE (Figure III.18b) does not change the behavior of the initial state, with still the same peak intensity. The PdH insertion procedure also proved identical as the previous

measurement, meaning that the scanning down to this potential does not allow to remove the PdH formed along the BOR. This suggests that hydrides are still inserted in the structure of the electrode at such potential, which is not expected following thermodynamics. Again, the hydrogen atoms should be released and then oxidized ($E > 0$ V *vs* RHE) but the presence of borohydrides, and other related adsorbates, might modify the desorption conditions and delay the reaction to higher potential values.

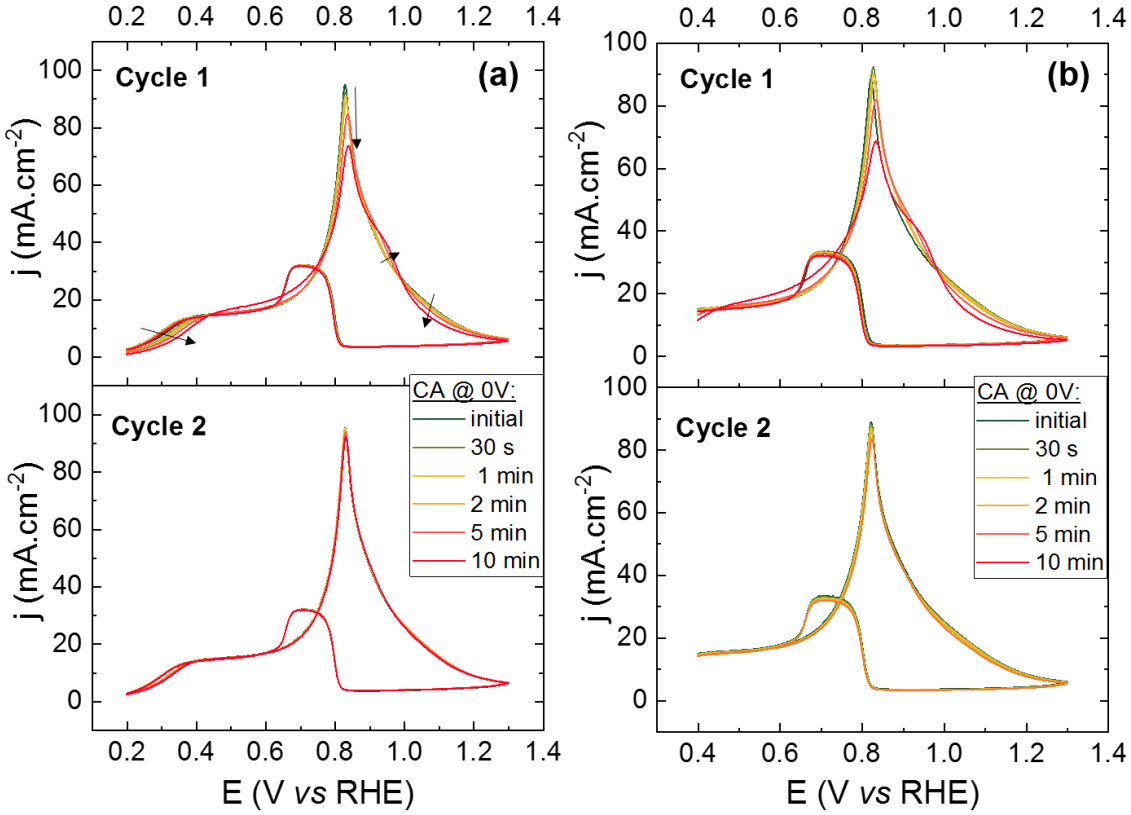

Figure III.18. PdH insertion procedure on the mirror-polished Pd electrode: 2 cycle CVs alternated with increasing time at E = 0 V *vs* RHE in 1 M NaOH + 5 mM $NaBH_4$. The lower potential limit ω = 1600 rpm. Ar-saturated electrolytes, T = 20°C, v_s = 20 $mV.s^{-1}$.

To investigate in more detail this surprising effect, it was necessary to reach a state where the BOR occurs on a PdH-free surface. As it was observed on Figure III.16a, the presence of oxides appeared as a key factor to reach this state, so the lower potential limit was increased even more to E = 0.6 V *vs* RHE (Figure III.16a). This time, the desorption peak started to shrink, but stabilized after 3 cycles at a current value almost 2 times smaller than the initial state. The potential limit was thus increased even more to E = 0.7 V *vs* RHE (Figure III.19b), which corresponds to the middle of the second BOR plateau on the cathodic scan and roughly to the peak of oxides reduction (Figure III.16a). In these conditions, the peak completely disappeared after only one cycle and a stable plateau is reached on both ongoing scan. The surface is quickly passivated, because the surface area is similar to the geometric one (with this S_{geo} = 0.031 cm^2 mirror-polished

electrode). For 0.7 < E < 1.3 V *vs* RHE, the BOR can now proceed on the targeted PdH-free surface.

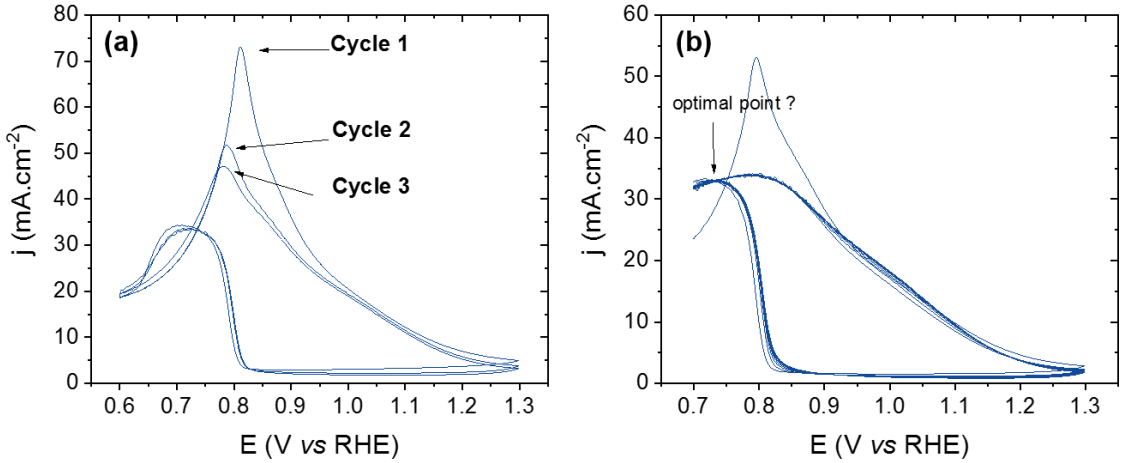

Figure III.19. CV on mirror-polished Pd electrode with lower potential limit increased to (a) E = 0.6 V *vs* RHE or (b) E = 0.7 V *vs* RHE. 1 M NaOH + 5 mM $NaBH_4$, ω = 1600 rpm, Ar-saturated electrolytes, T = 20°C, v_s = 20 mV.s^{-1}.

The PdH insertion procedure was thus reproduced using this potential window on the mirror-polished electrode in 1 M NaOH + 5 mM $NaBH_4$ (Figure III.20a). However, the insertion times had to be modified in order to correctly observe the changes of behavior. Indeed, after only 5 s of insertion at E_{oc} (≈ -50 mV *vs* RHE) the sharp desorption peak appears. For longer times, the peak only gets smaller and broader, meaning that as soon as the potential is released out of the studied window, the steady-state between PdH insertion and adsorption of intermediate species on the surface is reached in only few seconds. Because the surface is then completely blocked, increasing the insertion time only results in the morphology modifications presented previously. Because no more hydrides are inserted compared to previous measurements, they are again all desorbed and the second cycle shows that the surface is correctly regenerated/reorganized. As it was suggested that hydrogen atoms are still inserted in the structure during the first BOR plateau (up until E = 0.7 V *vs* RHE), the insertion procedure was performed again in the high potential window: the insertion potential was increased to E = 0.4 V *vs* RHE (Figure III.20b). Again, after few seconds the peak of desorption appears; however, this time, a new behavior is observed for longer insertion periods. Indeed, the intensity and potential of the peak only increase when the potential is maintained for longer steps at E = 0.4 V *vs* RHE between two CVs. This asserts that the amount of hydride inserted in the structure keeps increasing and no limitation by blockage of the surface appears like previously. Moreover, the initial state is recovered for all insertion times, as demonstrated by the second cycles which are all identical. In this configuration, the

morphology of the surface is then kept pristine and no structural deformations seem to appear (all the signals smoothly overlap the initial one).

This measurement demonstrated that hydrides are indeed formed in the structure at potential as high as E = 0.4 V *vs* RHE (and even 0.7 V *vs* RHE if this observation is extrapolated to Figure III.19). In this case, it is even favored at such potential, since no limitation is observed and the amount of hydride formed only increases with time. A proposed explanation is that during the first BOR plateau, the poisoning $BH_{3,ad}$ species are oxidized or dissociated and the produced H_{ad} are somehow forced into the structure of the electrode. Because the active sites are constantly freed at this potential, the hydride formation is not stopped until oxides are formed. Again, this was not expected from the literature, and does not follow the Pd-hydrogen thermodynamics (but in this case, $BH_{x,ad}$ species act as a source of surface hydrogen, and may be stable at the Pd surface even well-above 0 V *vs* RHE).

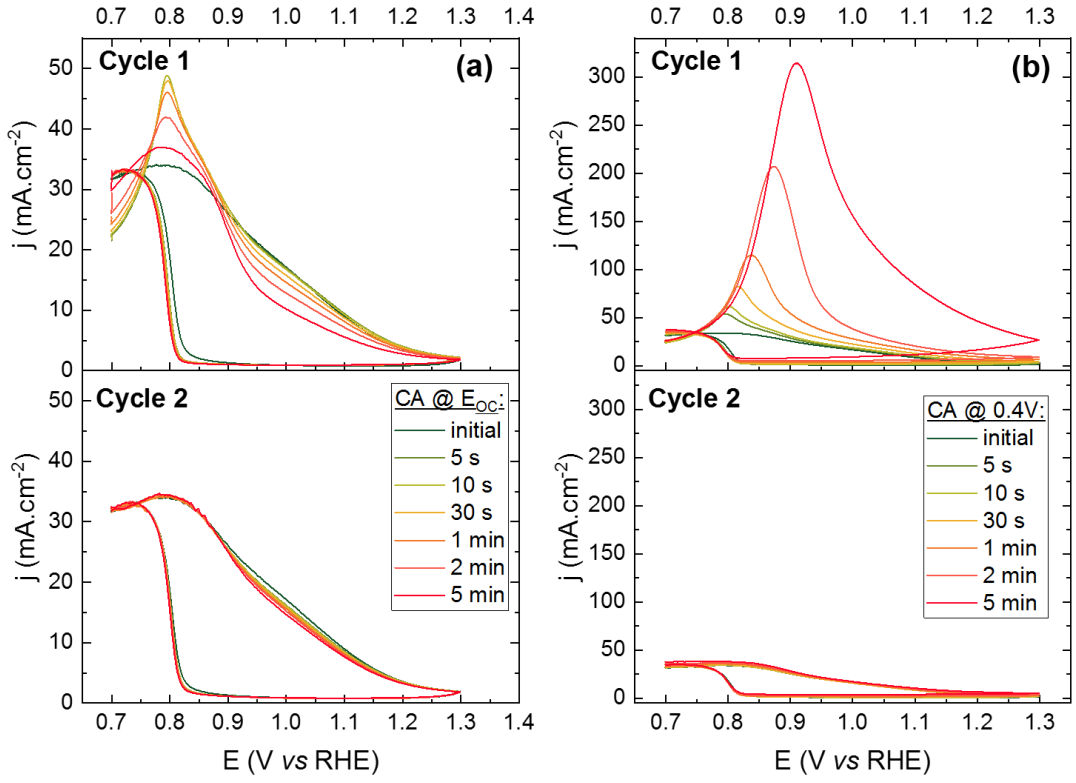

Figure III.20 PdH insertion procedure on the mirror-polished Pd electrode: 2 cycle CVs alternated with increasing time at (a) E_{OC} or (b) E = 0.4 V *vs* RHE in 1 M NaOH + 5 mM $NaBH_4$. The lower potential limit is increased to E = 0.7 V *vs* RHE to remove the PdH contribution. ω = 1600 rpm. Ar-saturated electrolytes, T = 20°C, v_s = 20 mV.s^{-1}.

Because of the thermodynamic contradiction about the formation of hydrides at such high potentials, another explanation was considered. It could be that other species are inserted in the structure, that are not oxidized until a higher potential is reached. The

only other possibility in this configuration would be the insertion of boron and the related formation of Pd-borides. Stable palladium borides do exist (mostly in the form of metal-rich structures) and the $Pd_{16}B_3$ or Pd_5B phase is apparently stable at ambient temperature, as described by the Pd-B phase diagram [253–256]. However, they require high temperature to be formed (around T = 400°C) and are usually obtained using arc melting or sintering. Moreover, the DFT calculations made by Rostamikia *et al.* do not forecast the formation of isolated boron atom on either Pt [215] or Au [217] surfaces, which does not support the hypothesis of the insertion of boron in the structure. Therefore, this second hypothesis does not appear more likely than the formation of hydride at high potential. In addition, preliminary *in situ* XRD measurements did not reveal the formation of crystallized PdB structures (however, an amorphous phase could still be formed)

To complete the study about this formation of "supposedly" hydrides, new DEMS measurements were performed to observe the hydrogen escape during the PdH insertion procedure. A new Pd electrode was considered to mimic the model conditions of the mirror-polished RDE electrode: a polycrystalline Pd plate (0.2 mm thick, S_{geo} = 0.785 cm²) was pierced by numerous holes and pressed against the PTFE membranes at the bottom of the cell, so that the gaseous species produced could be sucked by the vacuum and detected by the mass spectrometer. Isotopic $NaBD_4$ was used to differentiate the contributions from the decomposition of the water (H_2: $I_{m/z=2}$) and the species produced by the BOR (HD: $I_{m/z=3}$ and D_2: $I_{m/z=4}$). The concentration was kept at 1 mM $naBD_4$ in 1 M NaOH to avoid excessive formation of bubbles, parasitizing the spectrometric current with noise. Because of this low concentration and the large surface area of the electrode, it shall not be completely poisoned (as the RDE was), so the hydride formation will not be limited in the similar way as in Figures III.18 and III.20. Therefore, the lower potential window as well as the CA potential were decreased to E = -0.2 V *vs* RHE in order to ensure a good PdH insertion. The insertion times were also increased to reach overall conditions similar to for the first measurement (Figure III.17a). Both cycles measured after each of these periods are again represented separately and accompanied by their corresponding I_{D2} current (Figure III.21). No calibration of the cell was performed in supporting electrolyte, because of the hydride formation. For clarity reason, $I_{m/z=3}$ current is not displayed, since no significant information can be obtained from its value.

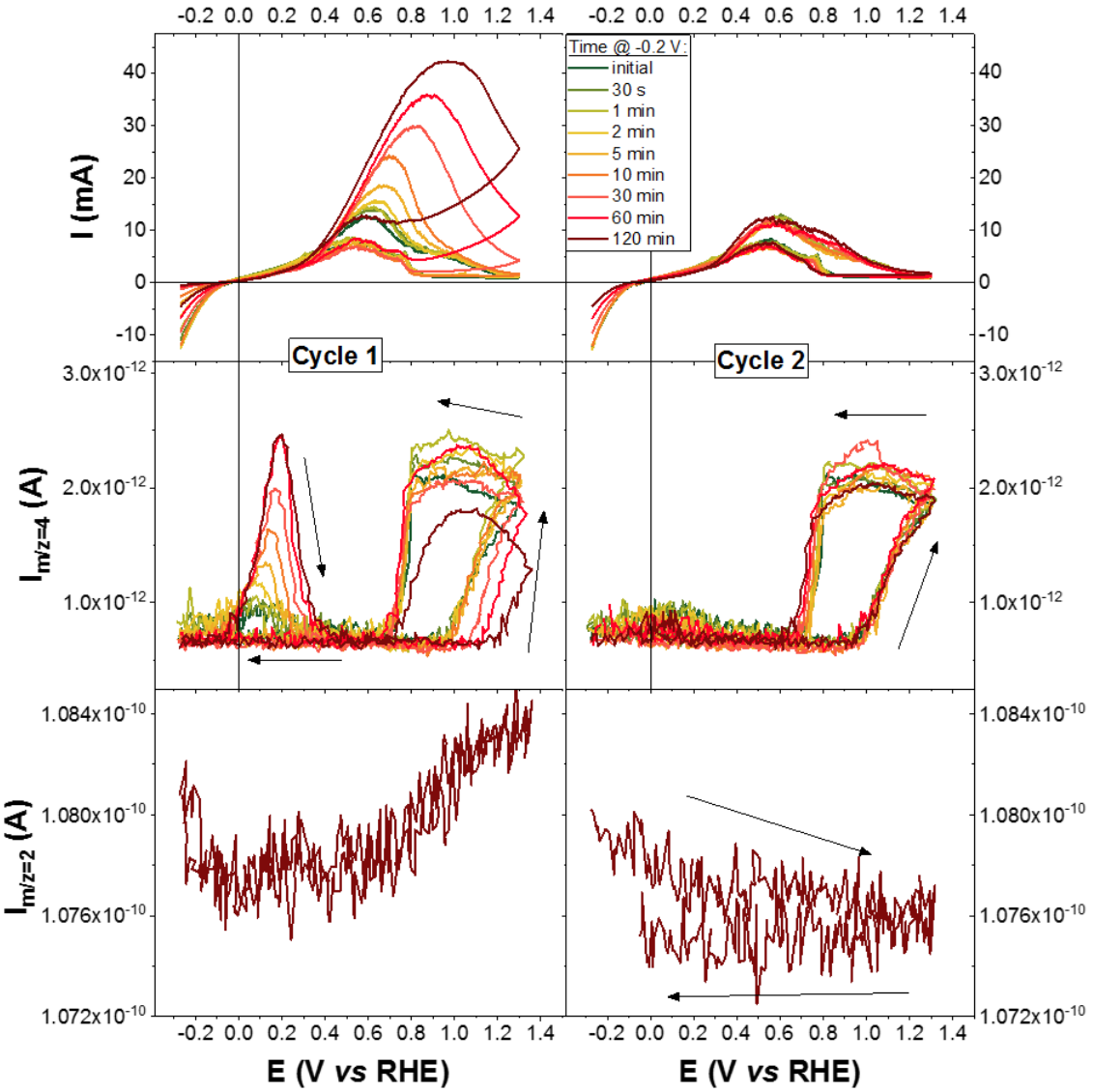

Figure III.21. PdH insertion procedure coupled with DEMS: 2 cycle CVs alternated with increasing time at E = -0.2 V *vs* RHE in 1 M NaOH + 1 mM $NaBD_4$. The electrode used is a pierced polycrystalline Pd disk (S_{geo} = 0.785 cm^2) to allow gaseous species to sucked by the vacuum and detect by the mass spectrometer. $I_{m/z=4}$ (D_2) and $I_{m/z=2}$ (H_2). Ar-saturated electrolytes, T = 20°C, v_s = 10 $mV.s^{-1}$.

First of all, the amount of hydrides formed in the electrode increases accordingly to the insertion time; so does the maximum current; the potential of the peak of desorption is once again directly related to the time spent at E = -0.2 V *vs* RHE. Because the surface of the electrode is not as well defined as the RDE tip, the shape of the CVs is less distinct and the peak is way broader. However, all signals reach back the initial state already on the cathodic scan of the first cycle (even after 120 min of insertion), which results in all the second cycles being similar. The corresponding D_2 current measured is however interesting, since for the first cycle a peak appears at the start of the BOR and decays around E = [0.3, 0.4] V *vs* RHE, its potential depending of the insertion time. Then all

D_2 is valorized until the formation of oxides starts: the more hydrides are released from the surface the later D_2 is detected. This corresponds to an Au-like behavior, where H_2 escapes the electrode in the kinetic limiting region of the "partial dissociation" pathway. The second region of D_2 detection is way more pronounced than on Au, because the oxides form at lower potential and at a slower rate (corresponding to the H_2 escape observed on Pt). However, on the second cycle, the $I_{m/z=4}$ contribution at low potential drastically decreased, since all the additional hydrides were stripped from the electrode. The remaining current results from the insertion of hydrides during the potential scan: as soon as the BOR starts, they are removed and the reaction can switch back to the "fully-dissociated" pathways. On the last cycles (after 60 and 120 min of insertion time), almost no D_2 species are detected in this low potential region, meaning that the surface is not forced to form the $BH_{3,ad}$; this suggests that the morphology of the electrode is again modified, even if it is not clearly observed on the faradic current.

Finally, a last observation can be made confirming the formation of hydrides in the Pd electrode. The $I_{m/z=2}$ current is present for the last CV after 120 min of insertion time at E = -0.2 V *vs* RHE (no significant signal emerged from the noise for the previous one). For E > 0.5 V *vs* RHE, the signal starts to increase and can now be discerned from the baseline. This potential corresponds to the moment where no more D_2 is detected and where the faradic current surpasses the maximum current reached at the initial state. This means that at this potential, the exceeding current is only produced from the hydride being released from the electrode structure. It is accompanied by a slight H_2 detection, confirming that the hydrides inserted at -0.2 V *vs* RHE originate from the water decomposition. This current is really small, because most of the species are directly oxidized, explaining why it is not observable for a shorter insertion time (and therefore smaller amount of H atom inserted). In the second cycle, no more H_2 is detected and the only decrease along the scan suggests that H_2 was gradually escaping the surface in the course of the characterization when the electrode was initially saturated from hydrides.

Overall, this study to observe the behavior of Pd and PdH during the BOR confirmed the reaction model proposed earlier. The interaction between H_{ad} species and other products of reaction, such as BH_{ad} and $BH_{3,ad}$ was demonstrated to be very complex. To understand how the hydrides still form at potentials higher than their standard potential on an active site-limited surface, further DFT calculations as well as kinetic simulation would be required. Moreover, *in situ* XRD of the electrode would allow to directly observe the change in its lattice parameter during this insertion confirming this hypothesis with physical characterization and not indirect effects resulting from this structure modification. Such measurements have been performed last July at the

European Synchrotron Research Facility (ESRF), and their future analysis (which is time-consuming) could enable to definitively unveil this PdH question.

III.4 Conclusion and moving to non-noble BOR catalysts

In this chapter, the effect of the borohydride concentration was presented on noble-metal catalysts, which are the most-used ones for the BOR and DBFC applications in the literature [120]. It was demonstrated that platinum electrocatalysts suffer from severe poisoning of their surface once the concentration is increased from the laboratory scale (5 mM $NaBH_4$) to the FC operation conditions (500 mM $NaBH_4$). This induces a modification of the borohydride oxidation reaction pathway from a "fully-dissociated", promoting fast charge-transfer kinetics and large current generation at low overpotential (for $E > 0$ V *vs* RHE), to the "partially-dissociated". In the latter, the formation of $BH_{3,ad}$ intermediate species is forced due to strong surface poisoning by BH_{ad} adsorbates, inducing significant faradic efficiency losses because (i) of their desorption or dehydrogenation and (ii) the slower charge-transfer kinetics of their oxidation reaction. The intensity of this detrimental poisoning effect depends on the ratio of the number of active sites over the number of active species brought to the surface. This means that a highly developed surface area composed of nanoparticles supported on carbon, used in DBFC systems, will be less affected by this poisoning at a given $NaBH_4$ concentration, but however will still require optimization of the operational conditions to minimize it.

Au electrodes were then demonstrated as poor BOR electrocatalysts with large activation overpotential, making them unsuited for use at a DBFC anode. This noble metal is still often investigated for this reaction though, because of its misleading open circuit potential and related poor activity for the HER. Indeed, rather lower OCP values (compared to a Pt electrode) are reached suggesting that the reaction would produce electrons for very low overpotential. However, unlike on Pt, the reaction on Au only proceeds through the "partially-dissociated pathway" with particularly slow charge-transfer kinetics. The only beneficial aspect of the BOR on Au following the same mechanism for all conditions, is that the poisoning of the surface is rather small even for large borohydride concentrations, resulting in a reaction only limited by the charge-transfer kinetics. Micro-kinetic simulations were performed based on the proposed BOR model, using the experimental data presented here and gathered from the literature, and the results of DFT calculations; it produced results agreeing adequately with these data, even at large borohydride concentrations, for both the Pt and Au electrodes.

Palladium was then tested for the BOR, since it presents promising performance and is often used as a substitute to Pt as anode catalyst in DBFC systems. However, less fundamental studies have been performed on this metal in the past. Previous DFT calculations [216] allowed to expect a full (to BH_{ad}) dissociation of BH_4^- ions on the Pd surface, suggesting a similar BOR behavior as on the Pt electrode. However, the data proved different with delayed onset of reaction and a first limitation plateau similar to the Au electrode, signifying a partial reaction with around 4 electrons produced per BH_4^- species oxidized. This unexpected result was accompanied by a sharp oxidation peak surpassing the theoretical maximum current of the BOR. A mechanism involving formation of structural hydride when H_{ad} are produced by dissociation of BH_4^- and $BH_{3,ad}$ species, forcing the reaction to occur (once again) through the "partially-dissociated pathway" was thus proposed. This tentative mechanism is capable to explain why the BOR on a Pd electrode is more similar to Au than Pt, with the benefit of having faster charge-transfer kinetics for the oxidation of $BH_{3,ad}$, though. A detailed study about this hydride allowed to demonstrate an odd behavior, where PdH is present at potential as high as 0.6 V *vs* RHE in presence of borohydride on a surface fully-blocked by intermediate species. This structure modification will need further investigations to be fully understood: detailed DFT calculations on both Pd and PdH surfaces will be required, to confirm the possible and stable adsorbed species, as well as *in situ* physical characterizations to certify that this different BOR mechanism is induced by hydride formation. Once all these data will be gathered, the micro-kinetic simulation would be possible to corroborate the proposed BOR mechanism on Pd electrodes.

This effect explains why the BOR occurs differently on Pd and why this metal is less affected by the poisoning of the surface, thanks to faster charge-transfer kinetics for the oxidation of $BH_{3,ad}$ [129]. It also explains why Pd electrodes could exhibit better performance than the Pt ones if the latter is not optimized in the system where it is used. However, the price of Pd started to noticeably increase in 2016, and reached the price of Pt in 2018 [257]. This trend was maintained to this day, making Pd more than 2 times more expensive than Pt [258,259]. The idea of using this metal as a substitution for Pt is therefore rather controversial.

Another detrimental and very important effect, in addition to this poisoning of the catalysts, has been demonstrated to appear on PGM nanoparticles supported on carbon substrates. Indeed, when used in alkaline media, critical degradation of the electrocatalysts has been observed, in particular for Pt-based nanoparticles. It can be observed on Figure III.22, Pt (a, b, c) and Pd (d, e, f) commercial catalysts and their corresponding particle size distribution before and after an Accelerated Stress Test (AST) in 0.1 M NaOH [260–262]. After only 150 cycles in the $0.1 < E < 1.23$ V *vs* RHE potential window, a huge surface area loss of around 60% has been measured for Pt/C

[260]. Since the particle size distribution is about the same before and after the AST, it means that this loss is mainly due to particle detachment, which is really prejudicial towards application in alkaline FCs. The same effect has been observed for Pd electrocatalysts but to a lesser extent, since the same loss is observed after 1000 cycles in the same conditions [261,262], suggesting once again that this PGM might be more suitable than Pt for such applications.

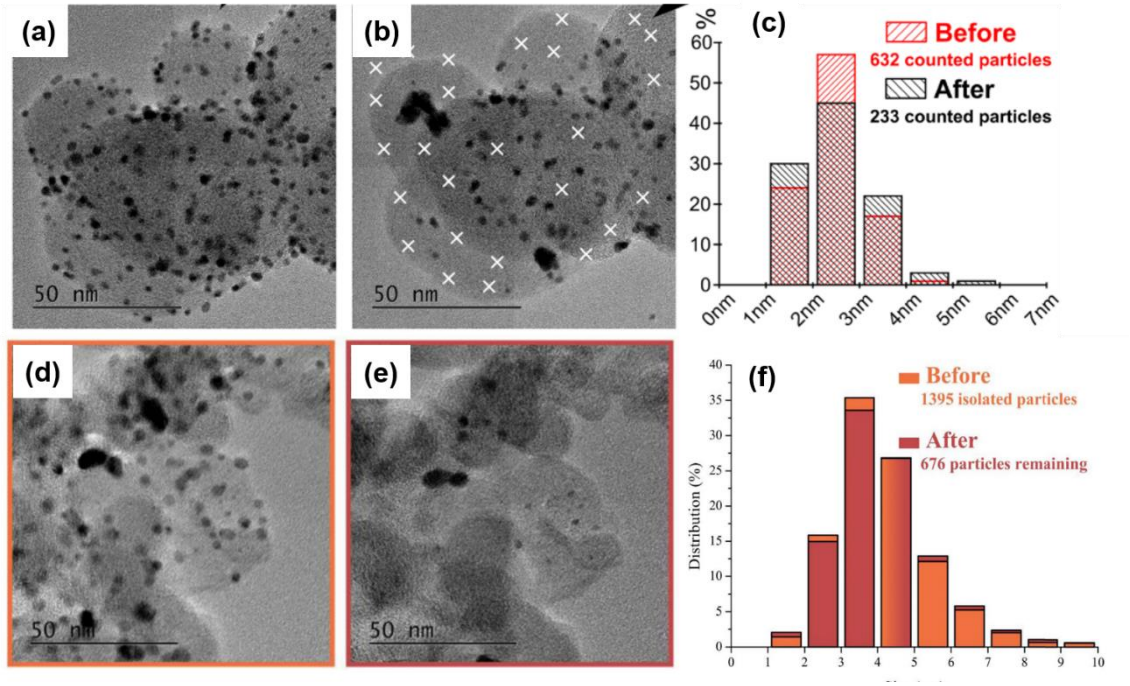

Figure III.22. Stability of PGM catalysts in 0.1 M NaOH: 150 AST cycle on Pt/C (a, b, c) and 1000 AST cycle on Pd/C (d, e, f) commercial electrocatalysts (c, f) shows large particle detachment. Adapted from Ref [260,261].

However, this instability is still really detrimental, since the AST have been performed in relatively mild conditions (supporting electrolyte, ambient temperature, $0.1 < E < 1.23$ V *vs* RHE potential window); besides, adding borohydride to the electrolyte will strongly affect the Pd morphology, as described previously, possibly enhancing the already significant degradation of the electrode. Lafforgue *et al.* [263,264] completed the previous stability studies on PGM in alkaline media to understand its mechanism. The formation of carbonate is accelerated through PGM-catalyzed carbon corrosion in the vicinity of PGM nanoparticles. This formation is favored at the anchoring point of the nanoparticles, breaking their bond with their support and resulting in the irreversible particle detachment. This instability was demonstrated less critical for non-noble based catalysts [195,265].

Indeed, since the DBFC operates in alkaline medium, non-noble metals such as Co, Cu, Fe, Mo or Ni are supposedly stable (against dissolution) and can therefore be used for FC applications. These transition metals are already being investigated in several AFC

technologies. They are often alloyed with the previously presented noble metals [266–272] or used in core-shell configuration [273–277] to reduce the overall costs of the catalysts while keeping rather good activities. However, using non-PGM catalysts in this manner will not change the detrimental effects previously described. PGM-free catalysts are also developed for the same applications with a particular focus on Co [270,278–281] and Ni-based materials [197,282–288]. However, because of the current critical situation of cobalt [89] (Co is the main element in the constitution of positive electrodes of the Li-ion batteries) the focus of the MobiDiC project and this PhD to develop efficient low-cost DBFC anode has been directed to Ni-based electrocatalysts. Promising results were obtained at LEPMI using Ni_3M/C catalysts for the ammonia borane oxidation reaction [195] with low activation overpotential (oxidation starting slightly below $E = 0$ V *vs* RHE). The reaction has some similarities with the BOR, so one could suppose that the good performance of this catalyst might be reproduced at the DBFC anodic reaction. Moreover, A. G. Oshchepkov, who studied in depth the nickel catalysts for the HOR and particularly the influence of the state of surface [186,187,289,290], joined the MobiDiC project to help and enhance such Ni-based catalysts for the BOR. These materials will be evaluated in the next chapter.

CHAPTER IV: Towards efficient Ni based BOR catalysts

In order to move towards non-noble BOR catalysts, a specific attention had to be given to the state of surface of the materials. This has been addressed in a recent review article, that presents the electrocatalytic activity of nickel in different oxidation states towards the hydrogen reactions encountered in AFC and more exotic fuels (hydrazine, borane or borohydride) [210]. The initial section of this chapter is largely based on this review. The influence of alloying Ni with another co-element to facilitate its depassivation will also be investigated in this chapter. Lastly, highly active metallic Ni catalysts will be presented and compared to PGM ones (the corresponding results having been published in [291]). A preliminary mechanism will be proposed for the BOR on such catalysts.

IV.1 Importance of the state of surface of Ni

Electrochemical behavior of Ni in alkaline medium

IV.1.1 Electrochemical properties of Ni electrodes have been widely studied since the beginning of the XXth century, starting from the works of Emelianova [292], Frumkin *et al.* [293,294], Conway *et al.* [295–302], Breiter *et al.* [303,304], Bockris and Potter [305] and others. The behavior of Ni in alkaline media has been recently summarized by the groups of MacDougall [306,307] and Jerkiewicz [308–310], who discussed in detail various potential-dependent processes taking place on the surface of Ni electrodes. In addition, Oshchepkov *et al.* have recently unveiled the influence of the surface state of Ni electrodes on their HOR/HER activity in the potential interval $-0.2 < E < 0.5$ V *vs* RHE [186,289,290,311,312]. Below the most relevant information regarding electrochemistry of Ni electrodes in alkaline media is briefly summarized.

To facilitate the discussion about characteristic features of CVs of a Ni electrode (Figure IV.1a) as well as its electrocatalytic properties in a number of oxidation reactions, it is convenient to define two potential intervals, that depend on the reversibility of the Ni oxidation. In the "low-potential region" at $-0.2 < E \leq 0.5$ V *vs* RHE, the surface of a Ni electrode can be reversibly oxidized and reduced, while in the "high-potential region" at $0.5 < E < 1.6$ V *vs* RHE, the formation of irreversible, passivating, Ni oxides occurs, the degree of irreversibility depending on the anodic potential limit. The high-potential region can be additionally split into two sub-regions, namely $0.5 < E < 1.2$ V *vs* RHE and $1.2 < E < 1.6$ V *vs* RHE, depending on the degree of Ni oxidation, as discussed further in this section. Below $E = 0$ V vs RHE and above *ca.* $E = 1.5$ V *vs* RHE the evolution of hydrogen and oxygen take place, respectively. In what follows, the processes taking place on Ni electrodes in the low- and the high-potential regions will be briefly

discussed, mainly focusing on the former one, for which the literature is still not consensual.

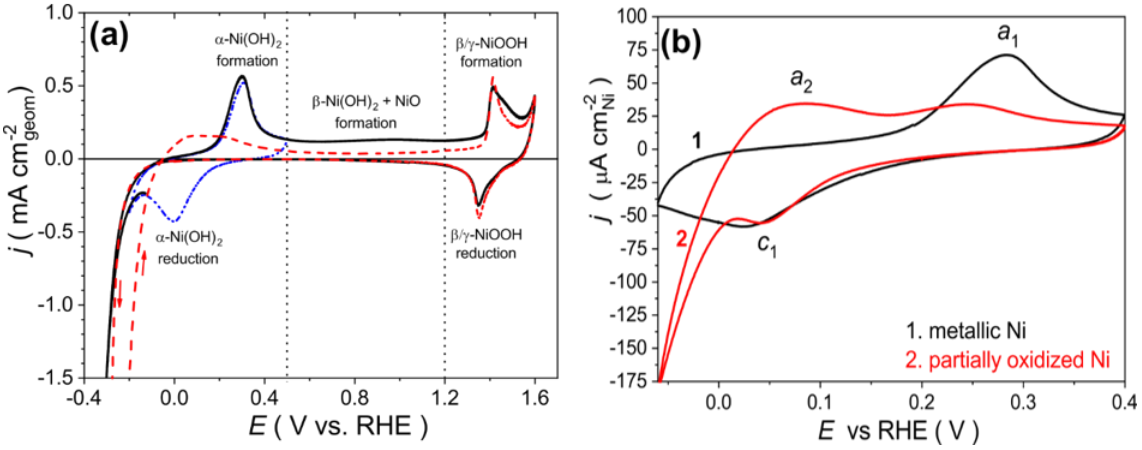

Figure IV.1. (a) CVs of a polycrystalline Ni electrode in N_2-saturated 0.1 mol.L^{-1} NaOH at a sweep rate v_s = 50 mV.s^{-1} and T = 25°C. The first CV in panel a (dash-dotted blue curve) covers the potential range from E = -0.2 to 0.5 V *vs* RHE, while two other CVs (first scan – solid black curve and second scan – dashed red curve) cover the potential range from E = -0.3 to 1.6 V *vs* RHE. (b) CVs obtained for metallic and partially oxidized polycrystalline Ni electrodes in N_2-saturated 0.1 mol.L^{-1} NaOH at a sweep rate v_s = 20 mV.s^{-1} and T = 25°C. Adapted from Ref. [186] with permission from Springer.

- α-$Ni(OH)_2$ formation

It is generally accepted that the main process occurring in the low-potential region is the reversible oxidation of Ni with the formation of surface α-$Ni(OH)_2$ during the anodic sweep, followed by its reduction in the cathodic sweep [306,308,313–315]. The common use of the term 'α-$Ni(OH)_2$' (suggesting formation of a 3D structure with H_2O molecules incorporated between $Ni(OH)_2$ layers [306]) is explained by the fact that it likely grows on the Ni surface through formation of 3D islands of α-$Ni(OH)_2$. This has been evidenced by the use of *in situ* scanning tunneling microscopy [316,317] as well as by the analysis of CVs monitored at low (< 263 K) temperatures [315]. According to the place-exchange model proposed by Conway *et al.* for noble metal surfaces [318] and later adapted by Alsabet *et al.* [308], the formation of α-$Ni(OH)_2$ proceeds through three consecutive steps: firstly, the discharge of OH^- anions at the Ni surface and formation of adsorbed OH species (Ni-OH_{ad}, equation 4.1), secondly, the incorporation of OH into subsurface between the first and the second layer of Ni atoms ((OH-Ni)quasi-3D lattice, equation 4.2) and thirdly, chemisorption of the second monolayer of OH groups on the (OH-Ni) quasi-3D lattice (equation 4.3):

$$Ni + OH^- \rightleftarrows Ni\text{-}OH_{ad} + e^- \quad \text{(equation 4.1)}$$

$$Ni\text{-}OH_{ad} \rightleftarrows (OH\text{-}Ni)\text{quasi-3D lattice} \quad \text{(equation 4.2)}$$

$$(OH\text{-}Ni)\text{quasi-3D lattice} + OH^- \rightleftarrows Ni(OH)_{2,ad} + e^- \quad \text{(equation 4.3)}$$

The existence of intermediate Ni-OH_{ad} species was suggested on the basis of electrochemical (mainly cyclic voltammetry) [304,319] and *in situ* scanning tunneling microscopy [317] measurements.

The influence of the crystallographic orientation of the Ni surface on its electrochemical behavior has been studied in several works, dealing either with acid or alkaline media [303,304,317,320–324]. While early studies [303,322,324] did not point towards noticeable differences in the formation of α-$Ni(OH)_2$ for low-index Ni planes (111), (110), (100), the recent work of Esau *et al.* clearly demonstrates that different crystallographic orientation of the Ni surface lead to typical CV profiles [323]: the anodic peak potential of α-$Ni(OH)_2$ formation shifts positive following the order (100) < (110) < (111), and an additional (pre-)peak appears at lower potential values for the Ni (100) and Ni (110) planes (with a less intense pre-peak in the latter case) [303,322,324]. This observation agrees with DFT calculations [325,326], which predict structure-sensitive adsorption of OH_{ad} and other species on the Ni surface (in vacuum). Meanwhile, the potential of the cathodic peak is very similar for the three Ni single crystal planes.

In addition to α-$Ni(OH)_2$, some works mention possible formation of NiO species sandwiched between the metal and the outer layer of α-$Ni(OH)_2$ [327–329]. However, the amount of NiO formed during potential cycling in the low-potential region can be considered insignificant, as evidenced by *in situ* Raman [313] and IR spectroscopy [330] as well as *ex situ* X-ray photoelectron spectroscopy (XPS) [331]. NiO can also form on the surface of Ni electrodes upon contact with oxygen species, followed by its partial transformation into α-$Ni(OH)_2$ by reaction with water, either from humid air or an aqueous alkaline electrolyte, which results in a three-layer structure Ni | NiO | α-$Ni(OH)_2$ [329]. Finally, unlike in acidic media, anodic dissolution and cathodic redeposition of Ni, which might be expected from Pourbaix diagram [332], have not been observed in alkaline electrolytes in the low-potential interval [315,328].

Except deliberately prepared otherwise (reduced), a Ni electrode surface is usually (at least partially) covered by stable Ni oxides (*e.g.* NiO or β-$Ni(OH)_2$); the oxide layer forms "spontaneously" either through oxidation of Ni in air (*i.e.* chemical oxidation) or *via* excursions to high anodic potentials (*i.e.* electrochemical oxidation). The shape of the CV changes substantially with the state of the Ni surface: an additional anodic peak shows up for $0.05 < E < 0.15$ V *vs* RHE (Figures IV.1a and 1b) for partially oxidized Ni surfaces, this observation being reproducible and reported in several publications [188,304,322,327,333–338]. The peak potential and the corresponding current density significantly depend on the surface state of the electrode, as well as on the cathodic potential limit of the CV [290,335,338]. The origin of that second anodic peak is still debated, some authors attributing it to the formation of Ni–OHad, [186,322], others to the oxidation of adsorbed/absorbed hydrogen [304,333,334,339], as discussed below.

- Hydrogen adsorption

Hydrogen adsorption is of paramount importance for the HOR/HER on metal electrodes (*vide infra*), and thus has widely been discussed in the literature (see Refs.[340–342] and references therein). On Pt and other PGM electrodes, the literature is consensual and points to the existence of two types of phenomena: "under-potential" deposition of hydrogen (H_{upd}) at potentials above E = 0 V *vs* RHE and "over-potential" deposition of hydrogen (H_{opd}) at potentials below E = 0 V *vs* RHE [340,341]. While the presence of H_{opd} on Ni is commonly accepted, there are significant controversies in the literature regarding the existence of H_{upd} on Ni electrodes. Some researchers insist that, above E = 0 V *vs* RHE, a Ni electrode is covered by adsorbed oxygenated species (OH_{ad}/OH^-_{ad} /H_2O_{ad}), which prevent adsorption of H_{ad} [308,328,340,343,344]. Others present evidence of the existence of H_{upd} on the surface of Ni electrodes. More specifically, Hu and Wen [333] investigated electrocatalytic hydrogenation of p-nitroaniline in alkaline medium, and found out that the reaction occurs in similar potential intervals on Ni and on Pt electrodes, below *ca.* E = 0.2 V *vs* RHE. Considering formation of H_{upd} on Pt in this potential window, they inferred the existence of adsorbed hydrogen on the surface of Ni under these conditions as well. The authors of Ref. [333] demonstrated that prior oxidation of the Ni electrode surface at T = 400°C leads to complete suppression of p-nitroaniline hydrogenation, and attributed this to the blocking of hydrogen adsorption by the formed passive layer of NiO, which cannot be electrochemically reduced due to insufficient electronic conductivity. In addition, several authors documented intersection (named "isopotential") points in the forward and backward scans of CVs recorded until different positive potential limits (for example, Hu and Wen [333], Katic *et al.* [345]), which they attributed to α-$Ni(OH)_2$ formation and hydrogen adsorption/desorption occurring in the same potential interval (above E = 0 V *vs* RHE) and competing for the Ni surface sites. This agrees with the adsorption isotherms calculated by Pshenichnikov for hydrogen and oxygen adsorption in the gas phase [334]. Finally, Oshchepkov [186,289,290,311] studied the HOR on Ni by combining electrochemical measurements with microkinetic modelling, and concluded that the existence of H_{upd} on Ni is the most consistent explanation of a large amount of experimental data for the HOR on Ni electrodes subjected to various surface treatments (reductive *vs* oxidative).

Along with experimental works, significant number of computational studies have explored the adsorption of H, OH, O and other species on Ni. Whereas the binding energy values computed using DFT and reported by different research groups, vary depending on the density functional used for the calculations, some general trends can be identified. Firstly, it is commonly accepted that oxygen atoms (O_{ad}) adsorb on Ni much stronger on nickel than hydrogen atoms [325,346,347]. Ranging the H and OH

binding energies is less evident: some studies report stronger adsorption of OH compared to H, others present similar H and OH adsorption. For example, the binding energy values computed by Bai *et al.* [347] for H and OH on different sites on Ni(111) using self-consistent GGAPW91 functional (at a ¼ monolayer coverage) are: H (−2.89 (fcc); −2.88 (hcp)); OH (−2.47 (top); −2.92 (bridge); −3.01 (fcc); −2.91 (hcp) eV); these figures highlight that the binding energy strongly depends on the type of surface site, and that H and OH adsorption energies are comparable. Taylor e*t al.* [348] performed *ab initio* calculations in order to probe the influence of water and surface charges on the hydrogen adsorption on Ni(111). Based on calculated Gibbs energies of adsorption, they constructed a potential-pH diagram for the hydrogen-Ni(111) system, which corroborates hydrogen adsorption on Ni above E = 0 V *vs* RHE (hence, H_{upd}), and suggests that equilibrium potential of the H_{ad}/H^+ couple shifts positive with pH. Besides, according to theoretical calculations, adsorption energies for H_{ad} and OH_{ad} demonstrate different coverage dependence. For Greeley and Mavrikakis, the strength of H_{ad} to Ni(111) only slightly decreases from 0 to 1 monolayer coverage [349], while Juares *et al.* [346] found that, because of their high negative charge, OH_{ad} on Ni strongly repel each other, leading to a significant decrease of the adsorption strength with the coverage. So, under certain conditions, adsorption of hydrogen may become more favorable than for OH_{ad} species. Also, according to DFT calculations [350,351], the state of the Ni surface (namely the presence of adsorbed oxygen in the vicinity of metallic Ni sites) largely affects the adsorption energy of the H_{ad}. This conclusion is also supported by microkinetic modelling [186,289,290] of the HOR on Ni electrodes, as discussed in the following sections.

In the end, if one acknowledges the existence of H_{upd} on Ni in the potential interval from E = 0 to 0.2 V *vs* RHE, the anodic CV peak at *ca.* E = 0.3 V *vs* RHE in Figure IV.1a should not be interpreted as α-$Ni(OH)_2$ formation on free Ni surface sites but rather as H_{upd} replacement by OH_{ad} followed by the conversion of the latter into a surface α-$Ni(OH)_2$ layer (equations 4.2 and 4.3). This parallels the case of hydrogen UPD on Pt, a supposedly well-understood phenomenon until recently: new evidence from electrochemical experiments, DFT calculations and surface science studies (see Janik *et al.* [352] and references therein) confirms that certain peaks observed in the potential interval of hydrogen UPD do not correspond to H_{upd}, but rather to the replacement of adsorbed H atoms by OH on low-coordinated Pt sites.

- α-/β-$Ni(OH)_2$ and $Ni(OH)_2$/NiOOH transition

In the high-potential region, increasing the potential from E = 0.5 to 1.2 V *vs* RHE leads to dehydration of α-$Ni(OH)_2$ and its irreversible transformation into β-$Ni(OH)_2$, along with the formation and/or thickening of the NiO [306,307,309,310,313,317,329,353]. Formation of a stable β-$Ni(OH)_2$ layer leads to an attenuation of the cathodic peak in

the low-potential region (Figure IV.1a), firstly followed by its shift towards more negative values [308,319,354], and finally, once β-$Ni(OH)_2$ fully covers the electrode surface (red curve on Figure IV.1a), complete disappearance of the peak in the low-potential region [306,336,338]. Above E = 1.2 V *vs* RHE, α/β-$Ni(OH)_2$ further transforms into γ/β-NiOOH, resulting in the emergence of an anodic peak around E = 1.4 V *vs* RHE (Figure IV. 1a). The corresponding cathodic peak appears around E = 1.3 V *vs* RHE and at low sweep rates is often split into two components, owing to the presence of two distinct (β and γ) phases of the surface NiOOH oxyhydroxide [355–357]. Above E = 1.5 V *vs* RHE, the surface of the Ni electrode is covered by NiOOH and NiO, as evidenced by *in situ* Raman spectroscopy [287,353,358–360] and both *ex* and *in situ* XPS measurements [331,361,362]. The crystal plane-orientation dependence of Ni oxidation in the high-potential region has not been observed, likely because of the fast structure disordering at high potentials [303,323,324].

- Activity of Ni towards the hydrogen reactions

Literature data regarding the kinetics of the HOR on Ni (and HER at low cathodic overpotentials) is very contradictory [190,304,305,322,344,363–366], which may be attributed to the strong influence of the electrode pre-treatment and thus the state of the surface on the reaction kinetics [186,289,290,367,368]. In the vicinity of the equilibrium potential, a purposely-reduced metallic Ni electrode (see black solid trace in Figure IV.2b) shows a very small HOR current, which then increases until it peaks at *ca.* E = 0.25 V *vs* RHE (*i.e.* close to the anodic peak position observed under N_2 atmosphere on Figure IV.2a), and then decays again. Oshchepkov *et al.* attributed this low activity of metallic Ni to the slow kinetics of the Volmer step, likely due to the strong adsorption of H_{ad} species already mentioned above [186,289,369,370]. Indeed, according to the results of kinetic modelling, the surface coverage of H_{ad} (θ_H) on metallic Ni is high under N_2 atmosphere, and further increases in the presence of H_2, adsorbed hydrogen atoms dominating on the surface until *ca.* E = 0.2 V *vs* RHE (Figures IV.2a and 2b, for details a reader is referred to Ref. [289]). The obtained data agree with the hydrogen adsorption isotherm (in the gas phase) reported by Pshenichnikov [334]. Besides, according to Taylor *et al.* at pH = 13 the equilibrium potential for H_{ad}/H^+ is similar to 0.2 V, which confirms the data of Figure IV.2a [348]. At higher potential values, formation of α-$Ni(OH)_2$, which proceeds through OH adsorption (see θ_{OH} and $\theta_{(OH)2}$ traces in Figures IV.2), results in blocking of the Ni active sites [186,308,325,351]. Thus, considering the kinetics of the HOR on Ni electrocatalysts also requires accounting for the processes of the Ni surface hydroxide formation and reduction, since they occur in the same potential range as the HOR. Besides, the coexistence of both Ni-H_{ad} and Ni-OH_{ad} species on the electrode surface might result in their recombination

with the formation of water through the following reaction ('bifunctional' mechanism)[368]:

$$Ni\text{-}H_{ad} + Ni\text{-}OH_{ad} \rightleftarrows H_2O + 2\ Ni \qquad \text{(equation 4.4)}$$

The contribution of the latter step to the HOR mechanism was shown unlikely on a pure metallic Ni surface, because of the very strong adsorption of H_{ad} on Ni and thus the high activation barrier for the recombination reaction [311]. Nevertheless, the recombination step might contribute to the HOR on bimetallic NiM electrocatalysts and/or partially-oxidized Ni electrodes, when the adsorption energies of H_{ad} and OH_{ad} are weakened [290,311].

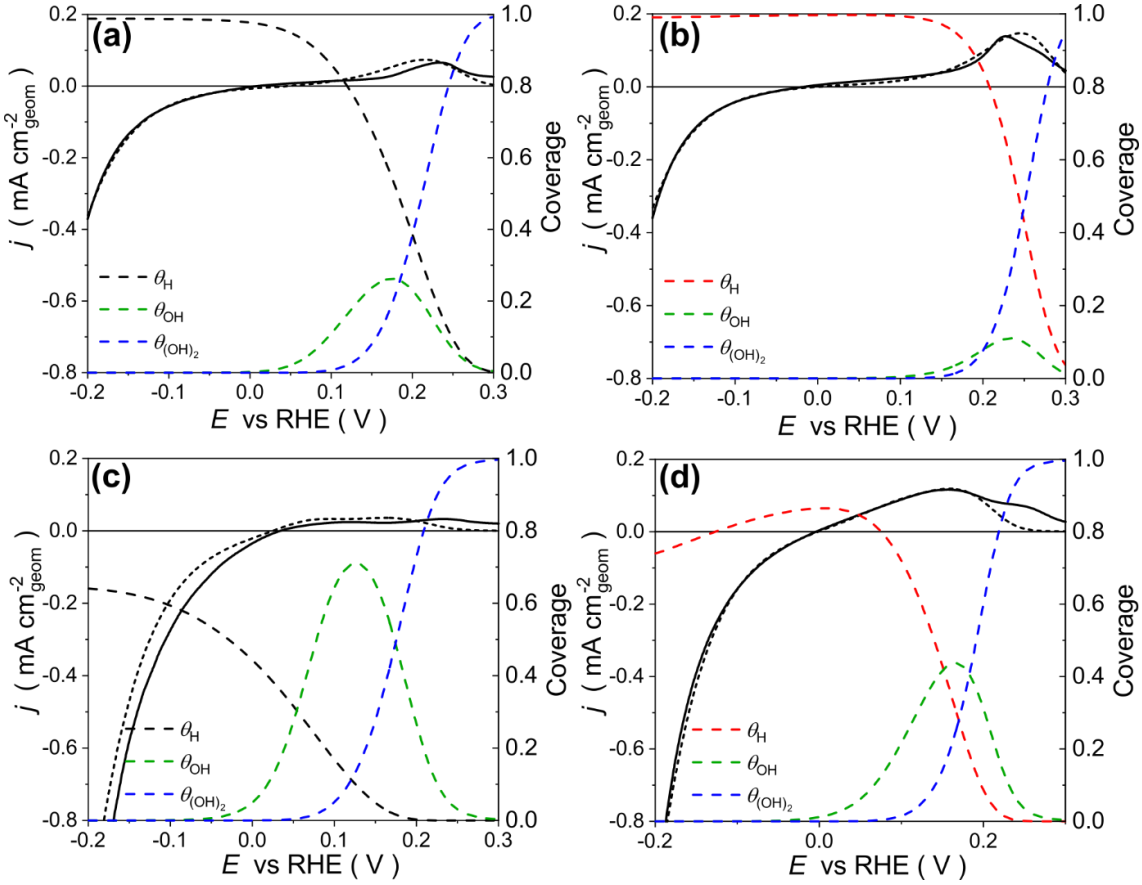

Figure IV.2. Experimental anodic scans of CVs (black solid curves) for (a, b) metallic and (c, d) partially oxidized polycrystalline Ni rod in (a, c) N_2- and (b, d) H_2-saturated 0.1 mol.L^{-1} NaOH at v_s = 5 mV.s^{-1} and T = 25°C. Dashed curves represent the simulated data of either CVs or coverage of the electrode surface by various adsorbates. Note that only Ni metal sites free from stable oxide species (NiOx surface coverage is estimated to be *ca.* 14 %) were considered for calculations. Data are replotted from Ref. [289] with permission from Elsevier.

The catalytic activity of metallic ('reduced') Ni electrodes being rather low, several approaches are currently proposed to improve the performance of Ni and Ni-based electrocatalysts in the HOR. It is possible to target (i) the decrease of the Ni-H_{ad} binding

energy and hence the increase of the Volmer step kinetics, (ii) the increase of the kinetics of the recombination step, or (iii) the modification of the oxidation propensity of Ni surface, thus extending the operating potential window of an AEMFC with a Ni anode.

IV.1.2 Activity of polycrystalline Ni for the BOR

The activity of Ni towards the BOR has been investigated since 1962 [371] and has been largely debated in the literature in recent years. Ni was commonly reported as poor electrode material with slow reaction kinetics [145,372,373]. Nevertheless, some studies presented promising results in particular regarding a low onset potential [374–376]. Most of the time, the state of surface of the Ni-based catalysts was however not investigated or even ignored. However, as presented above (for the hydrogen reactions) it can notably modify the electrochemical behavior of such materials. With the knowledge brought by Oshchepkov *et al.* regarding the hydrogen reactions and about the BOR on model surfaces (Chapter III), some hypotheses can already be made. As explained for noble surfaces, the onset of the BOR is a mixed potential resulting from the competition between the BOR, the HOR and the HER; this competition explains why Pt cannot exhibit onset potential below ca. -100 mV *vs* RHE (Pt is a very good HER/HOR catalyst, and its electrode potential is largely determined by hydrogen reactions as explained in Chapter III). The HER/HOR activity of Ni depends, however, on it oxidation state: a purely metallic surface presents really poor hydrogen evolution/oxidation kinetics. Some preliminary DFT calculations made by Rostamikia *et al.* predict that the adsorption of BH_4^- on Ni should occur dissociatively (similarly as on Pt) [216] and therefore the BOR kinetics should be fast at low potentials. Combined together, these two properties should lead to very low BOR onset potentials, provided the state of surface of the Ni electrode is indeed controlled as "reduced".

In order to confirm this hypothesis a polycrystalline Ni rod was used as an electrode in the RDE configuration, in similar conditions as the PGM model surfaces presented in Chapter III. The 5 mm (0.196 cm^2) rod was polished prior to each measurement to obtain a metallic surface. The experimental details to obtain such surface as well as different oxidation procedures applied in order to vary the oxidation state of the electrode are described in the section "II.1.2 Electrodes and catalyst inks preparation". The typical CVs obtained in supporting electrolyte of the polished and EC-oxidized Ni rod surfaces are presented on Figure IV.3a. The redox transition peak observed around E = 0.25 V *vs* RHE confirms the metallic state of the fresh electrode (black curve) and shows that even after partial oxidation (red curve), a fair amount of the surface is still metallic. The electrochemical surface area (ECSA) was calculated for each electrode following the

procedure detailed in section "II.2.2. Electrochemical Surface Area Determination". The ECSA of the fresh electrode is S_{Ni} = 0.56 cm² and $S_{EC\text{-}ox}$ = 0.54 cm² for the partially-oxidized one, showing an overall similar surface area. This is not expected since the ECSA measurement is supposed to only give the surface of metallic sites. For partially oxidized electrodes, this ECSA determination technique might not be adapted: a significant current in the 0 V < E < 0.2 V *vs* RHE potential region is measured and integrated in the surface calculation (see section "II.2.2 Electrochemical Surface Area Determination" for more details). Because this current is a result of hydrogen desorption/oxidation generated during the HER, the resulting ECSA calculated will be overestimated. The decrease of the transition peak observed around E = 0.25 V *vs* RHE confirms the decrease of the number of metallic site after the partial oxidation.

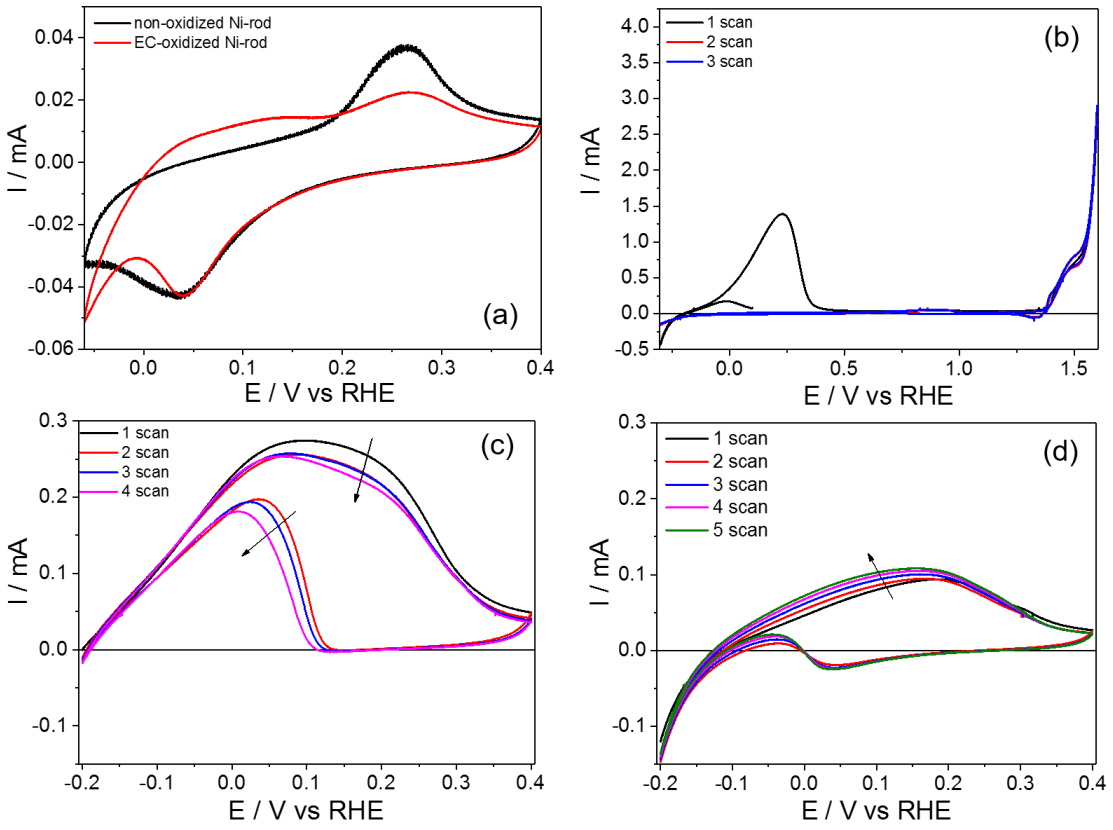

Figure IV.3. (a) CV in supporting electrolyte (1 M NaOH) in the low-potential region for non-oxidized and EC-oxidized Ni. (b) Irreversible oxidation of Ni in the "full" potential region in the presence of 50 mM $NaBH_4$. BOR characterizations (5 mM $NaBH_4$) for the (c) non-oxidized (metallic) Ni and (d) EC-oxidized Ni rod, ω = 0 rpm, v_s = 20 mV.s^{-1}.

Again, the better HER activity of the partially-oxidized surface can be observed in supporting electrolyte (Figure IV.3a): the reaction starts just below E = 0 V *vs* RHE, while only a pseudo-capacitive current is observed on the metallic surface at E = -0.11 V *vs* RHE. Figure IV.3b demonstrates the drastic effect of a strong oxidation of the Ni surface on the BOR kinetics, and explains why the potential range should be limited to ca. 0.4 V vs. RHE when dealing with Ni electrodes. While in BOR conditions, a faradic

current is observed already at potentials below 0 V *vs* RHE on the first anodic scan, when the α-$Ni(OH)_2$ layer formation begins, the current starts to drop and reaches zero once this layer is complete. At higher potential the surface α-$Ni(OH)_2$ layer transforms into a β-$Ni(OH)_2$ one and after E = 1.2 V *vs* RHE into a reversible γ/β-NiOOH form. This surface layer shows activity towards the BOR, but is unfortunately only stable at high potential, being irrelevant for a DBFC application. Because no metallic or α-$Ni(OH)_2$ species are present on the surface at this potential, no reactivation is observed at low potential for the cathodic sweep and for all followings scans. This is the first confirmation that the metallic phase of Ni is more active for the BOR than a strongly-oxidized one.

When the potential is maintained in the "low potential region" (from -0.2 V to 0.4 V *vs* RHE), oxidation of the Ni surface is reversible and repeated scans can be measured on either metallic or partially oxidized Ni electrode in supporting electrolyte (Figure IV.3a), which is not the case when the potential is swept to the high potential domain (Figure IV.3b). The metallic Ni electrode (non-oxidized Ni, Figure IV.3c) displays an astonishingly low BOR onset potential of -0.2 V *vs* RHE, confirming the hypothesis presented above. An equally important factor is the kinetics of reaction observed with this surface: a large faradic current is already observed below E = 0 V *vs* RHE, in opposition with noble metals presenting higher onset potentials (see Chapter III). A limiting current seems to appear at potentials slightly higher (*ca.* E = 0.1 V *vs* RHE), but quickly falls when the α-$Ni(OH)_2$ layer starts to form. The partially-oxidized surface (EC-oxidized Ni, Figure IV.3d) displays a significantly lower BOR activity with a higher onset potential, attributed to the better HER activity (similar to the case of Pt, whose high HOR/HER activity is responsible for the high BOR onset potential), and a maximum current two times smaller. This is explained by the fact that less metallic sites are available at the surface as demonstrated by the CV in supporting electrolyte (Figure IV.3a) where the α-$Ni(OH)_2$ peak is also around two times smaller. This experiment confirms that Ni is a good BOR catalyst, but only when its state of surface is precisely controlled, the slightest oxidation resulting in an irreversible performance loss.

The metallic Ni surface is subjected to a non-negligible BOR current decrease on both ongoing scans at each cycle iteration (Figure IV.3c). This could indicate either that scanning up to 0.4 V *vs* RHE results in a slight irreversible oxidation or that some intermediate BOR species start to poison the surface. On the contrary, for the partially-oxidized electrode (Figure IV.3d), the current slightly increases after each cycle, and the onset potential decreases in the meantime. This indicates that the strongly-reducing borohydride solution actually helps to depassivate (at least partly) the electrode. By looking at these two sets of CVs, it is difficult to answer if the current decrease for the metallic Ni electrode is caused by oxidation of the Ni surface, poisoning or maybe both

at the same time. The influence of the upper potential limit has been evaluated in order to understand the behavior of the metallic Ni electrode in BOR conditions. To control the mass-transport rate, the rotation of the RDE was set to ω = 1600 rpm. Figure IV.4 displays CVs obtained with the upper potential limit increased from 0.1 V to 0.4 V *vs* RHE in 0.1 V increments. When the potential scan is reversed at 0.1 V *vs* RHE (Figure IV.4a) the overall current decreases at each cycle, even more significantly than during the previous experiment. After only 5 cycles a significant 50% loss is observed. The onset potential is not affected, though, meaning that the surface remains metallic (in this potential region, Ni-oxide formation is unlikely). Overall, this means that a large poisoning of the surface occurs: the BOR is not complete, so intermediate species are progressively blocking the active sites.

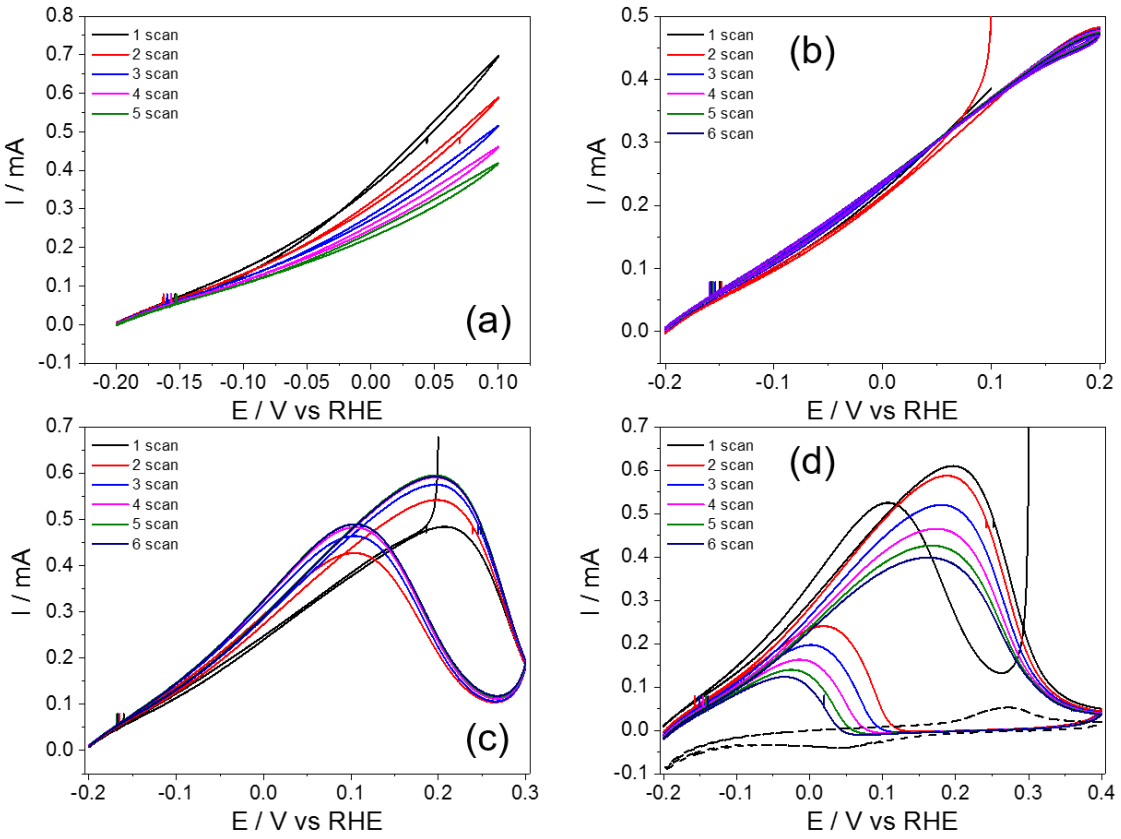

Figure IV.4. CVs of freshly polished Ni-rod (5 mm) in 1 M NaOH + 5 mM $NaBH_4$ with increasing upper potential limit. N_2 saturated electrolytes, room temperature, ω = 1600 rpm, v_s = 20 $mV.s^{-1}$. The dotted trace in (d) is the CV of the metallic Ni-rod in supporting electrolyte.

The CVs scanned up to 0.2 V *vs* RHE (Figure IV.4b) are essentially overlapped, except at the highest potential region, in which the current starts to (very slightly) decrease at each cycle, probably owing to the beginning of α-$Ni(OH)_2$ formation; increasing further the upper potential should then result in larger α-$Ni(OH)_2$ formation and further current loss. However, when cycling up to *E* = 0.3 V *vs* RHE (Figure IV.4c) the current

surprisingly increases and reaches a stable state after the third cycle. It can be explained by the fact that the same electrode was used successively for each measurement: over the cycles, the surface accumulated adsorbed intermediate BOR species (which could not be oxidized at low potential) and scanning to higher potentials enabled their oxidation, freeing the electrode surface. The positive effect is however only transient; if the potential is increased further to E = 0.4 V *vs* RHE, the decrease of the BOR current at each cycle observed on Figure IV.3 is again witnessed (Figure IV.4d). Moreover, the onset potential increases at the same time, suggesting a partial oxidation of the electrode; this partial oxidation does not prevent poisoning of the surface, which still occurs when the upper potential is maintained "too low" and the reaction is not complete, leaving intermediate species blocking the active sites. The CV in supporting electrolyte superposed with the BOR one (Figure IV. 4d) allows to clearly see that the current starts to drop as soon as the oxidation of the surface begins (E = 0.2 V *vs* RHE) and that the current tends to drop to almost 0 once the full α-$Ni(OH)_2$ layer is formed.

The poisoning effects can also be investigated by increasing the concentration of borohydride. Figure IV.5 presents the BOR activity of a metallic Ni-rod for $NaBH_4$ concentration varying from 0.5 mM to 500 mM with the same increasing upper potential limits. Only the fifth scan is represented for each concentration. First of all, the onset potential significantly decreases when the $NaBH_4$ concentration is increased from 0.5 to 5 mM (Figure IV.5a). For higher concentrations, it remains the same because BH_4^- adsorption becomes limited by the number of active sites on the electrode surface (polished bulk electrode). However, the concentration is really impactful on the reaction kinetics (BOR current). When the upper potential limit is insufficient to oxidize the adsorbed BOR intermediates (upper potential limit of 0.1 V *vs* RHE, Figure IV.5a), the current obtained at 50 mM is similar to that at 5 mM until E = -0.05 V *vs* RHE is reached, because of a significant poisoning by intermediate species that are not stripped fast enough at 0.1 V *vs* RHE. At higher upper potential limit, the current is less limited for E < 0 V *vs* RHE, because the surface is now blocked to a lesser extent (in each cycle, these adsorbed intermediates can be at least partially stripped for E > 0.1 V *vs* RHE, the stripping being more efficient when the upper potential limit increases). However, if the concentration is increased to DBFC operation values like 500 mM, the amount of species adsorbed on the surface increases sharply, and their stripping becomes incomplete within the surveyed potential window, which in the end limits the BOR. In consequence, a smaller current is recorded for 500 mM $NaBH_4$ than measured at 50 mM $NaBH_4$. It is also possible to observe on Figure IV.5d that this severe poisoning delays α-$Ni(OH)_2$ formation: the peak current is reached at a potential 50 mV higher than with smaller concentration. However, this delay, induced by the important coverage of the surface by adsorbed species, is also accompanied by slower charge transfer kinetics, resulting in an overall 50 mV loss in terms of voltage. This could be significant in a

DBFC, and a highly developed surface area must be used in order to limit this poisoning effect. In any case, with a smooth Ni surface like here (small roughness), 50 mM seems to be close to the optimal concentration for an efficient BOR; one can posit that the optimal concentration scales with the roughness of the Ni electrode, high roughness electrodes likely being capable to valorize larger $NaBH_4$ concentrations. This hypothesis will be tested in the forthcoming sections of this chapter.

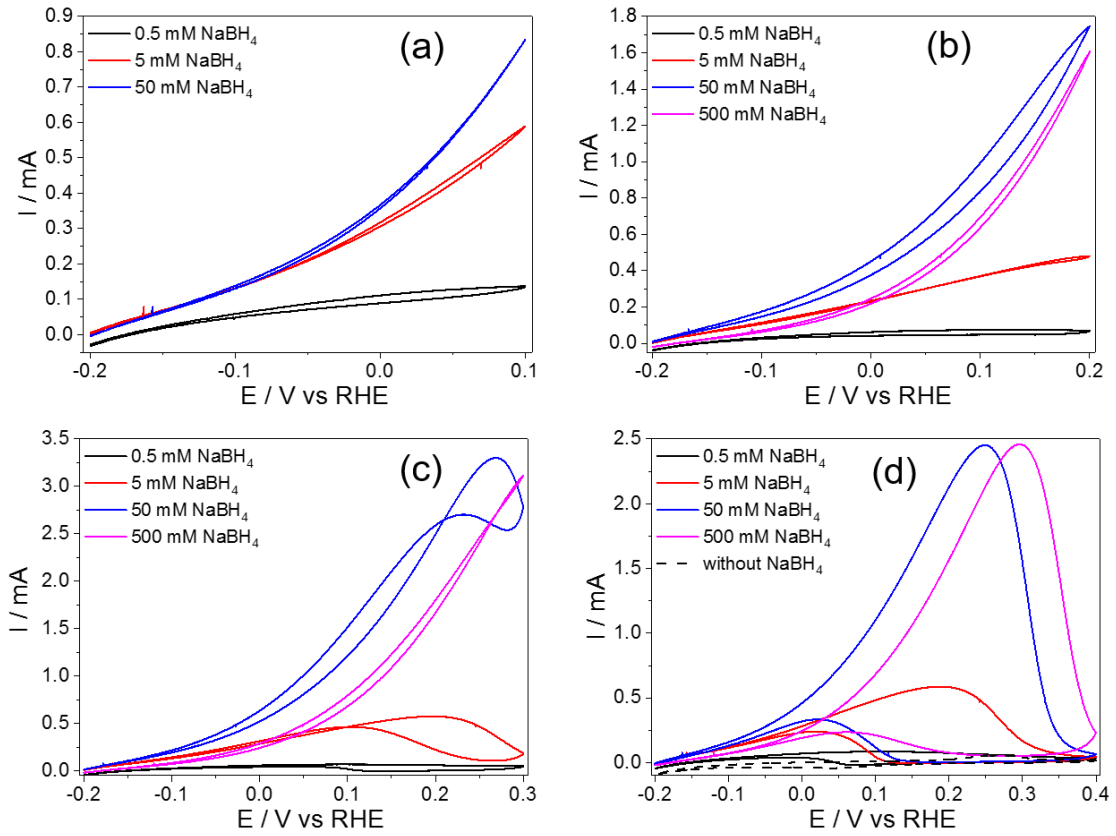

Figure IV.5. CVs of freshly polished Ni-rod (5 mm) with increasing upper potential and $NaBH_4$ concentration from 0.5 mM to 500 mM in 1 M NaOH. N_2 saturated electrolytes, room temperature, ω = 1600 rpm, v_s = 20 $mV.s^{-1}$.

To investigate further the reaction kinetics, the influence of the rotation rate was varied for 5 mM and 50 mM borohydride concentration (Figure IV.6). The rotation rate values were set in order to obtain a constant current increase and therefore to test whether the reaction is only limited by mass-transport and follows Levich's law (a constant plateau should appear for each rotation rate). A second cycle is measured at 0 rpm at the end of the measurement to check if the surface changed. At 5 mM (Figure IV.6a), when the convection is forced at 400 rpm, the current significantly increases compared to a static electrode (0 rpm); however, every time the rotation rate increases (900, 1600 then 2500 rpm), the current drops, which is unexpected if the reaction is mass-transport limited by diffusion-convection in the bulk electrolyte. Here, it can be postulated that the upper scan limit for this measurement is too low to enable complete stripping of BOR

intermediates (during the potential scan); thus, the reaction is not complete, reaction intermediates gradually block the electrode surface and the number of active sites (limited for the metallic Ni-rod) gradually decreases in the course of the measurement. It is also likely that the surface poisoning scales with the rotation rate: the more BH_4^- species are brought to the surface (at high rotation rates) the stronger the surface blocking by BOR intermediates. Within this hypothesis, it is no surprise that the same effect is observed at higher $NaBH_4$ concentration (Figure IV.6b), but in an enhanced manner, because of a higher coverage by the poisoning BOR intermediates at the electrode surface. The reaction then becomes completely limited by the charge-transfer kinetics (and hence the number of active sites on the electrode surface): as a result, the current increase measured with forced convection is not significantly higher than in a stagnant electrode configuration.

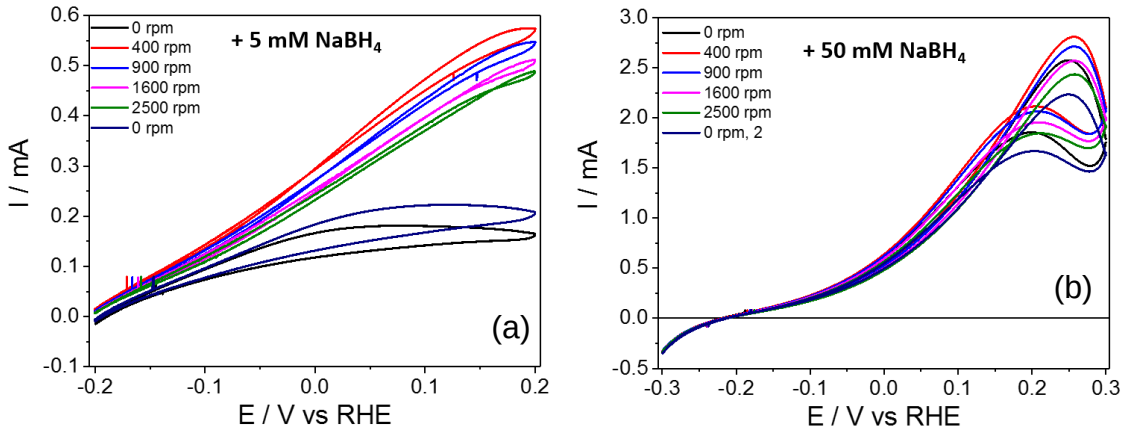

Figure IV.6. CVs of freshly polished Ni-rod (5 mm) with increasing rotation rate of the RDE in (a) 1 M NaOH + 5 mM $NaBH_4$ and (b) 1 M NaOH + 50 mM $NaBH_4$. v_s = 20 $mV.s^{-1}$ N_2 saturated electrolytes, room temperature.

Overall, the metallic Ni-rod proved to be an interesting model material to test the activity of metallic Ni for the BOR. Promising BOR activity is measured, especially in terms of the onset potential. The reaction rate increases noticeably above the onset potential and significant current is measured already below 0 V *vs* RHE; this is a positive behavior versus the case of Pd electrodes, where the onset potential is low but the reaction rate remains low below 0.2 V *vs* RHE (see Chapter III). The use of metallic Ni proved to be the key to reach such high activity using Ni surfaces; this finding explains why controversies are reported in the literature regarding the BOR activity of Ni surfaces. However, it was shown that maintaining this metallic state requires a precise control of the applied anodic potential and that even a slight oxidation immediately results in a noticeable activity loss. The kinetics of the reaction also appeared strongly limiting, because the number of active sites is quite limited for a smooth-polished 5 mm polycrystalline rod. Using highly developed surface area catalyst materials such as Ni-based nanoparticles supported on carbon supports will surely be key in reaching higher

apparent activities, especially at larger $NaBH_4$ concentrations. Such materials are studied in the following section.

IV.2 Bimetallic "Ni_xM" BOR catalysts

The issue encountered with commercial Ni-based electrocatalysts is their synthesis method, which often requires a passivating step at fairly high temperature in ambient atmosphere; this results in an irreversible oxide formation, which cannot be reduced electrochemically. Such step shall therefore make the materials inefficient as BOR catalysts, as it was just demonstrated that a purely metallic state is required to reach a good BOR activity.

Table IV.1: List of bimetallic Ni_xM catalysts tested for the BOR

Catalysts	Group	Year synthesized	Initial purpose	Ref
Ni_3Pd/KB	UNM	2016	Ammonia Borane Oxidation	[195]
Ni_3Ag/KB				
Ni_3Co/KB				
Ni_3Mo/KB	UNM	2015	Hydrazine Oxidation	[196]
Ni/C	Technion	2019	HOR	[283]
Ni_3Co/C				
Ni_3Fe/C				
Ni_3Cu/C				
Ni_7Co/C	Technion	2019	BOR	/
Ni_7Fe/C				
Ni_7Cu/C				

Alloying is one of the most commonly used methods to modify the physicochemical properties of a metal. In this section, bimetallic NiM catalysts are presented as potential catalysts for the BOR. Different co-elements are considered, as they may influence the propensity of Ni to depassivation in alkaline medium and therefore increase its overall activity to oxidize borohydride at low potential. Two different sets of catalysts were synthetized by the group of Prof. Atanassov (formerly University of New Mexico (UNM), now University of California, Irvine, USA) and Prof. Dekel (Technion, Israel) at different periods and using different co-elements. All the catalysts tested as well as their characteristics are presented in Table IV.1. The catalysts of UNM were synthetized several years ago and presented promising results towards the borane oxidation as mentioned in Chapter III [195], but also towards the hydrazine oxidation for Ni_xMo [196]. The set synthesized in Technion is composed of Ni_3M catalysts initially made for

HOR and Ni_7M (with the same co-elements) made specifically for this study in order to observe the influence of the co-element in different proportions. Figure IV.7 presents the TEM images of the fresh catalysts synthesized at Technion. All these catalysts were differentiated into two different morphologies: Ni/C, Ni_7Co/C, Ni_3Cu/C, Ni_7Cu/C presented NPs of around 20 nm diameter and a well-defined core-shell structure; Ni_3Co/C, Ni_3Fe/C, Ni_7Fe/C presented single-phased NPs, less homogenous in size with two populations: 20 nm and a few nm.

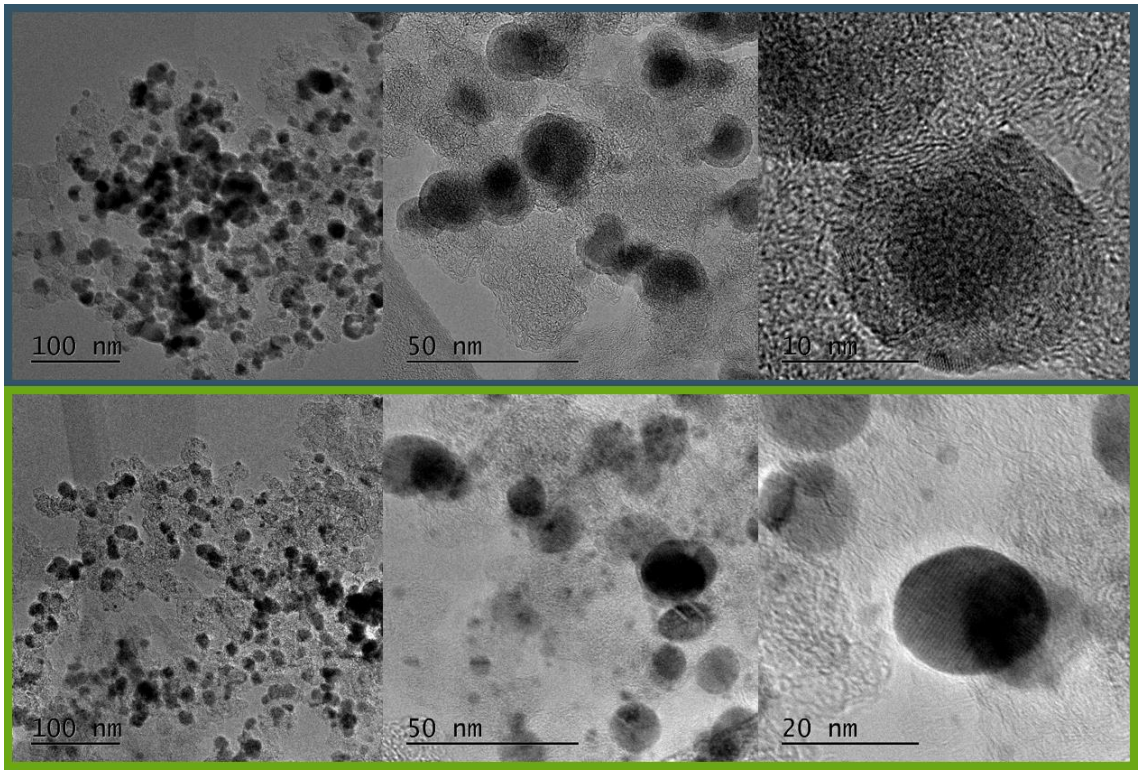

Figure IV.7. TEM images at different magnification of Ni_7Co (blue border) and Ni_3Fe (green border) revealing two different morphologies: core-shell and uniform nanoparticles.

IV.2.1

BOR activity of Ni_xM catalysts

The procedure to obtain RDE thin films using these Ni-based materials is detailed in the section 'II.2. Electrodes and catalysts ink preparation" as well as the activation step required to reduce as much as possible the surface of the nanoparticles. All electrodes were prepared with a metal loading of L_{metal} = 100 µg.cm^{-2}. In order to quickly establish the BOR activity of each catalyst, CVs were performed after conditioning in 50 mM $NaBH_4$, and using the [-0.2, 0.3] V *vs* RHE potential limit. To investigate the reaction kinetics, the forced mass-transport was changed following a sequence of six different rotation rates: 400 rpm, 900 rpm, 1600 rpm, 2500 rpm, 0 rpm, 400 rpm. This cycle was chosen to respect a linear current increase between each rotation rate from 400 to 2500 rpm, as mentioned in the previous section. The second 400 rpm is used as a marker to

control the possible change of the surface state of the catalyst in the course of the measurement, and therefore to check the reproducibility of the characterization. In a first step, the catalysts synthetized at UNM [195,196] were investigated and the obtained CVs are represented in Figure IV.8. Ni_3Pd/KB and Ni_3Ag/KB present relatively high onset potential (E > -0.1 V *vs* RHE), implying already that the surface might mainly expose oxidized nickel, in agreement with their rather good HER activity (surface enrichment in Pd for the former catalyst could also be an explanation, but not Ag enrichment for the latter – unlike Pd, Ag is a poor HER/HOR catalyst). Ni_3Mo/KB presents a lower onset potential around -150 mV *vs* RHE. This indicates a more reduced state of the Ni surface. However, when the rotation rate is increased, this potential also increases significantly and reaches E = -80 mV *vs* RHE for ω = 2500 rpm. This indicates that the electrode might be poisoned when too many BH_4^- species are brought to the surface. Ni_3Co/KB presents a similar onset potential but does not change with the rotation rate.

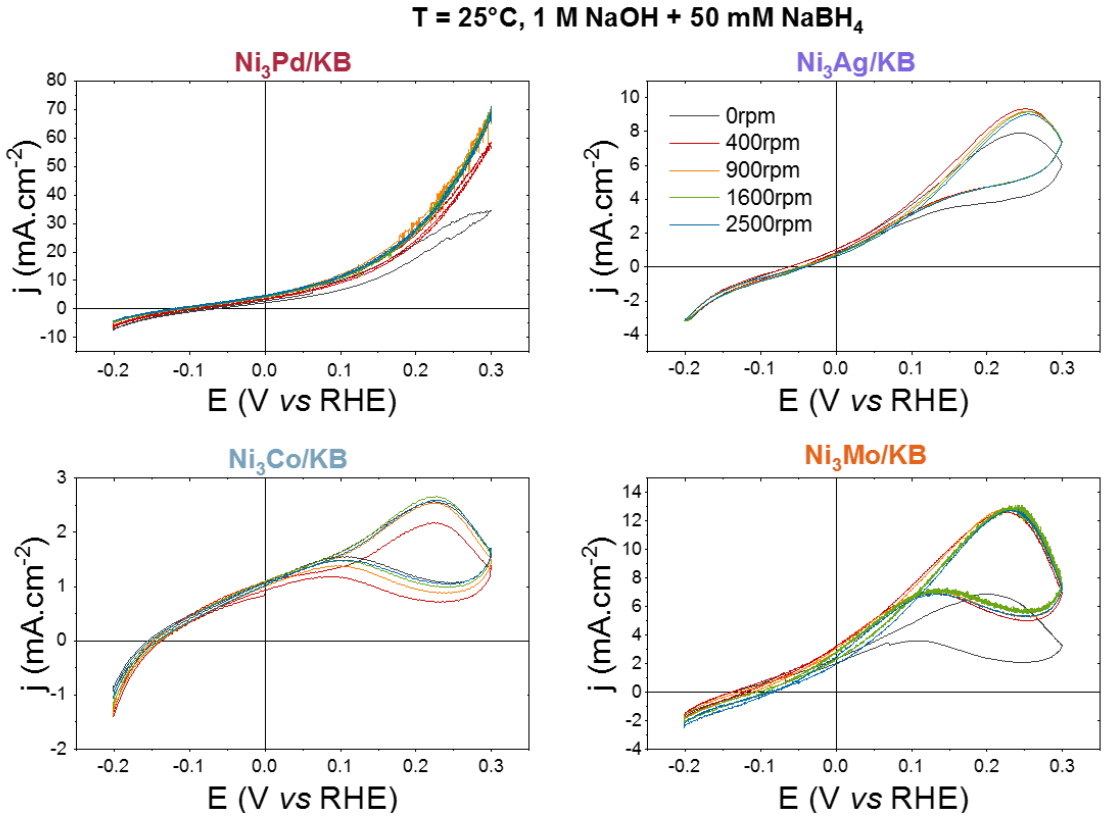

Figure IV.8. CVs of Ni3M/KB catalysts from UNM [195,196] at increasing rotation rate of the RDE in BOR conditions: 1 M NaOH + 50 mM $NaBH_4$, v_s = 20 $mV.s^{-1}$, room temperature, Ar-saturated electrolyte, metal loading: L_{metal} = 100 $\mu g.cm^{-2}$.

Regarding the reaction kinetics, the current density for the Ni_3Co/KB catalyst remains really low even at 0.2 V *vs* RHE, where only 2 $mA.cm^{-2}_{geo}$ is reached at 0 rpm. It is the lowest current of the four materials studied, and increasing the rotation rate only results in a 0.5 $mA.cm^{-2}_{geo}$ increase. Moreover, the current does not increase with the rotation

rate, which denotes a strongly limiting charge-transfer kinetics. These limitations are observed on all four materials, confirming the oxidized state of the catalysts (which is expected, owing to their long storage period, Table IV.1). Compared to other samples, Ni_3Pd/KB exhibits a high current density at potentials above 0 V *vs* RHE. This activity is mainly attributed to the contribution of Pd, this noble material only being significantly active for the BOR/HOR at positive potentials on the RHE scale.

Alloying noble metals with non-noble counterparts is a very common way to reduce the amount of the former while keeping their advantageous properties [269,377,378]. However, the small fraction of Pd in the Ni_3Pd/KB material does not prevent limitations by the reaction kinetics. Moreover, the main goal of this section and of the PhD was to move away from PGM and other rare metals. Ni_3Mo/KB presents the second best kinetics, but apparently suffers from significant poisoning at high rotation rate, a clear drawback for the envisaged application (DBFCs).

In a second time, the materials from Technion were tested in similar conditions in order to compare their activity towards the BOR (Figure IV.9). Overall, they all present a better onset potential around -200 mV *vs* RHE, except for Ni_7Cu/C for which the onset is 50 mV higher. The current density is still strongly limited by the reaction kinetics on all catalysts, since almost no current increase is observed with the rotation rate. The CVs of Ni_7Fe/C could lead us to think that the kinetics are not limiting as much because a clear current increase is observed for increasing rotation rates. However, the highest current is reached at the end of the cycle at a rotation rate of only ω = 400 rpm suggesting irreversible transformation of the catalyst during the test. This highlights a new behavior not observed on the previous set of catalysts (Ni_3M from UNM): the surface keeps gaining in activity, even though the activation step was applied before the RDE study. After the 20 activation cycles, the current was stable, meaning that the procedure used for the BOR characterization allowed to reduce even more the surface. The main difference between these two measurements is that between each rotation rate the electrode is let at OCP for 10 s. This effect is likely brought to light with this material, because the current density is really low, suggesting a more pronounced initial oxidation state than for the other materials. This residual activation upon BOR can actually be observed on all catalysts from Technion (although to a smaller extent) except for Ni_3Fe/C. For Ni_3Co/C and Ni_7/Cu, it is clearer with the second 400 rpm cycle, that presents the highest current, whereas for the other catalysts, the current improved compared to the first scan but was still smaller than the ones obtained at faster rotation rate. In general, all these materials exhibit a relatively low activity towards the BOR, but might be less oxidized than the previous set of catalysts (from UNM). This hypothesis is based on their lower onset potential (in agreement with their shorter

storage period prior use). However, only Ni_7Co/C and Ni_7Cu/C exhibit an overall current density slightly higher or similar (respectively) than Ni_3Mo/KB.

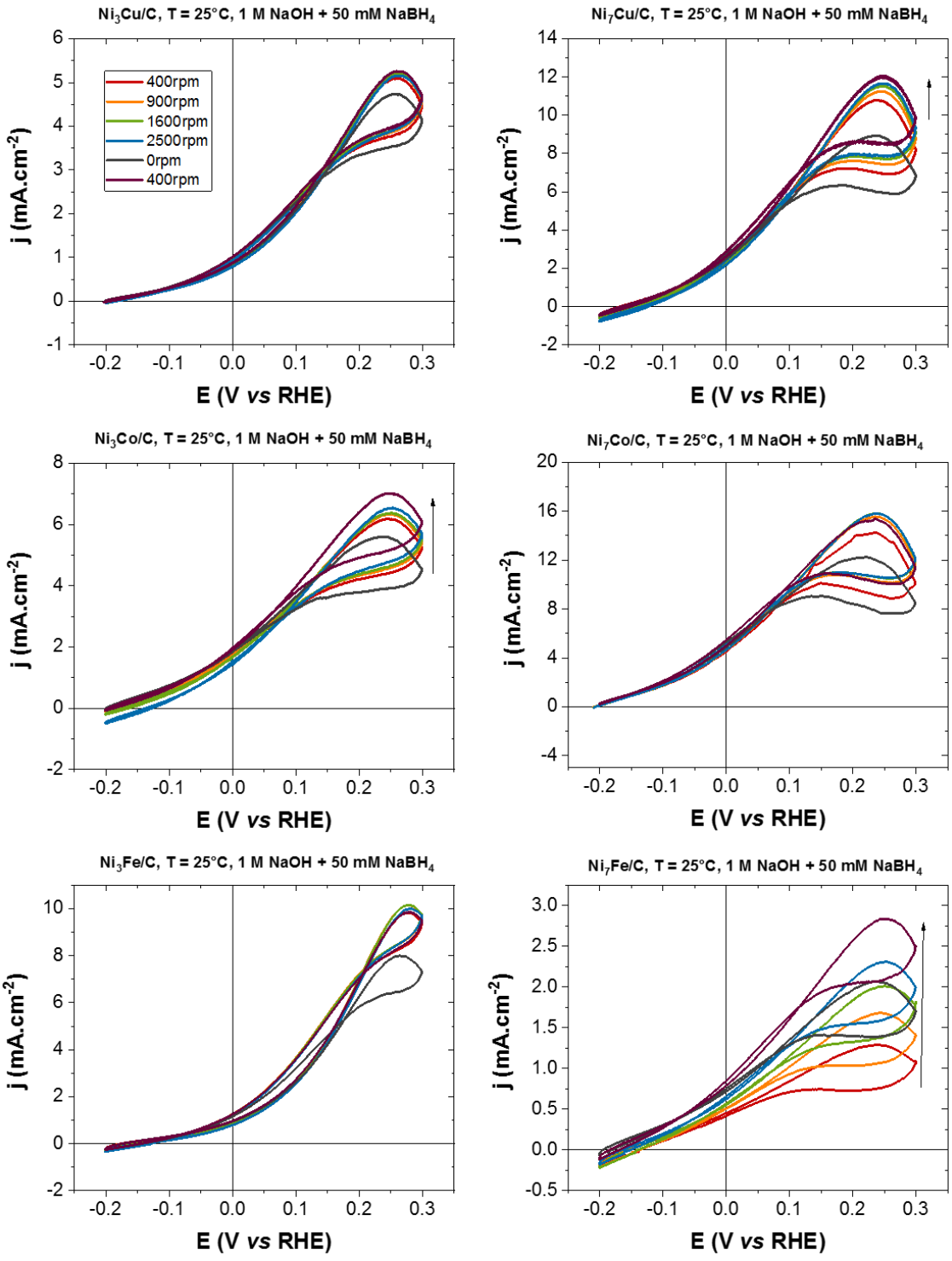

Figure IV.9. CVs of Ni_xM/C catalysts from Technion [283] at increasing rotation rate of the RDE in BOR conditions: 1 M NaOH + 50 mM $NaBH_4$, v_s = 20 $mV.s^{-1}$, room temperature, Ar-saturated electrolyte, metal loading: L_{metal} = 100 $\mu g.cm^{-2}$.

The stability of the BOR was also tested for these 8 catalysts (Ni_7Fe/C was not tested because of its more pronounced oxidized state), by performing stationary measurements

at 0.2 V *vs* RHE; the obtained CA curves are presented on Figure IV.10. As expected, Ni_3Pd exhibits the highest initial current followed by Ni_7Co, Ni_7Cu and Ni_3Mo. Nevertheless, it also presents one of the worst stability, with a 40% loss in current density after only 1 h of operation. This is typical of the surface poisoning observed on PGMs when the potential is maintained at low values. The least stable current is measured on Ni_3Ag with an already low initial current density and a severe (60%) loss after 1 h; on the contrary, the other Ni-based catalysts present a rather stable BOR current during the stationary measurement. The current recorded on Ni_3Mo and Ni_3Fe electrodes actually increases in the first minutes of the BOR and remains completely stable until the end. The apparent stability of the BOR on Ni-based catalysts not containing precious metals is nonetheless promising, as it means that no critical current decrease should appear at high voltage in DBFC conditions. However, the overall BOR activity of these materials is not high enough to make them suitable catalysts for a DBFC anode.

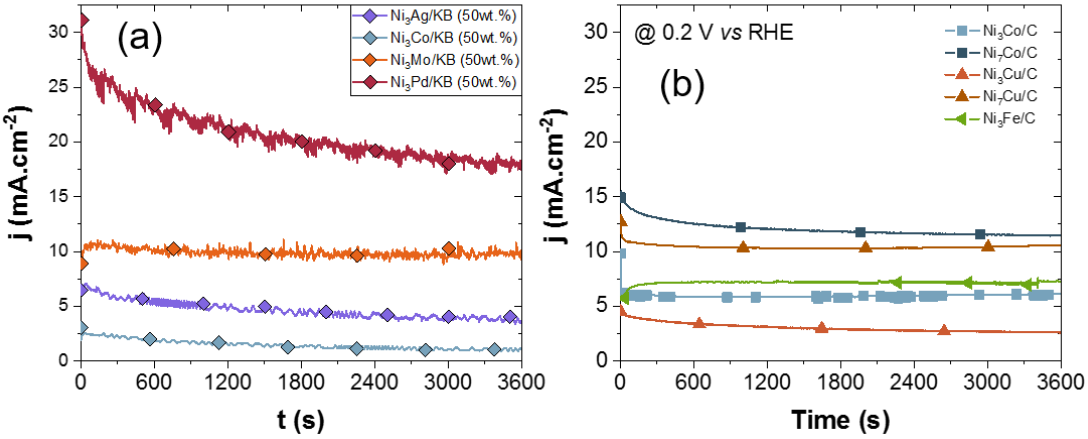

Figure IV.10. CA of all Ni-based catalysts synthetized at (a) UNM or (b) Technion in BOR conditions. E = 0.2 V *vs* RHE, 1 M + 50 mM $NaBH_4$, ω = 1600 rpm, room temperature, Ar-saturated electrolyte, metal loading: L_{metal} = 100 µg.cm^{-2}.

IV.2.2 Is there an effect of the co-element?

The bimetallic materials were synthetized to facilitate the depassivation of Ni and allow to reach a metallic state more easily. By looking at the BOR characterizations presented in the previous section, it is not clear if the co-element in each catalyst played an important or even noticeable role (except for Ni_3Pd/KB, but the contribution from Pd is not the one targeted). In order to have a comparison reference, the Ni/C catalyst was characterized in supporting electrolyte and in BOR conditions with similar conditioning steps as the other catalysts. The obtained CVs are represented in comparison with the

other catalysts from Technion on Figure IV.11. The CVs in supporting electrolyte (Figure IV.11a) already shows that Ni_7Cu/C and Ni_7Co/C would prove the most efficient catalysts, because they are the only ones exhibiting a clear α-$Ni(OH)_2$ transition peak. In fact, Ni_7Co/C presents a similar profile in supporting electrolyte to Ni/C, with almost identical oxidation and reduction currents (hence near-similar amount of reduced Ni sites). If this parameter is the key to the BOR activity, the monometallic Ni/C catalyst should be at least as effective towards the BOR as Ni_7Co/C. Surprisingly, in presence of $NaBH_4$ (Figure IV.11b), the monometallic Ni/C catalyst significantly surpasses all other catalysts, *e.g.* with twice the current density reached at E = 0.2 V *vs* RHE compared to Ni_7Co/C. A comparable onset potential is observed around -200 $mV.cm^{-2}$ confirming that the surface is, at least partially, metallic. Because the metallic ECSA between the two best catalysts is comparable (by looking at the $Ni/Ni(OH)_2$ transition peak in 1 M NaOH) it is possible that Ni/C is depassivated during the activation in presence of borohydride to a larger extent than the other catalysts. Overall, the first important conclusion of this study is that the best catalyst is pure Ni/C; alloying it with other transition metals proves rather (if not completely) ineffective and even detrimental towards the BOR activity of the material. As a marker of this effect, the more co-element is added in the matrix, the less active it is for the BOR (as observed on Figure IV.9 and IV.10). The behavior of Ni_7Fe/C does not fit this correlation, though, but the catalyst probably suffered extensive oxidation during its synthesis and/or preparation. If one nevertheless wanted to classify the co-elements, one could say that the Cu-containing sample is less active than the Co-containing one. Regarding the CV of Ni_3Fe compared to the other Ni_3M/C catalysts, one could propose that it is better than the Co-containing; however, the Ni_7Fe/C sample does not allow to affirm it.

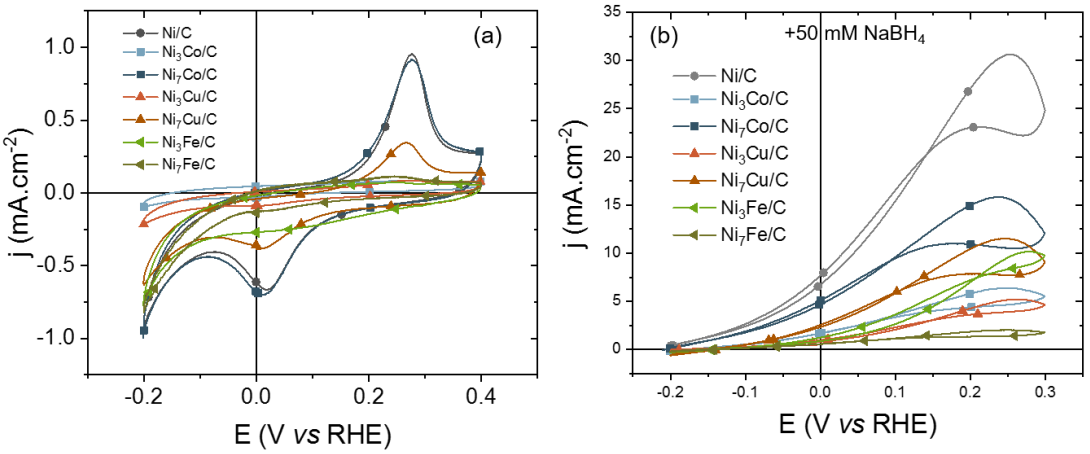

Figure IV.11. Comparison of all Technion catalysts in (a) supporting electrolyte (1 M NaOH) or BOR conditions at (b) 50 mM $NaBH_4$. v_s = 20 $mV.s^{-1}$, ω = 1600 rpm, room temperature, Ar-saturated electrolyte, metal loading: L_{metal} = 100 $\mu g.cm^{-2}$.

The onset potential already enabled to state that Technion's materials appear less oxidized than UNM ones. An interesting parallel between Ni metallic surface intentionally oxidized and these two sets of catalysts can be made using the cycles recorded during the activation step in 50 mM $NaBH_4$ (Figure IV.12). While the BOR onset potential significantly increases for a partially-oxidized Ni electrode versus a metallic electrode, cycling in presence of BH_4^- eases the reduction of oxides that were stable in supporting electrolyte. This improvement is therefore more limited on strongly-oxidized surface, where less oxidized sites are in a reversible state. This discrepancy is also observed when comparing the two sets of materials during their activation. Only two catalysts are represented on Figure IV.12; however, their activation behavior is representative of each set of materials. Only the current density increased depending on the catalyst, accordingly to the BOR activity described previously; in all cases, the ratio of current after activation over current before activation remains near-constant, though. This means that the freshly-synthetized Ni-based materials could be assimilated to partially-oxidized electrodes, while the ones from UNM appear strongly oxidized. This would explain why the catalysts from Technion exhibit lower onset potentials and slightly higher reaction kinetics even after similar conditioning. Surprisingly, Ni_3Mo/KB proved almost as active as fresh Ni_7M/C catalysts even though it is the oldest among the studied materials and was synthetized four years prior the BOR experiments. It was stored in similar conditions than the other catalysts from UNM, suggesting that Mo could be, in the end, the best co-element for bimetallic NiM/C materials.

This parallel shows that Ni-based catalysts synthetized *via* chemical routes are strongly oxidized during their preparation (most probably during the passivation step, and then non-negligibly either during their transport or/and handling prior to use) and that storing these materials under atmospheric conditions for an extended duration results in a further and deeper oxidation of their surface, leading to irreversible loss of activity towards the BOR. To obtain a good BOR catalyst, it is therefore mandatory to avoid any passivation or air-storing step prior their use in a DBFC, which is a complex task.

To conclude on these bimetallic catalysts, the overall activity of catalysts made by the chemical/thermal synthesis method is too poor to be considered viable for their use in DBFC anodes, in particular because of their non-negligible oxidized state of surface. Alloying Ni with other metals did not prove effective to depassivate the surface of the catalysts and actually, the lesser the amount of added co-element, the better is its BOR activity. This was attributed to the limited amount of metallic Ni sites on the surface of bimetallic Ni_xM catalysts, suggesting that Ni (when in the reduced state) is the most active non-noble metal among those studied in this work. However, it does not mean that alloying transition metals to a metallic Ni surface is necessarily detrimental. If

increasing the number of metallic Ni sites is favorable to the reaction kinetics, adding an element to delay the overall oxidation of the electrode and therefore enable to extend the potential window where the BOR is possible, might still be beneficial. This route will not be further studied though, and a new way to obtain highly-developed metallic Ni surfaces is required in order to pursue this study and obtain a highly active non-noble catalyst for the BOR.

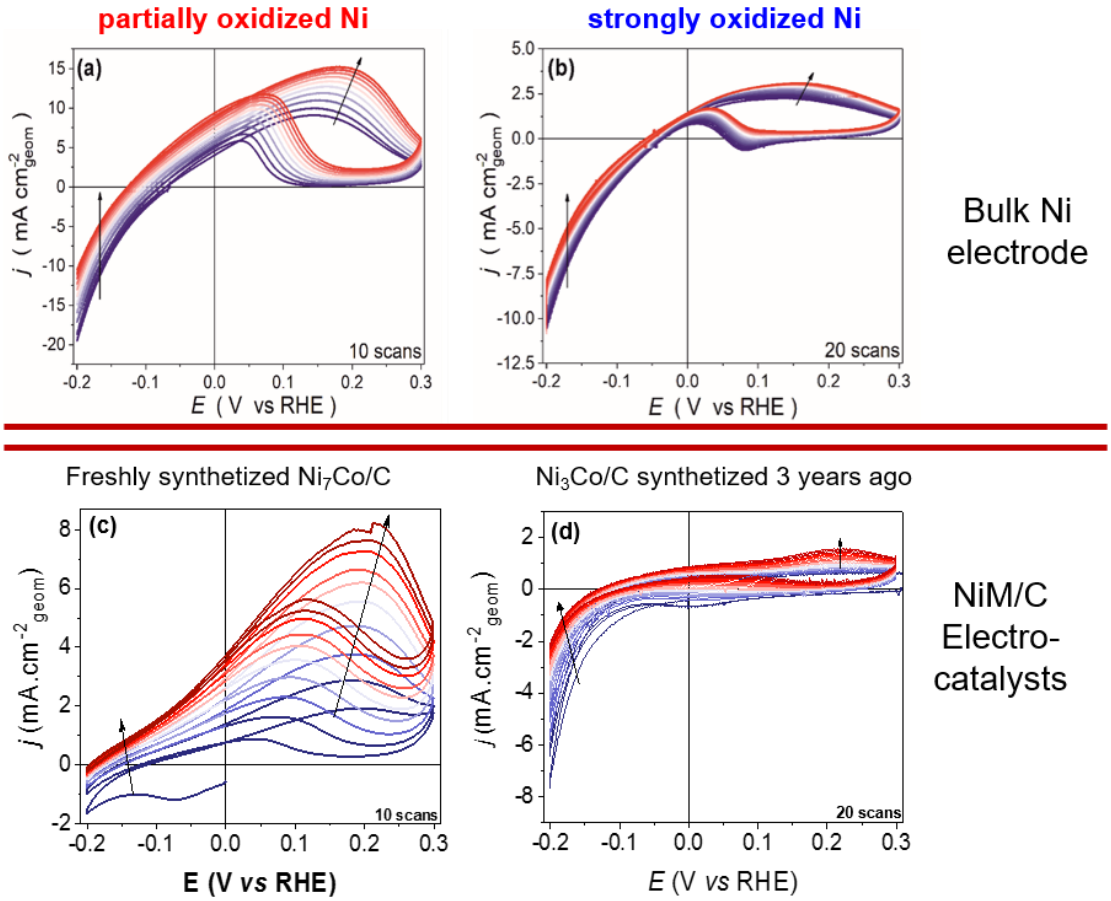

Figure IV.12. Parallel between (a, b) intentionally oxidized Ni surfaces and (c, d) Ni_xM/C nanoparticles synthetized 3 years apart during the activation procedure in BOR conditions. 1 M + 50 mM $NaBH_4$, v_s = 20 $mV.s^{-1}$, ω = 400 rpm, room temperature, Ar-saturated electrolyte.

IV.3.1

IV.3 Metallic Ni_{ED}/C: the best BOR catalysts?

Electrodeposited Ni nanoparticles for BOR

The most convenient way to obtain highly developed metallic Ni surface is to perform electrodeposition on a conductive and high-surface area support, typically carbon (*e.g.* Vulcan XC-72R). If performed in correct conditions, the obtained deposit consists of

nanoparticles that are in metallic state; from this point, one can oxidize them to different extents in order to study the influence of the state of the surface for a given reaction, for example the BOR. Such electrodeposition was already developed by Oshchepkov *et al.* [186,187,289]. The procedure to perform this electrodeposition is detailed in the section "II.2.1 Nickel nanoparticles electrodeposition".

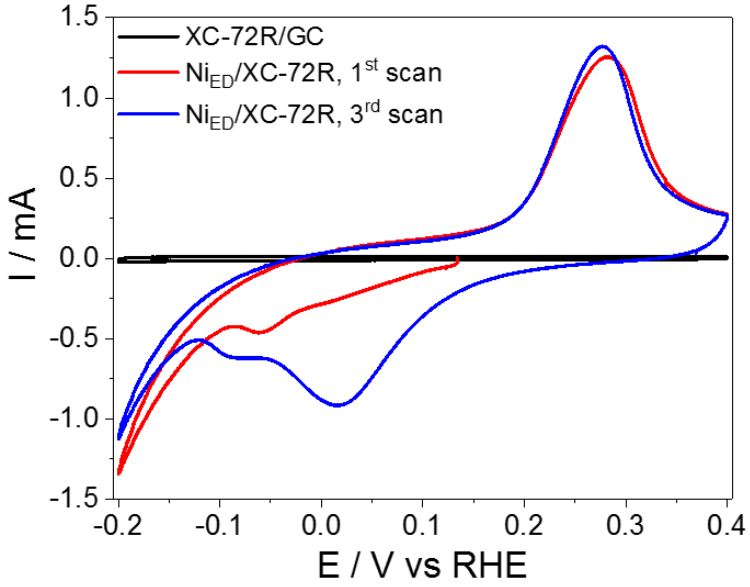

Figure IV.13. CVs obtained in N_2-saturated 1M NaOH at v = 20 mV·s^{-1} for XC-72R/GC (black curve) and Ni$_{ED}$/ XC-72R electrodes during 1st (red curve) and 3rd (blue curve) scans.

The resulting material was characterized in supporting electrolyte and the measured CVs are presented on Figure IV.13. The electrodeposition is proven effective, since the current measured upstream (prior electrodeposition) with only the Vulcan XC-72R layer is negligible. The transition peak from Ni to α-Ni(OH)$_2$ is clearly defined around E = 0.27 V *vs* RHE, signing the presence of a significant number of metallic nickel sites. Moreover, the HER starts only at potentials E < -0.125 V *vs* RHE (the obtained surface is not very active for this reaction), which confirms that the surface is overall metallic. The electrocatalyst was characterized by scanning transmission electron microscopy (STEM); STEM revealed formation of metal nanoparticles with a mean size of *ca.* 10 nm, homogeneously distributed over the Vulcan XC72R support surface (Figure IV.14). The estimated interplanar spacing of 0.205 nm, corresponds to the (111) plane of Ni (0.2034 nm, calculated for a theoretical lattice constant a = 0.35238 nm for crystalline Ni [ICDD PDF-2#00-004-0850]). The Ni loading was estimated as *ca.* 40 wt.% by inductively-coupled plasma atomic emission spectrometry (ICP-AES).

To observe the influence of the state of surface of Ni towards the BOR on this new electrocatalyst, the extent of oxidation of Ni nanoparticles was again purposely varied and three types of electrodes were considered: (i) strongly-oxidized Ni$_{ED}$/C, *i.e.* the sample subjected to potential cycling in a wide potential interval from -0.2 to 1.6 V *vs*

RHE as it is typically done in the literature; (ii) partially-oxidized Ni_{ED}/C, *i.e.* the sample subjected to electrochemical oxidation at 1.0 V *vs* RHE for t = 5 min and (iii) metallic Ni_{ED}/C, which was studied right after the preparation, without application of potentials above 0.5 V *vs* RHE. The ECSA was calculated using the method described in the section "II.2.2 Electrochemical Surface Area Determination" and the oxidation of the Ni_{ED}/C resulted in a decrease of this ECSA from 93.4 to 52.5 and 25.9 $m^2\ g_{Ni}^{-1}$ for metallic, partially-, and strongly-oxidized Ni_{ED}/C electrodes, respectively; this ECSA reflects the number of available Ni metal sites on the electrode surface.

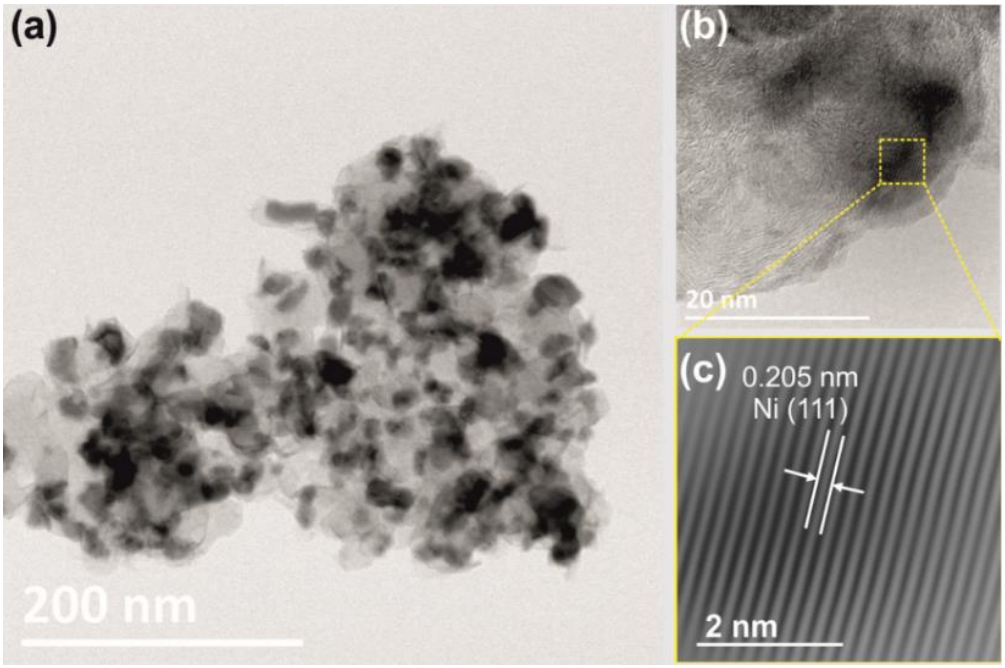

Figure IV.14. (a) Low and (b) high-resolution STEM images of the as-prepared Ni_{ED}/C electrocatalyst, (c) FFT-filtered magnified area highlighted in the dashed box in (b). Reprinted from [291].

These 3 surfaces were characterized in BOR conditions, where the effect of the state of surface can clearly be observed (Figure IV.15): strongly-oxidized Ni_{ED}/C shows the lowest BOR activity, while reduced Ni_{ED}/C demonstrates the highest, by far. The impressive onset potential of the BOR for the metallic Ni_{ED}/C can be attributed to the sluggish kinetics of the competing HER, confirming the explanation given in the previous sections. Regarding the partially-oxidized sample, its HER activity increase causes a significant decrease of the net BOR currents and a positive shift of the OCP. Interestingly, the BOR and the HER currents are not in direct anti-correlation, suggesting a complex interplay between the adsorption energies (the latter dependent on the Ni oxide coverage), the Ni site availability and the electrochemical kinetics of BOR/HER (and HOR). The onset-potential for the oxidation of 5 mM $NaBH_4$ is only -0.052 V *vs* RHE for strongly-oxidized Ni_{ED}/C, while it shifts to -0.152 V *vs* RHE and -0.235 V *vs* RHE in the case of partially-oxidized and metallic Ni_{ED}/C electrodes,

respectively. To sum up, by increasing the metallic character of the Ni surface, one can limit the rate of electrochemical HER and hence significantly improve the performance of Ni electrocatalysts in the BOR (Figure IV.15b). In particular, metallic Ni_{ED}/C demonstrates the highest BOR current densities measured at E = 0.1 V *vs* RHE, being *ca.* 1.5 and *ca.* 15 times larger compared to partially- and strongly-oxidized Ni_{ED}/C, respectively (Figure IV.15c). This time with a highly developed surface area, the reaction kinetics is much less limiting and mass-transport limitation plateau appears just below E = 0 V *vs* RHE, which was never observed on any of the catalysts presented above.

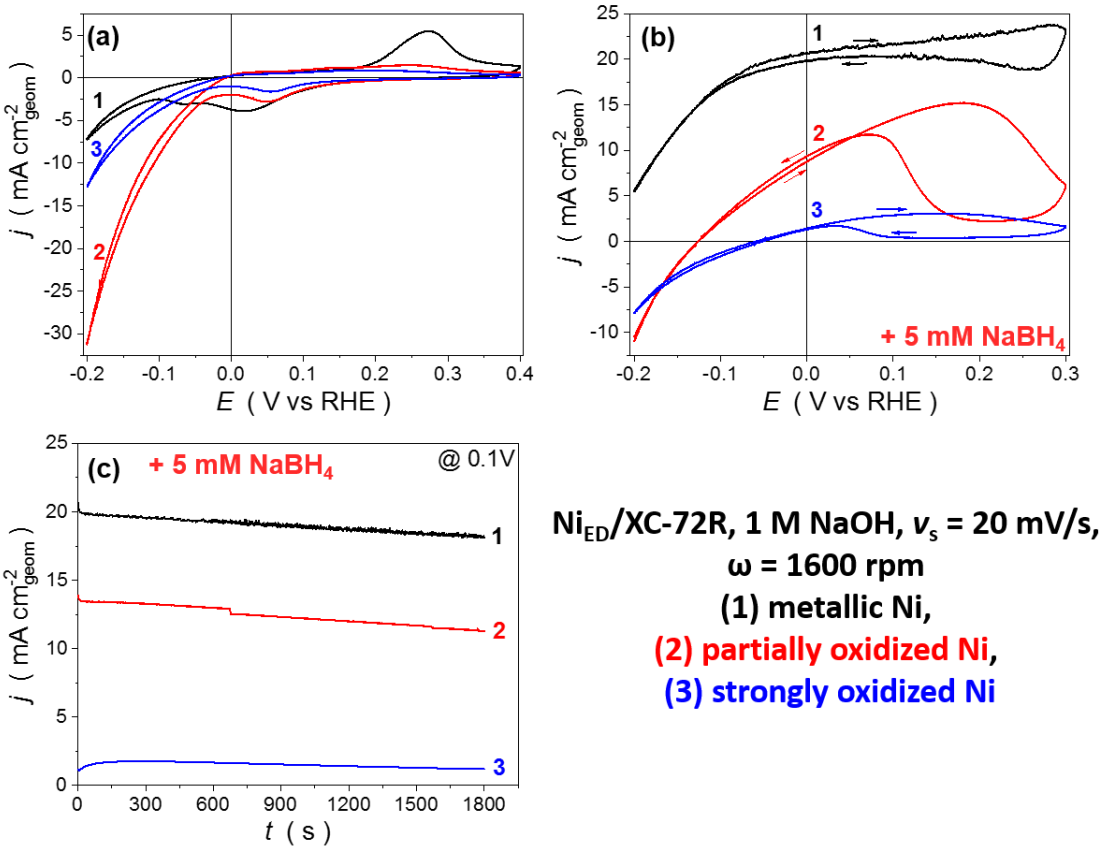

Figure IV.15. (a, b) CV and (c) chronoamperograms obtained for various Ni_{ED}/C rotating disk electrodes (RDE) under N_2 atmosphere at the following conditions: (a) 1.0 M NaOH, v_s = 20 mV s^{-1}, ω = 0 rpm, (b) 1.0 M NaOH + 5 mM $NaBH_4$, v_s = 20 mV s^{-1}, ω = 1600 rpm, (c) 1.0 M NaOH + 5 mM $NaBH_4$, ω = 1600 rpm, E = 0.1 V vs RHE.

A new electrodeposition was performed in a one-compartment cell using a Pt CE to simplify the procedure. In order to confirm that no Pt contaminated the Ni surface and could interfere during the BOR, the Ni_{ED}/C samples were analyzed after electrodeposition by X-EDS (Figure IV.16). No traces of Pt are found on the X-EDS spectra on several regions of the Ni nanoparticles. It confirms that the ED procedure is still valid using this one-cell compartment. It must be noted that the presence of Pt in combination with metallic Ni would induce better BOR apparent kinetics above E = 0 V *vs* RHE, thanks to the valorization of H_2 produced via fast HOR on Pt (a positive effect),

but because of the unmatched HER activity of Pt, it would in return drastically increase the onset potential and render the Pt-polluted (bimetallic) catalyst rather inefficient for the BOR below 0 V *vs* RHE (a very detrimental effect). It is generally admitted and consensual that noble, and in particular, Pt CE should be prohibited when characterizing non-noble catalysts. This is justified when studying processes, where Pt has high electrocatalytic activity, such as the oxygen reduction reaction (ORR), studied, for example on Fe-N-C-based materials (one of the most studied non-noble catalyst nowadays [379–382]). Because of the potentials scanned in those conditions, Pt CE suffers from significant degradation/oxidation and can be redeposited at the working electrode [223,224]. This results in an important ORR activity increase of the catalyst, thereby falsifying its real performance.

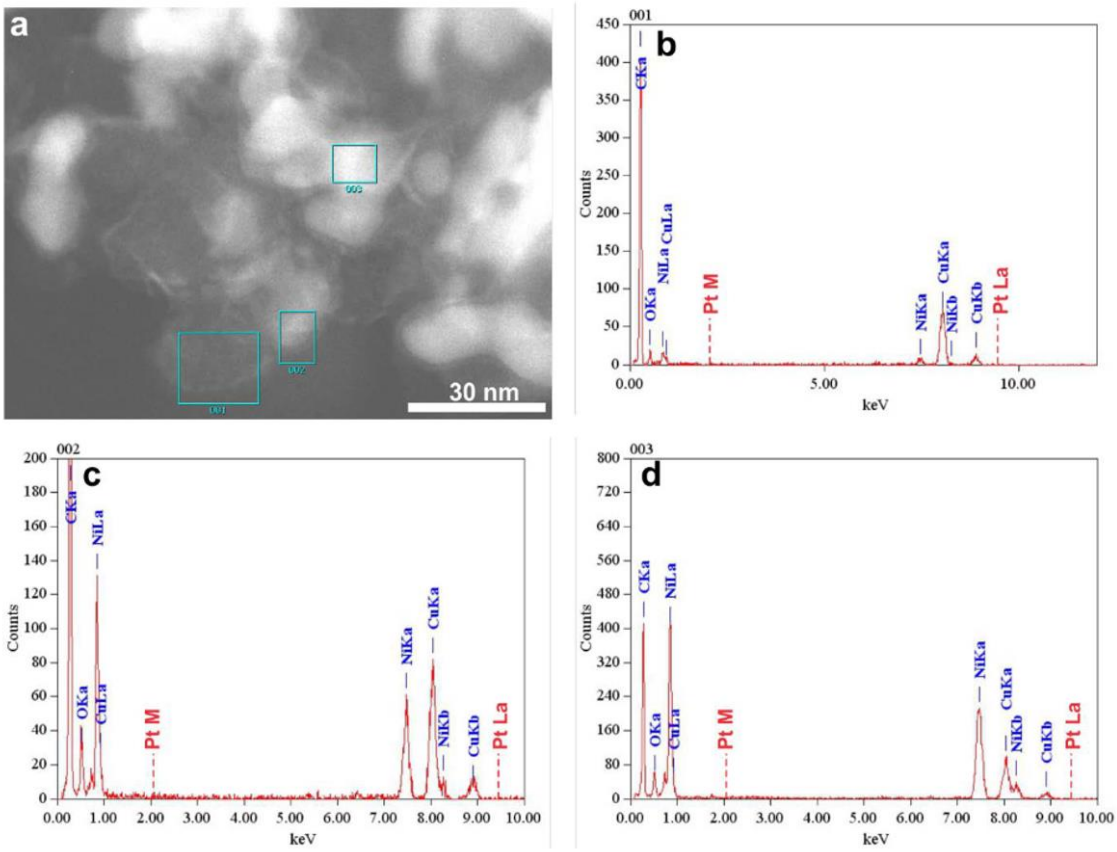

Figure IV.16. (a) TEM image of NiED/C sample and corresponding X-EDS analysis from the marked areas (b) 001, (c) 002, (d) 003

However, in BOR conditions, this effect does not appear, mainly because the CE acts as a cathode (hence rather protected from dissolution): when scanning from E = -0.2 V *vs* RHE to E = 0.3 V *vs* RHE with a Ni_{ED}/C WE, only positive current is measured on the WE. In addition, the very high HER activity of Pt maintains the applied overpotential too small to substantially degrade the material by cathodic corrosion [383–385]. Even if an oxidation current is forced at the CE, the presence of borohydride will also result in

a low overpotential, because of the activity of Pt at low potential towards the BOR. This is an important factor that overall prevents any significant degradation of a Pt CE during BOR characterizations of a non-Pt WE, hence not leading to detectable pollution of the WE by CE materials.

To investigate the reaction kinetics in more detail, the rotation rate was varied in similar conditions as for Figure IV.6; the measured CVs are represented on Figure IV.17. A Pt/C electrode with similar loading was used as a comparison (Figure IV.17b, d). The rotating rate dependence of the RDE polarization curves has been analyzed using the Koutecky-Levich equation (equation 4.4):

$$j^{-1} = j_k^{-1} + j_d^{-1} = j_k^{-1} + B^{-1}\omega^{-0.5} \qquad \text{(4.4 Koutecky-Levich)}$$

The Koutecky-Levich (KL) plots for Pt/C electrode (Figure IV.15d) almost cross 0, showing that the limiting currents are established at potentials above 0.1 V *vs* RHE. On the contrary for Ni_{ED}/C sample, a significant deviation from the plot obtained for Pt/C is observed (Figure IV.16c), likely due to a change of the number of released electrons of the BOR at different potentials. The extrapolation of the KL plots to the vertical axis gives non-zero intercepts, meaning that the reaction kinetics is still under mixed control until 0.25 V *vs* RHE, unlike what assumed just above by looking at the shape of the CV. Surprisingly, the Koutecky-Levich plot measured at E = 0.25 V *vs* RHE intercepts the Y-axis at the larger value of j_k^{-1} (compared to the cases at 0.1 and 0.2 V *vs* RHE). This unexpected result is likely explained by the additional contribution of the formation of α-$Ni(OH)_2$, that occurs simultaneously to the BOR in this potential region.

The slope B can be calculated according to the Levich equation as:

$$B = 0.62 \cdot nD^{\frac{2}{3}}Fv^{-\frac{1}{6}}C_0 \qquad \text{(4.5 Modified Levich)}$$

with:

n = Number of electrons transferred

F = Faraday's constant (96 485 C.mol^{-1})

C_0 = Concentration of borohydride (5 mM)

D = Diffusion coefficient of BH_4^- ($2.6 \cdot 10^{-5}$ cm^2 s^{-1} [227])

v = Kinematic viscosity of the electrolyte (0.0118 cm^2 s^{-1} [227])

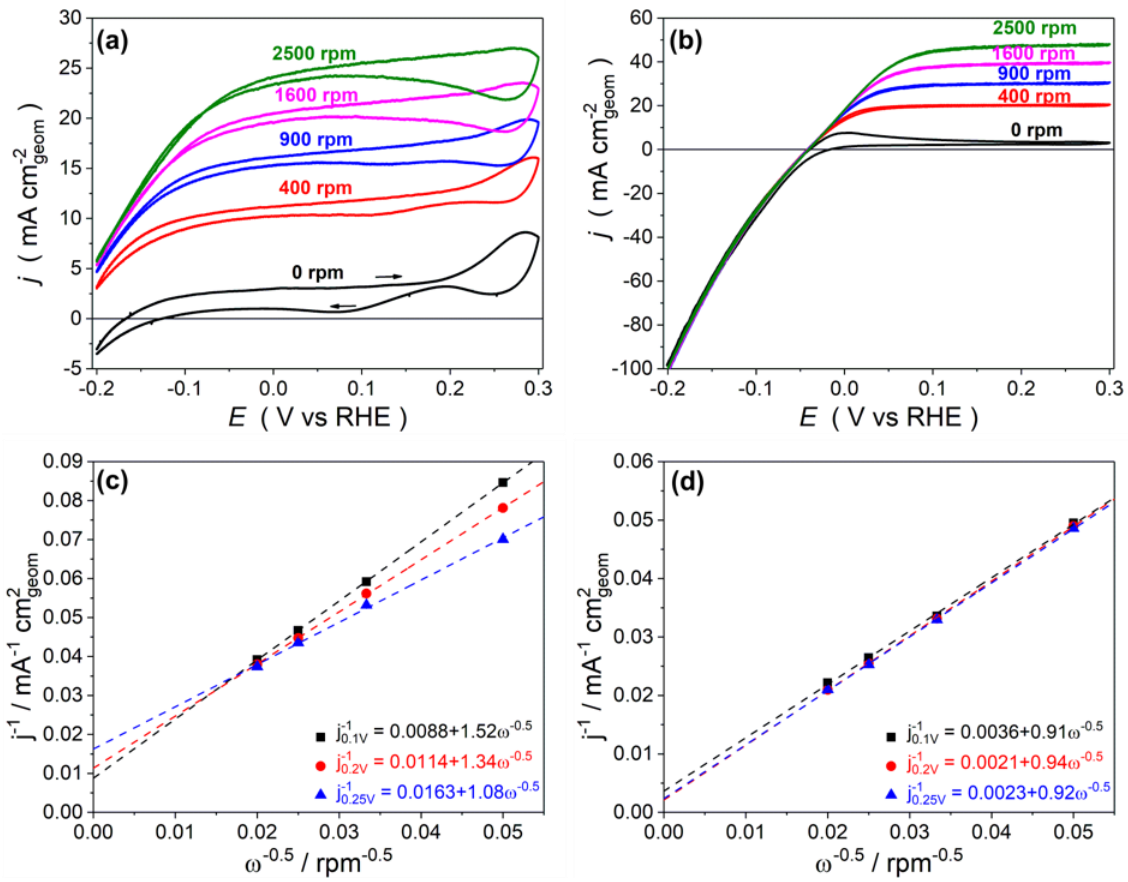

Figure IV.17. CV curves obtained for (a) Ni_{ED}/C and (b) Pt/C using rotating disk electrode in N_2-saturated 1.0 M NaOH + 5 mM $NaBH_4$ electrolyte at v_s = 20 mV·s^{-1} and various rotation speeds. (c, d) Corresponding Koutecky-Levich plots at various potentials.

The theoretical values of the *B* are calculated to be 2.81, 1.40, 0.94, 0.70, if one assumes the release of 2, 4, 6 and 8 electrons for the BOR, respectively. Therefore, analysis of the Koutecky-Levich plots presented on Figures IV.15c, d shows that the number of released electrons is close to 4 and 6 for Ni_{ED}/C and Pt/C catalysts, respectively (at 0.25 V *vs* RHE). By comparing the CVs of these two catalysts at different rotation rate the mass-transport limited current of Ni_{ED}/C appears around two times smaller than for Pt/C, which does not correspond to number of electrons calculated. It is usually accepted that 8 electrons are produced on Pt surface at small overpotentials (see Chapter III). This discrepancy might arise from the calculation approximations (value of *D* and *ν*), or from the fact that the thin-film of RDE is too thin to enable complete valorization of BH_4^- in these conditions [386]. Overall and importantly, Ni_{ED}/C displays BOR activity surpassing Pt/C at potential below 0 V *vs* RHE, which is really promising for DBFC applications, even if the number of electrons transferred above 0 V *vs* RHE is inferior to that of Pt.

To observe how increasing the number of active sites (compared to polycrystalline Ni rod) affected the kinetics and poisoning at higher potentials, the same Koutecky-Levich

measurement was reproduced on Ni_{ED}/C at 1 M NaOH + 50 mM $NaBH_4$ (Figure IV.18). Unlike Figure IV.6b, the reaction kinetics appears less limiting at the higher $NaBH_4$ concentration, as the current density clearly increases with the rotation rate for $E > 0$ V *vs* RHE. However, the maximum current density is only reached at $E = 0.2$ V *vs* RHE for all rotation rate, because of the higher concentration of borohydride (there are more species to valorize, and a higher potential is required to reach the mass-transport limitation): at $E = 0.1$ V *vs* RHE the reaction is still non-negligibly limited by the kinetics (Figure IV.18b). For the two higher potential values, this effect is limited and visually, it appears that the current increase is close to be proportional to the square root of the rotation rate; but the Koutecky-Levich plots infirm it, since their Y-intercepts are further from 0 than the one at 5 mM (Figure IV.17c). Overall, even at 50 mM the Ni_{ED}/C performs exceptionally well, particularly at low potential but also until 0.3 V *vs* RHE, and does not appear to suffer from strongly limiting surface poisoning.

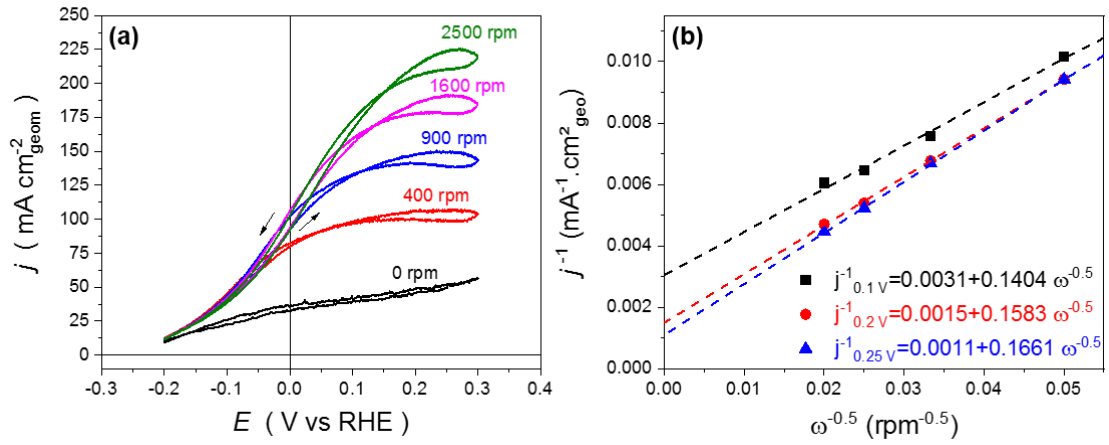

Figure IV.18. CV curves obtained for (a) Ni_{ED}/C using rotating disk electrode in N_2-saturated 1.0 M NaOH + 50 mM $NaBH_4$ electrolyte at $v = 20$ mV·s^{-1} and various rotation speeds. (c) Corresponding Koutecky-Levich plots at various potentials.

IV.3.2 BOR activity compared to most used catalysts

In order to benchmark the outstanding BOR activity of the Ni_{ED}/C electrodes, they were tested in a half-cell configuration in both potentio-dynamic and potentio-static conditions and compared to Ni/C NPs (provided by Prof. Dekel's group [283] presented in section IV.2), PGM catalysts (commercial Pt/C, Pd/C) and Au/C NPs, the most commonly-used electrocatalysts for the BOR. Commercially-available 40 wt. % Pt/C, Pd/C and Au/C electrocatalysts were used to obtain electrodes with similar metal loading (40 µg.cm^{-2}) to make a fair comparison. Two concentrations of $NaBH_4$ solution, namely 5 and 50 mM, in 1.0 M NaOH were chosen to compare the electrocatalysts, with

the purpose to evaluate an influence of the electrode surface-poisoning by boron-containing species. The measurements were performed under potentiodynamic and potentiostatic conditions in the potential range between -0.2 < *E* < 0.3 V *vs* RHE. Potentiodynamic measurements (Figure IV.19a, b) evidence unmatched activity for Ni_{ED}/C at potentials below 0 V *vs* RHE, both in 5 and 50 mM $NaBH_4$ solution. Metallic Ni_{ED}/C exhibits the lowest OCP with -230 mV *vs* RHE and -256 mV *vs* RHE at 5 mM and 50 mM respectively and displays an important current density, reaching limiting plateau above −0.05 V *vs* RHE. For Pt/C, the high rate of the HER limits the efficiency of the BOR below 0 V *vs* RHE, resulting in an OCP of -50 mV *vs* RHE at both concentrations. Mass-transport-limited current densities are only reached (in the studied potential window) by these two catalysts. For the other catalysts, an increase of the BH_4^- concentration requires to apply higher potential to reach the limiting current, because of the slower reaction kinetics. The activity of Pd/C and Au/C is much smaller than for Ni_{ED}/C and Pt/C in the studied potential range, especially at 50 mM $NaBH_4$, because of their different BOR mechanism and slower BOR kinetics (see Chapter III). Chemically synthesized Ni/C is nowhere near competing with the two best catalysts but still surpasses Pd/C until 0.3 V *vs* RHE.

While potentiodynamic measurements show higher BOR currents on Pt compared to Ni above *E* = 0.2 V *vs* RHE, potentiostatic measurements (Figure IV.19c, d) reveal that the BOR activity of Pt promptly decays, with a critical loss exceeding 90% after only 1 hour. Similar decrease, although in smaller extent, was observed for Pd/C, with *ca.* 80% current decay after 1 hour in 5 mM $NaBH_4$, while Au/C is almost inactive at potentials below 0.3 V *vs* RHE (see Chapter III). Contrary to the Pt/C and Pd/C electrocatalysts, the activity of Ni_{ED}/C is relatively stable over time, with only *ca.* 12 and 18% current decay after 1 hour at 5 and 50 mM $NaBH_4$, respectively. Besides, the BOR currents on Ni_{ED}/C are almost proportional to the concentration of $NaBH_4$, while the BOR performance of the Pt/C and Pd/C electrocatalysts at higher $NaBH_4$ concentrations are worse than expected. Again PGM electrocatalysts suffer from extensive poisoning by accumulation of adsorbed intermediate species such as BH_{ad}. This poisoning effect is very fast because it happens during the first steps of the BOR, thus explaining why the initial currents on Pt/C and Pd/C at 50 mM are not proportional to the concentration. However, it does not fully justify the progressive decay observed on Figure IV.19c, d. One hypothesis is that solid borate species (the BOR final product) slowly form a gel-like structure at the electrocatalyst surface and gradually block the active sites at longer reaction times.

This comparison allowed to highlight the superior BOR activity of Ni_{ED}/C at potentials below 0 V *vs* RHE; it also revealed interesting details regarding the reaction path on metallic Ni surfaces. First of all, the mass-transport-limited current is two times lower

than for Pt/C, suggesting a lower number of electrons produced (estimated at 4, Figure IV.17). Moreover, the current density increases quasi-linearly with the BH_4^- concentration for Ni_{ED}/C (suggesting first-order reaction kinetics), while for Pt/C and Pd/C electrocatalysts the current is not proportional to the concentration. This indicates a less pronounced surface poisoning by intermediate species and by final reaction products on metallic Ni: as a result, the BOR currents on Ni are more stable. These differences likely originate from different BOR mechanisms on Ni than the one detailed in chapter III. Several measurements using (coupled) spectroscopic methods and calculations will be presented in the next section in an attempt to shed light on the BOR mechanism on Ni.

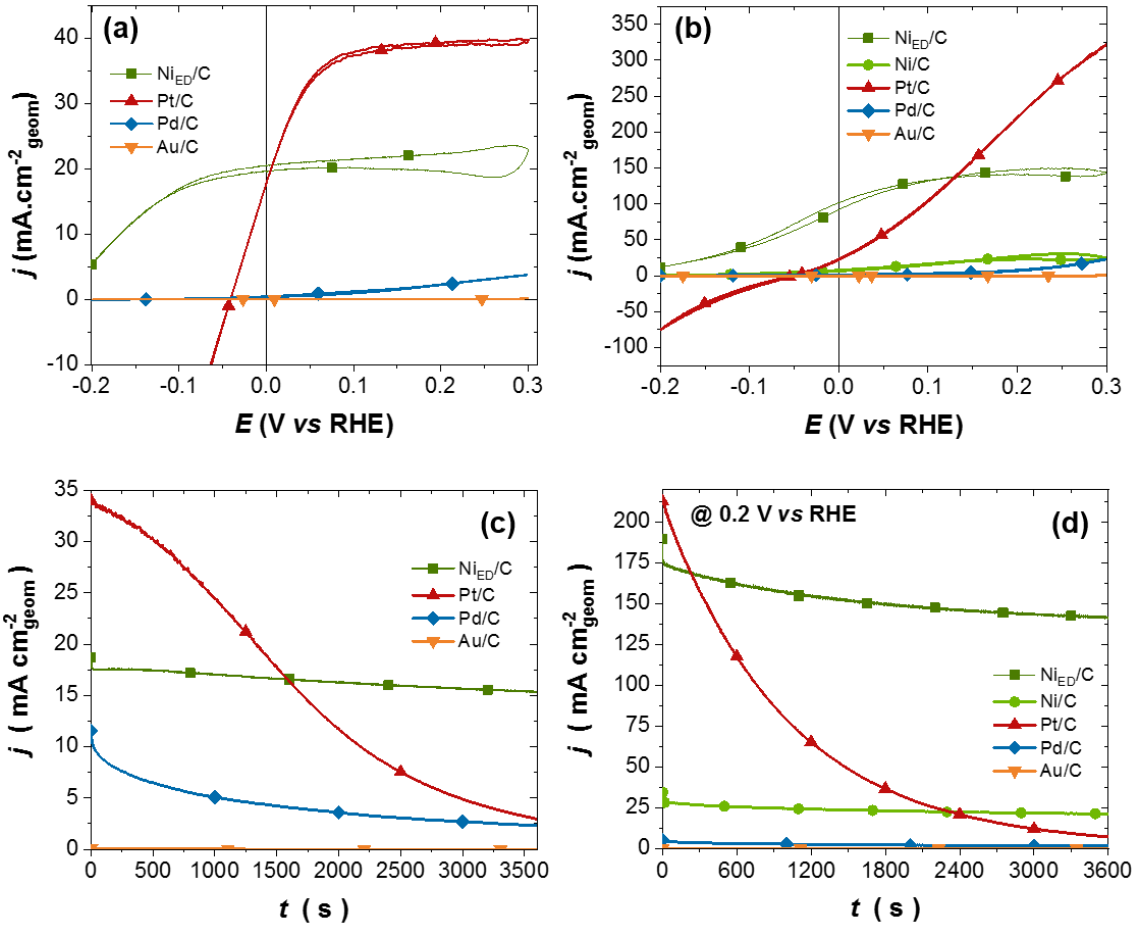

Figure IV.19. Comparison of the most commonly used catalysts for the BOR to the Ni_{ED}/C electrodes in 1 M NaOH + (a, c) 5 mM and (b, d) 50 mM $NaBH_4$ (Ar-saturated solution, T = 20°C, ω = 1600 rpm) in: (a, b) potentiodynamic conditions (v_s = 20 $mV.s^{-1}$) showing the lower onset potential on Ni_{ED}-based catalysts compared to PGMs and (b, d) potentiostatic conditions (E = 0.2 V *vs* RHE). All the M/C catalysts are loaded at l = 40 $\mu g.cm^{-2}$ of M (M = Pt, Pd, Au or Ni)

IV.4 Tentative BOR mechanism on Ni

IV.4.1 RDE and RRDE measurements

In order to investigate in more detail the BOR on Ni_{ED}/C, potentiostatic measurements were performed every 100 mV in the -0.2 < *E* < 0.3 V *vs* RHE potential region in 1 M NaOH + 5 mM or 50 mM $NaBH_4$ (Figure IV.20). As presented previously, Ni metallic surfaces exhibit oxidation currents already at -0.2 V *vs* RHE; however, below 0 V *vs* RHE, the current non-negligibly decreases versus time: the slow reaction kinetics prevents the reaction completion, and intermediate species likely and gradually block the surface. This poisoning effect is not observed anymore at 0.1 V *vs* RHE, where the current is stable at 5 mM (Figure IV.20a) or even increases over time at 50 mM $NaBH_4$ (Figure IV.20b); the same effect is witnessed for *E* = 0.2 V *vs* RHE. This shows that the poisoned sites are able to regenerate at positive potential since the rate determining step is probably slow but potential-activated. On Figure IV.19 the current density decreased at a similar potential, with the only difference being that the potential was directly set at 0.2 V *vs* RHE, where it is now progressively increased by steps of 100 mV: the initial current on Figure IV.19 c is greater and decreases to reach a similar value as the final current measured on Figure IV.20, suggesting a steady-state between poisoning and regeneration of active sites. Unfortunately, if the applied potential is increased to 0.3 V *vs* RHE, the oxidation of the nickel surface results in an immediate activity drop until the current becomes almost null. The electrode would require the application of a lower potential to reduce its (reversible) surface oxides and regain its initial activity, keeping in mind that applying an even higher potential instead would make this activity loss irreversible. This suggests already that the voltage applied in a DBFC setup using a Ni-based anode should carefully be controlled in order to preserve the anode state of surface/activity.

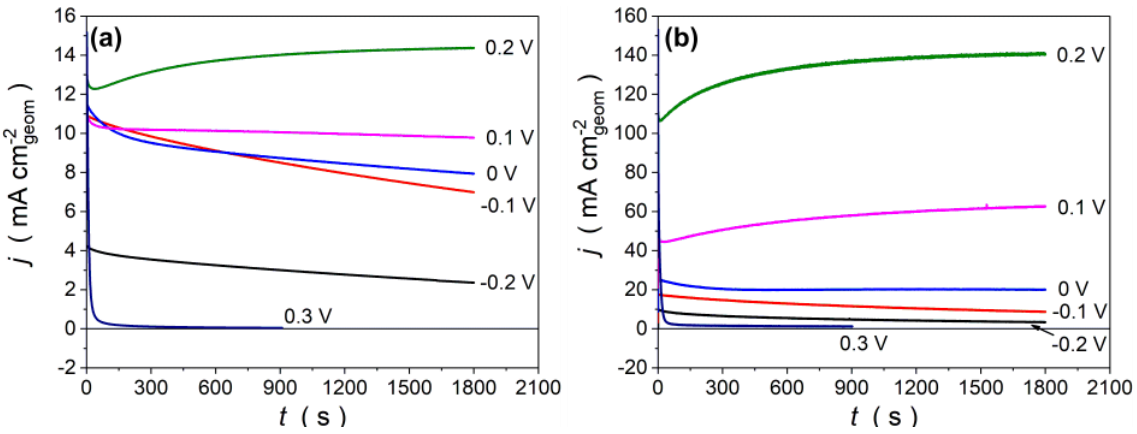

Figure IV.20. Potentiostatic measurements of the NiED/C electrode at different potentials in N2-saturated 1 M NaOH + (a) 5 mM or (b) 50 mM. (ω = 1600 rpm; -0.2 < E < 0.3 V *vs* RHE)

To investigate the reaction pathways of the BOR on Ni, RRDE measurements were performed with a Ni_{ED}/C disk and a concentric Au ring. The same RRDE setup detailed in section "II.1.3 Rotating Ring-Disk Electrode" and used in chapter III for the detection of BH_3OH^- was adapted to use Ni_{ED}/C disk. The bulk Pt or Au polycrystalline disk was replaced by GC and the ED procedure was applied in the dedicated cell before the BOR characterization. Because the rotating electrode requires to be positioned vertically, the bubbles formed at the interface are not expelled correctly, resulting in noisier signal as observed on Figure IV.21. At low concentration (5 mM $NaBH_4$, Figure IV.21 a) the ring current is constant throughout the whole potential window, meaning either no (or small amount of) BH_3OH^- is generated on Ni surface and thus that the reaction does not proceed *via* $BH_{3,ad}$ species (or their coverage is small under the applied conditions), or that the production is constant at all potentials. This second option is unlikely, because if BH_3OH^- is generated through the BOR, their production rate should be proportional to the faradic current. Moreover, the current at the ring is negative (probably because of reduction of residual O_2 from the electrolyte), suggesting no species are oxidized at its surface or that the oxidation current is inferior of the reduction current (the latter originating from the oxygen traces in the electrolyte as mentioned above). The potential window was increased (Figure IV.21 b) in order to observe if the formation of oxides could modify the reaction pathways (similarly to noble surfaces studied previously); even in these conditions, the ring current remained stable during the whole measurement. At higher concentration (Figure IV.21c, d), the CV was performed at two different rotation rates to observe if the ring response correctly follows mass-transport limitations. At 50 mM $NaBH_4$, the ring current is now positive (it may correspond to oxidation of hydrolysis products formed at the disk); it slightly decreases and is noisier when the disk potential is above E_{Disk} > 0 V *vs* RHE. It coincides with the potential at which the reaction reaches its stable state (Figure IV.20), suggesting that it is accompanied by bubbles (most probably H_2) generation.

At 500 mM $NaBH_4$ (Figure IV.21d) no mass-transport limitation is observed on the disk, because of the limitation by the reaction kinetics. However, the current measured on the gold ring is 10 times greater than at 50 mM $NaBH_4$, which means that this ring current is really linked to the concentration of borohydride and thus probably to the oxidation of hydrolysis products. The signal over noise ratio increased, because the disk current and therefore the gas generation remained the same; however, the *ca* 5-10 µA noise detected above 0 V *vs* RHE previously is now measured in the whole potential window. This means that at higher concentration, the surface reaches its "poisoning/regeneration stable state" already at -0.2 V *vs* RHE. The ring current decreases however in the same conditions (E_{Disk} > 0 V *vs* RHE) but still proportionally to the concentration, meaning that it is likely not due to the generation of BH_3OH^- species at the disk which explains this current (since the disk current remained the same

as in Figure IV.21c). Instead, the ring current is likely due to oxidation of hydrolysis products/intermediates on the Au ring (even though this current remains very small). In any case, these results enable to conclude that no significant amounts of BH_3OH^- species are generated on Ni surfaces in the course of the BOR (in the studied potential domain), unlike on noble surfaces. However, some BH_3OH^- species might be formed via heterogeneous hydrolysis of borohydride at the Ni electrode.

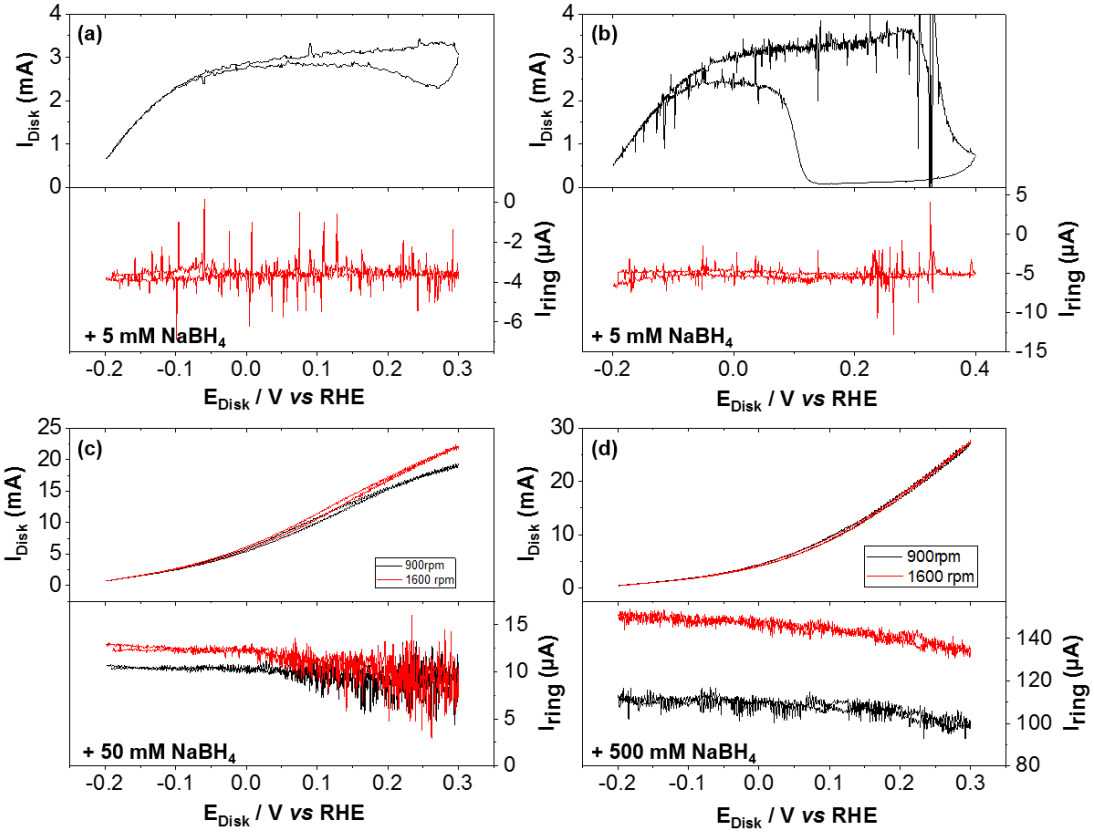

Figure IV.21. CVs of Ni_{ED}/C electrode in (a, b) 1 M NaOH + 5 mM $NaBH_4$ at ω = 900 rpm and 1 M NaOH + (c) 50 mM or (d) 500 mM $NaBH_4$ at ω = 900 or 1600 rpm. Ring current is recorded with a concentric Au ring set at 0.2 V *vs* RHE and reported to the WE potential.

IV.4.2 Coupled spectroscopic characterization on metallic Ni

To push further this investigation of the BOR on metallic Ni surfaces, *in situ* spectroscopic methods were used. First of all, the DEMS measurements performed on noble metals (see Chapter III) were reproduced to determine if the gas formation observed (from the noise) during RRDE measurements is indeed H_2. Secondly, *in situ* FTIR spectra were obtained, giving clues about reaction intermediate/product species produced at the interface of the electrode during the BOR.

IV.4.2.1 Hydrogen escape measurements using DEMS

The challenge to perform DEMS on Ni was to find a manner to obtain a porous structure, while maintaining its metallic state and therefore the good activity of Ni towards the BOR. This required a way to obtain our electrode just before installing the DEMS cell and, because it needs to be supported on a PTFE membrane, the ED procedure could not be adapted for this method in a straightforward manner. In the end, a nickel foam was used as the electrode, after acid etching (the use of this material will be explained and detailed in chapter V), and pressed between the PTFE membrane and the current collector (see cell description in section II.3.3). This current collector was also replaced by a Ni ring instead of the conventionally used gold, the latter not being inert towards the BOR. The surface of the Ni current collector was preliminarily strongly oxidized, so that it would still conduct electrons but not catalyze the BOR (at least at low potentials). In a similar manner as for the previous DEMS measurements presented in this work (chapter III), $NaBD_4$ was used instead of $NaBH_4$ to differentiate the detection of H_2 coming from the solvent (water) and from the fuel [201,387].

Figure IV.22 presents the CVs obtained at 10 $mV.s^{-1}$ in 1 M NaOH + 5 mM (a) or 50 mM (b, c, d) $NaBD_4$ with the faradic current and the corresponding calibrated ionic currents (H_2, HD, D_2). Because the nickel foam electrode is way thicker than the usual sputtered electrodes (500 µm and 50 nm, respectively) the ion over faradic current is smaller and therefore a greater calibration factor must be applied (from *ca* 10^7 to *ca* 10^{10}). Moreover, large noise is detected by the mass spectrometer, because of the morphology of the electrode. Bubbles are blocked in the pores of the electrode and released randomly, resulting in big spikes independently of the potential. This effect was significantly enhanced at 50 mM $NaBD_4$ and therefore the ion currents were smoothed post-measurements (50% percentile filter method with a 10-points window was used, because the other calculation methods required evenly spaced x data) in order to smooth the MS-CVs. At 5 mM $NaBD_4$ (Figure IV.22 a), the onset potential is higher than usual (-150 mV instead of -250 mV *vs* RHE), because even after acid etching, some sites of the Ni foam remained partially oxidized (see chapter V). It is also possible that the onset potential might be influenced by an isotopic effect H by D replacement in the borohydride). However, increasing the concentration to 50 mM $NaBD_4$ allowed to reduce a bit more those sites and an OCP of -220 mV *vs* RHE was reached. At low $NaBD_4$ concentration, H_2 is detected at -50 mV *vs* RHE on the cathodic sweep, as soon as the faradic current decreases and proportionally follows it throughout the whole HER region. On the anodic sweep, bubbles trapped in the pores delay the detection of H_2 resulting in a hysteresis. The slope of the $I_{m/z=2}$ current changes around $E = 0$ V *vs* RHE, because the generation of H_2 stops: this suggests that the remaining current detected for $E > 0$ V *vs* RHE originates from this residual H_2 trapped in the pores of the electrodes.

Because of this residual H_2, the calibration of the DEMS cell using this porous Ni electrode might be overestimated. It is difficult to observe the contributions from HD and D_2 at low concentrations because all signals do overlap. We can still observe that the D_2 seems to follow the faradic current and that, obviously, $I_{m/z=3}$ (HD) is measured only when both H_2 and D_2 are also detected.

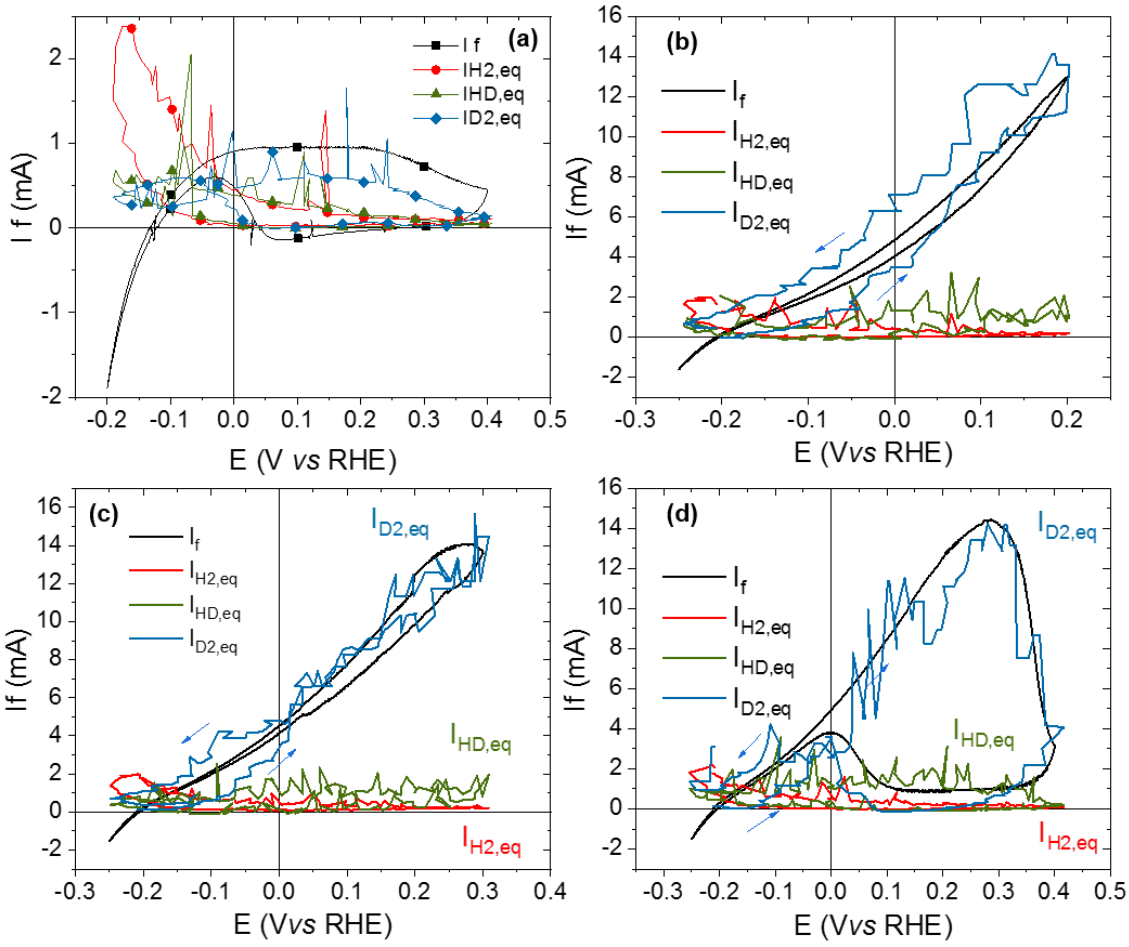

Figure IV.22. DEMS measurement of etched nickel felt in Ar-saturated 1 M NaOH + (a) 5 mM or (b, c, d) 50 mM $NaBD_4$, v_s = 10 mV.s^{-1}. The ionic (H_2, HD, D_2) currents are calibrated to the faradic current (K = 2.20 10^{10})

To have a clearer vision of the behavior of D_2, the concentration was increased to 50 mM $NaBD_4$ and the upper potential limit was varied from 0.2 to 0.4 V *vs* RHE (Figure IV.22b, c, d). Now that the H_2 contribution is smaller compared to the D_2, it is easier to observe how it is generated along the BOR. At potentials above E = 0 V *vs* RHE, the D_2 current is proportional to the faradic one, with a ratio of around 1:1 (with the error from the noise). For potentials below 0 V *vs* RHE, the D_2 contribution does not follow the faradic current and progressively increases with potential to match it around 0 V *vs* RHE. This agrees with the RDE and RRDE measurements: large gas generation is observed once the stable steady-state of the reaction is reached. This means that above 0 V *vs* RHE, 2 molecules of D_2 (or H_2 when using $NaBH_4$) are generated for one BD_4^- (or

BH_4^-) oxidized, translating in a 4-electron loss; this again fits our first calculations (Figure IV.17). When the upper potential limit is increased to the surface $Ni(OH)_2$ formation region (Figure IV.22d), the D_2 current falls to zero (at 5 mM $NaBD_4$ on the forward scan and 50 mM $NaBD_4$ on the backward scan) where a residual (and stable) current is still measured on the electrode.

The number of electrons valorized can be estimated using these DEMS CVs with calibrated ion currents. The equation 4.6 is taken from Ref [211] where the faradic current is reported to the ionic currents involved in the electron loss. In this case, the calculations were performed using either both D_2 and HD contributions or the D_2 current only, and the results are presented for both concentrations of $NaBD_4$ on Figure IV.23.

$$n_{electron\ per\ BD_4^-} = \frac{8\ I_f}{\frac{1}{2}\ I_{HD} + \ I_{D_2} + \ I_f} \qquad \text{(equation 4.6)}$$

with:

$n_{electronperBD_4^-}$= Number of electron valorized per BD_4^-

I_f= Faradic current (mA)

I_{HD} = Calibrated ionic current of HD (mA)

I_{D2} = Calibrated ionic current of D_2 (mA)

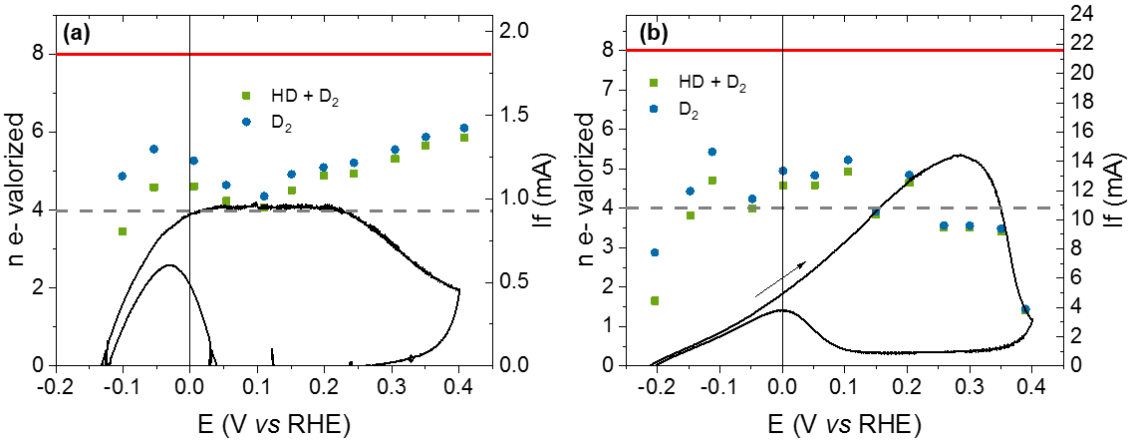

Figure IV.23. Estimation of the number of electron valorized by Ni surfaces during anodic sweep of the BOR in Ar-saturated 1 M NaOH + (a) 5 mM and (b) 50 mM $NaBD_4$. Calculation made with either the HD and D_2 or D_2 only contribution using equation 4.6.

Overall, including the HD contribution in the calculation decreases the number of electrons valorized by almost 1 at low potentials but is not so impactful above 0.1 V *vs* RHE, which seems logical because almost no HD is detected in this potential region. The estimation with D_2 only does not contain all D species lost and therefore the first estimation should be more accurate. At 5 mM $NaBD_4$, the estimated number of electrons

valorized is comprised between 4 and 5 until the formation of surface $Ni(OH)_2$, where it increases, because as mentioned previously, less D_2 is detected on an oxidized surface. For the 50 mM $NaBD_4$ concentration, the same conclusion is drawn, except that this time the number of electrons plummets with the faradic current (on the forward scan). The proposed hypothesis is that the passivation/poisoning occurs way faster at higher concentration, so the detection of D_2 is delayed to some extent, resulting in a significant variation of the I_f/I_{D2} ratio. This 4 to 5 electron valorized estimation is in agreement (but slightly greater) with what was expected from R(R)DE measurements; again, the calibration of the ionic current might have been overestimated and thus a slightly lower number of electrons should be expected, which strengthens the agreement. An observed decrease of the number of transferred electrons in the vicinity of mixed potential (especially noticeable at a higher borohydride concentration) may be attributed to the contribution of heterogeneous hydrolysis of borohydride on the Ni surface.

IV.4.2.2 Fourier Transform Infra-Red spectroscopy

In situ FTIR measurements were performed (by Alexandr Oshchepkov and Antoine Bonnefont, mostly) to investigate the nature of the intermediate species and products formed during the BOR on a Ni electrode. To study a metallic electrode, a 10 mm polycrystalline Ni disk was polished and directly installed in the N_2-purged FTIR cell. For more details about the cell and the acquisition parameters, refer to section "II.3.3 Coupled spectroscopic method".

Reference spectra using separately $NaBH_4$, $NaBD_4$, NH_3BH_3, $NaBO_2$, $Na_2B_4O_7$ were acquired at OCP to measure the wavenumber of the possible BOR intermediate species. Each band was assigned to a species using Refs [202–205] and the resulting spectra can be found in section II.3.3. Once the references were acquired, the Ni electrode was characterized in BOR conditions in both 0.1 M NaOH + 0.2 M $NaBH_4$ (this relatively low NaOH concentration was chosen to avoid degradation of the ZnSe prism) and 0.1 M NaOD + 0.2 M $NaBD_4$ electrolytes at increasing potentials from E_{OC} to E = 0.4 V *vs* RHE (Figure IV.24). This large fuel concentration was chosen to magnify the detection of boron-based species (note that at lower borohydride concentrations it was not possible to detect any spectral features corresponding to BOR products/intermediates). 11 spectra were measured every 100 mV and only the last ones are represented for each potential. In presence of borohydride, positive bands appear at 2264 (broad feature, comprising several absorption peaks) and at 1100 cm^{-1}, which correspond to B-H stretching and deformation vibrations of BH_4^-, correspondingly, and thus evidence consumption of the latter (Figure IV.24 a) already at E_{OC}, suggesting non-negligible hydrolysis of the fuel. Some B-O and/or B-OH bonds are also detected and originate

from the products of this hydrolysis, their tentative assignment being presented further in the text. This behavior, mainly driven by the heterogeneous hydrolysis process, remains similar until E = 0 V *vs* RHE, where new B-O based species, produced by the BOR, are evidenced by the appearance of rather intense 1410 cm^{-1} and 1380 cm^{-1} and less intense 1150 and 1050 cm^{-1} absorption bands. These peaks increase with the potential (and oxidation current), confirming that they mark the formation of BOR products. The hydrolysis product initially detected by the simultaneous appearance of 1150 and 960 cm^{-1} bands disappears. An important observation regarding the BOR mechanism is that no formation of B-H based species (1180 cm^{-1}) are detected in this potential window (above 0 V vs. RHE), suggesting once again a new reaction pathway avoiding $BH_{x,ad}$ intermediate species, unlike for the previously-studied PGM electrodes.

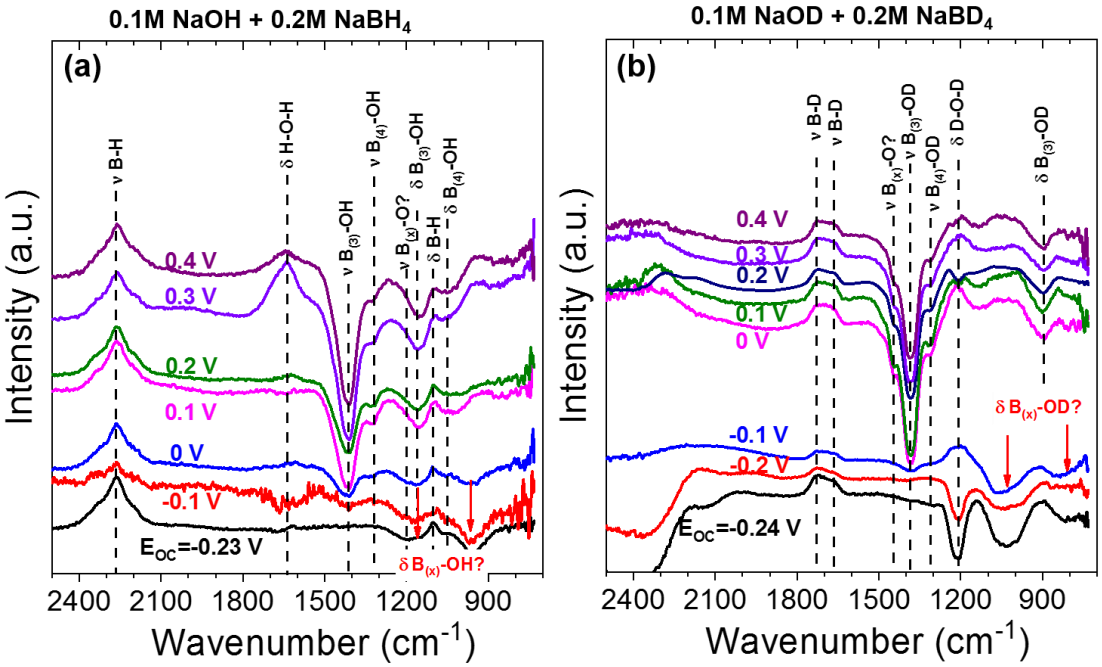

Figure IV.24. *In-situ* FTIR spectra obtained using a ZnSe prism on a Ni electrode in (a) 0.1 M NaOH + 0.2 M $NaBH_4$ or (b) 0.1 M NaOD + 0.2 M $NaBD_4$ electrolytes at potentials increasing from E_{OC} to E = 0.4 V *vs* RHE.

Using deuterated BD_4^- (Figure IV.24b) results in similar observations and allows one to assign the spectral features. The consumption of BD_4^- is detected already at E_{OC} (1667 cm^{-1} band corresponding to B-D stretching vibration). The hydrolysis products are now detected at 1050 and 850 cm^{-1}. The change of the wavenumber from 1150 and 960 cm^{-1} in BH_4^- to 1050 and 850 cm^{-1} in BD_4^- allows one to attribute them to B-O-H and B-O-D deformation vibrations of hydrolysis products/intermediates (likely some $BH_x(OH)_y$ species). The band at 1200 cm^{-1} corresponds to D-O-D scissor vibration of D_2O (note that the appearance of this band correlates with the *ca.* 2400 cm^{-1} one, the latter corresponding to the O-D stretch in D_2O). Similarly to Figure IV.24a, the hydrolysis products (evidenced by 1050 and 850 cm^{-1} bands) disappear once the potential is

increased above 0 V *vs* RHE, and again, B-O based species are produced, this time detected by bands at 1380, 1310, and 890 cm^{-1}, and again, no new B-D bonds are witnessed. Comparison of the spectral features observed at E ≥ 0 V *vs* RHE in $NaBH_4$ + NaOH and $NaBD_4$ + NaOD allows us to attribute them to the formation of $B(OH)_3$ and $B(OH)_4^-$ products as confirmed by the presence of stretching vibrations $\nu(B_{(3)}\text{-}OH)$ at 1410 cm^{-1} ($\nu(B_{(3)}\text{-}OD)$ at 1380 cm^{-1}), $\nu(B_{(4)}\text{-}OH)$ at 1315 cm^{-1} ($\nu(B_{(4)}\text{-}OD)$ at 1310 cm^{-1}), and deformation vibrations $\delta(B_{(3)}\text{-}OH)$ at 1150 cm^{-1} ($\delta(B_{(3)}\text{-}OD)$ at 890 cm^{-1}). Simultaneous detection of $B(OH)_3$ and $B(OH)_4^-$ products can be explained by the local pH change in the thin layer (due to an insufficient NaOH concentration) and the ensuing acid-base equilibrium ($B(OH)_3 + 2H_2O \rightleftharpoons [B(OH)_4]^- + [H_3O]^+$; $pK_a = 8.98$).

To conclude, the formation of B-O species during the BOR was clearly highlighted, while no B-H species were found. It was also observed that the hydrolysis of the fuel is significant at potentials below $E = 0$ V *vs* RHE (and likely occurs via formation of a $BH_x(OH)_y$ intermediate species), and that above this potential, the behavior changes, in accordance with the previous measurements.

IV.4.3 Computational modelling by DFT and Kinetic simulation of the BOR

IV.4.3.1 Binding energy of intermediate species by DFT calculations

To better understand the superior performance of Ni electrocatalysts in the BOR, DFT calculations (performed by Michael Janik, Pennsylvania State University and Gholamreza Rostamikia) were used to determine the binding energies of the key species on the Ni (111) surface and compare them with the ones published for Pt (111), Au (111) and Pd (111) surfaces. Differences among these metals are apparent in the initial adsorption and B-H bond dissociation of BH_4^-. As Table IV.2 shows, the binding of borohydride varies from strong on Pt to weak on Au surfaces, with Pd and Ni metals having intermediate values. The inability of Au to break B-H bonds at low BOR overpotentials [137,211,217] makes this metal inappropriate for practical applications. On the Pt (111) surface, the adsorption of BH_4^- species is detrimentally-strong, resulting in BH_4^-dissociation, with no barrier for B-H bond breaking [215]. This leads to fast poisoning of the Pt active sites with BH* species and formation of H* that contribute to the H_2 generation. Oxidation of the BH* species resulting from BH_4^- dissociation is the rate-determining step on Pt [215,216]. The interaction of BH_4* with the Ni surface is intermediate to that of Au and Pt. The binding is strong-enough to enable subsequent oxidation, but not too strong to induce severe surface poisoning. DFT calculations predict molecular (non-dissociative) adsorption of BH_4^- on Ni (111) surface, although the stretching of the B-H bond suggests its facile dissociation. Although the detailed

data regarding adsorption of various BH_xO_y species are not included for the Pd surface, the electrochemical results point to a similar behavior as for Pt surface.

Table IV.2 Binding energies of species bound to the M (111) surface at optimal binding sites.

Species	Binding energy (eV)			
	Ni (111)	Pt (111)	Au (111)	Pd (111)
BH_4*	-3.68; -3.50 [388]	-	-1.73 [217]; -1.96 [388]	-
BH+3H*	-	-4.73 [215]; -4.56 [388]	-	-3.63 [388]
BH_3*	-2.19	-1.94 [215]	-0.55 [217]	-
BH_2*	-4.10	-3.40 [215]	-2.64 [217]	-
BH*	-5.39	-6.14 [215]	-4.40 [217]	-
B*	-5.75	-6.50 [215]	-4.43 [217]	-
BH_3OH*	-2.77	-	-1.08 [217]	-
BH_2OH*	-1.27	-0.06 [215]	-0.06 [217]	-
BHOH*	-3.46	-3.31 [215]	-2.34 [217]	-
BOH*	-3.74	-4.41 [215]	-2.76 [217]	-
$BH(OH)_2$*	-0.49	-0.17 [215]	-0.05 [217]	-
$B(OH)_2$*	-2.36	-3.09 [215]	-2.20 [217]	-
$B(OH)_3$*	-0.22	-0.16 [215]	-	-
H*	-2.86; -2.94 [389]	-2.72 [215]; -2.72 [389]	-2.12 [217]; -2.18 [389]	-2.88 [389]
OH*	-3.37; -3.42 [390]	-2.26 [215]; -2.34 [390]	-1.79 [217]; -2.21 [390]	-2.62 [390]
H_2O*	-0.30; -0.33 [390]	-0.25 [215]; -0.29 [390]	-0.11 [217]; -0.12 [390]	-0.30 [390]

Subsequent reaction steps also suggest that reaching a limiting current for the borohydride oxidation can occur at low overpotentials on Ni (111) and *via* an alternative mechanism than found on Pt (111). Binding of the BH* species is weaker on the Ni (111) surface compared to the Pt (111) surface. Alternatively, BH_2OH* binds more strongly to Ni (111) surface compared to Pt (111) surface, causing B-OH bond formation to precede complete B-H dissociation, as BH_2OH* is the significantly-preferred 4-electron intermediate on Ni (111) over BH*, in agreement with the experimental data. The reaction energy for BH_4* conversion to BH* and BH_2OH* is calculated on the Ni (111) surface at 0 V *vs* RHE:

$BH_4^* + 3OH^- \rightarrow BH_2OH^* + 2H_2O + 3e^-$ ΔG = -0.47 eV (equation 4.7)

$BH_4^* + 3OH^- \rightarrow BH^* + 3H_2O + 3e^-$ ΔG = +0.17 eV (equation 4.8)

Therefore, unlike the Pt (111) surface, Ni (111) will not be poisoned by BH* species at low potentials, suggesting that Ni (111) can outperform Pt (111) surface below E = 0 V *vs* RHE (this agrees with the FTIR data: no B-H bonds were detected for Ni). However, some poisoning was still observed at low potential and a potentially activated step is required to regenerate the Ni surface (Figure IV.20). The expected higher coverage of OH* on Ni (111) at BOR-relevant potentials (see stronger OH* binding in Table IV.2) will also help to promote B-OH bond formation. This also fit the CA measurements, where the current was observed to be more stable on Ni. However, it is important to keep in mind that slight poisoning is still observed on Ni surfaces, as discussed above.

The HER competes with the BOR for E < 0 V *vs* RHE. The high HER activity of Pt (relative to Ni) results in intensive H_2 escape, while the relatively strong H* adsorption on metallic Ni [289], results in low activity in the HER. Based on DFT results, the BOR on Ni (111) is expected to be faster than on Pt (111) at low potentials, though one cannot differentiate whether this is the leading cause of the observed higher oxidation current on Ni at low potentials, rather than the lower competing reduction current for the HER on Ni.

IV.4.3.2 Kinetic simulation of the BOR on metallic Ni

By taking into account all the data gathered from the previous experiments and calculations, a tentative kinetic model was established (mostly by Antoine Bonnefont), so as to account for (i) the influence of the BH_4^- concentration, (ii) the influence of the Ni sites density, (iii) the hydrogen generation measured by DEMS and (iv) the intermediate species detected by FTIR and RRDE (only BO_2^- and related species but no BH_3OH^- or other B-H based species with x < 4). The proposed reaction pathway is described by equation 4.9 to 4.12. The values proposed for the reaction constant are used for the kinetic simulations but are still preliminary guesses.

$BH_4^- \leftrightarrow BH_{4,ad} + e^-$ (equation 4.9)

$BH_{4,ad} + 2\,OH^- \rightarrow B(OH)_{2,ad} + 2\,H_2 + 2\,e^-$ (equation 4.10)

$B(OH)_{2,ad} + OH^- \rightarrow B(OH)_{3,ad} + e^-$ (equation 4.11)

$B(OH)_{3,ad} + OH^- \rightarrow BO_2^- + 2\,H_2O$ (equation 4.12)

Step 1 (equation 4.9) is fast on Ni (k_1= 2.10^4 $mol^{-1}.L.s^{-1}$). It requires several adjacent Ni sites. It might be reversible with an equilibrium potential close to or even below E = -

0.5 V *vs* RHE, in accordance with the binding energy of BH_4^* on Ni. Step 2 (equation 4.10) is also fast (k_2 = 100 s^{-1}) on Ni and comprises several elementary steps (which are currently not fully understood). The kinetics of this step strongly influences the shape of the current-potential curves. This step is potential-activated. The H_2 produced might adsorb on the Ni surface and contribute to the surface blocking. Step 3 (equation 4.11) is slow; it is the rate-determining step (k_3 = 10 s^{-1}). It is potential-activated with a charge-transfer coefficient lower than 0.5. Step 4 (equation 4.12) is fast (k_4 = 500 s^{-1}). Preliminary simulations were performed using these elementary steps with their corresponding rate constants on two different Ni surfaces ('flat' and 'rough'). Details about the simulation and its parameters are given in section "II.5 Kinetic modelling". Figure IV.25 presents the simulation of a flat metallic surface (low active site density θ = 4.4 10^{-9} mol.cm^{-2}) in either supporting electrolyte or in BOR conditions. Such surface could be compared with the polished polycrystalline Ni disk studied in section IV.2. The behavior of metallic Ni in 1 M NaOH (Figure IV.25a) is correctly reproduced with a low HER activity and a Ni/surface α-$Ni(OH)_2$ transition peak at E = 0.25 V *vs* RHE. For E = -0.3 V *vs* RHE, in presence of borohydride (Figure IV.25b), $BH_{4,\,ad}$ species now covering the surface in competition with H_{ad}, delaying the HER and related H_2 generation at the electrode (in this preliminary model, only the hydrolysis at OCP is taken into account). This results in a BOR onset potential at -0.250 mV *vs* RHE, which is slightly lower than the experimental data (E_{onset} = -0.2 V *vs* RHE on Figure IV.4). The rest of the reaction fits correctly the faradic current measured on Figure IV.4 with the polycrystalline Ni disk. With this reaction pathway, two H_2 molecules are lost per one BH_4^- anion oxidized, resulting in a H_2 escape current equal to the faradic one (this corresponds to the DEMS experimental data and the number of electrons measured via RDE). The delayed gas generation below 0 V *vs* RHE observed with DEMS is now masked by the H_2 produced by the HER, since these two contributions cannot be separated anymore, because of the use of $NaBH_4$ and not $NaBD_4$. This will be considered for further updates of the model. Regarding the surface coverage, $BH_{4,ad}$ species are replaced by $B(OH)_{2,ad}$ when the reaction starts through Step 1 (equation 4.9) and when the potential exceeds E = 0 V *vs* RHE; all the $BH_{4,ad}$ are consumed and only $B(OH)_{2,ad}$ and H_{ad} adsorbates are present on the surface. The adsorption of OH_{ad} at higher potential results in a decay of $B(OH)_{2,ad}$ and therefore the faradic current as observed in the experiment. Overall, this first simulation is capable to reproduce the behavior observed on Ni disk electrode with a low active site density, where the reaction starts at low potential but does not reach a clearly marked plateau before the surface is oxidized.

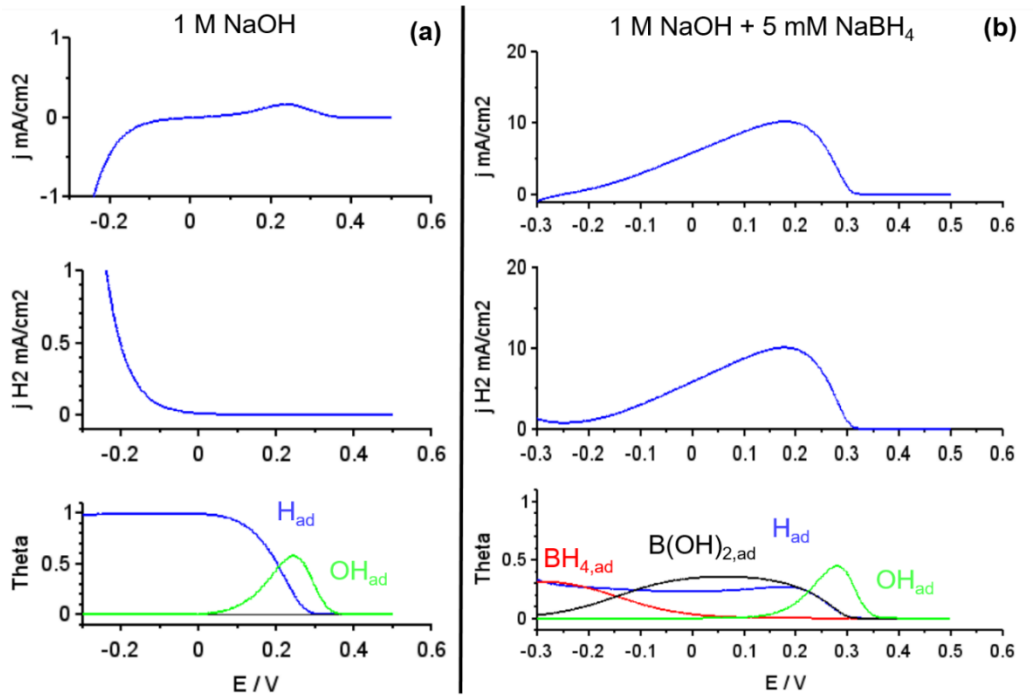

Figure IV.25. Kinetic simulation of a flat metallic Ni electrode (θ = 4.4 10^{-9} mol.cm^{-3}) in (a) supporting electrolyte: 1 M NaOH at ω = 0 rpm or (b) in BOR conditions: 1 M NaOH + 5 mM $NaBH_4$ at ω = 1600 rpm. For each conditions the hydrogen escape current as well as the surface coverage is represented along the faradic current *vs* the applied potential.

To simulate the Ni_{ED}/C electrodes the density of active sites was increased by a factor 1000 (θ = 4.4 10^{-8} mol.cm^{-3}) and the resulting calculations are presented on Figure IV.26. In supporting electrolyte, the behavior of the Ni surface is similar to the previous simulation, with only the current density being greater, because of the highest site density. In presence of 5 mM $NaBH_4$ (Figure IV.26b) the onset of reaction is still E_{onset} = -0.250 mV *vs* RHE, which now fits better the experimental data. A plateau is reached around E = -0.1 V *vs* RHE, in agreement with the RDE measurements (Figure IV.15). At this potential, the H_{ad} coverage increases at the expense of $B(OH)_{2,ad}$ originating from the release of H_2. It results in a small decrease of the faradic current until the formation of OH_{ad}, which will allow the oxidation of these poisoning H_{ad} species. This is not observed in the experiment, so the kinetic model can still be modified/improved. The hydrogen escape current also decreases from this potential, but this is also observed by DEMS at 5 mM $NaBD_4$, where the faradic current is superior (Figure IV.22a).

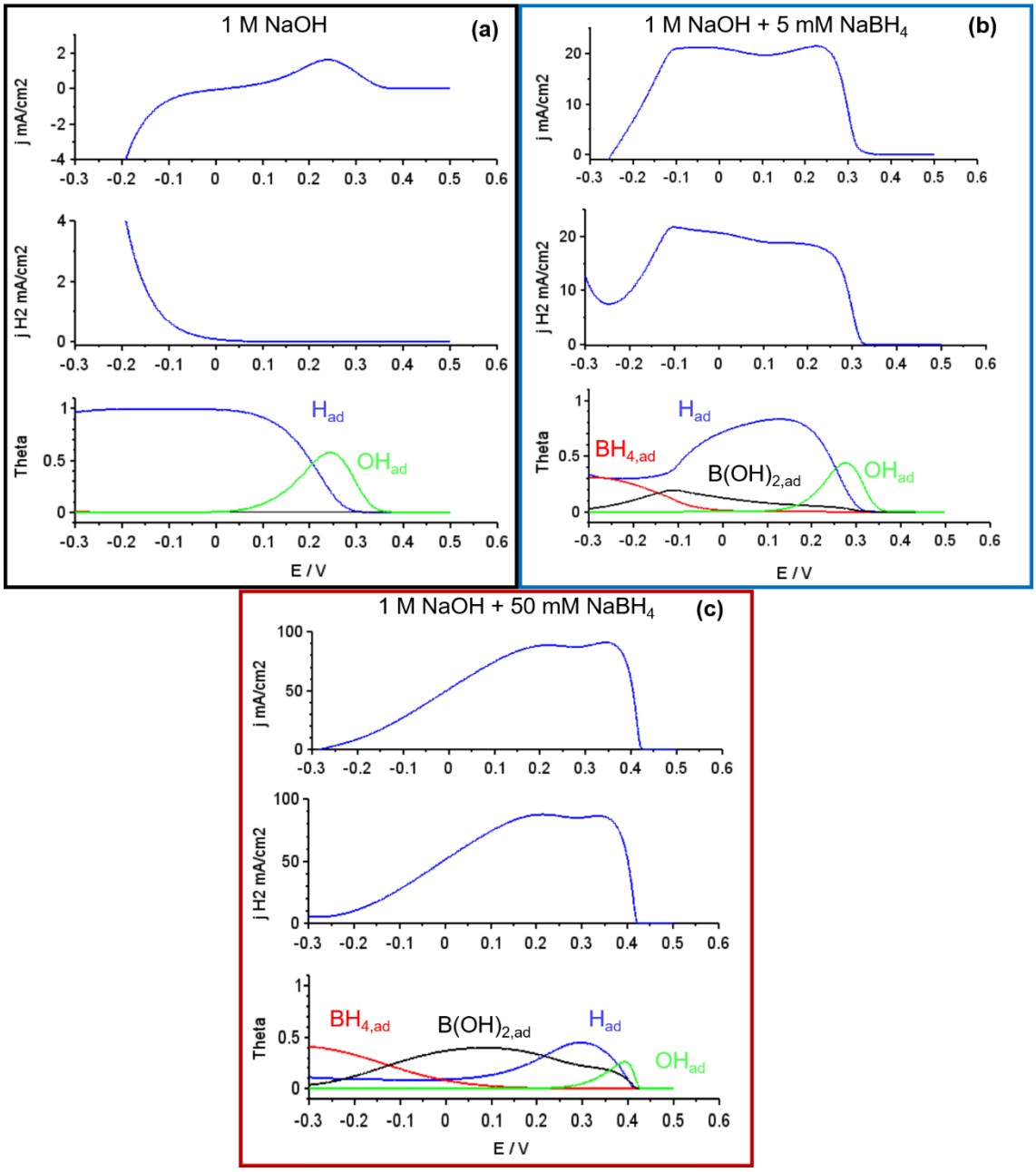

Figure IV.26. Kinetic simulation of a rough metallic Ni electrode (θ = 4.4 10^{-8} mol cm^{-3}) in (a) supporting electrolyte: 1 M NaOH at ω = 0 rpm or in BOR conditions: 1 M NaOH + (b) 5 mM or (c) 50 mM $NaBH_4$ at ω = 1600 rpm. For each conditions the hydrogen escape current as well as the surface coverage is represented along the faradic current *vs* the applied potential.

For [$NaBH_4$] = 50 mM (Figure IV.26 c), the simulation fits correctly the experimental data up to E = 0.3 V *vs* RHE, where the faradic current should quickly decrease because of the formation of surface oxides. On the simulated curves, an activity rebound is observed before passivation at E = 0.4 V *vs* RHE. By looking at the coverage of the surface, it is explained by the fact that the same resurgence of H_{ad} species is observed, but delayed from E = -0.1 to 0.1 V *vs* RHE, because of the higher concentration of $BH_{4,ad}$ and $B(OH)_{2,ad}$ species on the surface. At this concentration, the formation of OH_{ad}

species is also delayed, which explains why the passivation occurs at higher potential. The reactivation occurs once again when both H_{ad} and OH_{ad} are present at the surface, because of the activity towards the HOR increases in presence of surface oxides (as explained in the first section of this chapter). Overall, this proposed kinetic model gives promising simulation of the BOR on metallic Ni surfaces, fitting reasonably the experimental data while taking into account the influence of the active site density and the borohydride concentration. The effect observed where H_{ad} species reappear on the surface at a certain overpotential and the related hydrogen escape, does not correspond to the experimental behavior of metallic Ni electrode, though, and it should be reconsidered to keep improving this model. This is probably caused by the fact that the local H_2 concentration is overestimated in the kinetic model, since the formation of H_2 bubbles is not taken into account. This results in an artificial accumulation of hydrogen in the diffusion layer in the considered model, increasing the rate of H adsorption.

IV.5 Conclusions

In this chapter the ambiguities regarding the behavior of Ni electrodes towards the BOR were unveiled thanks to the work of Oshchepkov *et al.* on the influence of the state of surface for the hydrogen related reactions. The key factor to reach high BOR activity, particularly at potentials below $E = 0$ V *vs* RHE, was to use a purely metallic surface and avoid irreversible oxidation by maintaining the anodic potential below $E = 0.5$ V *vs* RHE. The use of polycrystalline Ni electrode proved its promising activity, but also revealed large limitations by reaction kinetics, due to a too low active site density.

Bimetallic Ni_xM catalysts obtained by conventional chemical synthesis were studied with the aim to palliate both the irreversible oxidation (the transition-metal co-elements M should help the depassivation of the surface) and the limited number of active sites encountered during the preliminary study on bulk electrodes. The results obtained using these catalysts were disappointing, but helped to reveal a major flaw of the conventional carbon-supported Ni nanoparticle catalysts: even after conditioning in supporting electrolyte and activation in presence of borohydride, the surfaces remained substantially oxidized, which did significantly limit their BOR activity. It confirms why such ambiguities have been observed in the literature, because almost each time this type of catalyst is used, the state of surface is rarely taken into account. A new synthesis procedure needed to be adapted to obtain highly developed metallic Ni surfaces.

The electrodeposition procedure developed by Oshchepkov was reproduced to obtain Ni nanoparticles deposited on a commercial carbon support. This non-noble catalyst presented an impressive BOR activity, especially at low potentials, surpassing even

Pt/C, the current best and most commonly used catalyst for the BOR. At higher potentials (E > 0 V *vs* RHE), Ni_{ED}/C still outperformed the best conventional Ni/C and also Pd/C catalysts, but was surpassed by Pt/C. Interestingly, mass-transport limitation was reached on Ni_{ED}/C at a current two times smaller than the one of Pt/C, and potentiostatic measurements revealed a much better BOR stability on metallic Ni electrodes than on any noble metal catalyst. These two observations suggest a different reaction pathway for the Ni electrode. To clarify the situation, electrochemical measurements with and without coupled spectroscopic method were performed: they confirmed that the BOR occurs following new steps (compared to noble metal electrodes), and that the model described in Chapter III is not valid for Ni electrodes. Combining these experimental data and DFT calculations of the binding energies of adsorbed species, a preliminary kinetic model was proposed. Promising simulation results fitting reasonably the experimental data were obtained. However, the model still needs to be improved to fully match the experimental data, especially regarding the adsorption of H_{ad} species at high overpotential.

CHAPTER V: Integration of Ni electrodes and optimization of DBFC parameters

The aim of this chapter is to move from laboratory-scale Ni surfaces presented in chapter IV towards efficient and non-noble DBFC anodes. Other full cell parameters, such as the cathode and the membrane, will also be investigated to improve the complete system. This chapter is based on an *ACS Catalysis* article about metallic nickel for the BOR [291] and on a more recent one addressing a new support material and its tuning to obtain optimal performance, published in *ChemElectroChem.* [391]. The chapter will be structured as follow: Ni_{ED}/C anodes of 8 cm² will be elaborated by adapting the electrodeposition procedure; then to optimize the anode properties the carbon support will be replaced by Ni 3D structures; from this point new membranes (commercial or made by collaborators) as well as new non-noble cathode catalysts (made by Prof. Jaouen's group) will be tested to improve the overall performance of the unit DBFC.

V.1 Elaboration of Ni_{ED}/C anodes

V.1.1 Upscaling the Ni_{ED}/C electrodes

V.1.1.1 Adapting the electrodeposition procedure

State-of-the-art FC electrodes are composed of a thick (ca. 200 µm) gas diffusion layer (GDL), usually made of carbon paper, used to ensure a good mass-transport of the fuel or oxidant to the active layer. The active layer is composed of the carbon-supported electrocatalysts nanoparticles (e.g. with Vulcan® XC72 or Ketjen Black® 600 carbon supports) combined with an appropriate amount of ionomer (most commonly Nafion® in PEMFC). It is very similar to the thin layer prepared as WE on RDE tips in half-cell configuration, described in the "II.2 Electrolytes and catalyst inks preparation" section. The active layer is elaborated from an ink, that can be deposited either on the GDL (Catalyst Coated Backing, CCB) or directly on the membrane (Catalyst Coated Membrane, CCM).

The Ni_{ED}/C samples presented in the previous chapter could have been transferred into active layers via inks. However, because Ni nanoparticles must be maintained metallic to keep their outstanding BOR activity at low potentials (E < 0 V *vs* RHE), it is not straightforward to create an ink to coat active layers on the GDL or the membrane. Indeed, this process involves mixing steps and a mild heat-treatment (usually performed under atmospheric air) and hence, would irreversibly oxidize the metallic nanoparticles. Operating in glove box from the ink preparation to the cell testing would have been a

possible but much time-consuming and tedious. A more convenient procedure not requiring any atmosphere-controlled environment, to move from Ni_{ED}/C electrodes for RDE (S_{geo} = 0.196 cm²) towards the bigger 8 cm² surface required in the unit DBFC, is to keep the same electrodeposition synthesis technique. The larger surface area at stake imposes to adapt the procedure. To keep it simple, the electrodeposition was firstly performed directly onto the carbon GDL fibers (from SGL, used bare, without carbon black-based microporous layer). That way, nanoparticles are grown directly in the pores of the carbon paper, hence merging the GDL and the active layer properties: the obtained simple final structure of the electrode will be called Gas Diffusion Electrode (GDE).

The ED procedure presented in Chapter IV was reproduced on these 8 cm² GDE with several modifications: the concentration of Ni_2SO_4 has been increased 10 times ($[Ni_2SO_4]_{GDE}$ = 0.1 M); a third conditioning potential has been added prior to the nucleation and growth ones (E_1 = 0.03 V *vs* RHE for 5 s) in order to avoid current overloads at the start of the deposition; the nucleation time was decreases from 15 s to 10 s but kept at the same potential (E_2 = -0.74 V *vs* RHE) and the growth step remained unchanged. The main modification is the possibility to reproduce this three-potential electrodeposition step (referred later as "one ED pulse") enabling to tailor the loading of Ni nanoparticles deposited at the surface of the support and to have a decent penetration of the Ni nanoparticles in the whole GDL thickness/volume. Thanks to this procedure, two sets of samples were obtained with distinct loadings; one pulse led to the low loading electrode (later on referred as Ni_{ED}/GDE-L) and six pulses to the high loading electrode (later on referred as Ni_{ED}/GDE-H). The detailed procedure and the typical electrodeposition transients for both loadings are presented in the section "II.4.1.2. Ni_{ED}/GDE anode elaboration procedure".

Both electrodes were characterized in supporting electrolyte and their respective CVs are represented on Figure V.1. The anodic peak corresponding to the conversion of metallic Ni sites into surface α-$Ni(OH)_2$ at 0.3 V *vs* RHE and the corresponding cathodic peak around 0 V *vs* RHE confirm the metallic state of the electrodeposited Ni. The main improvement observed with these new electrodes is that the ECSA can be tailored. With one pulse, the Ni_{ED}/GDE-L electrode already has a highly developed ECSA (540 cm²); it can be increased further with six pulses (2800 cm² for the Ni_{ED}/GDE-H electrode). The metal loading of the electrode likely grows with the number of pulses, but may not be directly proportional to the electrode ECSA. As described in Chapter IV about the Ni_{ED}/C synthesis procedure, even if the SGL carbon of the GDL and metallic Ni are poor catalysts towards the HER, at such low potentials (-0.74 or -0.54 V *vs* RHE) a large amount of H_2 is inevitably evolved, thereby affecting the overall faradaic efficiency of the deposition. The faradaic efficiency, which was estimated as *ca.* 35% for the Ni_{ED}

electrodes prepared in RDE configuration, must be recalculated because the conditions have been modified to produce the higher surface electrodes.

In order to have a precise idea of the Ni mass deposited on each of the electrodes, they were analyzed using ICP-MS. The procedure to prepare the electrodes for this characterization is detailed in the section "II.3.2.4 Inductively coupled Plasma Mass Spectrometry" and the following loadings were obtained: Ni_{ED}/GDE-L, m_{Ni} = 0.60 ± 0.05 $mg_{Ni}.cm^{-2}$); Ni_{ED}/GDE-H, m_{Ni} 3.6 ± 0.1 $mg_{Ni}.cm^{-2}$). Using the charge of the deposition transients (Figure V.1), and assuming 100% efficiency, the Faraday law (equation 5.1) gives deposited Ni masses respectively of 0.57 $mg_{Ni}.cm^{-2}$ and 4.01 $mg_{Ni}.cm^{-2}$; the expected Ni loading being directly proportional to the number of pulses.

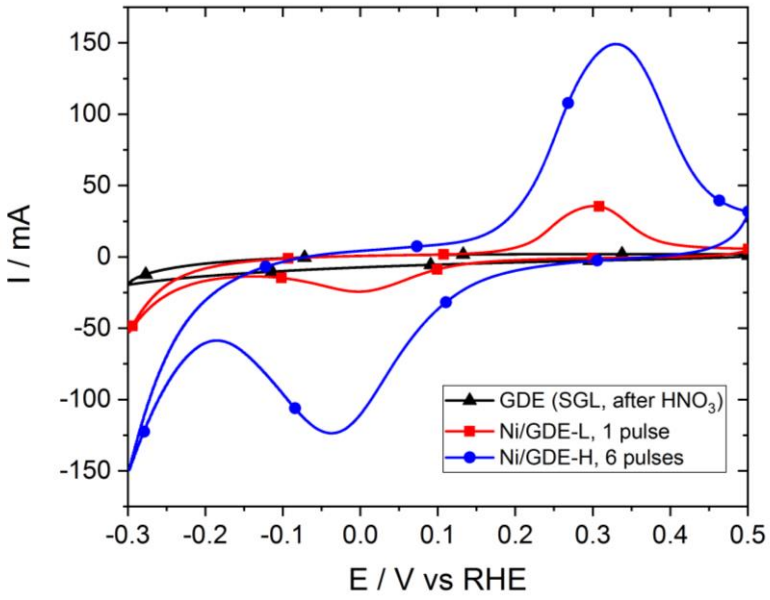

Figure V.1. CVs obtained in N_2-saturated 1 M NaOH at v_s = 20 $mV.s^{-1}$ for SGL (black curve) and new Ni_{ED} –based electrodes. Ni_{ED}/GDE-L (red curve, ECSA = 537 cm^2) is obtained with 1 pulse and Ni_{ED}/GDE-H (blue curve, ECSA = 2823 cm^2) with 6 pulses of electrodeposition.

Faraday' Law: $$m_{Ni} = \int_0^{\tau} I\left(\tau\right)d\tau \frac{M_{Ni}}{F.z.A}$$ (equation 5.1)

with:

m_{Ni} = Metal loading deposited ($g.cm^{-2}$)

I = Current (A)

τ = Time of the deposition (s)

M_{Ni} = Atomic mass of nickel (58.7 $mol.g^{-1}$)

F = Faraday's constant (96 485 $C.mol^{-1}$)

z = Number of electrons transferred (2 for Ni^{2+} reduction)

A = Geometric surface area of the electrode (8 cm^2)

Using Faraday's law, the calculated mass deposited for Ni_{ED}/GDE-L is within the error bar given by the ICP-MS analysis, but slightly exceeds that of the Ni_{ED}/GDE-H sample. This translates into an estimated faradic efficiency of 100% and 90% for the Ni_{ED}/GDE-L and Ni_{ED}/GDE-H sample, respectively. This difference can be explained by the pulsed nature of the deposition. Indeed, during the first pulse the electrodeposition occurs with close to 100% current efficiency, because the activity of the carbon support towards the HER is too low to generate substantial amount of H_2 at the applied potential. For the following pulses, metallic Ni is now present at the surface and, even though its HER activity is quite low, it is higher than that of carbon, and is sufficient to reduce the efficiency of deposition by 10%. Compared to the Ni_{ED}/C samples presented in Chapter IV, the efficiency of the Ni deposition was drastically improved, mostly because the Ni_2SO_4 concentration of the deposition bath was increased 10 times, ensuring a good supply of active species to the electrode surface. Moreover, the open porosity of the GDE, compared to a microporous layer, allowed a better mass-transport in the electrode.

The ratio between the ECSA of both electrodes is smaller than 6 ($\frac{2823}{537} = 5.27$). Even by correcting it using the estimated faradic efficiency calculated above, the ratio only reaches 5.8 (the calculation implies approximations). This difference may not only be related to the deposition efficacy, and suggests that the morphology of the electrodes may be different for the two deposits. The same discrepancy is obtained by calculating the specific surface area of both samples using the ECSA and the mass of Ni measured by ICP-AES: $S_{\mathrm{Ni}} = \frac{ECSA}{m_{\mathrm{Ni}}}$ giving S_{Ni} = 11.2 $m^2.g^{-1}$ and 9.8 $m^2.g^{-1}$, for the low and high loading electrode respectively (6 x 9.8/11.2 = 5.25). By comparing this specific surface area, measured from the ECSA, to the theoretical one, it is possible to estimate the degree of agglomeration of the obtained nanoparticles. The theoretical specific surface area can be calculated using equation 5.2:

$$S_{\mathrm{Ni}}^{\mathrm{th}} = \frac{A}{V \cdot \rho_{\mathrm{Ni}}} = \frac{3}{R \cdot \rho_{\mathrm{Ni}}} \qquad \text{(equation 5.2)}$$

with:

$S_{\mathrm{Ni}}^{\mathrm{th}}$ = Theoretical specific surface area of Ni ($m^2.g^{-1}$)

A = Geometric surface area of one crystallite (m^2)

V = Volume of one crystallite (m^3)

ρ_{Ni} = Nickel density ($g.m^{-3}$)

R = Radius of one crystallite (m)

The crystallites size for each sample has been determined by XRD diagrams analysis (Figure V.2b) to be 14 and 16 nm, giving a 'theoretical' specific surface area of 48.1 and 42.0 $m^2.g^{-1}$, for the low and high loading electrode respectively. The fact that the 'theoretical' specific surface area strongly exceeds the measured one (4.3 times both for

Ni_{ED}/GDE-L and Ni_{ED}/GDE-H electrode), suggests that Ni crystallites of 14 – 16 nm size (estimated from XRD) are agglomerated in larger aggregates. Comparing the 'theoretical' values to the measured S_{Ni}, the same 23.3% ratio is obtained for both electrodes suggesting a similar agglomeration degree. Agglomeration of Ni nanoparticles is confirmed by SEM images (Figure V.2), which present Ni particle size of around 200 nm and 500 nm for the low and high loading electrode respectively. Note however that 'compact' 200 to 500 nm diameter Ni particles would have specific surface area of 1 to 3 $m^2.g^{-1}$. This means that these bigger agglomerates are not compact and comprise of smaller nanoparticles, their surface area being partly accessible to the electrolyte.

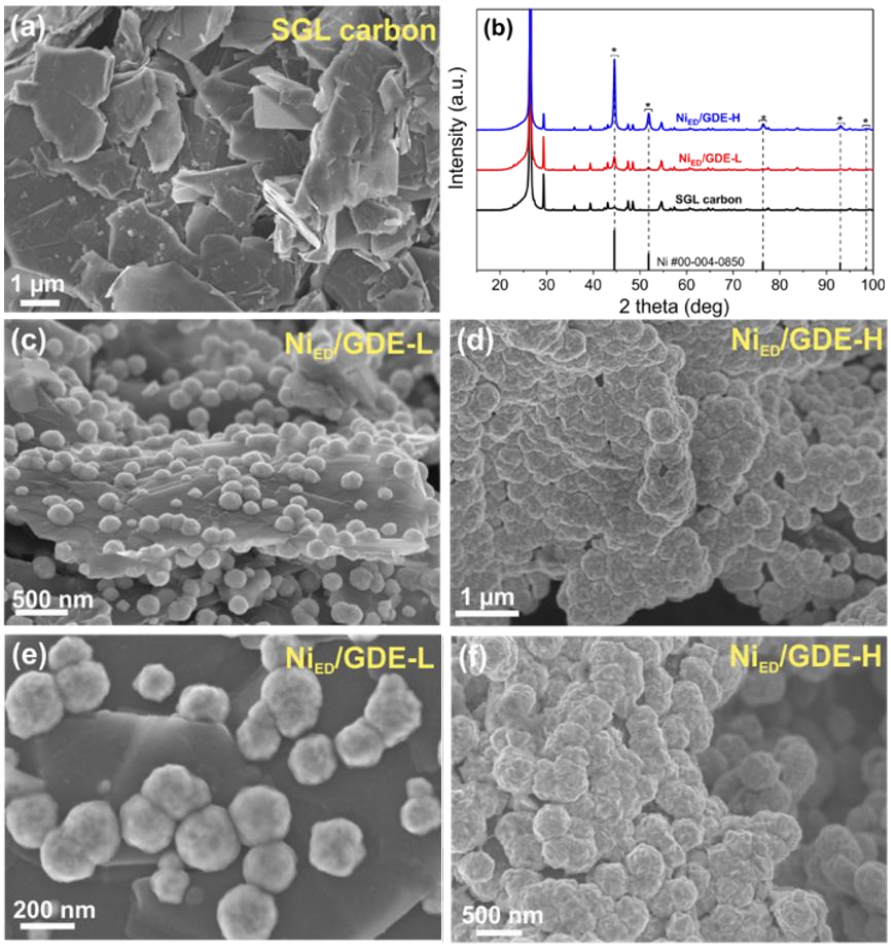

Figure V.2 Characterization of Ni_{ED}/GDE samples. SEM images of pure SGL carbon (a) and after electrodeposition of Ni nanoparticles at low (Ni_{ED}/GDE-L, c and e) and high (Ni_{ED}/GDE-H, d and f) metal loading; (b) XRD patterns obtained for the corresponding samples. Reprinted from Ref. [291].

Before testing these electrodes in DBFC conditions it is important to check if they have not been contaminated during their synthesis, notably by the counter-electrode material (a Pt counter electrode was still used in the same compartment as the working electrode during the first ED procedure). It had been proven in Chapter IV that no Pt re-deposition

occurred on the Ni_{ED}/C samples. However, the conditions of deposition are now harsher: lower applied potentials and higher currents. X-EDS characterization was performed on a Ni_{ED}/GDE-L sample as shown on Figure V.3. The first area (Area 1 on Figure V.3a) analyzed, contained as little particles as possible: mainly carbon with very low amount of Ni was detected (and no Pt). On both areas containing important amount of Ni, no signal was measured for either the Pt M edge (2.05 keV [392]) at low energies (Area 2 on Figure V.3a) or the Lα one (9.44 keV [392]) at higher energies (Area 1 on Figure V.3b). This analysis confirms that the electrodes are not contaminated by Pt and that their DBFC performance should only be attributed to the metallic Ni catalysts.

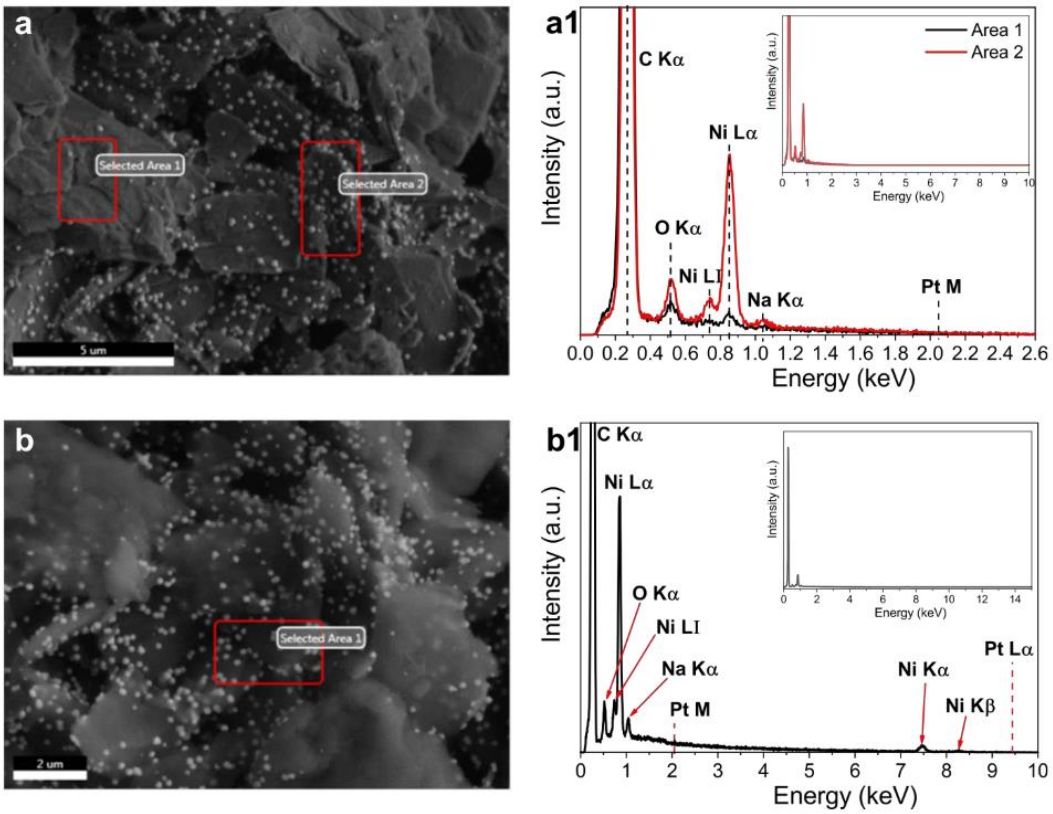

Figure V.3. SEM images of Ni_{ED}/GDE-L sample obtained at (a) 3 kV to scan the low energies region or (b) 10 kV to scan energies high enough to reveal Pt Lα and Ni K bands, and corresponding X-EDS analysis from the marked areas (a1, b1).

V.1.1.2 DBFC performance using Ni_{ED}/GDE anodes

In order to ensure the best state of surface of the Ni-based electrodes and avoid any involuntary oxidation that could occur if they had been exposed too long to O_2, they were prepared on the spot and directly transferred to the DBFC unit cell just after synthesis and a quick rinsing in water. The unit cell used was designed in LEMTA (Laboratoire Énergétique et Mécanique Théorique Appliquée, Nancy, France) and

consisted of an instrumented cell composed of 8 cm^2 electrodes (4 x 2 cm^2). Detailed information about the cell and the measurement protocol is described in section "II.4.2.1 BH_4^-/O_2 DBFC setup". Fresh anodes, with similar properties, were prepared for every new measurement.

As presented on Figure V.4, unit DBFCs using Pt-black/GDE and Ni_{ED}/ GDE anodes displayed open-circuit voltages of $U_{j=0}$ = 1.0 and 1.2 V, respectively, thus reflecting the same 200 mV improvement observed in RDE studies for Ni_{ED}/C samples compared to the Pt/C ones. More importantly, the cell with a Ni_{ED}/GDE-L anode significantly outperformed the Pt-black/GDE one, even at much lower loading of the metal (0.6 $mg_{Ni}.cm^{-2}$ versus 2 $mg_{Pt}.cm^{-2}$, respectively, Figure V.4a). Again, we emphasize that the reduced state (metallic) of the Ni surface is the key factor towards this impressive BOR activity and therefore towards high DBFC performance. For this reason, the cell voltage should not be lowered below U = 0.2 V during the test, to avoid irreversible Ni oxidation and ensure repeatable results. Surprisingly, both Ni_{ED}/GDE-L and Ni_{ED}/GDE-H show similar performance, despite a *ca.* six-fold difference in the Ni-loading. This suggests that the high-performing Ni-based DBFCs may be limited by either (i) the cathode and/or membrane used, (ii) partial utilization of the anode material (bubble formation in the pores of the electrode blocking some active surface), or (iii) mass-transport issues related to the construction of the cell. Although additional studies are necessary to optimize the preparation parameters of the membrane electrode assembly with Ni_{ED} electrocatalysts, DBFCs with Ni_{ED}/GDE anodes already show great promise and outperform DBFCs with Pt anodes in terms of maximum power density normalized by the mass of the active anode component. Besides, they show better performance compared to a hydrogen-fed alkaline membrane FC (AMFC) with a state-of-the-art PGM-free anode electrocatalyst NiMo/KB [197]. The latter system shows a power density of around P_{max} = 120 mW cm^{-2} at j = 0.22 A cm^{-2}, while it is as high as P_{max} = 155 mW cm^{-2} at the same current density for a DBFC with a Ni_{ED}/GDE-L anode, although lower metal loading and operating temperature were used in the latter case (0.6 *vs* 2 mg cm^{-2} and 60 *vs* 70°C for DBFC with Ni_{ED}/GDE and AMFC with NiMo/KB, respectively). Besides this impressive performance, Figure V.4c, d reveals the major drawback of using metallic Ni as the anode catalysts. The amount of H_2 escaping the cell was measured in real time using a PEMFC connected in line with the outlet of the DBFC and functioning in H_2 pump configuration, as detailed in section "II.4.2.1 BH_4^-/O_2 DBFC setup". This measurement revealed high *H_2 escape*, showing that the Ni-based anodes are inefficient to valorize the H_2 produced during the DBFC operation. The *H_2 escape* current only increases when the cell voltage drops, while when using a Pt anode, this current quickly drops as soon as the reaction starts, because of high HOR activity of platinum. This was expected, since metallic Ni is a poor HOR catalysts, as presented in Chapter IV. By looking at the first point on Figure V.4c, the intensity of the hydrolysis

of BH_4^- can be observed. Both Ni anodes produce less H_2 than Pt at the OCV and because of its smaller number of active sites Ni_{ED}/GDE-L exhibits the lowest *H_2 escape*. However, it also implies that, at low cell voltage, the amount of hydrogen escaping the cell will be the most important. By looking at Figure V.4d, it stabilizes around 45% which roughly corresponds to 4 e^- produced per BH_4^- species, as predicted by our tentative model of the BOR on Ni (section "IV.4.3"). For Ni_{ED}/GDE-H the amount of H_2 not valorized is a bit lower, probably because of the higher number of active sites. However, this should translate into higher power density, which is not obvious on the *I-P* curve (Figure V.4b), suggesting that a significant amount of H_2 produced could be trapped in the pores of the electrodes, diminishing both the active area available and the amount of escaping H_2 measured. This morphology issue of the electrode will be addressed in the next section.

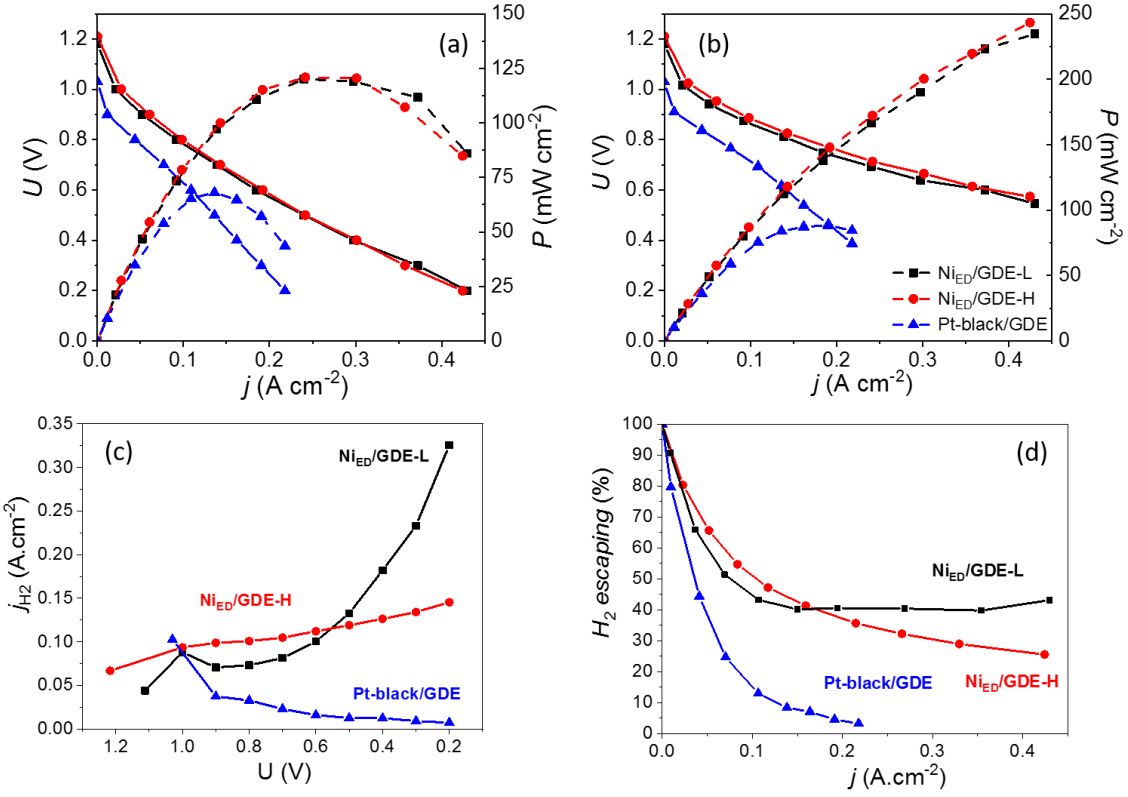

Figure V.4. (a) Raw curves and (b) Ohmic-drop corrected data of *I–U* (full lines) and *I–P* (dashed lines) comparing both Ni_{ED}/GDE loadings with a commercial Pt-black/GDE (2 mg.cm^{-2}) in fuel cell configuration using Pt-black/GDE (2 mg.cm^{-2}) cathode. (c) Equivalent *H_2 escape* current density and (d) corresponding percentage, measured using an in-line PEMFC in hydrogen pump configuration. T = 60°C, 0.5 M $NaBH_4$ + 4 M NaOH.

To improve the ability of the Ni electrode to valorize the produced hydrogen, one could modify the state of surface of the catalysts from metallic towards partially-oxidized, as the latter is very active for the HER/HOR [186,210,289,290]. To that goal, deliberate partial oxidation of Ni_{ED}/GDE-L was performed electrochemically; this resulted in an improvement of the HER activity, but led to inevitable decrease of the number of

metallic Ni sites (Figure V.5a). This electrode was then tested in the DBFC unit cell in similar conditions as for Figure V.4. The resulting *I-U* and *I-P* curve are presented on Figure V.5b: a *ca.* 12% loss compared the fresh Ni_{ED}/GDE-L is observed regarding the maximum power density. This loss was expected from the decreased ECSA observed in supporting electrolyte. However, the power density obtained is still high, meaning that the anode still contains significant amount of metallic Ni, which is confirmed by its near-similar OCV *vs* that for Figure V.4. Figure V.5c also shows that less H_2 escape is monitored during DBFC operation, as expected. Because the overall current density obtained with the partially-oxidized anode is lower, it is important to evaluate the normalized *H_2 escape* current (Figure V.5d): less hydrogen is globally lost with a stable 35% during operation (22% improvement), showing that partial oxidation of the Ni electrode can indeed enable to reduce the *H_2 escape*, but this strategy must be optimized to maintain as well the cell power density.

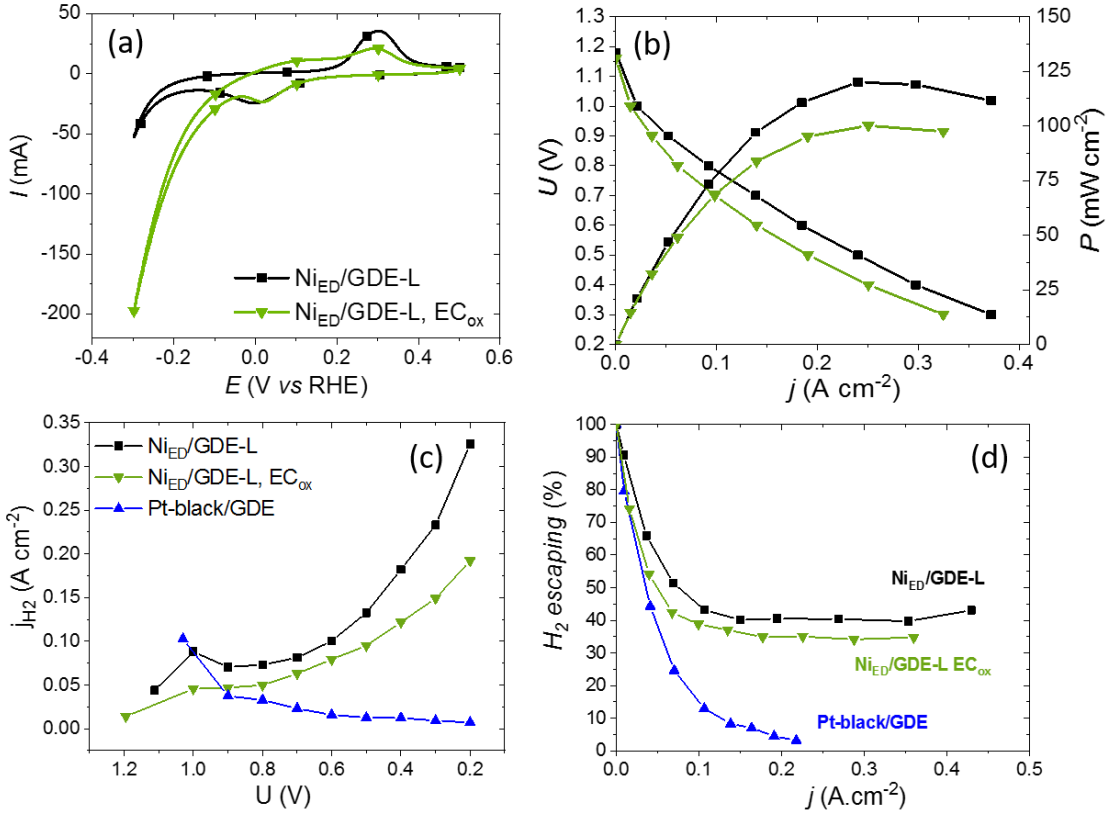

Figure V.5. (a) CVs in supporting electrolytes and (b) *I–U* and *I–P* comparing Ni_{ED}/GDE-L before and after partial oxidation. (c) Current density of escaping hydrogen and (d) corresponding percentage, measured using an in-line PEMFC in hydrogen pump configuration. T = 60°C, 0.5 M $NaBH_4$ + 4 M NaOH.

V.1.2 Stability of Ni_{ED}/GDE anode in DBFC conditions

To complement the study of the Ni_{ED}/GDE anode used in DBFC conditions, some tests were performed to address the question of the stability (both of the anode catalyst material and of the overall DBFC performance). Remarkably, relatively high and stable current densities were obtained for the first time through rather long-term (at least 10 hours) stability tests performed at cell voltages as high as 1.0 V using Ni_{ED}/GDE anodes (Figure V.6a). At such high voltage, noble metals are not able to catalyze the oxidation of BH_4^- (blue curve). This result holds great promises regarding applications requiring low power density but high energy (which depends on the cell efficiency, hence of the voltage efficiency). This 10-hours stability test was performed using both low- and high-loading Ni_{ED}/GDE anodes; the current reached on the high loading anode is significantly higher (more than 3 times) than with Ni_{ED}/GDE-L. This difference was not observed in the dynamic measurements discussed above (Figure V.4). This could indicate that electrodes with limited number of active sites are more prone to poisoning by intermediate ($BH_{x,ad}$) or product (BO_x) species. So, even if Ni_{ED}/GDE-L appeared the best performing electrode on Figure V.4, increasing its Ni loading 6 times could prevent significant performance loss in long-term operation. Such an option, unrealistic with PGM catalysts, becomes possible with the present non-noble Ni-based electrodes; as an example of this, higher metal loadings (up to 70 $mg.cm^{-2}$) have already been reported in the literature [372,381,393,394].

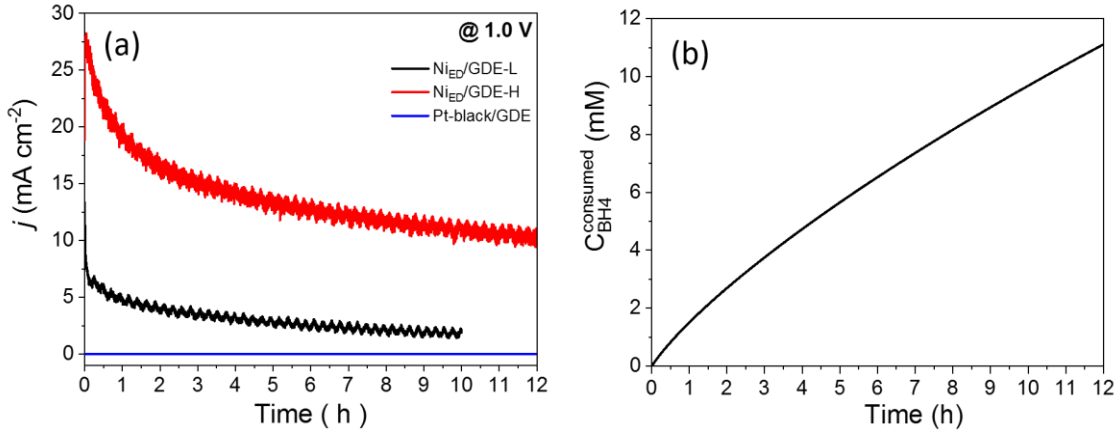

Figure V.6. (a) Stability test performed in fuel cell condition with both Ni_{ED}/GDE-L and Ni_{ED}/GDE-H electrodes at 1.0 V, where no current can be collected with a Pt-based anode. (b) Estimation of the BH_4^- consumption during the stability test calculated using Faraday's law (Ni_{ED}/GDE-H electrode).

By looking at the slowly declining profile of the red curve on Figure V.6a, one could wonder if the overall concentration of the electrolyte circulating in the cell did not decay significantly over the stability test. The consumption of BH_4^- during this test has been calculated using Faraday's law, adapted to give the borohydride concentration loss

during this measurement (equation 5.3); the resulting curve is presented on Figure V.6b (the number of electrons exchanged was set to 4, given the tentative BOR mechanism on Ni presented in Chapter IV).

Modified Faraday's law $$C = \frac{\int_0^\tau I\,(\tau)d\tau}{F.z.V}$$ (equation 5.3)

with:

C = Concentration of borohydride consumed (mmol.L^{-1})

I = Current (A)

τ = Time of the deposition (s)

F = Faraday's constant (96 485 C.mol^{-1})

z = Number of electrons transferred (estimated at 4)

V = Volume of the anolyte tank (L)

Overall, after the 12 hours of testing only 11 mM of sodium borohydride was consumed which represents *ca.* 2% of the initial concentration (0.5 M); this shows that the gradual decline of performance must not originate from a change in the fuel concentration. This calculation does not include the losses coming from the heterogeneous hydrolysis of the fuel or its crossover to the cathode, though. This observation highlights the high energy density of a DBFC.

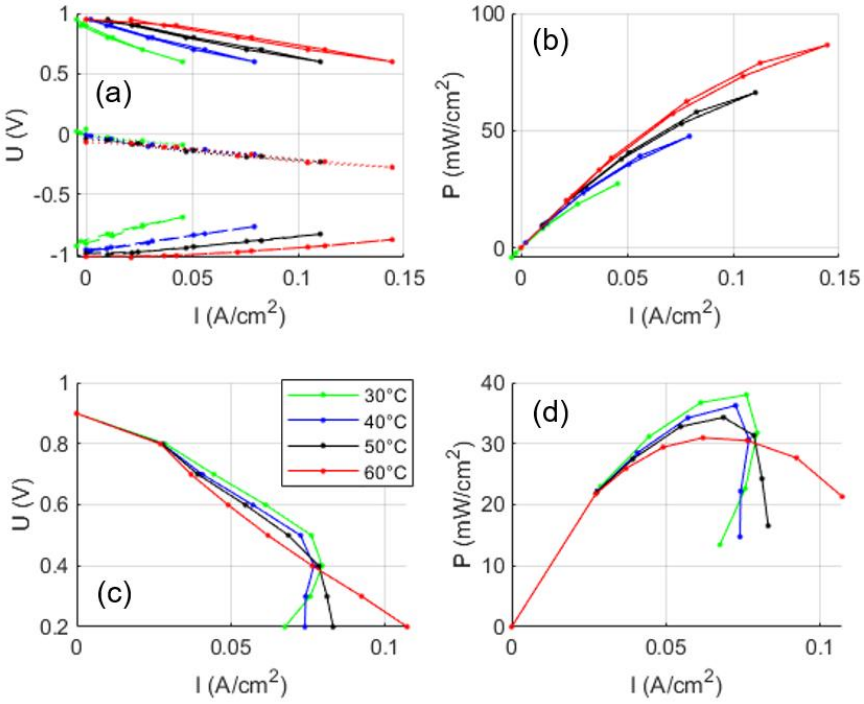

Figure V.7. *I-U* curves (a, c) and *I-P* curves (b, d) of a Ni_{ED}/GDE anode in DBFC operation conditions while (a, b) keeping the cell voltage above 0.5 V and (c, d) using the same electrode down to 0.2 V. On panel (a) the local potential of both the anode and cathode, measured using an *in situ* H_2 reference are represented.

To observe how the electrode would be affected if strongly oxidized in the cell, some tests were performed where an electrode was re-used: after a standard test for which the voltage was maintained above 0.5 V (Figure V.7a, b), the cell voltage was lowered down to 0.2 V (Figure V.7c, d). During this second measurement, the performance dropped drastically (for $U < 0.4$ V) and resulted in irreversible damage: the power density dropped at each iteration, even though the temperature was increased. One should note that the electrode used for this test was obtained using a preliminary electrodeposition procedure that resulted in bigger agglomerates, but other characteristics were not influenced. This shows the sensitivity of Ni_{ED}/GDE towards oxidation/passivation.

This electrode was observed by SEM at different magnifications (from × 10k to × 200k, Figure V.8). The first thing to notice is that the shape of the particles composing the Ni agglomerates has changed after the test. From spherical they transformed into flakes, which is a typical morphology of $Ni(OH)_2$-based materials. [395–398]. This suggests that when the anode potential exceeded 0.5 V *vs* RHE (cell voltage below ≈ 0.4 V), transition from α-$Ni(OH)_2$ to irreducible β-$Ni(OH)_2$ and growth of the latter from monolayer to a 3D phase has occurred. It confirms that lowering the voltage too much in the DBFC would irreversibly impact the anode state of surface and thus its performance. The pores of this electrode were also observed (Figure V.8e, f, g). The particles covering the carbon support are found to be smaller, but this is likely due to the ED procedure, which was performed faster than the one described previously. Because of that, the top surface agglomerates grew more compared to the inner layer ones. However, their shape is similar, with flakes appearing everywhere. This means that all the particles deposited on the support participate to the anodic reaction in the DBFC and not just the layer in contact with the membrane. It confirms that this ED procedure directly on the SGL carbon support allowed to simplify the elaboration of the anode, while keeping a major part of the deposited particles active.

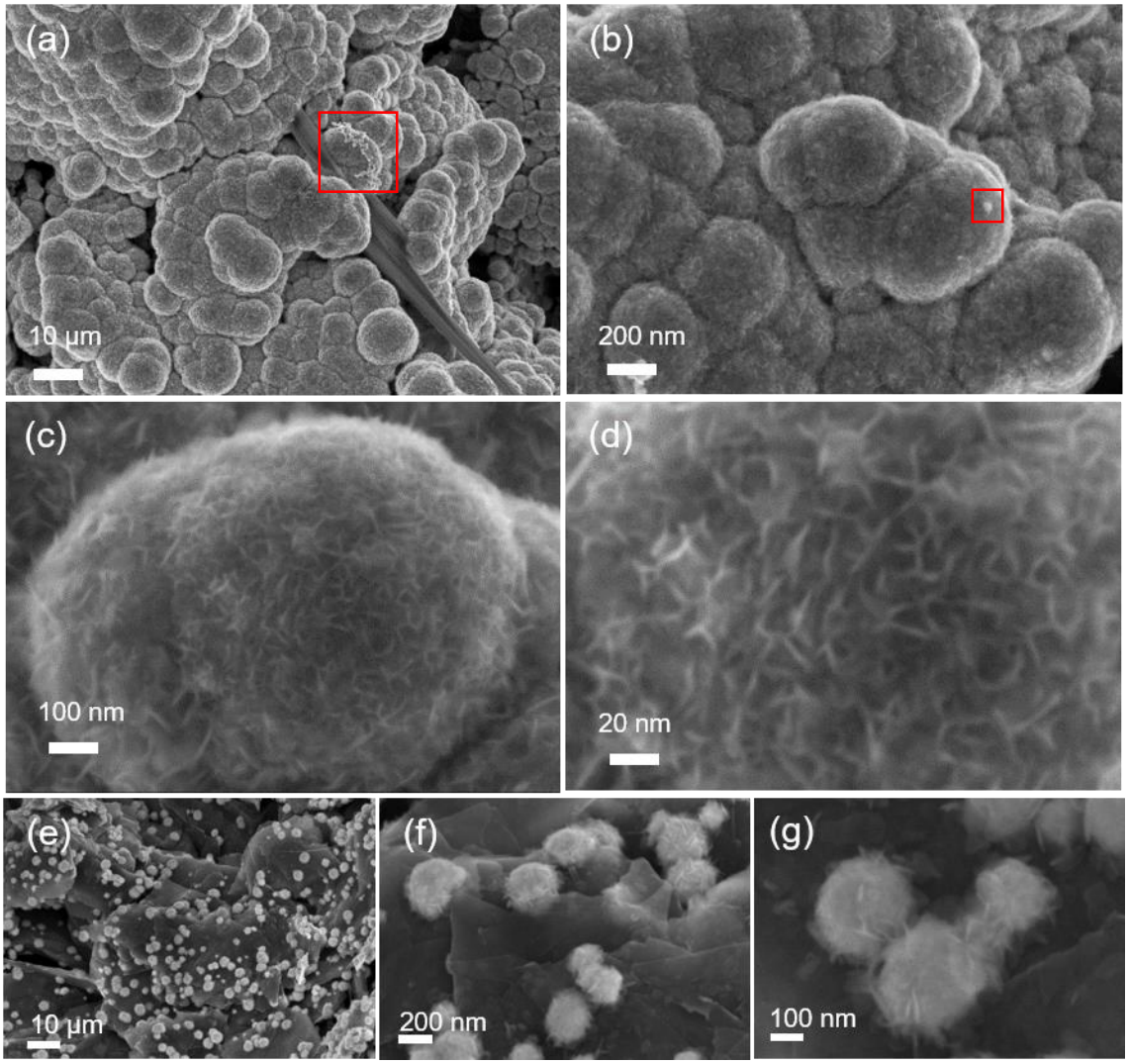

Figure V.8. SEM images taken with InLens sensor (secondary electrons) of a Ni_{ED}/GDE anode after measurements in DBFC conditions at (a, e) ×10k, (b, f) ×30k, (c, g) ×100k, d) ×200k magnification. The third row (e, f, g) corresponds to particles deposited in the pores of the electrode. The red squares highlight contaminant particles appearing on the surface after the DBFC tests.

The low magnification SEM images of Figure V.8 (red squares) reveal that some odd particles can now be found on top of the Ni agglomerates. In the first case (Figure V.8a), their size and shape clearly differentiate them from Ni particles. For the second case (Figure V.8b), they easily could have been missed at this magnification if the conventional secondary electron detector had been used. Indeed, their size and shape are quite similar to their surroundings. However, these images were taken using a InLens secondary electron detector, which also receive some back-scattered electrons (BSE images are brighter for heavier source element): these images therefore sign the presence of elements heavier than Ni. To confirm the nature and explain the origin of such potential contaminants, they were characterized using X-EDS (Figure V.9). The percentages given in each table give an idea of the composition of the scanned area and should not be used as quantitative. The first area measured (green borders) confirms

that the sample was composed only of Ni as already demonstrated before any DBFC tests (Figure V.3). The brighter particles (yellow borders) are mainly composed of gold. This is a surprising result, since no gold is used during the catalyst synthesis or in the MEA of the DBFC. Only the bipolar plates, which are covered by a layer of gold to prevent their deterioration in strong alkaline conditions (4 M NaOH), may be considered as the source of gold. This finding proves that even a supposedly inert (non-corrodible) gold layer is damaged during DBFC operation. Actually, the first bipolar plates used in LEMTA were completely destroyed after several tests: this layer was locally removed, thus revealing the inner plate material (brass). Secondly, the small particles (Figure V.8b) were found to be Pt agglomerates. Because the electrode was free of Pt before DBFC tests (even if the elaboration procedure was slightly different here, there is no reason to believe otherwise), the presence of Pt after the test means that Pt was deposited on the anode during the tests; the only place where to find Pt in the system was at the cathode active layer. The most realistic hypothesis is therefore that the cathode electrocatalyst was dissolved during the measurement and Pt-containing ions diffused/migrated through the membrane to the anode to be redeposited [223,224]. It is also possible that Pt nanoparticles would detach from their support at the cathode (a classical degradation process of Pt/C in alkaline environments[260,264], even though it is hard to believe (but not impossible, though) that they would cross the membrane and end up at the anode. Whatever the reason, having Pt at the anode is not desired: it would decrease its OCP, but could also increase its activity at higher potential (because Pt is a good HOR catalyst). In any case, the minimal amounts of Pt detected here should not lead to drastic changes in the cell performance. However, it would badly impact the overall effectiveness of the FC in long-term operation, since it means the cathode is slowly depraved of its catalyst (the cathode often being limiting in a DBFC).

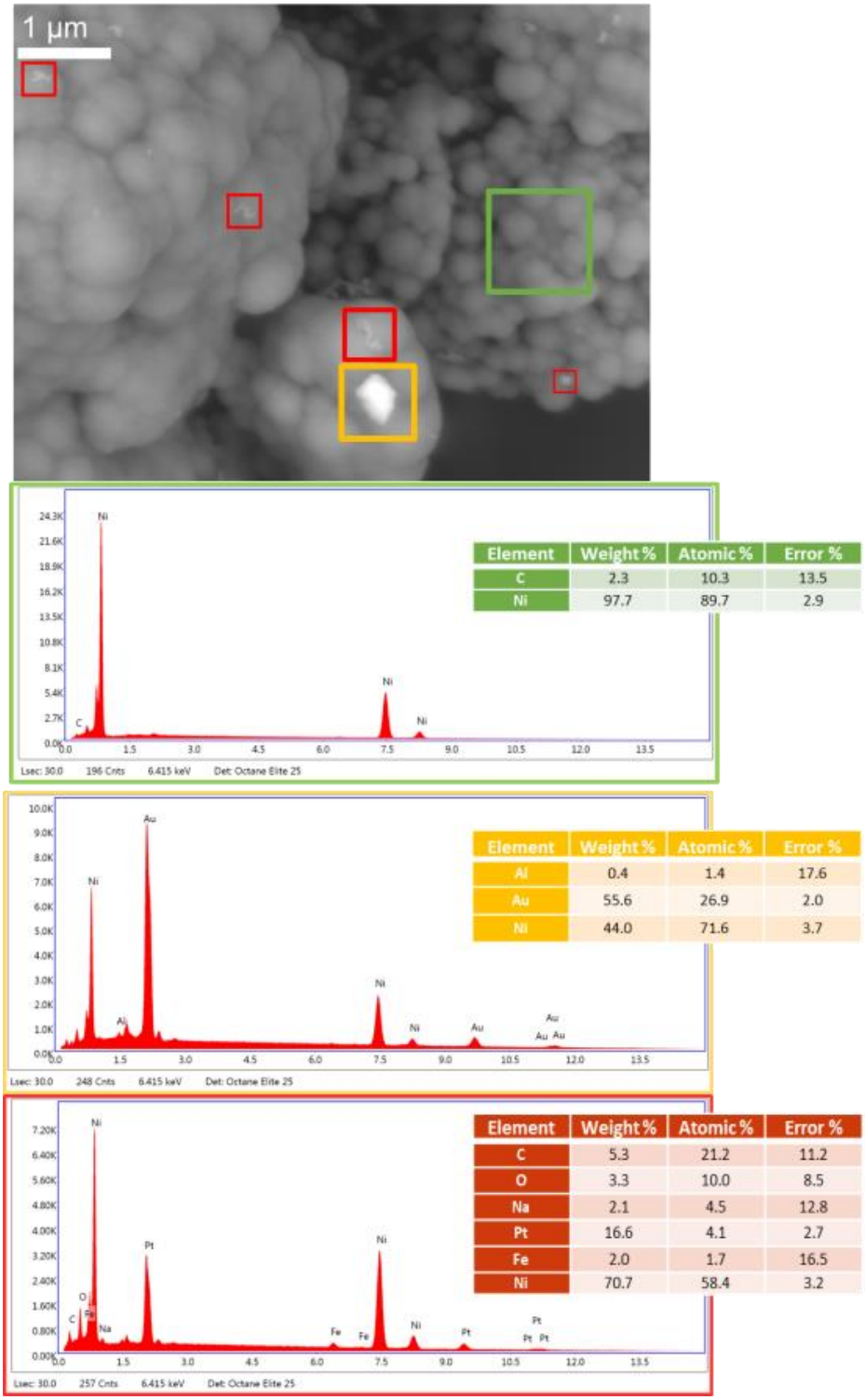

Figure V.9. SEM image of Ni_{ED}/GDE anode after DBFC measurements taken at ×16k magnification with BSE detection revealing several bright impurities on its surface. These impurities are scanned by X-EDS and their corresponding spectra are represented below with the composition percentage. These number are only for qualitative interpretation and should not be used to quantitative purposes.

V.2 Optimization of the anode properties

This section will focus on improving the morphology of the anode, following Olu *et al.* [129] conclusions: this study from 2015 specified that, with a given catalyst, a flat and dense catalysts layer (such structure is almost always used in the literature) results in poor performance compared to more open, porous and on-purpose defective structure. The Ni_{ED}/GDE anodes developed previously, to some extent fall in this latter category of structures, with the catalyst deposited in the thickness of the open and porous support. However, the GDL used in the previous section is not designed to be employed on purpose as an open electrode structure (it usually comprises a microporous layer). So, two commercial 3D Ni substrates of different porosity, tailored to be very open structures, will be investigated as potential Ni_{ED} support: a nickel foam (NFM) and a nickel felt (NFT)

V.2.1 Towards open nickel structures as Ni_{ED} support

V.2.1.1 Nickel structure characterization

Details about the two structures can be found in the section "II.2.3 Surface treatments on 3D structured Ni supports". The morphology and surface characterizations (SEM, X-EDS and XRD) of the Ni foam (NFM) and the Ni felt (NFT) can be found in section II.3.2. "Structural and compositional characterization". The pore size in NFM is bigger than in NFT (Figure II.10a, b, d, e), and its surface is apparently rougher (Figure II.10.c, f). Unfortunately, N_2 sorption would not be reliable with these materials (the specific area is well below 1 $m^2\ g^{-1}$) and no data were given by the suppliers; thus no precise pore size value can be determined other than visually. The specific surface area of each material has been estimated by electrochemical characterization in supporting electrolyte (1 M NaOH, Figure V.10a): the double layer capacitance of NFT is larger than that of NFM in their respective initial state, indicating larger specific area for the NFT, which corresponds to the apparent smaller pore size. Besides, an anodic broad peak around 0.3 V *vs* RHE, corresponding to the conversion of metallic Ni sites into surface α-$Ni(OH)_2$ and the corresponding cathodic peak around 0 V *vs* RHE can already be distinguished for the untreated NFT structure, while the CV profile of NFM is completely flat within the discussed potential region. The last thing to notice on these initial CVs is that NFT is more active in the HER than NFM. These findings all indicate that, after the cycling in supporting electrolyte, the NFT structure presents more metallic sites than the NFM (which is strongly passivated). This difference could be explained by the presence of metallic impurities such as Fe, Mo or Cr, in the matrix of

NFT, as shown on the X-EDS spectrum (see section II.3.2.2) and in the XRD diffractograms (see section II.3.2.1), while only Ni is detected on NFM, these additional metals rendering the Ni-rich alloy of the NFM more prone to remain partially-reduced [210]. The different manufacturing process of the NFT and NFM may also account for these differences: NFM was sintered at high temperature in air and is therefore strongly-oxidized throughout the whole thickness of the material. Unfortunately, no information regarding the manufacture of NFT could be obtained, but these first results suggest that the material could be passivated by only a (thin) native oxide layer.

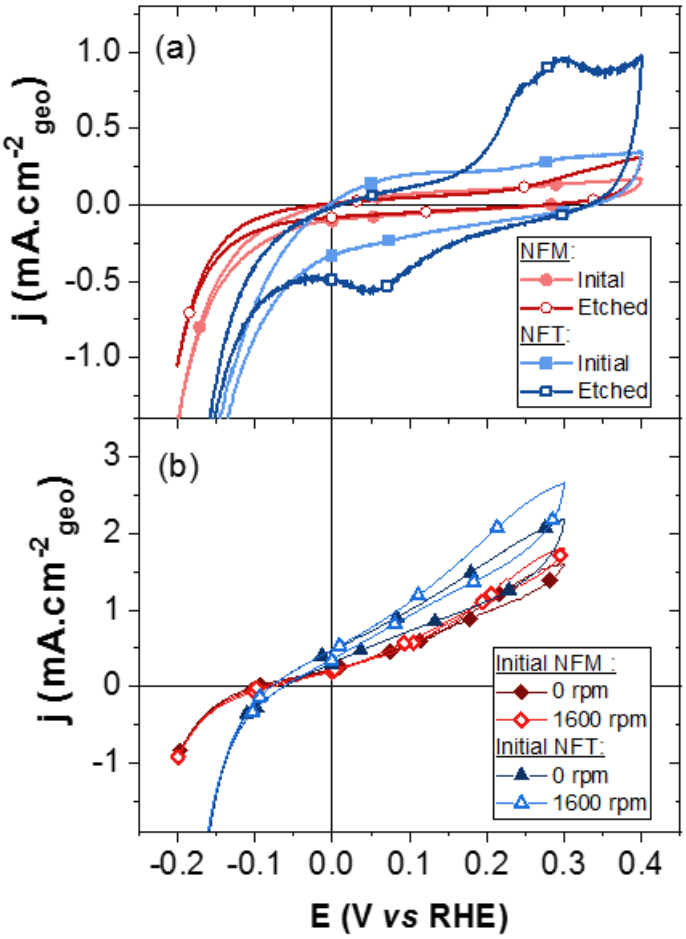

Figure V.10. Cyclic voltammograms at v_s = 20 mV.s^{-1} of NFM and NFT in (a) Ar-saturated supporting electrolyte (1 M NaOH, T = 25°C) showing their electrochemical profile at their initial state and after acid etching for 2 hours in 2 M $C_6H_8O_6$ and in (b) BOR conditions (Ar-saturated 50 mM $NaBH_4$ + 1 M NaOH, T = 25°C) showing their performance with or without rotation of the RDE (ω = 0 or 1600 rpm) at their initial state. Reprinted from Ref. [391].

The BOR performance of the pristine NFT and NFM was very modest (Figure V.10b). Despite the high concentration of $NaBH_4$ (50 mM), none of the materials was able to oxidize borohydride below -0.10 V *vs* RHE, which is well above the OCP of -0.25 V *vs*

RHE reported in Chapter IV for Ni_{ED}/C. This high BOR onset potential is accompanied by very slow BOR kinetics: the current density obtained at higher potentials (up to 0.3 V *vs* RHE) does not exceed a few mA.cm^{-2} and no significant improvement is observed when the rotation of the RDE is set to 1600 rpm, meaning that the reaction occurs under severe kinetic limitation. This is described by [291] as a typical behavior of strongly-oxidized nickel towards the BOR, in agreement with the previous findings. Because of its higher ECSA and more reduced state of surface (small contribution of α-$Ni(OH)_2$), the BOR currents registered on NFT exceed those of NFM by a factor *ca.* 2 (0.5 mA.cm^{-2} *vs* 0.2 mA.cm^{-2} at 0 V *vs* RHE and 2.7 mA.cm^{-2} *vs* 1.8 mA.cm^{-2} at 0.3 V *vs* RHE and 1600 rpm, respectively). Note that the onset potential of the BOR on NFT is slightly higher compared to NFM, which is ascribed to its higher HER activity, as observed in supporting electrolyte.

A preliminary ED of Ni nanoparticles was performed on pristine NFT and only small coverage of the NFT surface by Ni agglomerates was obtained (Figure V.11a). This translates in a really small increase of the ECSA and the peak at 0.3 V *vs* RHE is still quite undefined (Figure V.11b): the resulting surface remains essentially oxidized. This is explained by the fact that the nucleation of Ni NPs is too difficult on the oxidized surface of the pristine NFT: the HER activity of the support is not negligible and almost all the reduction current during the Ni deposition procedure leads to H_2 evolution through the HER.

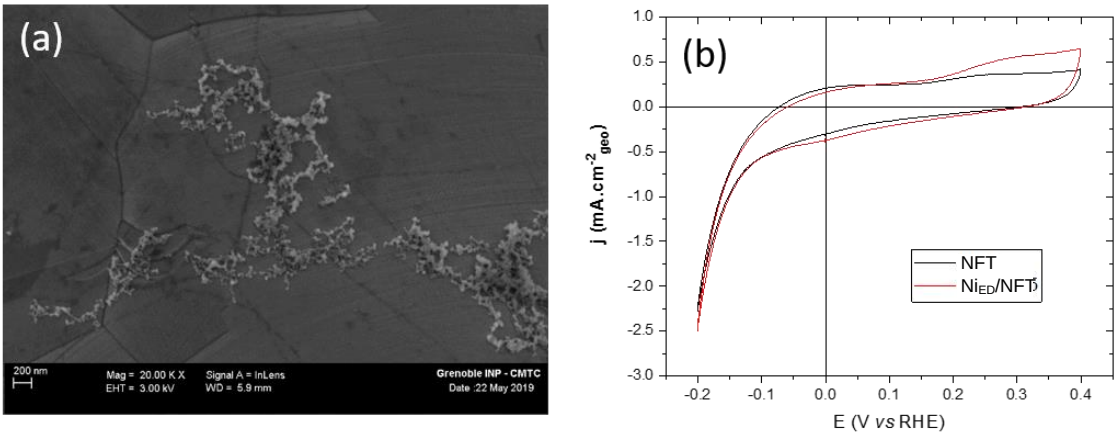

Figure V.11. (a) SEM image of Ni electrodeposited on NFT (F 0.5) without etching at ×20k magnification. (b) Corresponding electrochemical profiles of the felt before and after Ni_{ED} in 1 M NaOH at v_s = 20 mV.s^{-1} and T = 25°C. No major improvement of the peak at 0.25 V *vs* RHE is observed.

V.2.1.2 Tuning of the state of surface of the NFM and NFT.

One of the advantages of using NFM and NFT as anodes for DBFCs is that the whole electrode (including the surface of their open pores) can be active for the anodic reaction, due to the nature and the very open structure of these materials. However, the modest results obtained when they are in their pristine state shows that they must be tuned for higher activity. Modifying the state of the surface of the NFM and NFT materials to obtain metallic nickel at the surface is one good way to enhance their BOR performance [291]. The most common way to reduce oxidized nickel surfaces is to perform a heat-treatment under reducing atmosphere, *e.g.* H_2 [189,195–197]. This approach has been used following the procedure described in the section 4.2. "Surface treatments on Ni structures", where the electrochemical profile of the nickel felt obtained after H_2 thermal treatment can also be found. An increase of the Ni(0)/Ni(II) transition peak as well as of the HER current is indeed observed. However, the shape of the CV (additional anodic peak at potentials close to 0 V *vs* RHE) suggests [186,290] that the NFT is in a partially-oxidized rather than fully-reduced metallic state (probably because of the repassivation step in the oven). Moreover, this procedure needs cumbersome equipment and is time-consuming (mainly because of the natural cooling to room temperature). The efficacy of thermal treatments under H_2 atmosphere was demonstrated by Gdreń *et al.* [189]. The authors also showed that an acid etching (AE) procedure had numerous advantages to remove oxides and expose metallic Ni to the surface: (1) simplicity, (2) shorter time needed to obtain metallic Ni sites and (3) increase of the surface roughness during the AE treatment, an advantage for electrochemical reactions. This effect is clearly demonstrated by Figure V.12, where the intensity of peak 1 increases with the amount of metallic Ni available for oxidation into surface α-$Ni(OH)_2$ [189]. Starting from the same initial state, AE is more efficient to reveal Ni metal on a NFM structure. This is ascribed to the increase of the surface roughness, but might also arise from the fact that during the etching, the hollow structure can be pierced (see reference [189]), making the inner surface of the foam or felt accessible to the electrolyte. This is not necessarily an advantage, since it means that the mechanical strength of the support might be weakened if too severe AE is performed: a balance must be found between activation (oxide removal) and mechanical integrity of the support.

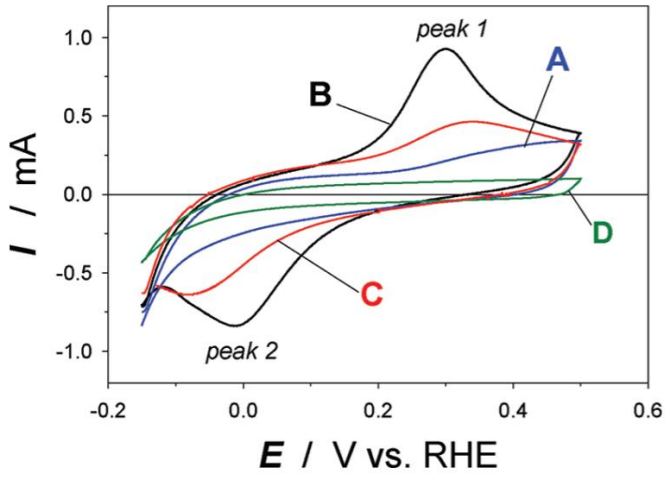

Figure V.12.Cyclic voltammograms in 0.5 M aqueous KOH solution obtained at T = 298 K and v_s = 100 mV.s^{-1} in the −0.15 ≤ E ≤ 0.50 V potential range for (A) the "as-received" Ni foam, (B) the "etched" Ni foam for 2 min, (C) the "reduced" Ni foam, and (D) the "passivated" Ni foam. Figure reproduced from Grdeń *et al* [189].

Based on these results, the chosen approach to remove the oxide layer from the nickel NFT and NFM structures thereafter will be the AE. The first procedure was based on the utilization of concentrated ascorbic acid ($C_6H_8O_6$) solutions (described in the section "II.2.3. Surface treatments on 3D structured Ni support") in order to avoid fast materials degradation. Weak organic acids are known as etchants for Ni and Ni oxide surfaces [399]. The CV profiles for both materials after 2 hours AE in 2 M ascorbic acid solution can be found in Figure V.11a (hollow symbol curves) and compared to the initial state of the electrode. The effect of etching on the NFM does not appear significant. Indeed, one can neither observe well-defined anodic peak around 0.3 V *vs* RHE nor any substantial increase of the double layer currents. This may either be due to a large oxide thickness (which could not be removed during the 2 h AE treatment), or to poor reactivity of "thermal" Ni oxides, which were formed during manufacturing of the NFM. This translates into poor BOR activity, even after the AE, as shown in Figure V.13d. The onset potential of the reaction slightly decreased, but the CV profile shows, again, really small BOR current densities and very poor kinetics. This material is therefore not suited as DBFC anode and only NFT will be considered in the next sections of this chapter.

The AE treatment was much more effective when applied to the Ni felt. SEM images of the surface after this treatment can be found in Figure V.13a, b and V.14 a respectively, at ×200 and ×2000 and ×50k magnification. It clearly appears that the top layers of the felt were removed and the surface becomes rougher compared to the initial state (Figure II.10 f). A large anodic peak appeared at 0.3 V *vs* RHE on the voltammograms of Figure V.10 a, corresponding to the formation of surface α-Ni$(OH)_2$, which is reduced back to metallic Ni at *ca.* 0.1 V *vs* RHE during the cathodic scan (corresponding to peak 2 in

Figure V.12). The anodic peak in acid-etched NFT is not as well defined as the one observed in Figure V.12. One can also notice a significant discrepancy between the anodic and cathodic charges (1.85 mC and 1.05 mC respectively). The most likely hypothesis regarding these two aspects is that evolved hydrogen, trapped in the pores of the material, is oxidized only once the α-$Ni(OH)_2$ phase is formed. The HER activity after AE decreased compared to the initial state and the wide peak at the start of the anodic sweep, corresponding to the oxidation of remaining H_2/H_{ad} produced during HER or the formation of $NiOH_{ad}$, also disappeared. Another fact that arises from the AE treatment is that some regions appear more etched than others (Figure V.13b). The detachment of matter may be influenced by the crystallographic orientation, creating stepped structures and thus making some grains rougher than others [322]. Overall, the surface is less active in catalyzing the hydrogen reactions after the etching, suggesting that (i) it is more reduced and (ii) it will be more active for the BOR.

This is confirmed by Figure V.13c, that shows the BOR CV profile of the etched NFT (eNFT) in 50 mM $NaBH_4$ + 1 M NaOH. The BOR starts now at a lower potential of around -180 mV *vs* RHE, which is already better than the initial reaction onset but still not as good as the one observed for Ni_{ED}/C nanoparticles (see Chapter IV, Ref [291]). The reaction kinetics increased as well: a clear influence of the mass-transport is now observed when increasing the rotation rate of the RDE. However, no limiting plateau is reached and the Levich law is not respected (the current is not proportional to the square-root of the rotation rate), suggesting strong charge-transfer kinetic limitation in this potential range. This could be explained by either a non-optimal state of surface, even after the AE, or by surface-poisoning by intermediate BOR species, that could already occur at this concentration (see Chapter III, Ref. [212]) if the amount of active sites is insufficient. The hydrogen bubbles mentioned above could also limit the access to the active surface. It is important to note that this available surface area is really essential regarding such poisoning and the smaller its value, the faster the poisoning. For example, the diffusion-limiting current at this concentration is reached around 0.2 V *vs* RHE for Pt/C nanoparticles [291] and only around 0.5 V *vs* RHE for bulk polycrystalline Pt (S_{geo} = 0.031 cm^2) [212]).

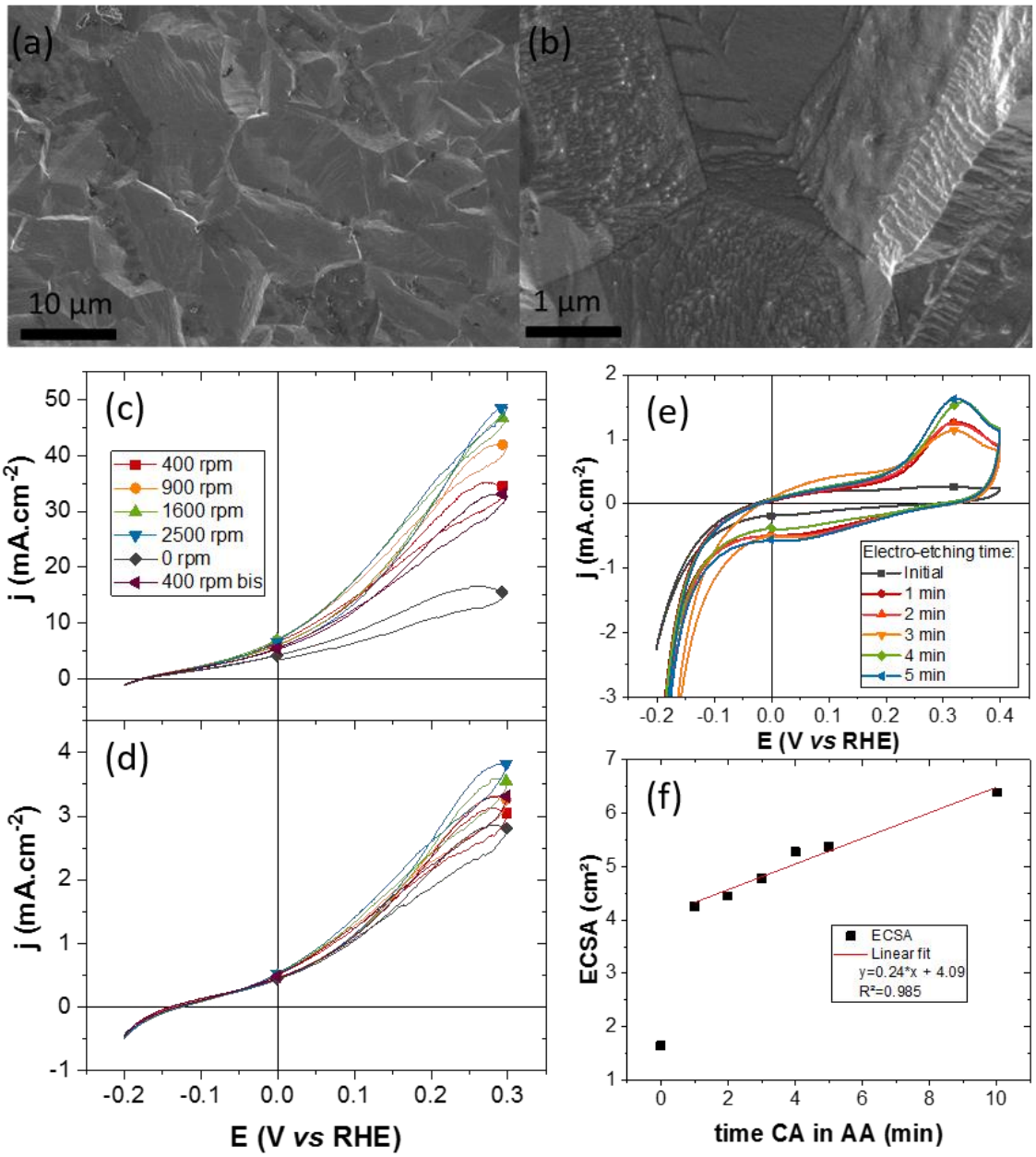

Figure V.13.SEM images (a, b) of NFT after 2 h etching in 2 M $C_6H_8O_6$ at (a) ×200 and (b) ×2000 magnification. (c, d) Cyclic voltamograms of NFT (c) and NFM (d) in 50 mM $NaBH_4$ + 1 M NaOH (T = 25°C) after 2 h etching in 2 M C6H8O6 with RDE rotation variation: [0, 400, 900, 1600, 2500] rpm. (e) CVs of NFT in supporting electrolyte (1 M NaOH, T = 25°C) probing the surface modifications between 1 min electro-assisted etching steps (1 min CA at 0.715 V *vs* RHE in 2 M $C_6H_8O_6$ + 0.1 M $(NH_4)_2SO_4$). (f) Linear fit of the ECSA increase with the CA time in 2 M $C_6H_8O_6$ + 0.1 M $(NH_4)_2SO_4$). Reprinted from Ref. [391].

In order to greatly diminish the etching time and thus facilitate the optimization of the nickel felt, another potential-assisted etching procedure has been tested. The surface was probed between several 1 min CA at 0.715 V *vs* RHE in the concentrated ascorbic acid, as described by Figure V.13e. The ECSA for each curve was then estimated and plotted against the etching time. The resulting fit shows a linear relation between the

etching time and the increase of the ECSA, and thus the roughness of the surface (Figure V.13f). Of course, this relation is only valid for a certain time, where the roughness will reach a maximum value and the felt mechanical integrity will start to crumble [189].

V.2.1.3 Nickel nanoparticle electrodeposition on etched Ni felt

The two likely issues limiting the activity of the Ni anode, namely the surface state and the surface area, can be resolved by replacing the carbon substrate by the etched nickel felt and by creating metallic nickel nanoparticles on its surface using the electrodeposition procedure [186,289,291] already described above. That way, more active sites will be available, attenuating the electrode poisoning by intermediate species, and most importantly, these new sites will be in the right (metallic) state to provide fast BOR kinetics. Before trying this potential support in DBFC conditions, a preliminary Ni electrodeposition study was performed using a RDE (0.196 cm^2). The procedure to obtain such Ni_{ED}/eNFT electrodes is described in more detail and the corresponding CA transients of the electrodeposition can be found in the section "II.4.1.3 Ni_{ED}-based anodes elaboration using Ni based support". Figure V.14 shows (a, b) the SEM images and (c, d) the CV profiles in, respectively, supporting electrolyte and in the presence of $NaBH_4$, before and after the electrodeposition step. The formation of Ni nanoparticles is confirmed by the SEM image, which reveals formation of agglomerates of *ca.* 10 nm Ni particles. In addition, even though the surface was already really rough before the electrodeposition, it is also possible to observe smaller agglomerates or individual particles all over the surface. To make a comparison, a Ni_{ED}/C sample has been reproduced following the exact procedure from Chapter IV and is represented by the red curves in Figure V.14.

The ECSA values have been measured for each sample, revealing almost 4 times higher surface area of the Ni_{ED}/eNFT compared to the Ni_{ED}/C. This large improvement is attributed to the use of the etched felt as the nanoparticle support. It confirms the results obtained by using the pristine support for the ED of Ni (Figure V.11). The behavior of the etched felt towards the BOR is also greatly improved by the electrodeposition: the reaction onset potential is now -220 mV *vs* RHE, which is still not as low as for the Ni_{ED}/C (-260 mV *vs* RHE), probably because the support still comprises some partially-oxidized regions. This is confirmed by the CV in supporting electrolyte (Figure V.14a), where the HER activity is still large and the shape of the anodic region, before the peak at 0.3 V *vs* RHE, is typical of the behavior of a partially-oxidized surface. This dual state of surface affects the reaction onset, owing to the appearance of a mixed potential (between BOR on Ni_{ED} and HER on eNFT). However, the current density measured on Ni_{ED}/eNFT quickly catches up with Ni_{ED}/C (at around -190 mV *vs* RHE) and stays slightly above at potentials below 0 V *vs* RHE and even more so above 0 V *vs* RHE. This slightly higher current could come from (i) the higher surface area of Ni_{ED}/eNFT,

limiting the effects of the poisoning, or (ii) the positive influence of the eNFT support, that has some activity in the HOR. This latter fact would explain why the current density of Ni_{ED}/eNFT is above that of Ni_{ED}/C (which corresponds to 4 e^- per BH_4^- [291]). Regarding the higher potential region, the current density of Ni_{ED}/eNFT stays higher than Ni_{ED}/C but most importantly, no limitation appears when the oxide formation potential is reached (until 0.3 V *vs* RHE) as it is observed on Ni_{ED}/C.

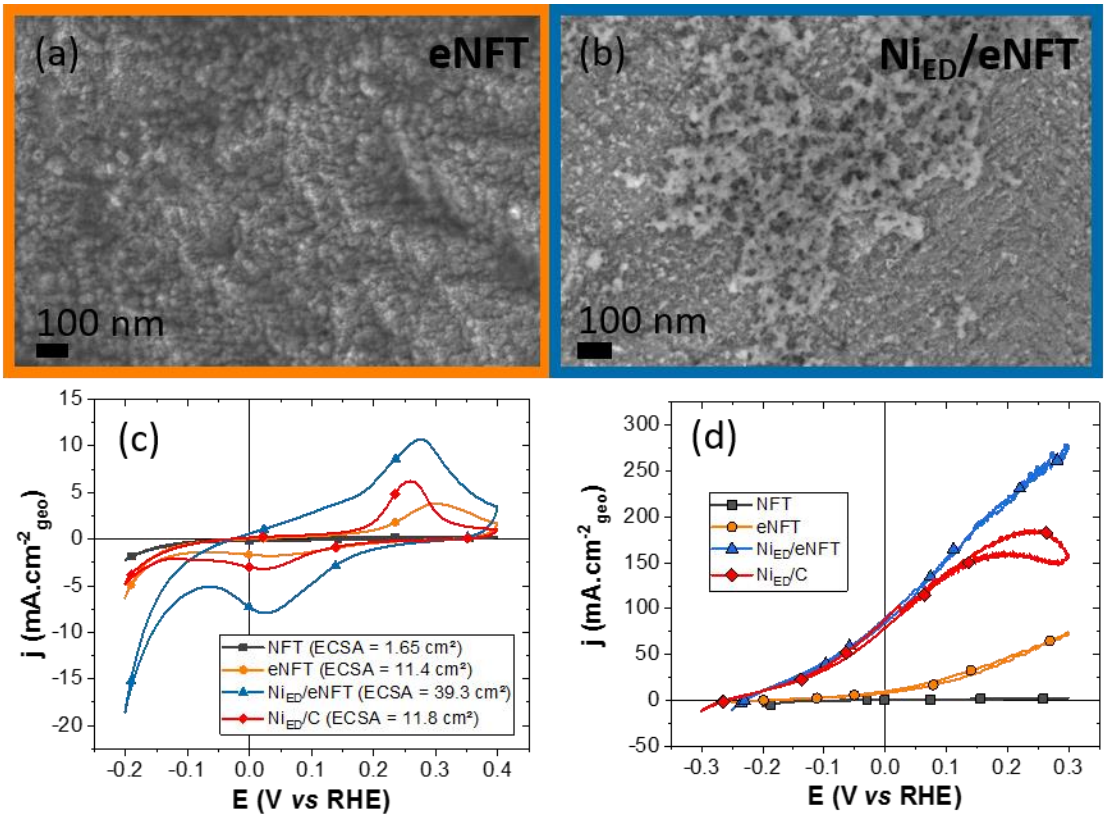

Figure V.14 (a, b) SEM images at ×50k magnification of NFT (a) after 2 hours AE in 2 M $C_6H_8O_6$ at T = 25°C and (b) after 2 hours AE in 2 M $C_6H_8O_6$ + Ni electrodeposition in 0.01 M $NiSO_4$ + 0.1 M $(NH_4)_2SO_4$. (c) CVs profile in 1 M NaOH at T = 25°C and v_s = 20 $mV.s^{-1}$ of NFT at its initial state, after AE in 2 M $C_6H_8O_6$ and after Ni electrodeposition and Ni_{ED}/C used as reference catalyst. (d) BOR profiles of these three different states of NFT compared with Ni_{ED}/C in 50 mM $NaBH_4$ + 1 M NaOH at T = 25°C and ω = 1600 rpm. Reprinted from Ref [391]

In addition to the positive influence of the eNFT support regarding the HOR, another explanation could be put forth. The two materials are not exactly in the same oxidation state for the same potential: it is possible that some metallic Ni remains as high as 0.3 V *vs* RHE for Ni_{ED}/eNFT, owing to the existence of porosity in this sample, these sites remaining active for the BOR. This absence of limitation could also arise from a better management of intermediate species, thanks to the more open porosity of the nickel felt compared to the XC-72R carbon support of Ni_{ED}/C. Finally, the distribution of current, potential and pH within the pores of the Ni_{ED}/eNFT could "delay" the oxidation/passivation of the surface, but this is hard to experimentally demonstrate.

Whatever the tentative explanation, the BOR performance of Ni_{ED}/eNFT is obviously better than that of the Ni_{ED}/C in the RDE configuration. This means that it can be a viable candidate as a fully PGM- and carbon-free anode for DBFC applications, and will be upscaled.

DBFC tests using Ni_{ED}/eNFT anodes

In order to test the Ni_{ED}/eNFT materials as a DBFC anode, both acid etching and Ni electrodeposition preparation procedures had to be modified because of the larger
V.2.2 geometric surface area of the single cell setup: 8 cm². It was found that the current required to etch the surface of the Ni felt was too high (exceeding the potentiostat limit) making the potential-assisted etching procedure impossible. Because of this limitation, we applied chemical etching, but this time in concentrated strong acids in order to reduce the time of the treatment. The etching solution was reproduced from Ref. [189] and is described in the section "II.4.1.2 Ni_{ED}-based anodes elaboration using Ni based support". The electrodeposition step was also upscaled and consisted of 10 pulses (20 s each) between -0.32 and -0.57 V *vs* RHE in 0.1 M $NiSO_4$ + 0.1 M $(NH_4)_2SO_4$. The resulting surface can be observed at different magnifications on Figure V.15. Bigger agglomerates (around 100 nm) are now covering the whole surface of the wires composing the Ni felt (Figure V.15b, d) and thicker agglomerates are also dispersed over all the wires (Figure V.15a, c). CVs before and after the AE as well as after the electrodeposition are shown in Figure V.16.a. Large increase of the surface of metallic nickel is observed, resulting in an ECSA of around 1900 cm². This enhanced felt could then be tested in a DBFC and compared to Pt black/GDL and Ni_{ED}/GDE anodes.

The performance obtained with a commercial Pt black electrode are low, likely because of the low porosity and thus bad fuel management of the catalyst layer as, described by Olu *et al.* [129]. In order to make a fair comparison, a new Pt-based electrode was tested, where Pt nanoparticles were deposited directly in the pores of a GDL (Pt/GDL). A quick description of the electrode synthesis and SEM image showing its surface and the particle size can be found in section II.4.1.3 "Pt/GDL anode elaboration".

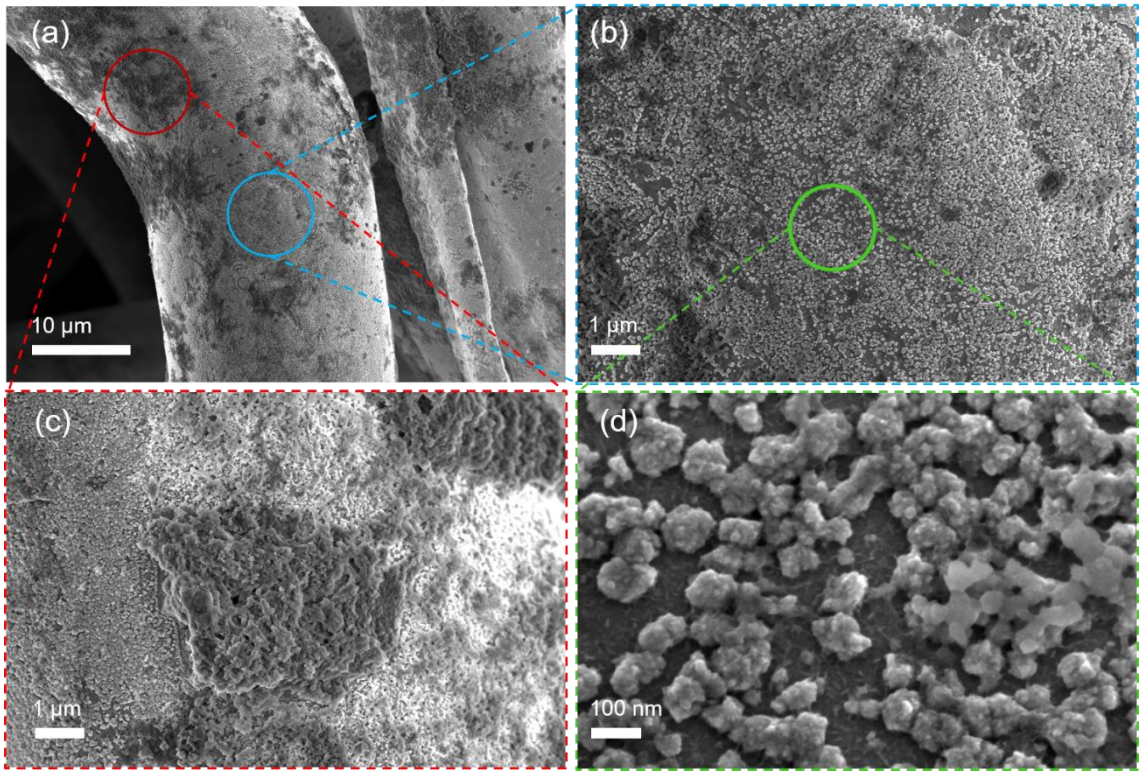

Figure V.15. SEM images of Ni_{ED} particles deposited on etched NFT (Ni_{ED}/eNFT) at different magnifications: (a) ×2k; (b, c) ×10k; (c, f) ×100k.

The DBFC performance of these four anodes is displayed on Figure V.16b. Because of the use of a commercial Nafion NRE-212 membrane in Na^+ form, the resistance of the cell was quite high (0.65 Ω) but already smaller than with the previous carbon-supported anodes (≈ 0.8 Ω). Considering that the Ohmic drop can be significantly improved in the future by using more appropriate anion-exchange membranes, the voltage and the power density are represented in the Ohmic drop-corrected form.

Overall, the same outstanding OCV of 1.2 V, observed by using Ni_{ED}/GDL, is obtained with Ni_{ED}/eNFT, while the voltage of the cell with a Pt-based anode is limited to 1 V. This high OCV is attributed to the metallic surface state of the Ni anode (appropriate for fast BOR, enabling to limit the HER). The high power density reached with a Ni_{ED}/NFT and Pt/GDL (Figure V.16b), confirms the benefits of a DBFC anode with open structure. In the same way, the difference in the maximum power density between a non-porous Pt/C layer and an open Pt/GDL electrode is about 300 $mW.cm^2$. Concerning the nickel electrodes, the use of the felt led to a large boost in the power density as well. We assume that this performance gain is due to combined more efficient mass-transport, high surface area of Ni-metal and an optimized residence time of the intermediate species.

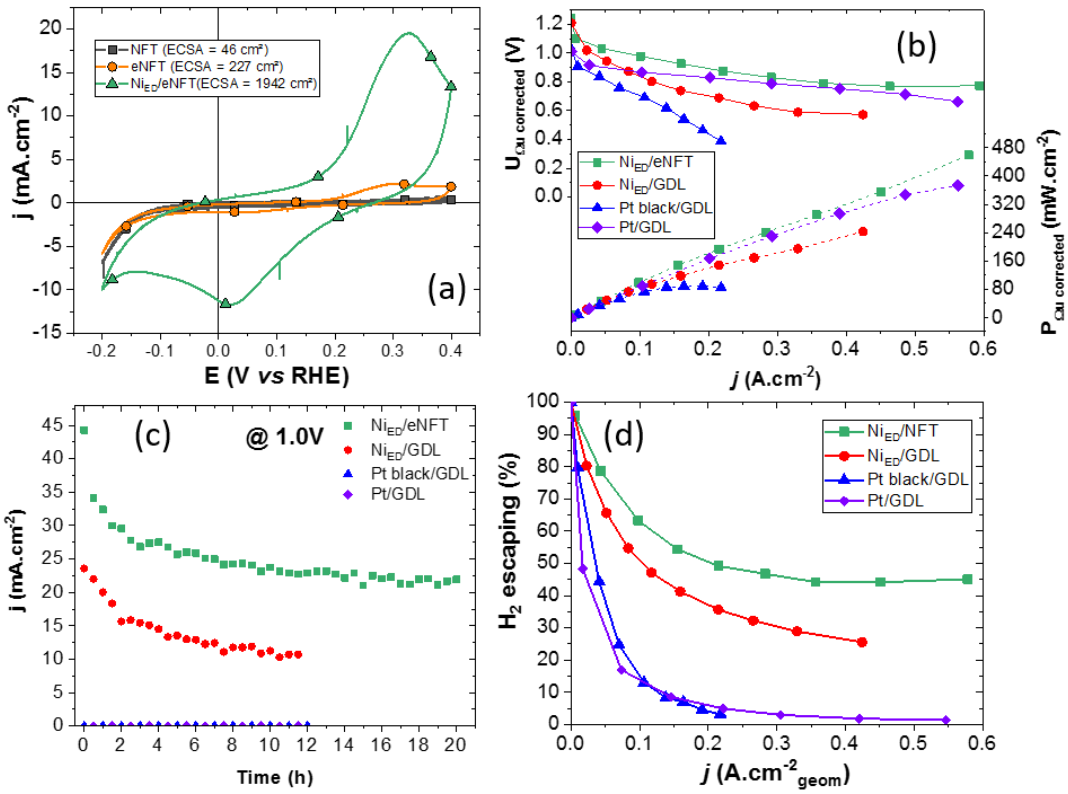

Figure V.16. (a) CV profiles at v_s = 20 mV.s^{-1} in 1 M NaOH, T = 25°C of the preparation of 8 cm² electrodes for DBFC. (b) DBFC performance of the prepared electrode compared to Ni$_{ED}$/GDL and Pt black/GDL from [33] and Pt/GDL,4 M NaOH + 0.5 M NaBH$_4$, T = 60°C, f = 50 mL.min^{-1}. (c) Stability measurements obtained at 1 V for the four different electrodes. (d) Hydrogen escaping (%) during DBFC test measured using a H_2 pump connected to the outlet of the cell. Reprinted from [391].

A 20-hour measurement performed at 1 V (where no current can be obtained with Pt electrodes) on the Ni$_{ED}$/eNFT has shown (Figure V.16c), again, a non-negligible and higher current density than on Ni$_{ED}$/GDL (respectively 23 mA.cm^{-2} *vs* 11 mA.cm^{-2} after 12 hours). The CA profiles obtained on the two materials are similar, suggesting a similar BOR behavior; the better performance can once again be attributed to the open architecture of the Ni$_{ED}$/eNFT electrode and the higher amount of available metallic Ni sites. However, because of this similar behavior, the Ni$_{ED}$/eNFT electrode also failed to valorize significant amounts of produced H_2 in the same manner as Ni$_{ED}$/GDL (Figure V.16d). Once again, the Pt-based electrodes quickly (for E > 0.2 V *vs* RHE) and near-completely oxidize all the H_2 formed during the reaction. For a given current density, the potential applied at the anode will be smaller for Ni$_{ED}$/eNFT than Ni$_{ED}$/GDL, meaning a smaller propensity to promote the HOR, thus allowing more H_2 to escape the cell. The effect observed in RDE configuration, where the partially-oxidized support supposedly helped to avoid a current limitation at higher potential via the HOR (Figure V.14d), is therefore not observed with this upscaled electrode. One explanation could be

the difference between the amount of deposited nickel versus the amount of available sites of the support. In the first case, a ratio of 3.4 between the ECSA before and after electrodeposition is measured; this ratio is increased to 8.6 for the 8 cm² sample. This suggests that the beneficial effect of the support (which might be partly-oxidized and therefore enables HOR) might be lost, because it is masked by a too high amount of metallic Ni (which catalyzes BH_4^- oxidation but not the HOR, thus allowing H_2 to escape).

V.3 Improving the DBFC system

The results obtained with the fully Ni-based Ni_{ED}/eNFT anodes present the best OCV and power densities of all the anodes tested by our group, which already fits the main goal of this PhD. In order to keep improving these results and reach a performance suited for application in mobile devices, we must look at the other parameters of the cell, because no other anode catalyst has been proven more effective than metallic Ni. Firstly, the membrane will be considered and several options will be presented to improve the ion conduction in the unit cell. A preliminary study will then consider non-noble catalysts at the cathode, giving a fully non-noble DBFC.

V.3.1 Integration of bipolar interfaces with Ni-based anodes

In this section, DBFC experiments performed at the University of Washington in Saint Louis (Missouri, USA) will be presented. They developed a "**p**H-gradient enabling **m**icroscale **b**ipolar **i**nterface" (PMBI) which enabled to reach impressive values when used at the anode of a BH_4^-/H_2O_2 DBFC, by keeping separated the drastically different pH of the anode and the cathode (pH = 14 and pH = 1, respectively) [151]. This bipolar interface is created when an anion exchange ionomer (AEI, SEBS55) is deposited on the anode active layer and in contact with a commercial Nafion membrane. This way, the ion exchange is ensured by the AEI at the anode and by the Nafion at the cathode, which allows it to stay in H^+ form and prevent the really slow exchange of Na^+ from the anolyte to the catholyte. This interface was proven more effective than either a CEM or an AEM on their own [151], and an impressive OCV of 1.8 V and a maximum power density of 300 $mW.cm^{-2}$ were reached using PGM-based electrodes in a 5 cm² unit cell. The aim of my stay at Prof. Ramani's group was to adapt this bipolar interface to the Ni_{ED}/eNFT electrodes presented in the previous section. The details about the AEI deposition and the unit cell used can be found respectively in sections "II.4.1.2 Ni_{ED}-based anodes elaboration using Ni supports" and "II.4.2.2 BH_4^-/H_2O_2 DBFC setup".

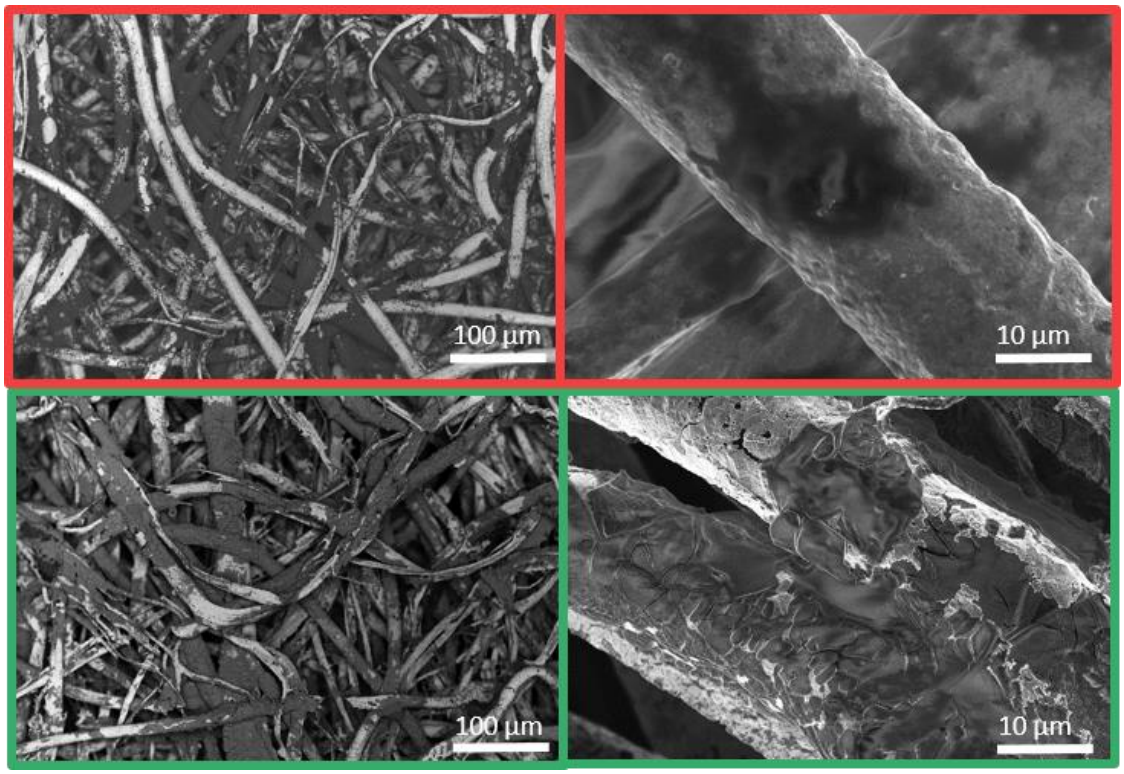

Figure V.17. SEM images of the SEBS/Ni_{ED}/eNFT electrodes prepared via either spraying (S) of the ionomer solution onto the electrode (red borders) or dipping (D) of the anode in SEBS-55 solution (green borders) or at different magnification(×200 and ×5k).

Deposition of the AEI layer on the DBFC anode is an essential step in the elaboration of a PMBI [151], the latter ensuring efficient separation of the alkaline anolyte and the acidic catholyte. Considering the influence of the state of the Ni surface on its BOR activity, the challenge was to develop a deposition procedure ensuring uniform coating, while maintaining the reduced (metallic) state of the Ni_{ED}/eNFT anode. Several deposition procedures have been evaluated and compared. The spraying method (in what follows labelled with S) was adapted from Wang *et al.* [151], where it was applied to a Pd/C DBFC anode. After the ED of Ni NPs, the sample was dried using absorbent paper and then placed on a heating plate (70°C) and the SEBS55 polymer (see Refs. [151,169]) was sprayed directly on it; in these conditions, water is still present in the pores of the electrode, while chlorobenzene solvent evaporated. After the coating, the SEBS55 was functionalized in NMP + TMA, yielding the AEI. The SEM images of Figure V.17 (red frame) were acquired after DBFC measurements in which the anode was pressed against the membrane. The AEI layer directly in contact with the anode was therefore essentially removed from it when it was separated from the membrane. This explains why most of the outer nickel wires appears without the AEI layer, but the ionomer was most probably present before and during the DBFC tests. The electrodes were evaluated in DBFC conditions using a commercial Nafion-117® membrane and a Pt/C (1 $mg.cm^{-2}$) cathode

for H_2O_2 reduction (the resulting current-voltage characteristics and the power density are presented on Figure V.18.).

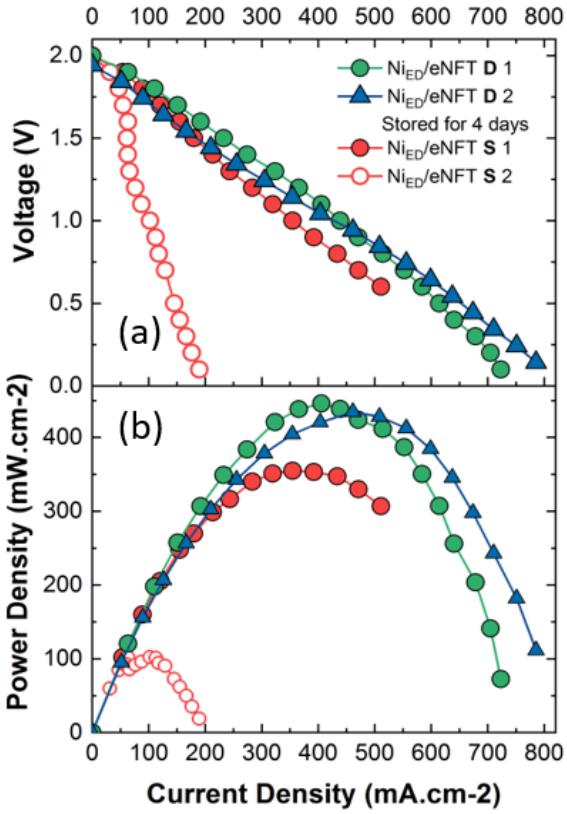

Figure V.18. Polarization (a) and power density (b) curves of the SEBS/Ni$_{ED}$/eNFT electrodes prepared via either dipping (D) or spraying (S) in DBFC conditions (T = 70°C, anolyte: 3 M KOH + 1.5 M $NaBH_4$, catholyte: 1.5 M H_2SO_4 + 15 wt.% H_2O_2, flow rate: 0.4 mL.min^{-1}.cm^{-2}).

The Ni$_{ED}$/eNFT-S 1 anode reached an impressive OCV of 2.0 V (red curve in Figure V.18), where only 1.8 V was reached in the same conditions using Pd/C anodes [151]. This corresponds to the 200 mV improvement compared to PGM catalysts observed during the previous tests, ascribed to the use of Ni metal anodes (suggesting that the Ni$_{ED}$/eNFT-S 1 anode exhibits some reduced Ni metal sites). Such high OCV values also confirm the effectiveness of the PMBI to maintain the pH gradient between the anode and the cathode, even if the layer does not cover the entire anode surface. The peak power density for the Ni$_{ED}$/eNFT-S 1 sample was achieved at 1.0 V and reached 355 mW.cm^{-2}. One must remember that spraying was performed in air at T = 70°C, conditions where the surface of Ni nanoparticles might be partly-oxidized, so this performance is already outstanding. A second electrode was prepared in the exact similar conditions (Ni$_{ED}$/eNFT-S 2) and the same OCV was reached: the state of surface of the anode is still metallic, in majority. However, this second test showed a very low peak power density (P_{max} = 102 mW.cm^{-2} at 1.0 V). This is attributed to a non-

reproducibility in the spraying deposition method: (i) it is almost impossible to assert that the sprayed AEI layer fully penetrates the whole thickness of the Ni_{ED}/eNFT, leaving uncoated Ni fibers for which the PMBI is not well-established and the Ni-metal state of surface might be locally-lost, while (ii) in some cases, fibers might be surrounded by thick pockets of AEI, thereby increasing the Ohmic drop and preventing mass-transfer of reactant to the Ni catalytic sites. In order to solve this issue, another method, namely dipping (in what follows labelled as D) was evaluated. To this end, the Ni_{ED}/eNFT was simply dipped (at room temperature) in the solution of SEBS-55 in chlorobenzene after removing any excess of water (by pressing of the electrode on an absorbent paper) to allow solvent penetration in the Ni_{ED}/eNFT pores. Then, the AEI layer was dried for 1 h in a vacuum oven (preventing irreversible oxidation of the Ni_{ED}/eNFT) at T = 60°C, prior to the functionalization step. This strategy enables more homogeneous coating of the AEI in the whole Ni_{ED}/eNFT structure and better preserves the metallic state of the electrode. As such, the dipping procedure resulted in reproducible anodes, leading to OCV values of 2.0 V and a yet higher (compared to the S1 electrode) peak power density of *ca.* 450 mW.cm^{-2}. This confirms the importance of the AEI deposition procedure for the overall performance and suggests that the targeted metallic surface state of the Ni_{ED}/eNFT-D 1 electrode was indeed achieved. This method resulted in a more reproducible ionomer deposition, as attested by the comparable performance obtained with the two electrodes prepared this way (Figure V.18), although the coating was not strictly homogenous on their entire surface (some areas were not covered by the ionomer). Moreover, this second electrode (Ni_{ED}/eNFT-D 2) was stored in water for four days prior to the DBFC test. While exhibiting somewhat lower OCV (1.94 V, likely due to formation of some surface oxides on the outer Ni sites), the latter shows comparable overall performance (blue curve), thus confirming that the developed approach is fully-compatible with practical applications, where exposure to air may be inevitable (a result of utmost importance).

The OCV (2.0 V) and peak power density (450 mW.cm^{-2}) reached with the Ni_{ED}/eNFT-D anodes confirm the advantageous combination of the PMBI, the high-surface area 3D-open structure metallic Ni catalyst and the optimized AEI deposition procedure: this impressive result largely surpasses that of a PGM-based cell (with the same geometry and operating conditions), as displayed on Figure V.19. Additional comparative values of peak power density and OCV with recently-published studies are listed in Table V.1, corroborating the unprecedented performance of BH_4^-/H_2O_2 DBFC achieved in this work using non-PGM anode catalysts.

Table V.1: Comparison of recent DBFC performance data.

Ref	Anode (loading, $mg.cm^{-2}$)	Cathode (loading, $mg.cm^{-2}$)	Separator (thickness, µm)	Oxidant	*T* (°C)	P_{max} ($mW.cm^{-2}$)	OCV (V)
[129]	Pt/C(0.5)	Pt/C (2)	Nafion 212 (50)	O_2	60	420	0.94
[372]	NiB/C (70)	$LaNi_{0.9}Ru_{0.1}O_3$/C (7.5)	PEM (*NA.*)	O_2	25	180	1.09
[149]	Pd/C (0.3)	Pt/C (0.3)	Nafion 117 (183)	H_2O_2	25	211	1.72
[149]	Pt/C (0.3)	Pt/C (0.3)	Nafion 117 (183)	H_2O_2	25	275	1.67
[291]/ This work	Ni_{ED}/C (0.6)	Pt/C (2)	Nafion 212 (50)	O_2	60	108	1.21
[391]	Pt/C (0.16)	Pt/C (2)	Nafion 212 (50)	O_2	60	194	1.01
[391]/This work	Ni_{ED}/eNFT (1.2)	Pt/C (2)	Nafion 212 (50)	O_2	60	180	1.24
[151]	Pd/C(1)+Ni	Pt/C (1)	Bipolar Interface (175)	H_2O_2	70	300	1.80
This work	Ni_{ED}/eNFT-**D** (0.7)	Pt/C (1)	Bipolar Interface (175)	H_2O_2	70	446	2.0

The improvement of 200 mV on the OCV by using Ni electrodes (in their metallic state of surface) over Pt or Pd is clearly observed with either O_2 or H_2O_2 oxidant. Ni-based anodes perform better at high cell voltage in both conditions, and similarly (within the error bar) as Pt anodes combined with a CEM and O_2 at the cathode at lower cell voltage. In addition, the power density drops more abruptly at high current density with Pt/C than with Ni_{ED}/eNFT, which can be associated with more efficient mass-transport in the open porosity 3D-structured NFT support than in the more closed GDL porosity. Regarding the PMBI + H_2O_2 results, polarization curves for Ni_{ED}/eNFT-D and Pd/C are rather parallel, signing the overall better catalytic performance of Ni_{ED}/eNFT versus Pd/C (all other limitations, *e.g.* related to Ohmic drop and mass-transfer, being identical). The slope of the polarization curves for the PMBI cells is however steeper in these conditions. This is explained by the use of a significantly thicker (175 µm) Nafion-117 membrane than the one used during the O_2 tests (Nafion-212, 50 µm). While using thinner CEM would lower the cell resistance and therefore improve its performance, it could lead to larger risks of membrane perforation and of mixing of the strongly-reducing alkaline anolyte with a strongly-oxidizing acidic catholyte, adversely-affecting the durability of the cell.

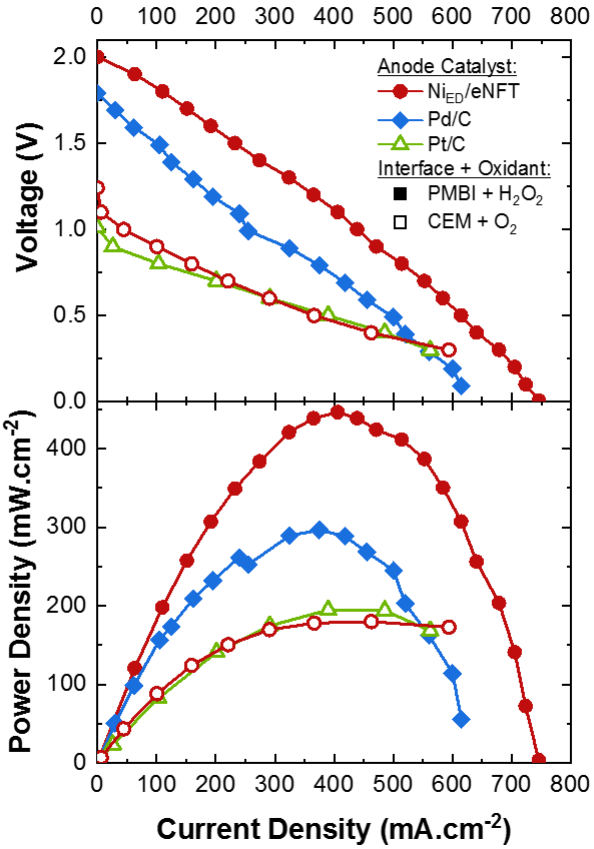

Figure V.19. DBFC performance of Ni_{ED}/eNFT anodes compared to PGM ones using PMBI (Dipping deposition) and H_2O_2 oxidant at T = 70°C (full symbols) or CEM and O_2 at T = 60°C (hollow symbols). Commercial Pt/C electrodes (1 mg.cm^{-2}) are used at the cathodes in all configurations. Pd/C data was reproduced from Ref.[151] with permission from Nature-Springer and CEM+O_2 data was reproduced from Ref.[391].

V.3.2

Towards efficient anion exchange DBFCs

The last experiments presented in this manuscript will be a preliminary study on BH_4^-/O_2 DBFC operating using AEM, which enables the use of non-noble cathode catalysts. Using these simultaneously with Ni-based anodes creates fully non-noble systems, which is a great advancement towards our aim to reduce our dependence to PGM catalysts. AEM are used since several years at the lab scale [156,168,169,400–402] but massive progress has been made recently allowing AEMFC to reach high power density [170,403] (> 1-2 W.cm^{-2}) which led to an important development of commercially available membranes. Commercial Xion (Xergy Inc®.) and PTFE Reinforced X37-50 (Sustainion®) membrane, referred later as Xion and Sustainion respectively, will be tested in the LEMTA's unit cell.

V.3.2.1 Investigating anion exchange membranes

Besides enabling the use of non-noble cathode catalysts, employing an AEM in DBFC would also theoretically reduce the overall cell resistance, especially at low temperature, because of its increased (OH^-) conductivity compared to a Nafion membrane in Na^+ form. It would therefore also prevent the crossing of sodium species to the cathode and the induced formation of NaOH crystals in its pores, which is a real drawback regarding the development of the DBFC in terms of fluidic management. The main drawback of using an AEM is that, by its nature of anion conduction, BH_4^- species would now be able to cross to the cathodic side. This means that the cathode catalyst must be tolerant to BH_4^- and still be active towards the ORR. Moreover, if this catalyst is active towards the BOR, the presence of borohydride at its vicinity will inevitably lower its potential and thus the overall cell voltage. For the first tests, the same BH_4^-/O_2 unit cell will be used in similar conditions as for Figure V.16, with only the membrane replaced by either the Xion or Sustainion AEM. These two membranes are thin: 20 µm and 50 µm, respectively, so a low resistivity should be expected. They possess a similar specific anionic conductivity comprised between 60 and 80 $mS.cm^{-2}$ (in OH^- conduction form). It is important to mention that the Sustainion is also reinforced by PTFE mesh for a better structural stability, which could impact the overall performance of the membrane. Because of the lower thermal stability of AEMs, compared to Nafion, it is not possible to bind them to the cathode by hot pressing: the contact between the active layer and the AEM will only be assured by physical pressing once assembled in the cell. Using an AEM also requires to change the ionomer binder in the cathode catalyst layer, in order to ensure a proper ion conduction. Pt/C (2 $mg.cm^{-2}$) cathodes were produced at LEMTA using commercial Sustainion ionomer with spray coating.

Figure V.20 reports the performance obtained using the Ni_{ED}/eNFT anode and Pt/C (2 $mg.cm^{-2}$) cathode with the two commercial AEMs. With the Xion membrane, the OCV decreases by *ca.* 0.15 V, compared to previous test using CEM (from 1.24 V to 1.10 V) (Figure V.20a). As explained above, this drop was expected from the use of Pt at the cathode: because of its ability to dissociate BH_4^- ions into BH_{ad} and H_{ad} adsorbates, as soon as some borohydride species cross the membrane, the local potential at the cathode decreases. What was not expected is the negative current recorded when the voltage of the cell is decreased to 1 V; when the voltage keeps diminishing, the current becomes positive. This effect could come from a non-stationary state of the membrane at the start of the measurements; however, the OCV is stable and this behavior is enhanced when the temperature is increased. One possible explanation is that some borohydride starts to be oxidized at the cathode at the start of the measurements, because the local potential is still high, enabling prevalent BOR over slow ORR at this cathode potential. This effect severely impacts the performance of the cell, because it artificially delays the

cell OCV (current can only be drawn below 0.9 V). This results in a maximum power density of only 90 mW.cm^{-2} at 60°C (Figure V.20b) and therefore a 50% loss compared to a conventional cell with a CEM. However, the performance at low temperature is rather good with 49 mW.cm^{-2} reached at 30°C. Similar power density was obtained with the CEM cell (Table V.2 in the conclusion of this chapter gathers data of all DBFC configurations presented for an easier comparison), which is already a good result considering the negative current effect observed. The cell resistance was measured at 60°C to be 1.25 Ω.cm², which is two times higher than the CEM cells (0.65 Ω.cm²). This high resistivity can be explained by the bad contact between the membrane and the cathode or a bad ion conduction between the Xion polymer of the membrane and the Sustainion of the catalysts binder.

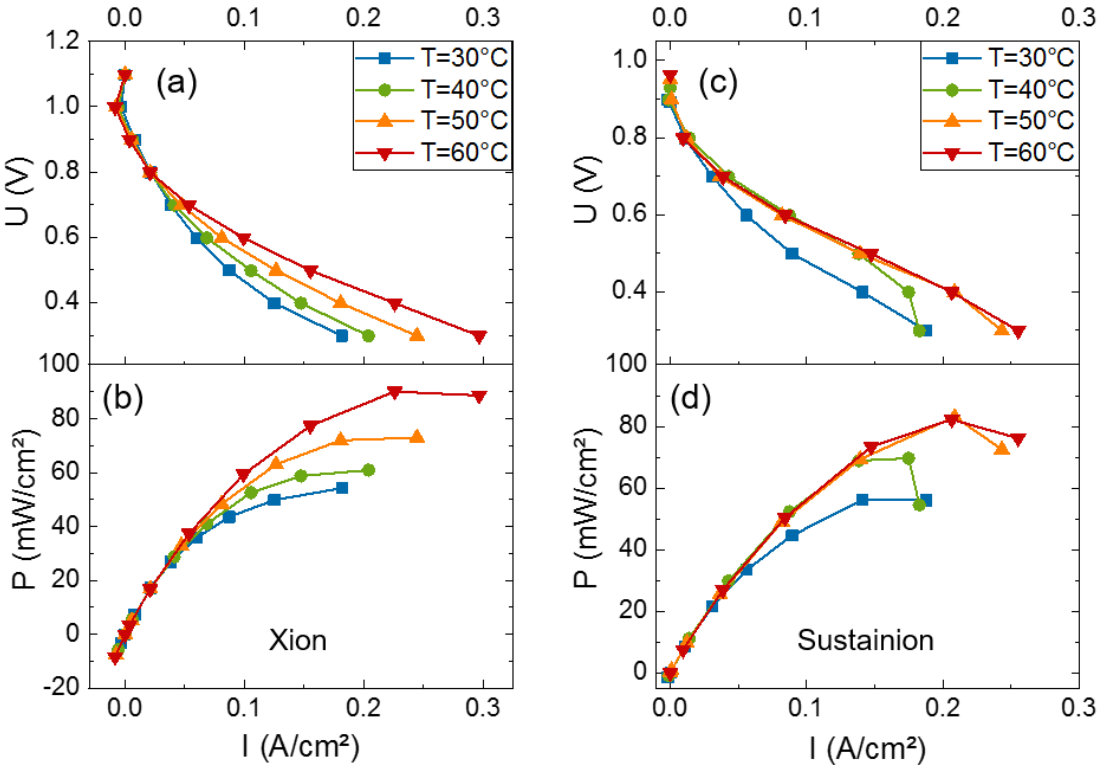

Figure V.20.(a, c) *I-U* curves and (b, d) *I-P* curves of DBFC using Ni_{ED}/eNFT anodes and Pt/C (1 mg.cm^{-2}, Sustainion binder) cathodes in alkaline conditions. Performance obtained using (a, b) a commercial Xion AEM and (c, d) a commercial Sustainion AEM.

Regarding the results obtained using the Sustainion AEM (Figure V.20c, d), the OCV is lowered to 0.9 V. Compared to the Xion AEM, both the OCV and P_{max} are lower, which probably means that this AEM allows more BH_4^- to cross to the cathode. This was unexpected since the Sustainion AEM is thicker. The effect of negative current at 1 V is however not observed using this membrane. If more BH_4^- is present at the cathode it should be exacerbated. The explanation given regarding the BOR occurring at cathode at high voltage is thus probably not valid, and it must be associated with the Xion AEM.

It is possible that an effect similar to fuel starvation occurs resulting in a behavior reversal in certain region of the cathode [404]. It should be possible to confirm this effect by performing ascending I-V measurements: no negative current should be measured around 1 V on the backward scan (but this has not been done during these tests). Regarding the behavior of the cell at lower cell voltage, reasonable power density is obtained at 30°C (P_{max} = 56 mW.cm^{-2}). However, it is strongly limited once the temperature is increased higher than 40°C and almost no improvement is observed between 50 and 60°C. An EIS measurement was performed at 30 and 60°C and surprisingly the measured high frequency resistance increased from 1.24 to 2.51 Ω.cm². One possible explanation is that the BH_4^- cross-over also increases with the temperature, replacing OH^- in the membrane and therefore increasing the resistivity. However, the OCV is stable for all temperature where it should decrease if more BH_4^- crosses to the cathode. Overall, a power density of P = 86 mW.cm^{-2} is reached at 60°C (and therefore also at 50°C), which is comparable to the Xion results but with an 0.2 V lower OCV. Since the normal operation of the cell using the latter membrane is delayed, this result is coherent.

V.3.2.2 DBFC tests using only non-noble catalysts

In this section, the same AEMs will be used but this time using non-noble Fe-N-C cathode catalysts provided by the group of Prof. Jaouen (Institut Charles Gerhardt Montpellier, Université de Montpellier). These materials were proven good ORR catalysts [379,405,406] and recently quite tolerant to BH_4^- [382]. Their synthesis is detailed in Ref [405]. The first results obtained in DBFC with these cathode catalysts are presented on Figure V21. Once again, an OCV of 1.1 V is obtained by using a Xion membrane and Fe-N-C cathode (Figure V.21a, b). To avoid the negative current effect observed on the previous measurement using this membrane (Figure V.20a) the potential was directly decreased to 0.9V after the OCV. This time, an impressive power density of 78 mW.cm^{-2} at 0.5 V was reached at 30°C without negative current. By looking at the shape of the power-density curve, one could expect it to keep increasing as at this voltage the slope is still positive. At low cell voltage (0.3 V and also 0.4 V at 30°C) the current drops significantly resulting in polarization and power curves with "hook shapes". However, the increase of temperature seems to limit this effect and it disappears at 60°C. Looking at the local potential of the electrodes (Figure V.21a), that at the cathode drops where it is stable at the anode (except for 30°C). Thus, this current drop must be due to the use the Fe-N-C catalyst. One explanation for these "hook shapes" is the oxidation of the cathode catalysts *via* the formation of H_2O_2 (HO_2^-). This oxidized catalyst being less active towards the ORR, the currents drop. After each increase of temperature, the performances are back to the initial state, which can be due to reduction of the formed oxides thanks to BH_4^- crossing at the cathode. By looking

closely at the data, the OCV slightly decreases at each measurement (from 1.11 V at T = 30°C to 1.06 V at T = 60°C), which could indicate some irreversible degradation every time the cell voltage is lowered too much. The kinetics of reactions did not really increase either with the temperature, where it was the case when a Pt/C cathode was used with this membrane (Figure V.20a, b). It could indicate that the cathode is strongly limiting the cell. Despite these oxidation effects, a reasonable power density of 101 mW.cm^{-2} is reached with this fully non-noble cell, which is better than the results obtained using AEMs and a Pt/C cathode.

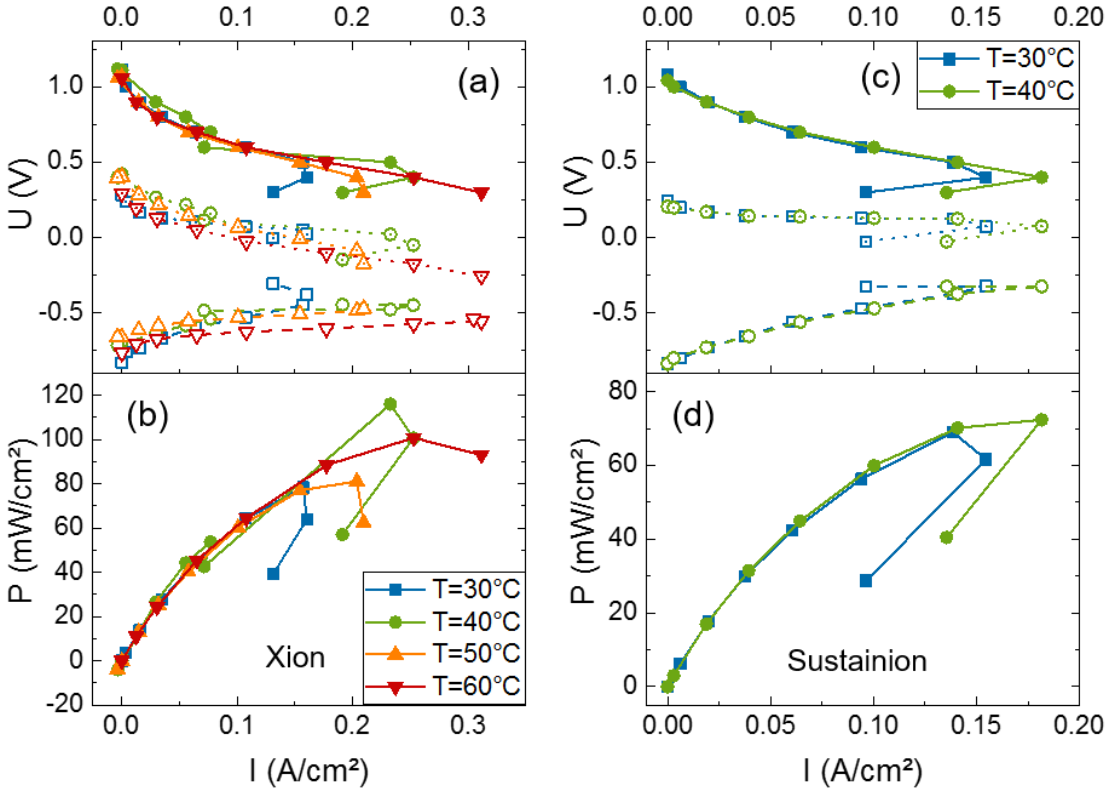

Figure V.21. (a, c) *I-U* curves with cathode (dotted lines) and anode (dash lines) potentials measured using an *in situ* H_2 reference and (b, d) *I-P* curves of DBFC using Ni_{ED}/eNFT anodes and Fe-N-C (Sustainion binder) cathodes in alkaline conditions. Performance obtained using (a, b) a commercial Xion AEM and (c, d) a commercial Sustainion AEM.

The same test was reproduced but with the Sustainion membrane (Figure V.21c, d) and a similar OCV of 1.08 V was obtained. This already indicates that the Fe-N-C catalyst is better suited than Pt/C for the DBFC cathode if an AEM is used (the OCV dropped to 0.9 V with Pt/C, Figure V.20c) and confirms that it is quite tolerant to borohydride even in large amounts [382]. Unfortunately, a hardware error occurred during the test which stopped the measurement at 40°C. Since the amounts of cathode catalyst available were limited, it was not possible to reproduce it. However, some interesting results can still be observed for these two temperatures. First of all, the same "hook" effect is observed,

which confirms that it really originated from the Fe-N-C catalyst. Besides it also is limited at higher temperature, as the 40°C curve suggest: the current does not drop at 0.4 V anymore. A maximum power density of 69 $mW.cm^{-2}$ is reached, which is slightly lower than with the Xion membrane but is again higher than for a Pt/C cathode, while using the same membrane.

Overall, promising results were obtained using commercial AEMs in the unit DBFC. They could still be largely improved, since the results presented here are only preliminary. Better knowledge of the behavior of commercial AEMs should be acquired in order to solve the issues encountered when they are used. Moreover, we think the performance acquired during this campaign were mainly limited by the interface between the membrane and the catalyst layer, where the ion conduction between the membrane and the catalytic layer was only ensured by cell-assembling pressure. One option to ward off this issue would be to deposit the catalyst layer directly on the membrane to obtain a CCM. That way, the ion conduction should be greatly increased. Besides, better performing AEMs from J. Varcoe's group (University of Surrey, Great Britain) should be tested in DBFC in a near future.

V.4 Conclusions

To conclude this chapter, the electrodeposition method to acquire highly active metallic Ni nanoparticle presented in Chapter IV was successfully adapted to reproducibly prepared electrode of larger surfaces. The procedure was adapted to enable a control on the loading of Ni deposited on the carbon support, resulting in two typical electrodes with respectively a low (0.6 $mg.cm^{-2}$) and high (3.6 $mg.cm^{-2}$) loading with their distinct Ni agglomerates morphology. The choice of performing the ED directly in the pores of a GDL (without a micro-porous layer) was made to simplify the procedure and allow NPs to be deposited in the deeper layer of the support. These electrodes were tested in unit (8 cm^2) DBFC cell and presented impressive results, such as a really high OCV of 1.21 V and a peak power density of 121 $mW.cm^{-2}$ at 0.5 V and 60°C, largely surpassing those of a commercial Pt black anode. Table V.2 compiles the performance of each BH_4^-/O_2 DBFC configuration presented in this chapter. The only aspect not in favor of the Ni_{ED}/GDE is the amount of hydrogen escaping the cell during operation. Indeed, in Chapter 4 it was presented that metallic Ni was a bad HER/HOR catalyst and this was actually one of the reasons for its outstanding BOR activity at low potential. Unfortunately, it translates in poor H_2 valorization in a DBFC resulting in loss of potential efficiency.

Table V.2: Comparison of all BH_4^-/O_2 DBFC configurations presented in this Chapter. The binder used in each cathode is specified in brackets with the following abbreviations code: Nafion (Naf); Sustainion (Sust); Fumasep (Fum). / symbol specify missing data due to technical errors.

Cell configuration (A//M//C)	OCV (V)	P_{max} (mW.cm^{-2}) @30°C	P_{max} (mW.cm^{-2}) @60°C	% H_2 escape (0.3V, 60°C)	R_{HF} @60°C (Ω.cm²)
Pt/C//Nafion//Pt/C(Naf)	1.00	42	68	3	0.90
Pt/GDL//Nafion// Pt/C(Naf)	1.05	53	195	1	0.86
Ni_{ED}/GDE//Nafion// Pt/C(Naf)	1.21	50	121	30	0.85
Ni_{ED}/eNFT//Nafion// Pt/C(Naf)	1.24	54	180	50	0.65
Ni_{ED}/eNFT //Xion// Pt(Sust)	1.10	50	90	49	1.25
Ni_{ED}/eNFT //Sustainion// Pt/C(Sust)	0.96	56	82	55	2.5
Ni_{ED}/eNFT //Xion// Fe-N-C(Fum)	1.10	41.3	37	54	0.71
Ni_{ED}/eNFT //Xion// Fe-N-C(Sust)	1.11	78	101	51	0.86
Ni_{ED}/eNFT //Sustainion// Fe-N-C(Sust)	1.08	69	/	/	1.09> @40°C

Because no other anode catalyst present better activity than metallic Ni to this day, the only way to increase the performance of the cell was to improve its other parameters. The first modification was to replace the carbon support by a more open one to improve the fuel management in the electrode as demonstrated by Olu *et al.* [129]. To improve the overall performance of the anode, 3D Ni structure such as nickel foam or felt were investigated. They quickly demonstrated to be poor candidate as the Ni nanoparticles supports if used in their pristine state, mainly because of their native oxidized state of surface. To address this issue, surface treatment such as acid etchings were performed to obtain rougher and more metallic surfaces. The Ni foam properties did not improve enough to be used as anode catalyst support, thus only the felt was considered. Once the electrodeposition procedure adapted to this new support, the fully Ni-based anodes presented the best BOR activity so far. The procedure to obtain such surface and the improvement link to each step is summarized on Figure V.22.

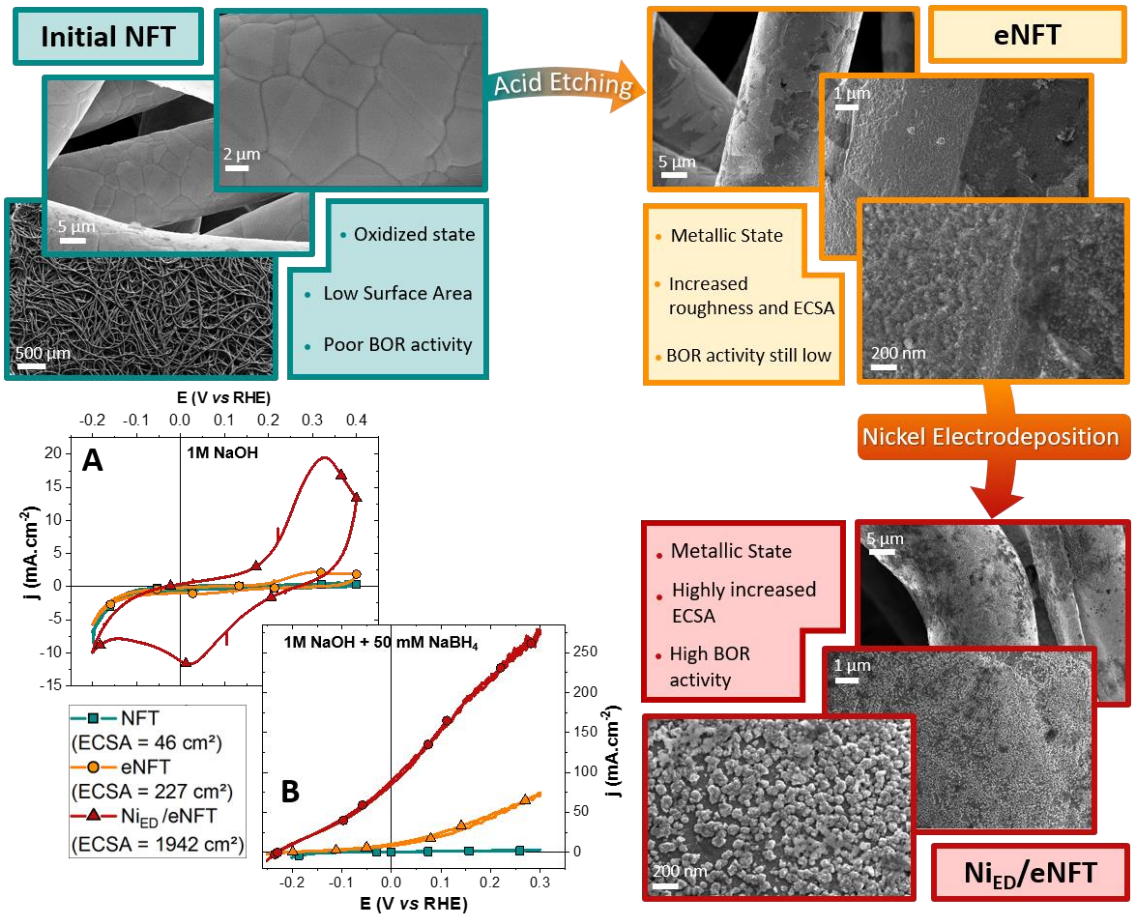

Figure V.22. Evolution of the morphology, electrochemical surface area (ECSA), and BOR activity of the NFT following consecutive steps of the electrode elaboration process. The oxidation state and the amount of active site is tuned through a two-steps process: (i) an acid etching of the initial NFT to reveal metallic sites and increase the roughness (ii) and an electrodeposition of Ni NPs to highly increase the number of active sites and the BOR activity as observed on both voltammograms in (A) supporting electrolyte (1 M NaOH) and (B) BOR conditions (1 M NaOH + 50 mM NaBH4). CV conditions: Ar-saturated solutions, T = 20°C, v_s = 20 mV.s^{-1}, ω = 1600 rpm

Pt nanoparticles were deposited is the pores of the supporting GDL to create a more open Pt-based anode and make a fairer comparison. These two electrodes were tested in the unit DBFC cell and again the Ni-based electrode presented the best OCV (1.24 V) and comparable power density. The resistivity of the cell significantly decreased by using the fully metallic anode; however, it also resulted in a more important hydrogen escape of 50%. This important value actually fits well the 4 electrons produced per BH_4^- oxidized proposed by our tentative model described in Chapter IV. This loss of H_2 will be measured similar every time a Ni_{ED}/eNFT anode will be used.

To keep improving the DBFC, the membrane and cathode were optimized. Indeed, using a state-of-the-art Nafion CEM in presence of alkaline solution shifts its "normal" H^+ conduction to Na^+ conduction. This greatly diminishes the conductivity of the membrane. To avoid such ion exchange, a bipolar interface was tested in a BH_4^-/H_2O_2

unit cell. The procedure to deposit the AEI on the anode catalyst was adapted to the fully Ni-based anodes and impressive performance was obtained in DBFC conditions: an OCV of 2.0 V and a peak power density of 446 $mW.cm^{-2}$ were reached surpassing the already impressive results obtained using a Pd-based anode in the same conditions. Lastly, commercial AEMs were tested in the BH_4^-/O_2 cell. The preliminary results obtained are promising especially using non-noble cathode catalysts for the ORR making the cell completely PGM-free. However, a better understanding of the AEMs and these materials is required to maximize the impressive potential of such unit cell.

GENERAL CONCLUSION & PERSPECTIVES

The general problematics of this thesis, driven by the MobiDiC project, were all connected to two main objectives: to understand the BOR in DBFC conditions and develop efficient and low-cost anodes. To complete this global task, the problematic was divided in three chapters presenting the results of this work: (i) the first one (Chapter III) was dedicated to the understanding of the BOR mechanism on noble electrodes in FC operation conditions; (ii) then (Chapter IV) the focus was put on replacing such noble materials by non-noble Ni-based electrocatalysts and provide a preliminary explanation of the reaction behavior on such surfaces; (iii) the final chapter (Chapter V) aimed to develop efficient DBFC anodes using the Ni-based materials developed previously and compare their performance to state of the art Pt-based anodes.

- Conclusions on Chapter III

At first, the BOR model proposed by Olu in his thesis (2015) was updated using the mechanistic studies performed at high borohydride concentrations for Pt surfaces. The reaction behavior for Au electrode was also included in this model since it was revealed that they behave in a similar manner once Pt is strongly poisoned. If the number of active site is too low compared to the borohydride concentration, the surface of Pt will be covered by stable BH_{ad} species forcing the reaction to switch from a "fully dissociative pathway" (occurring via BH_{ad}) to a less efficient "partially dissociative pathway" (proceeding via $BH_{3,ad}$). Indeed, the $BH_{3,ad}$ intermediate species formed during this second mechanism are less stable and result in a faradic efficiency loss from their desorption into BH_3OH^- or dissociation into BH_{ad}. The formation of surface oxide is required to regenerate the surface from this poison but should not be performed in FC configuration to avoid huge degradation of the cathode. Regarding gold, its inefficiency towards the BOR at low potentials was explained by the fact that the only possible reaction mechanism is the "partially dissociative pathway", resulting in the same $BH_{3,ad}$ desorption as on 'poisoned' Pt. In addition, because of the weak H adsorption on Au and its poor HOR activity, the dissociation of these $BH_{3,ad}$ species into BH_{ad} and $2H_{ad}$ followed by ionization of the latter in a Volmer step is not possible, leading to their dehydrogenation into BH_{ad} releasing one H_2 molecule and decreasing even more the efficiency of the reaction with two additional electrons lost.

Lastly, Pd model electrodes were studied to unveil the behavior of these electrocatalyst towards the BOR. In addition to being poisoned by intermediate species, like Pt and Au, the structure of the electrode itself was demonstrated to be modified in presence of borohydride. The two considered possibilities were the formation of either PdB or PdH. The first experimental clues tend to favor the formation of palladium hydride that will, contrary to expectations, be desorbed only at high potential, once the boron-based adsorbates are stripped from the surface. This results in a BOR behavior significantly different from the one predicted by DFT calculations on model Pd surfaces. However, if

this hypothesis is correct, the electrode surface is in reality composed of PdH and these calculations cannot be used and must be rectified considering the PdH structure of the electrode. Preliminary *in situ* XRD measurements performed with synchrotron radiation at ESRF in July 2020 tend to confirm this hydride formation and exclude the presence of (crystalline) PdB.

- Conclusions on Chapter IV

Even if Pd-based anodes exhibit comparable (or even higher) performance to Pt-based ones in DBFC configuration, it is debatable to consider them as good substitute considering the 2020 market prices: Pd is now more expensive than Pt. Furthermore, huge instabilities of PGM nanoparticles supported on carbon substrates were reported in alkaline medium, with drastic particle detachment even after stability test under mild conditions. These two factors highly motivated us to consider non-noble materials as BOR electrocatalysts. Amongst all transition metals available, Ni appeared the most promising. However, its catalytic activity towards this reaction was highly debated in the scientific community. Some studies reported significantly low onset potentials and decent charge-transfer kinetics while others pointed to an overall inactivity of Ni towards the BOR. Compared to previously studied noble metals, a new factor must now be considered for non-noble catalysts elaboration: the oxidation state of its surface.

Indeed, Oshchepkov demonstrated during his thesis that such state of surface will greatly affect the electrochemical behavior of Ni electrodes towards the hydrogen reactions: metallic surfaces present a really poor activity for both the HER/HOR, but when it is partially oxidized (covered by the surface oxide islands) this activity is drastically enhanced. Completely oxidizing the surface however results in decreasing the charge transfer kinetics. Such oxide formation on Ni is moreover electrochemically irreversible and the potential applied to the electrode must thus be precisely controlled at all times. By applying this knowledge to the BOR, metallic Ni electrode revealed impressive onset potentials (down to E = -0.250 mV *vs* RHE) and the best charge-transfer kinetic recorded, to the authors knowledge, for potentials below E = 0 V *vs* RHE. Bimetallic Ni_xM nanoparticles deposited on carbon support were investigated to observe if alloying Ni with other elements would ease its depassivation to reach this pursued metallic state. However, it appeared that Ni-based electrocatalysts synthesized by standard chemical/thermal procedures are irreversibly oxidized so only a state comparable to the partially oxidized Ni electrode is attainable.

Electrodeposition of Ni nanoparticles (Ni_{ED}) was therefore chosen to elaborate highly developed surface area electrode. The resulting surfaces surpassed the activity of Pt at low potential. However, the BOR appeared limited at a faradic efficiency of 50% (4 electrons instead of 8 released). Mechanistic studies as well as computational

calculations (DFT + microkinetic modelling) allowed to draw a preliminary model for the BOR on metallic Ni. Because of the strong adsorption of H_{ad} species, the BOR on Ni can start at low potential; however, 2 molecules of H_2 are released per BH_4^- species oxidized, explaining the 50% efficiency and the observation made by Indig and Snyder in the first study reported on the BOR (using a Ni electrode): "The gassing rate increased with the electrochemical oxidation, and at a rate of 775 mA.cm^{-2} much hydrogen was evolved. This indicated that hydrogen was formed as a product of the electrochemical oxidation.".

- Conclusions on Chapter V

Finally, these Ni_{ED} electrocatalysts were used to elaborate low cost anode by adapting the electrodeposition procedure to a larger scale. To simplify it, no microporous layer was used and the particles were directly deposited in the pores of the diffusion layer. This resulted in higher performance in a DBFC configuration than for a commercial Pt black electrode, both in terms of OCV and power density. To further increase this performance, Ni 3D structures were investigated to substitute the carbon paper as electrocatalyst support. They present the advantages of a more open structure (better mass-transport conditions), which was demonstrated by Olu to be one of the key factors to increase DBFC performance, a better conductivity, and being also active for the BOR. After etching treatments to optimize their state of surface, such structures were used to produce fully Ni-based anodes with improved power density compared to the first Ni/GDE ones.

From this point, such anodes were tested in various DBFC configurations: (i) a H_2O_2 DBFC unit cell with a bipolar interface, which leads to an impressive OCV of 2.0 V and a peak power density 50% higher than a Pd-based anode in similar conditions; (ii) The same O_2 DBFC unit cell used for the first test was used but with commercial AEMs instead of the standard Nafion membrane. Both commercial Pt black and Fe-N-C (made by Prof. Jaouen's group) were tested at the cathode. In such conditions, the non-noble cathode proved more effective than the Pt one, because of its higher tolerance to BH_4^- species crossing the membrane. These preliminary tests did not fully meet our expectations, especially because of the high cell resistance measured (where the use of AEM should help to decrease it), but were also encouraging, especially for low temperature applications, with a peak power density of almost P = 80 mW.cm^{-2} reached at T = 30°C.

- Perspectives for the development of DBFCs

Overall, the problematics of the thesis were well answered by these three main sections. However, they also raised some questions and obviously did not address all the different aspects of the studied BOR mechanism. First, the BOR mechanism on Pd needs

additional studies in order to be fully understood: the formation of hydride must be confirmed by several characterization methods and the proposed mechanism should be corroborated by DFT calculations performed for a PdH surface. However, such calculations are probably complex and will require much efforts because this structure is not as well defined as the Pd (1 1 1) single crystal one usually considered. Moreover, since the Pd electrode serves as a hydride reservoir, the PdH composition itself will vary during the BOR.

This task might however fall behind, because of the emergence of metallic Ni electrocatalysts and their impressive activity towards the BOR. Indeed, the novelty and performance of such materials will most probably drive the focus of mechanistic studies to them. The mechanism proposed in this manuscript was literally the first one established and it should therefore be further modified and updated towards elementary steps, that could fit better the experimental data. In the same manner as for Pd, *in situ* XRD synchrotron measurements are considered by our group to investigate the variation of the Ni electrode structure and surface composition during the reaction.

Regarding the development of DBFC, to the point of view of the author, the fully Ni-based anode is no longer the limiting piece of the system and the focus should be turned to the other parameters of the cell. The preliminary tests using AEMs should be pursued, since such membranes are being improved at a really fast pace (last year almost no commercial AEM were available). Moreover, the very high performance reached recently with AFC systems should also encourage DBFC users to adapt such membranes. The cathode material should also be considered and optimized. Overall, the reactant transport was recently demonstrated by Prof. Ramani's group to be a major factor for performance optimization in a DBFC and a particular attention should be given to this aspect. Overall, with these promising results and the development of materials suitable for a DBFC, the author strongly believes that a highly efficient, fully non-noble system will be obtained in a near future.

REFERENCES

[1] S.E. Perkins-Kirkpatrick, S.C. Lewis, Increasing trends in regional heatwaves, Nat. Commun. 11 (2020) 1–8. doi:10.1038/s41467-020-16970-7.

[2] Global Temperature Report for 2019 - Berkeley Earth, (n.d.). http://berkeleyearth.org/archive/2019-temperatures/ (accessed August 20, 2020).

[3] A. Buis, Milankovitch (Orbital) Cycles and Their Role in Earth's Climate, Clim. Chang. Vital Signs Planet. (2020). https://climate.nasa.gov/news/2948/milankovitch-orbital-cycles-and-their-role-in-earths-climate/ (accessed August 25, 2020).

[4] D.A. Lashof, D.R. Ahuja, Relative global warming potentials of greenhouse gas emissions, Nature. 344 (1990) 529–531.

[5] S.H. Schneider, Global warming : are we entering the greenhouse century?, Sierra Club Books, 1989.

[6] R.E. Dickinson, R.J. Cicerone, Future global warming from atmospheric trace gases, Nature. 319 (1986) 109–115. doi:10.1038/319109a0.

[7] P.D. Jones, T.M.L. Wigley, Global Warming Trends, Sci. Am. 263 (1990) 84–91. doi:10.2307/24996902.

[8] R.K. Kaufmann, D.I. Stern, Evidence for human influence on climate from hemispheric temperature relations, Nature. 388 (1997) 39–44. doi:10.1038/40332.

[9] Overview of Greenhouse Gases | Greenhouse Gas (GHG) Emissions | US EPA, (n.d.). https://www.epa.gov/ghgemissions/overview-greenhouse-gases (accessed August 25, 2020).

[10] US EPA, Sources of Greenhouse Gas Emissions, (n.d.). https://www.epa.gov/ghgemissions/sources-greenhouse-gas-emissions (accessed August 25, 2020).

[11] H. Ritchie, M. Roser, CO_2 and Greenhouse Gas Emissions, OurWorldinData.Org. (2017). https://ourworldindata.org/co2-and-other-greenhouse-gas-emissions#citation (accessed August 25, 2020).

[12] M. Meinshausen, N. Meinshausen, W. Hare, S.C.B. Raper, K. Frieler, R. Knutti, D.J. Frame, M.R. Allen, Greenhouse-gas emission targets for limiting global warming to 2°C, Nature. 458 (2009) 1158–1162. doi:10.1038/nature08017.

[13] On the U.S. Withdrawal from the Paris Agreement - United States Department of State, (n.d.). https://www.state.gov/on-the-u-s-withdrawal-from-the-paris-agreement/ (accessed August 25, 2020).

[14] C. Le Quéré, R.B. Jackson, M.W. Jones, A.J.P. Smith, S. Abernethy, R.M. Andrew, A.J. De-Gol, D.R. Willis, Y. Shan, J.G. Canadell, P. Friedlingstein, F. Creutzig, G.P. Peters, Temporary reduction in daily global CO2 emissions during the COVID-19 forced confinement, Nat. Clim. Chang. 10 (2020) 647–653. doi:10.1038/s41558-020-0797-x.

[15] M.A. Zambrano-Monserrate, M.A. Ruano, L. Sanchez-Alcalde, Indirect effects of COVID-19 on the environment, Sci. Total Environ. 728 (2020) 138813. doi:10.1016/j.scitotenv.2020.138813.

[16] M. Roser, H. Ritchie, E. Ortiz-Ospina, World Population Growth,

OurWorldinData.Org. (2019). https://ourworldindata.org/world-population-growth (accessed August 25, 2020).

[17] J.M. Calm, Emissions and environmental impacts from air-conditioning and refrigeration systems, Int. J. Refrig. 25 (2002) 293–305. doi:10.1016/S0140-7007(01)00067-6.

[18] L.W. Davis, P.J. Gertler, Contribution of air conditioning adoption to future energy use under global warming, Proc. Natl. Acad. Sci. U. S. A. 112 (2015) 5962–5967. doi:10.1073/pnas.1423558112.

[19] J.L. Cohen, J.C. Furtado, M. Barlow, V.A. Alexeev, J.E. Cherry, Asymmetric seasonal temperature trends, Geophys. Res. Lett. 39 (2012). doi:10.1029/2011GL050582.

[20] J. Cohen, J.A. Screen, J.C. Furtado, M. Barlow, D. Whittleston, D. Coumou, J. Francis, K. Dethloff, D. Entekhabi, J. Overland, J. Jones, Recent Arctic amplification and extreme mid-latitude weather, Nat. Geosci. 7 (2014) 627–637. doi:10.1038/ngeo2234.

[21] J. Cohen, K. Pfeiffer, J.A. Francis, Warm Arctic episodes linked with increased frequency of extreme winter weather in the United States, Nat. Commun. 9 (2018) 1–12. doi:10.1038/s41467-018-02992-9.

[22] M. Mori, M. Watanabe, H. Shiogama, J. Inoue, M. Kimoto, Robust Arctic sea-ice influence on the frequent Eurasian cold winters in past decades, Nat. Geosci. 7 (2014) 869–873. doi:10.1038/ngeo2277.

[23] A. Dai, Increasing drought under global warming in observations and models, Nat. Clim. Chang. 3 (2013) 52–58. doi:10.1038/nclimate1633.

[24] K.E. Trenberth, A. Dai, G. Van Der Schrier, P.D. Jones, J. Barichivich, K.R. Briffa, J. Sheffield, Global warming and changes in drought, Nat. Clim. Chang. 4 (2014) 17–22. doi:10.1038/nclimate2067.

[25] Q. Schiermeier, Increased flood risk linked to global warming, Nature. 470 (2011) 316. doi:10.1038/470316a.

[26] L. Alfieri, B. Bisselink, F. Dottori, G. Naumann, A. de Roo, P. Salamon, K. Wyser, L. Feyen, Global projections of river flood risk in a warmer world, Earth's Futur. 5 (2017) 171–182. doi:10.1002/2016EF000485.

[27] M. Yamaguchi, J.C.L. Chan, I.J. Moon, K. Yoshida, R. Mizuta, Global warming changes tropical cyclone translation speed, Nat. Commun. 11 (2020) 1–7. doi:10.1038/s41467-019-13902-y.

[28] Q. Sun, C. Miao, M. Hanel, A.G.L. Borthwick, Q. Duan, D. Ji, H. Li, Global heat stress on health, wildfires, and agricultural crops under different levels of climate warming, Environ. Int. 128 (2019) 125–136. doi:10.1016/j.envint.2019.04.025.

[29] G. Di Virgilio, J.P. Evans, H. Clarke, J. Sharples, A.L. Hirsch, M.A. Hart, Climate Change Significantly Alters Future Wildfire Mitigation Opportunities in Southeastern Australia, Geophys. Res. Lett. 47 (2020). doi:10.1029/2020gl088893.

[30] A.H. Sobel, S.J. Camargo, T.M. Hall, C.Y. Lee, M.K. Tippett, A.A. Wing, Human influence on tropical cyclone intensity, Science (80-.). 353 (2016) 242–246.

doi:10.1126/science.aaf6574.

[31] Y. Ding, S. Zhang, L. Zhao, Z. Li, S. Kang, Global warming weakening the inherent stability of glaciers and permafrost, Sci. Bull. 64 (2019) 245–253. doi:10.1016/j.scib.2018.12.028.

[32] V. Romanovsky, M. Burgess, S. Smith, K. Yoshikawa, J. Brown, Permafrost temperature records: Indicators of climate change, Eos, Trans. Am. Geophys. Union. 83 (2002) 589. doi:10.1029/2002EO000402.

[33] D.A. Sutherland, R.H. Jackson, C. Kienholz, J.M. Amundson, W.P. Dryer, D. Duncan, E.F. Eidam, R.J. Motyka, J.D. Nash, Direct observations of submarine melt and subsurface geometry at a tidewater glacier, Science (80-.). 365 (2019) 369–374. doi:10.1126/science.aax3528.

[34] G.C. Johnson, J.M. Lyman, Warming trends increasingly dominate global ocean, Nat. Clim. Chang. 10 (2020) 757–761. doi:10.1038/s41558-020-0822-0.

[35] M. Hieronymus, An update on the thermosteric sea level rise commitment to global warming, Environ. Res. Lett. 14 (2019) 054018. doi:10.1088/1748-9326/ab1c31.

[36] E. Bekkers, J.F. Francois, H. Rojas-Romagosa, Melting ice Caps and the Economic Impact of Opening the Northern Sea Route, Econ. J. 128 (2018) 1095–1127. doi:10.1111/ecoj.12460.

[37] B.P. Horton, N.S. Khan, N. Cahill, J.S.H. Lee, T.A. Shaw, A.J. Garner, A.C. Kemp, S.E. Engelhart, S. Rahmstorf, Estimating global mean sea-level rise and its uncertainties by 2100 and 2300 from an expert survey, Npj Clim. Atmos. Sci. 3 (2020) 1–8. doi:10.1038/s41612-020-0121-5.

[38] K.F. Davis, A. Bhattachan, P. D'Odorico, S. Suweis, A universal model for predicting human migration under climate change: Examining future sea level rise in Bangladesh, Environ. Res. Lett. 13 (2018) 064030. doi:10.1088/1748-9326/aac4d4.

[39] C.D. Thomas, A. Cameron, R.E. Green, M. Bakkenes, L.J. Beaumont, Y.C. Collingham, B.F.N. Erasmus, M. Ferreira De Siqueira, A. Grainger, L. Hannah, L. Hughes, B. Huntley, A.S. Van Jaarsveld, G.F. Midgley, L. Miles, M.A. Ortega-Huerta, A.T. Peterson, O.L. Phillips, S.E. Williams, Extinction risk from climate change, Nature. 427 (2004) 145–148. doi:10.1038/nature02121.

[40] M. Bálint, S. Domisch, C.H.M. Engelhardt, P. Haase, S. Lehrian, J. Sauer, K. Theissinger, S.U. Pauls, C. Nowak, Cryptic biodiversity loss linked to global climate change, Nat. Clim. Chang. 1 (2011) 313–318. doi:10.1038/nclimate1191.

[41] R. Warren, J. Vanderwal, J. Price, J.A. Welbergen, I. Atkinson, J. Ramirez-Villegas, T.J. Osborn, A. Jarvis, L.P. Shoo, S.E. Williams, J. Lowe, Quantifying the benefit of early climate change mitigation in avoiding biodiversity loss, Nat. Clim. Chang. 3 (2013) 678–682. doi:10.1038/nclimate1887.

[42] C.S. Mantyka-Pringle, P. Visconti, M. Di Marco, T.G. Martin, C. Rondinini, J.R. Rhodes, Climate change modifies risk of global biodiversity loss due to land-cover change, Biol. Conserv. 187 (2015) 103–111. doi:10.1016/j.biocon.2015.04.016.

[43] R. Shope, Global climate change and infectious diseases., Environ. Health

Perspect. 96 (1991) 171–174. doi:10.1289/ehp.9196171.

[44] A.A. Khasnis, M.D. Nettleman, Global warming and infectious disease, Arch. Med. Res. 36 (2005) 689–696. doi:10.1016/j.arcmed.2005.03.041.

[45] J.C. Semenza, B. Menne, Climate change and infectious diseases in Europe, Lancet Infect. Dis. 9 (2009) 365–375. doi:10.1016/S1473-3099(09)70104-5.

[46] B.A. Revich, M.A. Podolnaya, Thawing of permafrost may disturb historic cattle burial grounds in East Siberia, Glob. Health Action. 4 (2011) 8482. doi:10.3402/gha.v4i0.8482.

[47] M. Legendre, J. Bartoli, L. Shmakova, S. Jeudy, K. Labadie, A. Adrait, M. Lescot, O. Poirot, L. Bertaux, C. Bruley, Y. Couté, E. Rivkina, C. Abergel, J.M. Claverie, Thirty-thousand-year-old distant relative of giant icosahedral DNA viruses with a pandoravirus morphology, Proc. Natl. Acad. Sci. U. S. A. 111 (2014) 4274–4279. doi:10.1073/pnas.1320670111.

[48] K.D. Bidle, S.H. Lee, D.R. Marchant, P.G. Falkowski, Fossil genes and microbes in the oldest ice on Earth, Proc. Natl. Acad. Sci. U. S. A. 104 (2007) 13455–13460. doi:10.1073/pnas.0702196104.

[49] H. Ritchie, M. Roser, Energy, OurWorldinData.Org. (2018). https://ourworldindata.org/energy (accessed August 26, 2020).

[50] H. Ritchie, M. Roser, Renewable Energy, OurWorldinData.Org. (2017). https://ourworldindata.org/renewable-energy (accessed August 26, 2020).

[51] Renewable energy statistics - Statistics Explained, (n.d.). https://ec.europa.eu/eurostat/statistics-explained/index.php/Renewable_energy_statistics (accessed August 26, 2020).

[52] P.A. Kharecha, J.E. Hansen, Prevented mortality and greenhouse gas emissions from historical and projected nuclear power, Environ. Sci. Technol. 47 (2013) 4889–4895. doi:10.1021/es3051197.

[53] H. Ritchie, Global renewables are growing, but are only managing to offset the decline in nuclear production, OurWorldinData.Org. (2017). https://ourworldindata.org/global-renewables-are-growing-but-are-only-managing-to-offset-a-decline-in-nuclear-production (accessed August 26, 2020).

[54] Building ITER, (n.d.). https://www.iter.org/construction/construction (accessed August 26, 2020).

[55] A.C. Lees, C.A. Peres, P.M. Fearnside, M. Schneider, J.A.S. Zuanon, Hydropower and the future of Amazonian biodiversity, Biodivers. Conserv. 25 (2016) 451–466. doi:10.1007/s10531-016-1072-3.

[56] G. Ziv, E. Baran, S. Nam, I. Rodríguez-Iturbe, S.A. Levin, Trading-off fish biodiversity, food security, and hydropower in the Mekong River Basin, Proc. Natl. Acad. Sci. U. S. A. 109 (2012) 5609–5614. doi:10.1073/pnas.1201423109.

[57] K.O. Winemiller, P.B. McIntyre, L. Castello, E. Fluet-Chouinard, T. Giarrizzo, S. Nam, I.G. Baird, W. Darwall, N.K. Lujan, I. Harrison, M.L.J. Stiassny, R.A.M. Silvano, D.B. Fitzgerald, F.M. Pelicice, A.A. Agostinho, L.C. Gomes, J.S. Albert, E. Baran, M. Petrere, C. Zarfl, M. Mulligan, J.P. Sullivan, C.C. Arantes, L.M. Sousa,

A.A. Koning, D.J. Hoeinghaus, M. Sabaj, J.G. Lundberg, J. Armbruster, M.L. Thieme, P. Petry, J. Zuanon, G. Torrente Vilara, J. Snoeks, C. Ou, W. Rainboth, C.S. Pavanelli, A. Akama, A. Van Soesbergen, L. Sáenz, Balancing hydropower and biodiversity in the Amazon, Congo, and Mekong, Science (80-.). 351 (2016) 128–129. doi:10.1126/science.aac7082.

[58] S. Wang, S. Wang, Impacts of wind energy on environment: A review, Renew. Sustain. Energy Rev. 49 (2015) 437–443. doi:10.1016/j.rser.2015.04.137.

[59] C. kang Gao, H. ming Na, K. hui Song, N. Dyer, F. Tian, Q. jiang Xu, Y. hong Xing, Environmental impact analysis of power generation from biomass and wind farms in different locations, Renew. Sustain. Energy Rev. 102 (2019) 307–317. doi:10.1016/j.rser.2018.12.018.

[60] P.A.J. Bonar, I.G. Bryden, A.G.L. Borthwick, Social and ecological impacts of marine energy development, Renew. Sustain. Energy Rev. 47 (2015) 486–495. doi:10.1016/j.rser.2015.03.068.

[61] T. Tsoutsos, N. Frantzeskaki, V. Gekas, Environmental impacts from the solar energy technologies, Energy Policy. 33 (2005) 289–296. doi:10.1016/S0301-4215(03)00241-6.

[62] B.K. Sovacool, The intermittency of wind, solar, and renewable electricity generators: Technical barrier or rhetorical excuse?, Util. Policy. 17 (2009) 288–296. doi:10.1016/j.jup.2008.07.001.

[63] J.P. Barton, D.G. Infield, Energy storage and its use with intermittent renewable energy, IEEE Trans. Energy Convers. 19 (2004) 441–448. doi:10.1109/TEC.2003.822305.

[64] J. Rugolo, M.J. Aziz, Electricity storage for intermittent renewable sources, Energy Environ. Sci. 5 (2012) 7151–7160. doi:10.1039/c2ee02542f.

[65] S. Ould Amrouche, D. Rekioua, T. Rekioua, S. Bacha, Overview of energy storage in renewable energy systems, Int. J. Hydrogen Energy. 41 (2016) 20914–20927. doi:10.1016/j.ijhydene.2016.06.243.

[66] Y. Yang, S. Bremner, C. Menictas, M. Kay, Battery energy storage system size determination in renewable energy systems: A review, Renew. Sustain. Energy Rev. 91 (2018) 109–125. doi:10.1016/j.rser.2018.03.047.

[67] P. Alotto, M. Guarnieri, F. Moro, Redox flow batteries for the storage of renewable energy: A review, Renew. Sustain. Energy Rev. 29 (2014) 325–335. doi:10.1016/j.rser.2013.08.001.

[68] Z. Abdin, A. Zafaranloo, A. Rafiee, W. Mérida, W. Lipiński, K.R. Khalilpour, Hydrogen as an energy vector, Renew. Sustain. Energy Rev. 120 (2020) 109620. doi:10.1016/j.rser.2019.109620.

[69] J.A. Turner, Sustainable hydrogen production, Science (80-.). 305 (2004) 972–974. doi:10.1126/science.1103197.

[70] C. Koroneos, A. Dompros, G. Roumbas, N. Moussiopoulos, Life cycle assessment of hydrogen fuel production processes, Int. J. Hydrogen Energy. 29 (2004) 1443–1450. doi:10.1016/j.ijhydene.2004.01.016.

[71] J.D. Holladay, J. Hu, D.L. King, Y. Wang, An overview of hydrogen production technologies, Catal. Today. 139 (2009) 244–260. doi:10.1016/j.cattod.2008.08.039.

[72] M. Kayfeci, A. Keçebaş, M. Bayat, Hydrogen production, in: Sol. Hydrog. Prod. Process. Syst. Technol., Elsevier, 2019: pp. 45–83. doi:10.1016/B978-0-12-814853-2.00003-5.

[73] The Future of Hydrogen – Analysis - IEA, (n.d.). https://www.iea.org/reports/the-future-of-hydrogen (accessed August 27, 2020).

[74] J.D. Fonseca, M. Camargo, J.M. Commenge, L. Falk, I.D. Gil, Trends in design of distributed energy systems using hydrogen as energy vector: A systematic literature review, Int. J. Hydrogen Energy. 44 (2019) 9486–9504. doi:10.1016/j.ijhydene.2018.09.177.

[75] Hydrogen – Analysis - IEA, (n.d.). https://www.iea.org/reports/hydrogen (accessed August 27, 2020).

[76] Z. Li, W. Luo, M. Zhang, J. Feng, Z. Zou, Photoelectrochemical cells for solar hydrogen production: Current state of promising photoelectrodes, methods to improve their properties, and outlook, Energy Environ. Sci. 6 (2013) 347–370. doi:10.1039/c2ee22618a.

[77] Z. Szklarska-Smialowska, M. Smialowski, Electrochemical Study of the Nickel-Hydrogen System, J. Electrochem. Soc. 110 (1963) 444–448. doi:10.1149/1.2425783.

[78] Y. Zhu, C. Yang, J. Zhu, L. Li, Structural and electrochemical hydrogen storage properties of Mg 2Ni-based alloys, J. Alloys Compd. 509 (2011) 5309–5314. doi:10.1016/j.jallcom.2011.02.017.

[79] M. Mohan, V.K. Sharma, E.A. Kumar, V. Gayathri, Hydrogen storage in carbon materials—A review, Energy Storage. 1 (2019) e35. doi:10.1002/est2.35.

[80] E. Fakioğlu, Y. Yürüm, T.N. Veziroğlu, A review of hydrogen storage systems based on boron and its compounds, Int. J. Hydrogen Energy. 29 (2004) 1371–1376. doi:10.1016/j.ijhydene.2003.12.010.

[81] Aaron Isenstadt, N. Lutsey, Developing hydrogen fueling infrastructure for fuel cell vehicles: A status update, (2017) 1–22. https://www.theicct.org/publications/developing-hydrogen-fueling-infrastructure-fuel-cell-vehicles-status-update.

[82] Hydrogen Refuelling Infrastructure | Hydrogen Mobility Europe, (n.d.). https://h2me.eu/about/hydrogen-refuelling-infrastructure/ (accessed August 27, 2020).

[83] W. Vielstich, A. Lamm, H.A. (Hubert A. Gasteiger, H. Yokokawa, Handbook of fuel cells : fundamentals, technology, and applications, Wiley, Wiley, 2003. https://www.wiley.com/en-af/Handbook+of+Fuel+Cells%3A+Fundamentals%2C+Technology%2C+Applications%2C+4+Volume+Set-p-9780471499268 (accessed April 18, 2019).

[84] S. Abbou, Phénomènes locaux instationnaires dans les piles à combustible à membrane (PEMFC) fonctionnant en mode bouché (dead end), Université de Lorraine, 2015.

[85] D. Hart, F. Lehner, S. Jones, J. Lewis, The Fuel Cell Industry Review, 2019. www.FuelCellIndustryReview.com.

[86] E. Weidner, R. Ortiz Cebolla, J. Davies, Global deployment of large capacity stationary fuel cells, 2019. doi:10.2760/372263.

[87] Early Markets: Fuel Cells for Backup Power Overview, 2014. http://www.nrel.gov/hydrogen/cfm/im-.

[88] About Symbio – Symbio, (n.d.). https://www.symbio.one/en/about-symbio/ (accessed August 30, 2020).

[89] P.C.K. Vesborg, T.F. Jaramillo, Addressing the terawatt challenge: Scalability in the supply of chemical elements for renewable energy, RSC Adv. 2 (2012) 7933–7947. doi:10.1039/c2ra20839c.

[90] NAVIBUS – Symbio, (n.d.). https://www.symbio.one/en/navibus-2/ (accessed August 30, 2020).

[91] Mémento de l ' Hydrogène: Daimler Revue, 2018. http://www.afhypac.org/documents/tout-savoir/Fiche 9.1.1 - Daimler rev. Dec. 2018 Th.A.pdf.

[92] H.I. Schlesinger, H.C. Brown, A.E. Finholt, The Preparation of Sodium Borohydride by the High Temperature Reaction of Sodium Hydride with Borate Esters, J. Am. Chem. Soc. 75 (1953) 205–209. doi:10.1021/ja01097a054.

[93] U.B. Demirci, Impact of H.I. Schlesinger's discoveries upon the course of modern chemistry on B–(N–)H hydrogen carriers, Int. J. Hydrogen Energy. 42 (2017) 21048–21062. doi:10.1016/j.ijhydene.2017.07.066.

[94] Y. Wu, M.T. Kelly, J. V Ortega, Review of Chemical Processes for the Synthesis of Sodium Borohydride, 2004. https://www1.eere.energy.gov/hydrogenandfuelcells/pdfs/review_chemical_processes.pdf.

[95] D.M.F. Santos, C.A.C. Sequeira, Sodium borohydride as a fuel for the future, Renew. Sustain. Energy Rev. 15 (2011) 3980–4001. doi:10.1016/j.rser.2011.07.018.

[96] D.M.F. Santos, C.A.C. Sequeira, Cyclic voltammetry investigation of borohydride oxidation at a gold electrode, Electrochim. Acta. 55 (2010) 6775–6781. doi:10.1016/j.electacta.2010.05.091.

[97] Y. Kojima, T. Haga, Recycling process of sodium metaborate to sodium borohydride, Int. J. Hydrogen Energy. 28 (2003) 989–993. doi:10.1016/S0360-3199(02)00173-8.

[98] Z.P. Li, N. Morigazaki, B.H. Liu, S. Suda, Preparation of sodium borohydride by the reaction of MgH2 with dehydrated borax through ball milling at room temperature, J. Alloys Compd. 349 (2003) 232–236. doi:10.1016/S0925-8388(02)00872-1.

[99] United States Geological Survey (USGS), Mineral Commodity Summaries 2020, 2020. doi:https://doi.org/10.3133/mcs2020.

[100] U.B. Demirci, O. Akdim, J. Andrieux, J. Hannauer, R. Chamoun, P. Miele, Sodium Borohydride Hydrolysis as Hydrogen Generator: Issues, State of the Art and

Applicability Upstream from a Fuel Cell, Fuel Cells. 10 (2010) 335–350. doi:10.1002/fuce.200800171.

[101] J. Hannauer, U.B. Demirci, C. Geantet, J.M. Herrmann, P. Miele, Enhanced hydrogen release by catalyzed hydrolysis of sodium borohydride–ammonia borane mixtures: a solution-state 11B NMR study, Phys. Chem. Chem. Phys. 13 (2011) 3809. doi:10.1039/c0cp02090g.

[102] H.C. Brown, B.C.S. Rao, Hydroboration. III. The Reduction of Organic Compounds by Diborane, an Acid-type Reducing Agent, J. Am. Chem. Soc. 82 (1960) 681–686. doi:10.1021/ja01488a045.

[103] S.W. Chaikin, W.G. Brown, Reduction of Aldehydes, Ketones and Acid Chlorides by Sodium Borohydride, J. Am. Chem. Soc. 71 (1949) 122–125. doi:10.1021/ja01169a033.

[104] M.L. Wolfrom, K. Anno, Sodium Borohydride as a Reducing Agent in the Sugar Series [1], J. Am. Chem. Soc. 74 (1952) 5583–5584. doi:10.1021/ja01142a010.

[105] L. Dubau, T. Asset, R. Chattot, C. Bonnaud, V. Vanpeene, J. Nelayah, F. Maillard, Tuning the Performance and the Stability of Porous Hollow PtNi/C Nanostructures for the Oxygen Reduction Reaction, ACS Catal. 5 (2015) 5333–5341. doi:10.1021/acscatal.5b01248.

[106] K.C. Song, S.M. Lee, T.S. Park, B.S. Lee, Preparation of colloidal silver nanoparticles by chemical reduction method, Korean J. Chem. Eng. 26 (2009) 153–155. doi:10.1007/s11814-009-0024-y.

[107] A.K. Samal, T.S. Sreeprasad, T. Pradeep, Investigation of the role of NaBH4 in the chemical synthesis of gold nanorods, J. Nanoparticle Res. 12 (2010) 1777–1786. doi:10.1007/s11051-009-9733-8.

[108] H.C. Brown, B.C.S. Rao, A New Powerful Reducing Agent—Sodium Borohydride in the Presence of Aluminum Chloride and Other Polyvalent Metal Halides [1,2], J. Am. Chem. Soc. 78 (1956) 2582–2588. doi:10.1021/ja01592a070.

[109] W.M. Haynes, CRC Handbook of Chemistry and Physics, 95th editi, 2014.

[110] U.B. Demirci, P. Miele, F. Garin, Catalysis in hydrolysis of sodium borohydride and ammonia borane, and electrocatalysis in oxidation of sodium borohydride, Catal. Today. 170 (2011) 1–2. doi:10.1016/j.cattod.2011.04.005.

[111] R.E. Davis, E. Bromels, C.L. Kibby, Boron Hydrides. III. Hydrolysis of Sodium Borohydride in Aqueous Solution, J. Am. Chem. Soc. 84 (1962) 885–892. doi:10.1021/ja00865a001.

[112] J.B. Brown, M. Svensson, The Stability of Potassium Borohydride in Alkaline Solutions, J. Am. Chem. Soc. 79 (1957) 4241–4242. doi:10.1021/ja01572a071.

[113] P.-Y. Olu, Study of the anode in direct borohydride fuel cells, Université Grenoble-Alpes, 2015.

[114] J. Andrieux, U.B. Demirci, J. Hannauer, C. Gervais, C. Goutaudier, P. Miele, Spontaneous hydrolysis of sodium borohydride in harsh conditions, Int. J. Hydrogen Energy. 36 (2011) 224–233. doi:10.1016/j.ijhydene.2010.10.055.

[115] M.E. Indig, R.N. Snyder, Sodium Borohydride, An Interesting Anodic Fuel (1), J.

Electrochem. Soc. 109 (1962) 1104. doi:10.1149/1.2425247.

[116] N.A. Choudhury, R.K. Raman, S. Sampath, A.K. Shukla, An alkaline direct borohydride fuel cell with hydrogen peroxide as oxidant, J. Power Sources. 143 (2005) 1–8. doi:10.1016/j.jpowsour.2004.08.059.

[117] D. Cao, Y. Gao, G. Wang, R. Miao, Y. Liu, A direct NaBH4-H2O2 fuel cell using Ni foam supported Au nanoparticles as electrodes, Int. J. Hydrogen Energy. 35 (2010) 807–813. doi:10.1016/j.ijhydene.2009.11.026.

[118] W. Haijun, W. Cheng, L. Zhixiang, M. Zongqiang, Influence of operation conditions on direct NaBH4/H2O2 fuel cell performance, Int. J. Hydrogen Energy. 35 (2010) 2648–2651. doi:10.1016/j.ijhydene.2009.04.020.

[119] C. Lafforgue, Activity and degradation mechanisms of anodic electrocatalysts for the direct borohydride fuel cell, Grenoble-INP, 2019.

[120] P.Y. Olu, N. Job, M. Chatenet, Evaluation of anode (electro)catalytic materials for the direct borohydride fuel cell: Methods and benchmarks, J. Power Sources. 327 (2016) 235–257. doi:10.1016/j.jpowsour.2016.07.041.

[121] S. Li, X. Yang, H. Zhu, Y. Chen, Y. Liu, Investigation of amorphous CoB alloy as the anode catalyst for a direct borohydride fuel cell, J. Power Sources. 196 (2011) 5858–5862. doi:10.1016/j.jpowsour.2011.02.016.

[122] C. Kim, K.J. Kim, M.Y. Ha, Performance enhancement of a direct borohydride fuel cell in practical running conditions, J. Power Sources. 180 (2008) 154–161. doi:10.1016/j.jpowsour.2008.01.042.

[123] K.T. Park, U.H. Jung, S.U. Jeong, S.H. Kim, Influence of anode diffusion layer properties on performance of direct borohydride fuel cell, J. Power Sources. 162 (2006) 192–197. doi:10.1016/j.jpowsour.2006.07.040.

[124] F.G. Boyaci San, O. Okur, Ç. Iyigün Karadağ, I. Isik-Gulsac, E. Okumuş, Evaluation of operating conditions on DBFC (direct borohydride fuel cell) performance with PtRu anode catalyst by response surface method, Energy. 71 (2014) 160–169. doi:10.1016/j.energy.2014.04.037.

[125] M.H. Atwan, C.L.B. Macdonald, D.O. Northwood, E.L. Gyenge, Colloidal Au and Au-alloy catalysts for direct borohydride fuel cells: Electrocatalysis and fuel cell performance, J. Power Sources. 158 (2006) 36–44. doi:10.1016/j.jpowsour.2005.09.054.

[126] H. Cheng, K. Scott, Influence of operation conditions on direct borohydride fuel cell performance, J. Power Sources. 160 (2006) 407–412. doi:10.1016/j.jpowsour.2006.01.097.

[127] Z. Wang, M. Mandal, S. Sankarasubramanian, G. Huang, P.A. Kohl, V.K. Ramani, Influence of Water Transport across Microscale Bipolar Interfaces on the Performance of Direct Borohydride Fuel Cells, ACS Appl. Energy Mater. 3 (2020) 4449–4456. doi:10.1021/acsaem.0c00145.

[128] Z. Wang, S. Sankarasubramanian, V. Ramani, Reactant-Transport Engineering Approach to High-Power Direct Borohydride Fuel Cells, Cell Reports Phys. Sci. 1 (2020) 100084. doi:10.1016/j.xcrp.2020.100084.

[129] P.Y. Olu, F. Deschamps, G. Caldarella, M. Chatenet, N. Job, Investigation of platinum and palladium as potential anodic catalysts for direct borohydride and ammonia borane fuel cells, J. Power Sources. 297 (2015) 492–503. doi:10.1016/j.jpowsour.2015.08.022.

[130] O.Z. Sharaf, M.F. Orhan, An overview of fuel cell technology: Fundamentals and applications, Renew. Sustain. Energy Rev. 32 (2014) 810–853. doi:10.1016/j.rser.2014.01.012.

[131] P.Y. Olu, A. Bonnefont, M. Rouhet, S. Bozdech, N. Job, M. Chatenet, E. Savinova, Insights into the potential dependence of the borohydride electrooxidation reaction mechanism on platinum nanoparticles supported on ordered carbon nanomaterials, Electrochim. Acta. 179 (2015) 637–646. doi:10.1016/j.electacta.2015.02.158.

[132] N.M. Marković, S.T. Sarraf, H.A. Gasteiger, P.N. Ross, Hydrogen electrochemistry on platinum low-index single-crystal surfaces in alkaline solution, J. Chem. Soc. - Faraday Trans. 92 (1996) 3719–3725. doi:10.1039/ft9969203719.

[133] N.M. Marković, T.J. Schmidt, B.N. Grgur, H.A. Gasteiger, R.J. Behm, P.N. Ross, Effect of Temperature on Surface Processes at the Pt(111) - Liquid Interface: Hydrogen Adsorption, Oxide Formation, and CO Oxidation, J. Phys. Chem. B. 103 (1999) 8568–8577. doi:10.1021/jp991826u.

[134] W. Sheng, H.A. Gasteiger, Y. Shao-Horn, Hydrogen Oxidation and Evolution Reaction Kinetics on Platinum: Acid vs Alkaline Electrolytes, J. Electrochem. Soc. 157 (2010) B1529. doi:10.1149/1.3483106.

[135] E. Gyenge, Electrooxidation of borohydride on platinum and gold electrodes: Implications for direct borohydride fuel cells, Electrochim. Acta. 49 (2004) 965–978. doi:10.1016/j.electacta.2003.10.008.

[136] E. Gyenge, M. Atwan, D. Northwood, Electrocatalysis of Borohydride Oxidation on Colloidal Pt and Pt-Alloys (Pt-Ir, Pt-Ni, and Pt-Au) and Application for Direct Borohydride Fuel Cell Anodes, J. Electrochem. Soc. 153 (2006) A150. doi:10.1149/1.2131831.

[137] D.A. Finkelstein, C.D. Letcher, D.J. Jones, L.M. Sandberg, D.J. Watts, Self-Poisoning during BH4– Oxidation at Pt and Au, and in Situ Poison Removal Procedures for BH4– Fuel Cells, J. Phys. Chem. C. 117 (2013) 1571–1581.

[138] S.C. Amendola, P. Onnerud, M.T. Kelly, P.J. Petillo, S.L. Sharp-Goldman, M. Binder, A novel high power density borohydride-air cell, J. Power Sources. 84 (1999) 130–133. doi:http://dx.doi.org/10.1016/S0378-7753(99)00259-1.

[139] M. V. Mirkin, Borohydride Oxidation at a Gold Electrode, J. Electrochem. Soc. 139 (1992) 2212. doi:10.1149/1.2221204.

[140] K. Wang, J. Lu, L. Zhuang, Direct determination of diffusion coefficient for borohydride anions in alkaline solutions using chronoamperometry with spherical Au electrodes, J. Electroanal. Chem. 585 (2005) 191–196. doi:10.1016/j.jelechem.2005.08.009.

[141] H. Cheng, K. Scott, Determination of kinetic parameters for borohydride oxidation on a rotating Au disk electrode, Electrochim. Acta. 51 (2006) 3429–3433. doi:10.1016/j.electacta.2005.09.038.

[142] M. Chatenet, F.H.B. Lima, E.A. Ticianelli, Gold is not a Faradaic-Efficient Borohydride Oxidation Electrocatalyst: An Online Electrochemical Mass Spectrometry Study, J. Electrochem. Soc. 157 (2010) B697. doi:10.1149/1.3328179.

[143] M. Chatenet, M.B. Molina-Concha, J.P. Diard, First insights into the borohydride oxidation reaction mechanism on gold by electrochemical impedance spectroscopy, Electrochim. Acta. 54 (2009) 1687–1693. doi:10.1016/j.electacta.2008.09.060.

[144] B.M. Concha, Étude d'électrocatalyseurs d'anode de DBFC et du mécanisme d'électrooxydation de BH4- ., University Grenoble-Alpes, 2009.

[145] X. Ma, K. Ye, G.G.G. Wang, M. Duan, K. Cheng, G.G.G. Wang, D. Cao, Facile fabrication of gold coated nickel nanoarrays and its excellent catalytic performance towards sodium borohydride electro-oxidation, Appl. Surf. Sci. 414 (2017) 353–360. doi:10.1016/j.apsusc.2017.04.104.

[146] R. Valiollahi, R. Ojani, J.B. Raoof, Gold Nano-Cages on Graphene support for Sodium Borohydride Electrooxidation, Electrochim. Acta. 191 (2016) 230–236. doi:10.1016/j.electacta.2016.01.082.

[147] J. Milikić, U. Stamenović, V. Vodnik, S.P. Ahrenkiel, B. Šljukić, Gold nanorod-polyaniline composites: Synthesis and evaluation as anode electrocatalysts for direct borohydride fuel cells, Electrochim. Acta. 328 (2019) 135115. doi:10.1016/j.electacta.2019.135115.

[148] R.C.P. Oliveira, M. Vasić, D.M.F. Santos, B. Babić, R. Hercigonja, C.A.C. Sequeira, B. Šljukić, Performance assessment of a direct borohydride-peroxide fuel cell with Pd-impregnated faujasite X zeolite as anode electrocatalyst, Electrochim. Acta. 269 (2018) 517–525. doi:10.1016/j.electacta.2018.03.021.

[149] R.M.E. Hjelm, C. Lafforgue, R.W. Atkinson, Y. Garsany, R.O. Stroman, M. Chatenet, K. Swider-Lyons, Impact of the Anode Catalyst Layer Design on the Performance of H 2 O 2 -Direct Borohydride Fuel Cells, J. Electrochem. Soc. 166 (2019) F1218–F1228. doi:10.1149/2.0681914jes.

[150] N.A. Choudhury, J. Ma, Y. Sahai, High performance and eco-friendly chitosan hydrogel membrane electrolytes for direct borohydride fuel cells, J. Power Sources. 210 (2012) 358–365. doi:10.1016/j.jpowsour.2012.03.013.

[151] Z. Wang, J. Parrondo, C. He, S. Sankarasubramanian, V. Ramani, Efficient pH-gradient-enabled microscale bipolar interfaces in direct borohydride fuel cells, Nat. Energy. 4 (2019) 281–289. doi:10.1038/s41560-019-0330-5.

[152] M. Simoes, S. Baranton, C. Coutanceau, Electrooxidation of sodium borohydride at Pd, Au, and Pd xLAu1-x carbon-supported nanocatalysts, J. Phys. Chem. C. 113 (2009) 13369–13376. doi:10.1021/jp902741z.

[153] C. Grimmer, M. Grandi, R. Zacharias, B. Cermenek, H. Weber, C. Morais, T.W. Napporn, S. Weinberger, A. Schenk, V. Hacker, The electrooxidation of borohydride: A mechanistic study on palladium (Pd/C) applying RRDE, ^{11}B-NMR and FTIR, Appl. Catal. B Environ. 180 (2016) 614–621. doi:10.1016/j.apcatb.2015.07.028.

[154] A. Aziznia, C.W. Oloman, E.L. Gyenge, Experimental advances and preliminary mathematical modeling of the Swiss-roll mixed-reactant direct borohydride fuel

cell, J. Power Sources. 265 (2014) 201–213. doi:10.1016/j.jpowsour.2014.04.037.

[155] A. Verma, S. Basu, Experimental evaluation and mathematical modeling of a direct alkaline fuel cell, J. Power Sources. 168 (2007) 200–210. doi:10.1016/j.jpowsour.2007.02.069.

[156] F.A. Coowar, G. Vitins, G.O. Mepsted, S.C. Waring, J.A. Horsfall, Electrochemical oxidation of borohydride at nano-gold-based electrodes: Application in direct borohydride fuel cells, J. Power Sources. 175 (2008) 317–324. doi:10.1016/j.jpowsour.2007.09.063.

[157] H.Y. Qin, Z.X. Liu, W.X. Yin, J.K. Zhu, Z.P. Li, A cobalt polypyrrole composite catalyzed cathode for the direct borohydride fuel cell, J. Power Sources. 185 (2008) 909–912. doi:10.1016/j.jpowsour.2008.08.047.

[158] J. Ma, Y. Liu, P. Zhang, J. Wang, A simple direct borohydride fuel cell with a cobalt phthalocyanine catalyzed cathode, Electrochem. Commun. 10 (2008) 100–102. doi:10.1016/j.elecom.2007.11.006.

[159] H. Cheng, K. Scott, Investigation of non-platinum cathode catalysts for direct borohydride fuel cells, J. Electroanal. Chem. 596 (2006) 117–123. doi:10.1016/j.jelechem.2006.07.031.

[160] J. Ma, J. Wang, Y. Liu, Iron phthalocyanine as a cathode catalyst for a direct borohydride fuel cell, J. Power Sources. 172 (2007) 220–224. doi:10.1016/j.jpowsour.2007.07.031.

[161] X. Yang, Y. Liu, S. Li, X. Wei, L. Wang, Y. Chen, A direct borohydride fuel cell with a polymer fiber membrane and non-noble metal catalysts, Sci. Rep. 2 (2012) 567. doi:10.1038/srep00567.

[162] J.G. Goodwin, K. Hongsirikarn, S. Greenway, S. Creager, Effect of cations (Na+, Ca2+, Fe3+) on the conductivity of a Nafion membrane, J. Power Sources. 195 (2010) 7213–7220. doi:10.1016/j.jpowsour.2010.05.005.

[163] B.H. Liu, Z.P. Li, J.K. Zhu, S. Suda, Influences of hydrogen evolution on the cell and stack performances of the direct borohydride fuel cell, J. Power Sources. 183 (2008) 151–156. doi:10.1016/j.jpowsour.2008.04.079.

[164] B.H. Liu, Z.P. Li, K. Arai, S. Suda, Performance improvement of a micro borohydride fuel cell operating at ambient conditions, Electrochim. Acta. 50 (2005) 3719–3725. doi:10.1016/j.electacta.2005.01.018.

[165] D. Chen, S. Yu, X. Liu, X. Li, Porous polybenzimidazole membranes with excellent chemical stability and ion conductivity for direct borohydride fuel cells, J. Power Sources. 282 (2015) 323–327. doi:10.1016/j.jpowsour.2015.02.082.

[166] R. Jamard, J. Salomon, A. Martinent-Beaumont, C. Coutanceau, Life time test in direct borohydride fuel cell system, J. Power Sources. 193 (2009) 779–787. doi:10.1016/j.jpowsour.2009.03.057.

[167] Z. Yang, J. Ran, B. Wu, L. Wu, T. Xu, Stability challenge in anion exchange membrane for fuel cells, Curr. Opin. Chem. Eng. 12 (2016) 22–30. doi:10.1016/j.coche.2016.01.009.

[168] C. Qu, H. Zhang, F. Zhang, B. Liu, A high-performance anion exchange

membrane based on bi-guanidinium bridged polysilsesquioxane for alkaline fuel cell application, J. Mater. Chem. 22 (2012) 8203–8207. doi:10.1039/c2jm16211c.

[169] Z. Wang, J. Parrondo, V. Ramani, Anion Exchange Membranes Based on Polystyrene- Block -Poly(ethylene- ran -butylene)- Block -Polystyrene Triblock Copolymers: Cation Stability and Fuel Cell Performance , J. Electrochem. Soc. 164 (2017) F1216–F1225. doi:10.1149/2.1561712jes.

[170] L. Wang, J.J. Brink, J.R. Varcoe, The first anion-exchange membrane fuel cell to exceed 1 W cm-2 at 70 °c with a non-Pt-group (O2) cathode, Chem. Commun. 53 (2017) 11771–11773. doi:10.1039/c7cc06392j.

[171] R. Simons, Preparation of a high performance bipolar membrane, J. Memb. Sci. 78 (1993) 13–23. doi:10.1016/0376-7388(93)85243-P.

[172] L. Bazinet, F. Lamarche, D. Ippersiel, Bipolar-membrane electrodialysis: Applications of electrodialysis in the food industry, Trends Food Sci. Technol. 9 (1998) 107–113. doi:10.1016/S0924-2244(98)00026-0.

[173] T. Xu, Development of bipolar membrane-based processes, Desalination. 140 (2001) 247–258. doi:10.1016/S0011-9164(01)00374-5.

[174] J. Dai, Y. Dong, P. Gao, J. Ren, C. Yu, H. Hu, Y. Zhu, X. Teng, A sandwiched bipolar membrane for all vanadium redox flow battery with high coulombic efficiency, Polymer (Guildf). 140 (2018) 233–239. doi:10.1016/j.polymer.2018.02.051.

[175] C.P. de León, F.C. Walsh, A. Rose, J.B. Lakeman, D.J. Browning, R.W. Reeve, A direct borohydride-Acid peroxide fuel cell, J. Power Sources. 164 (2007) 441–448. doi:10.1016/j.jpowsour.2006.10.069.

[176] R.W. Reeve, A Sodium Borohydride-Hydrogen Peroxide Fuel Cell Employing a Bipolar Membrane Electrolyte, Fuel Cell Semin. 2011. 42 (2012) 117–129. doi:Doi 10.1149/1.4705487.

[177] C.G. Arges, V. Prabhakaran, L. Wang, V. Ramani, Bipolar polymer electrolyte interfaces for hydrogen-oxygen and direct borohydride fuel cells, Int. J. Hydrogen Energy. 39 (2014) 14312–14321. doi:10.1016/j.ijhydene.2014.04.099.

[178] A. Hohenadel, D. Powers, R. Wycisk, M. Adamski, P. Pintauro, S. Holdcroft, Electrochemical Characterization of Hydrocarbon Bipolar Membranes with Varying Junction Morphology, ACS Appl. Energy Mater. 2 (2019) 6817–6824. doi:10.1021/acsaem.9b01257.

[179] C. Shen, R. Wycisk, P.N. Pintauro, High performance electrospun bipolar membrane with a 3D junction, Energy Environ. Sci. 10 (2017) 1435–1442. doi:10.1039/c7ee00345e.

[180] K.J.J. Mayrhofer, A.S. Crampton, G.K.H. Wiberg, M. Arenz, Analysis of the Impact of Individual Glass Constituents on Electrocatalysis on Pt Electrodes in Alkaline Solution, J. Electrochem. Soc. 155 (2008) P78. doi:10.1149/1.2904882.

[181] A.J. Bard, L.R. Faulkner, Electrochemical Methods: Fundamentals and Applications vol. 2, 2001. doi:10.1038/s41929-019-0277-8.

[182] P. Krishnan, T.H. Yang, S.G. Advani, A.K. Prasad, Rotating ring-disc electrode (RRDE) investigation of borohydride electro-oxidation, J. Power Sources. 182

(2008) 106–111. doi:10.1016/j.jpowsour.2008.03.064.

[183] L.C. Nagle, J.F. Rohan, Ammonia Borane Oxidation at Gold Microelectrodes in Alkaline Solutions, J. Electrochem. Soc. 153 (2006) C773. doi:10.1149/1.2344842.

[184] L.C. Nagle, J.F. Rohan, Investigation of DMAB Oxidation at a Gold Microelectrode in Base, Electrochem. Solid-State Lett. 8 (2005) C77–C80. doi:10.1149/1.1883905.

[185] M. Belén Molina Concha, M. Chatenet, F.H.B. Lima, E.A. Ticianelli, In situ Fourier transform infrared spectroscopy and on-line differential electrochemical mass spectrometry study of the NH3BH3 oxidation reaction on gold electrodes, Electrochim. Acta. 89 (2013). doi:10.1016/j.electacta.2012.11.027.

[186] A.G. Oshchepkov, A. Bonnefont, V.A. Saveleva, V. Papaefthimiou, S. Zafeiratos, S.N. Pronkin, V.N. Parmon, E.R. Savinova, Exploring the Influence of the Nickel Oxide Species on the Kinetics of Hydrogen Electrode Reactions in Alkaline Media, Top. Catal. 59 (2016) 1319–1331. doi:10.1007/s11244-016-0657-0.

[187] A.G. Oshchepkov, Investigation of the hydrogen electrode reactions on Ni electrocatalysts in alkaline medium, Université de Strasbourg, 2017.

[188] S.A.S. Machado, L.A. Avaca, The hydrogen evolution reaction on nickel surfaces stabilized by H-absorption, Electrochim. Acta. 39 (1994) 1385–1391. doi:10.1016/0013-4686(94)E0003-I.

[189] M. Grdeń, M. Alsabet, G. Jerkiewicz, Surface Science and Electrochemical Analysis of Nickel Foams, ACS Appl. Mater. Interfaces. 4 (2012) 3012–3021. doi:10.1021/am300380m.

[190] A. Lasia, A. Rami, Kinetics of hydrogen evolution on nickel electrodes, J. Electroanal. Chem. 294 (1990) 123–141. doi:10.1016/0022-0728(90)87140-F.

[191] L. Bai, D.A. Harrington, B.E. Conway, Behavior of overpotential-deposited species in Faradaic reactions-II. ac Impedance measurements on H2 evolution kinetics at activated and unactivated Pt cathodes, Electrochim. Acta. 32 (1987) 1713–1731. doi:10.1016/0013-4686(87)80006-3.

[192] X. Li, P.F. Liu, L. Zhang, M.Y. Zu, Y.X. Yang, H.G. Yang, Enhancing alkaline hydrogen evolution reaction activity through Ni-Mn3O4 nanocomposites, Chem. Commun. 52 (2016) 10566–10569. doi:10.1039/c6cc04141h.

[193] C.C.L. McCrory, S. Jung, I.M. Ferrer, S.M. Chatman, J.C. Peters, T.F. Jaramillo, Benchmarking Hydrogen Evolving Reaction and Oxygen Evolving Reaction Electrocatalysts for Solar Water Splitting Devices, J. Am. Chem. Soc. 137 (2015) 4347–4357. doi:10.1021/ja510442p.

[194] D.S. Hall, C. Bock, B.R. MacDougall, An Oxalate Method for Measuring the Surface Area of Nickel Electrodes, J. Electrochem. Soc. 161 (2014) H787–H795. doi:10.1149/2.0711412jes.

[195] A. Zadick, L. Dubau, K. Artyushkova, A. Serov, P. Atanassov, M. Chatenet, Nickel-based electrocatalysts for ammonia borane oxidation: enabling materials for carbon-free-fuel direct liquid alkaline fuel cell technology, Nano Energy. 37 (2017) 248–259. doi:10.1016/j.nanoen.2017.05.035.

[196] T. Asset, A. Roy, T. Sakamoto, M. Padilla, I. Matanovic, K. Artyushkova, A. Serov,

F. Maillard, M. Chatenet, K. Asazawa, H. Tanaka, P. Atanassov, Highly active and selective nickel molybdenum catalysts for direct hydrazine fuel cell, Electrochim. Acta. 215 (2016) 420–426. doi:10.1016/j.electacta.2016.08.106.

[197] S. Kabir, K. Lemire, K. Artyushkova, A. Roy, M. Odgaard, D. Schlueter, A. Oshchepkov, A. Bonnefont, E. Savinova, D.C. Sabarirajan, P. Mandal, E.J. Crumlin, I.V. Zenyuk, P. Atanassov, A. Serov, Platinum group metal-free NiMo hydrogen oxidation catalysts: high performance and durability in alkaline exchange membrane fuel cells, J. Mater. Chem. A. 5 (2017) 24433–24443. doi:10.1039/C7TA08718G.

[198] J.P.I. De Souza, S.L. Queiroz, F.C. Nart, Uso de espectrometria de massas em medidas eletroquímicas - A técnica de DEMS, Quim. Nova. 23 (2000) 384–391. doi:10.1590/S0100-40422000000300016.

[199] J.P.I. De Souza, S.L. Queiroz, K. Bergamaski, E.R. Gonzalez, F.C. Nart, Electro-oxidation of ethanol on Pt, Rh, and PtRh electrodes. A study using DEMS and in-situ FTIR techniques, J. Phys. Chem. B. 106 (2002) 9825–9830. doi:10.1021/jp014645c.

[200] K. Bergamaski, A.L.N. Pinheiro, E. Teixeira-Neto, F.C. Nart, Nanoparticle size effects on methanol electrochemical oxidation on carbon supported platinum catalysts, J. Phys. Chem. B. 110 (2006) 19271–19279. doi:10.1021/jp063337h.

[201] Z. Jusys, R.J. Behm, Borohydride electrooxidation over Pt/C, AuPt/C and Au/C catalysts: Partial reaction pathways and mixed potential formation, Electrochem. Commun. 60 (2015) 9–12. doi:10.1016/j.elecom.2015.07.021.

[202] M. Tammer, G. Sokrates: Infrared and Raman characteristic group frequencies: tables and charts, Colloid Polym. Sci. 283 (2004) 235–235. doi:10.1007/s00396-004-1164-6.

[203] J. Chalmers, P. Griffiths, Handbook of Vibrational Spectroscopy, 5 volumes set., 2002.

[204] B.M. Concha, M. Chatenet, C. Coutanceau, F. Hahn, In situ infrared (FTIR) study of the borohydride oxidation reaction, Electrochem. Commun. 11 (2009) 223–226. doi:10.1016/j.elecom.2008.11.018.

[205] B.M. Concha, M. Chatenet, F. Maillard, E.A. Ticianelli, F.H.B. Lima, R.B. de Lima, In situ infrared (FTIR) study of the mechanism of the borohydride oxidation reaction, Phys. Chem. Chem. Phys. 12 (2010) 11507. doi:10.1039/c003652h.

[206] G. Kresse, J. Hafner, Ab initio molecular dynamics for liquid metals, Phys. Rev. B. 47 (1993) 558–561. doi:10.1103/PhysRevB.47.558.

[207] G. Kresse, J. Furthmüller, Efficient iterative schemes for ab initio total-energy calculations using a plane-wave basis set, Phys. Rev. B - Condens. Matter Mater. Phys. 54 (1996) 11169–11186. doi:10.1103/PhysRevB.54.11169.

[208] J.P. Perdew, Y. Wang, Accurate and simple analytic representation of the electron-gas correlation energy, Phys. Rev. B. 45 (1992) 13244–13249. doi:10.1103/PhysRevB.45.13244.

[209] H.J. Monkhorst, J.D. Pack, Special points for Brillouin-zone integrations, Phys. Rev. B. 13 (1976) 5188–5192. doi:10.1103/PhysRevB.13.5188.

[210] A.G. Oshchepkov, G. Braesch, A. Bonnefont, E.R. Savinova, M. Chatenet, Recent advances in the understanding of Ni-based catalysts for the oxidation of hydrogen-containing fuels in alkaline media, ACS Catal. (2020) acscatal.0c00101. doi:10.1021/acscatal.0c00101.

[211] P.-Y. Olu, A. Bonnefont, G. Braesch, V. Martin, E.R. Savinova, M. Chatenet, Influence of the concentration of borohydride towards hydrogen production and escape for borohydride oxidation reaction on Pt and Au electrodes – experimental and modelling insights, J. Power Sources. 375 (2018) 300–309. doi:10.1016/J.JPOWSOUR.2017.07.061.

[212] G. Braesch, A. Bonnefont, V. Martin, E.R. Savinova, M. Chatenet, Borohydride oxidation reaction mechanisms and poisoning effects on Au, Pt and Pd bulk electrodes: From model (low) to direct borohydride fuel cell operating (high) concentrations, Electrochim. Acta. 273 (2018) 483–494. doi:10.1016/j.electacta.2018.04.068.

[213] W. Sheng, Z. Zhuang, M. Gao, J. Zheng, J.G. Chen, Y. Yan, Correlating hydrogen oxidation and evolution activity on platinum at different pH with measured hydrogen binding energy, Nat. Commun. 6 (2015) 1–6. doi:10.1038/ncomms6848.

[214] D.A. Finkelstein, N. Da Mota, J.L. Cohen, H.D. Abruña, Rotating Disk Electrode ({RDE)} Investigation of {BH4–} and {BH3OH–} Electro-oxidation at Pt and Au: Implications for {BH4–} Fuel Cells, J. Phys. Chem. C. 113 (2009) 19700–19712. doi:10.1021/jp900933c.

[215] G. Rostamikia, M.J. Janik, First principles mechanistic study of borohydride oxidation over the Pt(1 1 1) surface, Electrochim. Acta. 55 (2010) 1175–1183. doi:10.1016/j.electacta.2009.10.002.

[216] G. Rostamikia, M.J. Janik, Direct borohydride oxidation: mechanism determination and design of alloy catalysts guided by density functional theory, Energy Environ. Sci. 3 (2010) 1262. doi:10.1039/c0ee00115e.

[217] G. Rostamikia, M.J. Janik, Borohydride Oxidation over Au(111): A First-Principles Mechanistic Study Relevant to Direct Borohydride Fuel Cells, J. Electrochem. Soc. 156 (2009) B86. doi:10.1149/1.3010382.

[218] M.C.S. Escaño, R.L. Arevalo, E. Gyenge, H. Kasai, Electrocatalysis of borohydride oxidation: a review of density functional theory approach combined with experimental validation, J. Phys. Condens. Matter. 26 (2014) 353001. doi:10.1088/0953-8984/26/35/353001.

[219] M.C.S. Escaño, E. Gyenge, R.L. Arevalo, H. Kasai, Reactivity descriptors for borohydride interaction with metal surfaces, J. Phys. Chem. C. 115 (2011) 19883–19889. doi:10.1021/jp207768e.

[220] I. Merino-Jiménez, C. Ponce De León, A.A. Shah, F.C. Walsh, Developments in direct borohydride fuel cells and remaining challenges, J. Power Sources. 219 (2012) 339–357. doi:10.1016/j.jpowsour.2012.06.091.

[221] P. Grauel, J. Christoph, G. Flätgen, K. Krischer, Stationary potential patterns during the reduction of peroxodisulfate at Ag ring electrodes, J. Phys. Chem. B. 102 (1998) 10264–10271. doi:10.1021/jp982841m.

[222] K. Krischer, H. Varela, A. Bîrzu, F. Plenge, A. Bonnefont, Stability of uniform

electrode states in the presence of ohmic drop compensation, Electrochim. Acta. 49 (2003) 103–115. doi:10.1016/j.electacta.2003.04.006.

[223] E. Guilminot, A. Corcella, F. Charlot, F. Maillard, M. Chatenet, Detection of Pt[sup z+] Ions and Pt Nanoparticles Inside the Membrane of a Used PEMFC, J. Electrochem. Soc. 154 (2007) B96. doi:10.1149/1.2388863.

[224] E. Guilminot, A. Corcella, M. Chatenet, F. Maillard, F. Charlot, G. Berthomé, C. Iojoiu, J.-Y. Sanchez, E. Rossinot, E. Claude, Membrane and Active Layer Degradation upon PEMFC Steady-State Operation, J. Electrochem. Soc. 154 (2007) B1106. doi:10.1149/1.2775218.

[225] F.H.B. Lima, A.M. Pasqualeti, M.B. Molina Concha, M. Chatenet, E.A. Ticianelli, Borohydride electrooxidation on Au and Pt electrodes, Electrochim. Acta. 84 (2012) 202–212. doi:10.1016/j.electacta.2012.05.030.

[226] A.M. Pasqualeti, P.Y. Olu, M. Chatenet, F.H.B. Lima, Borohydride electrooxidation on carbon-supported noble metal nanoparticles: Insights into hydrogen and hydroxyborane formation, ACS Catal. 5 (2015) 2778–2787. doi:10.1021/acscatal.5b00107.

[227] M. Chatenet, M.B. Molina-Concha, N. El-Kissi, G. Parrour, J.P. Diard, Direct rotating ring-disk measurement of the sodium borohydride diffusion coefficient in sodium hydroxide solutions, Electrochim. Acta. 54 (2009) 4426–4435. doi:10.1016/j.electacta.2009.03.019.

[228] E.L. Littauer, K.C. Tsai, Observations of the diffusion coefficient of the hydroxyl ion in lithium hydroxide solutions, Electrochim. Acta. 24 (1979) 351–355. doi:10.1016/0013-4686(79)87018-8.

[229] S.H. Lee, J.C. Rasaiah, Proton transfer and the mobilities of the H+ and OH- ions from studies of a dissociating model for water, J. Chem. Phys. 135 (2011) 124505. doi:10.1063/1.3632990.

[230] B. Molina Concha, M. Chatenet, E.A. Ticianelli, F.H.B. Lima, In Situ Infrared (FTIR) Study of the Mechanism of the Borohydride Oxidation Reaction on Smooth Pt Electrode, J. Phys. Chem. C. 115 (2011) 12439–12447. doi:10.1021/jp2002589.

[231] K. Wang, J. Lu, L. Zhuang, A mechanistic study of borohydride anodic oxidation, Catal. Today. 170 (2011) 99–109. doi:10.1016/j.cattod.2010.12.023.

[232] B.H. Liu, Z.P. Li, S. Suda, Electrocatalysts for the anodic oxidation of borohydrides, Electrochim. Acta. 49 (2004) 3097–3105. doi:10.1016/j.electacta.2004.02.023.

[233] M. Simoes, S. Baranton, C. Coutanceau, Electrooxidation of sodium borohydride at Pd, Au, and Pd(x)Au(1-x) carbon-supported nanocatalysts, J. Phys. Chem. C. 113 (2009) 13369–13376. doi:10.1021/jp902741z.

[234] M. Simões, S. Baranton, C. Coutanceau, C. Lamy, J.-M. Léger, The Electrocatalytic Oxidation of Sodium Borohydride at Palladium and Gold Electrodes for an Application to the Direct Borohydride Fuel Cell, ECS Trans. 25 (2009) 1413–1421. doi:10.1149/1.3210697.

[235] M. Simões, S. Baranton, C. Coutanceau, Influence of bismuth on the structure and

activity of Pt and Pd nanocatalysts for the direct electrooxidation of NaBH4, Electrochim. Acta. 56 (2010) 580–591. doi:10.1016/j.electacta.2010.09.006.

[236] J.Q. Yang, B.H. Liu, S. Wu, Carbon-supported Pd catalysts: Influences of nanostructure on their catalytic performances for borohydride electrochemical oxidation, J. Power Sources. 194 (2009) 824–829. doi:10.1016/j.jpowsour.2009.06.034.

[237] C. Lafforgue, R.W. Atkinson, K. Swider-Lyons, M. Chatenet, Evaluation of carbon-supported palladium electrocatalysts for the borohydride oxidation reaction in conditions relevant to fuel cell operation, Electrochim. Acta. 341 (2020). doi:10.1016/j.electacta.2020.135971.

[238] S.N. Pronkin, P.A. Simonov, V.I. Zaikovskii, E.R. Savinova, Model Pd-based bimetallic supported catalysts for nitrate electroreduction, J. Mol. Catal. A Chem. 265 (2007) 141–147. doi:10.1016/j.molcata.2006.10.007.

[239] H. Qin, K. Chen, C. Zhu, J. Liu, J. Wang, Y. He, H. Chi, H. Ni, Z. Ji, High electrocatalytic activity for borohydride oxidation on palladium nanocubes enclosed by {200} facets, J. Power Sources. 299 (2015) 241–245. doi:10.1016/j.jpowsour.2015.09.007.

[240] M. Alesker, M. Page, M. Shviro, Y. Paska, G. Gershinsky, D.R. Dekel, D. Zitoun, Palladium/nickel bifunctional electrocatalyst for hydrogen oxidation reaction in alkaline membrane fuel cell, J. Power Sources. 304 (2016) 332–339. doi:10.1016/J.JPOWSOUR.2015.11.026.

[241] H.A. Miller, A. Lavacchi, F. Vizza, M. Marelli, F. Di Benedetto, F. D'Acapito, Y. Paska, M. Page, D.R. Dekel, A Pd/C-CeO2Anode Catalyst for High-Performance Platinum-Free Anion Exchange Membrane Fuel Cells, Angew. Chemie - Int. Ed. 55 (2016) 6004–6007. doi:10.1002/anie.201600647.

[242] J. Zheng, S. Zhou, S. Gu, B. Xu, Y. Yan, Size-Dependent Hydrogen Oxidation and Evolution Activities on Supported Palladium Nanoparticles in Acid and Base, J. Electrochem. Soc. 163 (2016) F499–F506. doi:10.1149/2.0661606jes.

[243] V. Yarmiayev, M. Alesker, A. Muzikansky, M. Zysler, D. Zitoun, Enhancement of Palladium HOR Activity in Alkaline Conditions through Ceria Surface Doping, J. Electrochem. Soc. 166 (2019) F3234–F3239. doi:10.1149/2.0291907jes.

[244] V.L. Oliveira, E. Sibert, Y. Soldo-Olivier, E.A. Ticianelli, M. Chatenet, Investigation of the electrochemical oxidation reaction of the borohydride anion in palladium layers on Pt(111), Electrochim. Acta. 209 (2016) 360–368. doi:10.1016/j.electacta.2016.05.093.

[245] V.L. Oliveira, E. Sibert, Y. Soldo-Olivier, E.A. Ticianelli, M. Chatenet, Borohydride electrooxidation reaction on Pt(111) and Pt(111) modified by a pseudomorphic Pd monolayer, Electrochim. Acta. 190 (2016) 790–796. doi:10.1016/j.electacta.2016.01.013.

[246] Y. Soldo-Olivier, M.C. Lafouresse, M. De Santis, C. Lebouin, M. de Boissieu, E. Sibert, Hydrogen Electro-Insertion into Pd/Pt(111) Nanofilms: An in Situ Surface X-ray Diffraction Study, J. Phys. Chem. C. 115 (2011) 12041–12047. doi:10.1021/jp201376d.

[247] C. Lebouin, Y.S. Olivier, E. Sibert, P. Millet, M. Maret, R. Faure, Electrochemically

elaborated palladium nanofilms on Pt(1 1 1): Characterization and hydrogen insertion study, J. Electroanal. Chem. 626 (2009) 59–65. doi:10.1016/J.JELECHEM.2008.11.005.

[248] C. Lebouin, Y. Soldo-Olivier, E. Sibert, M. De Santis, F. Maillard, R. Faure, Evidence of the Substrate Effect in Hydrogen Electroinsertion into Palladium Atomic Layers by Means of in Situ Surface X-ray Diffraction, Langmuir. 25 (2009) 4251–4255. doi:10.1021/la803913e.

[249] B. Sakintuna, F. Lamari-Darkrim, M. Hirscher, Metal hydride materials for solid hydrogen storage: A review, Pergamon, 2007. http://www.sciencedirect.com/science/article/pii/S0360319906005866 (accessed December 5, 2017).

[250] S.K. Singh, Y. Iizuka, Q. Xu, Nickel-palladium nanoparticle catalyzed hydrogen generation from hydrous hydrazine for chemical hydrogen storage, Int. J. Hydrogen Energy. 36 (2011) 11794–11801. doi:10.1016/J.IJHYDENE.2011.06.069.

[251] M. Yamauchi, R. Ikeda, H. Kitagawa, M. Takata, Nanosize effects on hydrogen storage in palladium, J. Phys. Chem. C. 112 (2008) 3294–3299. doi:10.1021/jp710447j.

[252] S. Kishore, J.A. Nelson, J.H. Adair, P.C. Eklund, Hydrogen storage in spherical and platelet palladium nanoparticles, J. Alloys Compd. 389 (2005) 234–242. doi:10.1016/J.JALLCOM.2004.06.105.

[253] E. Hassler, T. Lundström, L.E. Tergenius, The crystal chemistry of platinum metal borides, J. Less-Common Met. 67 (1979) 567–572. doi:10.1016/0022-5088(79)90042-0.

[254] P.K. Liao, K.E. Spear, The B-Pd (Boron-Palladium) System, J. Phase Equilibria. 17 (1996) 340–346.

[255] M. Beck, M. Ellner, E.J. Mittemeijer, The structure of the palladium-rich boride Pd5 B (Pd16 B3), Z. Krist. 216 (2001) 591–594.

[256] T.G. Berger, A. Leineweber, E.J. Mittemeijer, The Pd-rich part of the Pd – B phase diagram, Z. Met. 97 (2006) 3–9.

[257] Mickey Fulp, The 48-Year Record of Pt:Pd Ratios | Kitco News, (n.d.). https://www.kitco.com/commentaries/2018-01-17/The-48-Year-Record-of-Pt-Pd-Ratios.html (accessed August 4, 2020).

[258] Platinum Prices - Interactive Historical Chart | MacroTrends, (n.d.). https://www.macrotrends.net/2540/platinum-prices-historical-chart-data (accessed August 4, 2020).

[259] Palladium Prices - Interactive Historical Chart | MacroTrends, (n.d.). https://www.macrotrends.net/2542/palladium-prices-historical-chart-data (accessed August 4, 2020).

[260] A. Zadick, L. Dubau, N. Sergent, G. Berthomé, M. Chatenet, Huge Instability of Pt/C Catalysts in Alkaline Medium, ACS Catal. 5 (2015) 4819–4824. doi:10.1021/acscatal.5b01037.

[261] A. Zadick, L. Dubau, U.B. Demirci, M. Chatenet, Effects of Pd Nanoparticle Size

and Solution Reducer Strength on Pd/C Electrocatalyst Stability in Alkaline Electrolyte, J. Electrochem. Soc. 163 (2016) F781–F787. doi:10.1149/2.0141608jes.

[262] S. Kabir, A. Zadick, P. Atanassov, L. Dubau, M. Chatenet, Stability of carbon-supported palladium nanoparticles in alkaline media: A case study of graphitized and more amorphous supports, Electrochem. Commun. 78 (2017) 33–37. doi:10.1016/j.elecom.2017.03.017.

[263] C. Lafforgue, M. Chatenet, L. Dubau, D.R. Dekel, Accelerated Stress Test of Pt/C Nanoparticles in an Interface with an Anion-Exchange Membrane - An Identical-Location Transmission Electron Microscopy Study, ACS Catal. 8 (2018). doi:10.1021/acscatal.7b04055.

[264] C. Lafforgue, A. Zadick, L. Dubau, F. Maillard, M. Chatenet, Selected Review of the Degradation of Pt and Pd-based Carbon-supported Electrocatalysts for Alkaline Fuel Cells: Towards Mechanisms of Degradation, Fuel Cells. 18 (2018) 229–238. doi:10.1002/fuce.201700094.

[265] C. Lafforgue, F. Maillard, V. Martin, L. Dubau, M. Chatenet, Degradation of Carbon-Supported Platinum-Group-Metal Electrocatalysts in Alkaline Media Studied by in Situ Fourier Transform Infrared Spectroscopy and Identical-Location Transmission Electron Microscopy, ACS Catal. (2019) 5613–5622. doi:10.1021/acscatal.9b00439.

[266] C. Song, D. Zhang, B. Wang, Z. Cai, P. Yan, Y. Sun, K. Ye, D. Cao, K. Cheng, G. Wang, Uniformly grown PtCo-modified Co3O4 nanosheets as a highly efficient catalyst for sodium borohydride electrooxidation, Nano Res. 9 (2016) 3322–3333. doi:10.1007/s12274-016-1209-4.

[267] F. Pei, Y. Wang, X. Wang, P. He, Q. Chen, X. Wang, H. Wang, L. Yi, J. Guo, Performance of supported Au-Co alloy as the anode catalyst of direct borohydride-hydrogen peroxide fuel cell, Int. J. Hydrogen Energy. 35 (2010) 8136–8142. doi:10.1016/j.ijhydene.2010.01.016.

[268] L. Tamasauskaite-Tamasiunaite, A. Bal??iunaite, A. Zabielaite, I. Stankevi??iene, V. Kepeniene, A. Selskis, R. Ju??kenas, E. Norkus, Investigation of electrocatalytic activity of the nanostructured Au-Cu catalyst deposited on the titanium surface towards borohydride oxidation, J. Electroanal. Chem. 700 (2013) 1–7. doi:10.1016/j.jelechem.2013.04.011.

[269] D.M.F. Santos, B. Šljukić, L. Amaral, J. Milikić, C.A.C. Sequeira, D. Macciò, A. Saccone, Nickel-rare earth electrodes for sodium borohydride electrooxidation, Electrochim. Acta. 190 (2016) 1050–1056. doi:10.1016/j.electacta.2015.12.218.

[270] A. Balciunaite, Z. Sukackiene, L. Tamašauskaite-Tamašiunaite, Z. Cinciene, A. Selskis, E. Norkus, CoB/Cu and PtCoB/Cu catalysts for borohydride fuel cells, Electrochim. Acta. 225 (2017) 255–262. doi:10.1016/j.electacta.2016.12.155.

[271] D.C. de Oliveira, W.O. Silva, M. Chatenet, F.H.B. Lima, NiOx-Pt/C nanocomposites: Highly active electrocatalysts for the electrochemical oxidation of hydrazine, Appl. Catal. B Environ. 201 (2017) 22–28. doi:10.1016/j.apcatb.2016.08.007.

[272] A. Allagui, S. Sarfraz, E.A. Baranova, NixPd1-x (x = 0.98, 0.93, and 0.58) nanostructured catalysts for ammonia electrooxidation in alkaline media,

Electrochim. Acta. 110 (2013) 253–259. doi:10.1016/j.electacta.2013.06.148.

[273] V. Di Noto, E. Negro, S. Lavina, N. Boaretto, M. Piga, Platinum-free Carbon Nitride Electrocatalysts for PEMFCs Based on Pd, Co and Ni: Effect of Nitrogen on the Structure and Electrochemical Performance, ECS Trans. . 16 (2008) 123–137. doi:10.1149/1.2981849.

[274] M.G. Hosseini, R. Mahmoodi, Ni@M (M = Pt, Pd and Ru) core@shell nanoparticles on a Vulcan XC-72R support with superior catalytic activity toward borohydride oxidation: electrochemical and fuel cell studies, New J. Chem. 41 (2017) 13408–13417. doi:10.1039/C7NJ02585H.

[275] D. Duan, J. Liang, H. Liu, X. You, H. Wei, G. Wei, S. Liu, The effective carbon supported core-shell structure of Ni@Au catalysts for electro-oxidation of borohydride, Int. J. Hydrogen Energy. 40 (2015) 488–500. doi:10.1016/j.ijhydene.2014.10.101.

[276] S. Saha, A. Basu, D. Das, S. Ganguly, D. Banerjee, K. Kargupta, Novel graphene supported Co rich connected core(Pt)-shell(Co) nano-alloy catalyst for improved hydrogen generation and electro-oxidation, Int. J. Hydrogen Energy. 41 (2016) 18451–18464. doi:10.1016/j.ijhydene.2016.07.148.

[277] D. Duan, H. Liu, X. You, H. Wei, S. Liu, Anodic behavior of carbon supported Cu@Ag core-shell nanocatalysts in direct borohydride fuel cells, J. Power Sources. 293 (2015) 292–300. doi:10.1016/j.jpowsour.2015.05.086.

[278] R. Edla, S. Gupta, N. Patel, N. Bazzanella, R. Fernandes, D.C. Kothari, A. Miotello, Enhanced H2 production from hydrolysis of sodium borohydride using Co3O4 nanoparticles assembled coatings prepared by pulsed laser deposition, Appl. Catal. A Gen. 515 (2016) 1–9. doi:10.1016/j.apcata.2016.01.031.

[279] P. Krishnan, S.G. Advani, A.K. Prasad, Cobalt oxides as Co2B catalyst precursors for the hydrolysis of sodium borohydride solutions to generate hydrogen for PEM fuel cells, Int. J. Hydrogen Energy. 33 (2008) 7095–7102. doi:10.1016/j.ijhydene.2008.09.026.

[280] K. Asazawa, K. Yamada, H. Tanaka, M. Taniguchi, K. Oguro, Electrochemical oxidation of hydrazine and its derivatives on the surface of metal electrodes in alkaline media, J. Power Sources. 191 (2009) 362–365. doi:10.1016/j.jpowsour.2009.02.009.

[281] S. Li, Y. Liu, Y. Liu, Y. Chen, Study of CoO as an anode catalyst for a membraneless direct borohydride fuel cell, J. Power Sources. 195 (2010) 7202–7206. doi:10.1016/j.jpowsour.2010.05.016.

[282] A. Aytaç, M. Gürbüz, A.E. Sanli, Electrooxidation of hydrogen peroxide and sodium borohydride on Ni deposited carbon fiber electrode for alkaline fuel cells, Int. J. Hydrogen Energy. 36 (2011) 10013–10021. doi:10.1016/j.ijhydene.2011.05.079.

[283] E.S. Davydova, F.D. Speck, M.T.Y. Paul, D.R. Dekel, S. Cherevko, Stability Limits of Ni-Based Hydrogen Oxidation Electrocatalysts for Anion Exchange Membrane Fuel Cells, ACS Catal. 9 (2019) 6837–6845. doi:10.1021/acscatal.9b01582.

[284] M. Guo, Y. Cheng, Y. Yu, J. Hu, Ni-Co nanoparticles immobilized on a 3D Ni foam template as a highly efficient catalyst for borohydride electrooxidation in alkaline

medium, Appl. Surf. Sci. 416 (2017) 439–445. doi:10.1016/j.apsusc.2017.04.193.

[285] O. V. Cherstiouk, P.A. Simonov, A.G. Oshchepkov, V.I. Zaikovskii, T.Y. Kardash, A. Bonnefont, V.N. Parmon, E.R. Savinova, Electrocatalysis of the hydrogen oxidation reaction on carbon-supported bimetallic NiCu particles prepared by an improved wet chemical synthesis, J. Electroanal. Chem. 783 (2016) 146–151. doi:10.1016/j.jelechem.2016.11.031.

[286] H. Tanaka, K. Asazawa, T. Sakamoto, T. Kato, M. Kai, S. Yamaguchi, K. Yamada, H. Fujikawa, The platinum-free anionic fuel cells for automotive applications, ECS Trans. 16 (2008) 459–464. doi:10.1149/1.2981880.

[287] B.J. Trzesniewski, O. Diaz-Morales, D.A. Vermaas, A. Longo, W. Bras, M.T.M. Koper, W.A. Smith, In Situ Observation of Active Oxygen Species in Fe-Containing Ni-Based Oxygen Evolution Catalysts: The Effect of pH on Electrochemical Activity, J. Am. Chem. Soc. 137 (2015) 15112–15121. doi:10.1021/jacs.5b06814.

[288] A.G. Oshchepkov, P.A. Simonov, O. V. Cherstiouk, R.R. Nazmutdinov, D. V. Glukhov, V.I. Zaikovskii, T.Y. Kardash, R.I. Kvon, A. Bonnefont, A.N. Simonov, V.N. Parmon, E.R. Savinova, On the effect of Cu on the activity of carbon supported Ni nanoparticles for hydrogen electrode reactions in alkaline medium, Top. Catal. 58 (2015) 1181–1192. doi:10.1007/s11244-015-0487-5.

[289] A.G. Oshchepkov, A. Bonnefont, V.N. Parmon, E.R. Savinova, On the effect of temperature and surface oxidation on the kinetics of hydrogen electrode reactions on nickel in alkaline media, Electrochim. Acta. 269 (2018) 111–118. doi:10.1016/j.electacta.2018.02.106.

[290] A.G. Oshchepkov, A. Bonnefont, E.R. Savinova, On the Influence of the Extent of Oxidation on the Kinetics of the Hydrogen Electrode Reactions on Polycrystalline Nickel, Electrocatalysis. 11 (2020) 133–142. doi:10.1007/s12678-019-00560-3.

[291] A.G. Oshchepkov, G. Braesch, S. Ould-Amara, G. Rostamikia, G. Maranzana, A. Bonnefont, V. Papaefthimiou, M.J. Janik, M. Chatenet, E.R. Savinova, Nickel Metal Nanoparticles as Anode Electrocatalysts for Highly Efficient Direct Borohydride Fuel Cells, ACS Catal. 9 (2019) 8520–8528. doi:10.1021/acscatal.9b01616.

[292] N. V. Emelianova, Researches with the dropping mercury cathode: Part VII. Nickel and Cobalt, Recl. Des Trav. Chim. Des Pays-Bas. 44 (1925) 528–548. doi:10.1002/recl.19250440611.

[293] P. Lukovtsev, S. Levina, A. Frumkin, Hydrogen Overpotential on Nickel, Acta Physicochim. U.S.S.R. 11 (1939) 916–930.

[294] A. Frumkin, Hydrogen overvoltage, Discuss. Faraday Soc. 1 (1947) 57–67. doi:10.1039/df9470100057.

[295] B.E. Conway, P.L. Bourgault, The Electrochemical Behavior of the Nickel – Nickel Oxide Electrode: Part I. Kinetics of Self-Discharge, Can. J. Chem. 37 (1959) 292–307. doi:10.1139/v59-038.

[296] P.L. Bourgault, B.E. Conway, The Electrochemical Behavior of the Nickel Oxide Electrode: Part II. Quasi-Equilibrium Behavior, Can. J. Chem. 38 (1960) 1557–1575. doi:10.1139/v60-216.

[297] B.E. Conway, P.L. Bourgault, Electrochemistry of the Nickel Oxide Electrode: Part III. Anodic Polarization and Self-Discharge Behavior, Can. J. Chem. 40 (1962) 1690–1707. doi:10.1139/v62-256.

[298] B.E. Conway, E. Gileadi, Electrochemistry of the Nickel Oxide Electrode: Part IV. Electrochemical Kinetic Studies of Reversible Potentials as a Function of Degree of Oxidation, Can. J. Chem. 40 (1962) 1933–1942. doi:10.1139/v62-297.

[299] B.E. Conway, M.A. Sattar, Electrochemistry of the nickel oxide electrode, J. Electroanal. Chem. Interfacial Electrochem. 19 (1968) 351–364. doi:10.1016/s0022-0728(68)80098-1.

[300] B.E. Conway, M.A. Sattar, D. Gilroy, Electrochemistry of the nickel-oxide electrode—V. Self-passivation effects in oxygen-evolution kinetics, Electrochim. Acta. 14 (1969) 677–694. doi:10.1016/0013-4686(69)80024-1.

[301] M.A. Sattar, B.E. Conway, Electrochemistry of the nickel-oxide electrode-VI. Surface oxidation of nickel anodes in alkaline solution, Electrochim. Acta. 14 (1969) 695–710. doi:10.1016/0013-4686(69)80025-3.

[302] B.E. Conway, M.A. Sattar, D. Gilroy, Electrochemistry of the nickel-oxide electrode-VII. Potentiostatic step method for study of adsorbed intermediates, Electrochim. Acta. 14 (1969) 711–724. doi:10.1016/0013-4686(69)80026-5.

[303] J.L. Weininger, M.W. Breiter, Effect of Crystal Structure on the Anodic Oxidation of Nickel, J. Electrochem. Soc. 110 (1963) 484–490. doi:10.1149/1.2425798.

[304] J.L. Weininger, M.W. Breiter, Hydrogen Evolution and Surface Oxidation of Nickel Electrodes in Alkaline Solution, J. Electrochem. Soc. 111 (1964) 707–712. doi:10.1149/1.2426216.

[305] J.O.M.O. Bockris, E.C. Potter, The mechanism of hydrogen evolution at nickel cathodes in aqueous solutions, J. Chem. Phys. 20 (1952) 614–628. doi:10.1063/1.1700503.

[306] D.S. Hall, C. Bock, B.R. MacDougall, The Electrochemistry of Metallic Nickel: Oxides, Hydroxides, Hydrides and Alkaline Hydrogen Evolution, J. Electrochem. Soc. 160 (2013) F235–F243. doi:10.1149/2.026303jes.

[307] D.S. Hall, D.J. Lockwood, C. Bock, B.R. MacDougall, Nickel hydroxides and related materials: a review of their structures, synthesis and properties, Proc. R. Soc. A Math. Phys. Eng. Sci. 471 (2014) 20140792. doi:10.1098/rspa.2014.0792.

[308] M. Alsabet, M. Grden, G. Jerkiewicz, Electrochemical Growth of Surface Oxides on Nickel. Part 1: Formation of α-$Ni(OH)_2$ in Relation to the Polarization Potential, Polarization Time, and Temperature, Electrocatalysis. 2 (2011) 317–330. doi:10.1007/s12678-011-0067-9.

[309] M. Alsabet, M. Grden, G. Jerkiewicz, Electrochemical Growth of Surface Oxides on Nickel. Part 2: Formation of β-$Ni(OH)_2$ and NiO in Relation to the Polarization Potential, Polarization Time, and Temperature, Electrocatalysis. 5 (2014) 136–147. doi:10.1007/s12678-013-0172-z.

[310] M. Alsabet, M. Grdeń, G. Jerkiewicz, M. Grden, G. Jerkiewicz, Electrochemical Growth of Surface Oxides on Nickel. Part 3: Formation of β-NiOOH in Relation to the Polarization Potential, Polarization Time, and Temperature,

Electrocatalysis. 6 (2015) 60–71. doi:10.1007/s12678-014-0214-1.

[311] D. Salmazo, M.F. Juarez, A.G. Oshchepkov, O. V. Cherstiouk, A. Bonnefont, S.A. Shermukhamedov, R.R. Nazmutdinov, W. Schmickler, E.R. Savinova, On the feasibility of bifunctional hydrogen oxidation on Ni and NiCu surfaces, Electrochim. Acta. 305 (2019) 452–458. doi:10.1016/j.electacta.2019.03.030.

[312] A.N. Kuznetsov, A.G. Oshchepkov, O. V. Cherstiouk, P.A. Simonov, R.R. Nazmutdinov, E.R. Savinova, A. Bonnefont, Influence of the NaOH Concentration on the Hydrogen Electrode Reaction Kinetics of Ni and NiCu Electrodes, ChemElectroChem. 7 (2020) 1438–1447. doi:10.1002/celc.202000319.

[313] C.A. Melendres, M. Pankuch, On the composition of the passive film on nickel: a surface-enhanced Raman spectroelectrochemical study, J. Electroanal. Chem. 333 (1992) 103–113. doi:10.1016/0022-0728(92)80384-G.

[314] M. Grdeń, K. Klimek, A. Czerwiński, A quartz crystal microbalance study on a metallic nickel electrode, J. Solid State Electrochem. 8 (2004) 390–397. doi:10.1007/s10008-003-0461-1.

[315] R. Šimpraga, B.E. Conway, Realization of monolayer levels of surface oxidation of nickel by anodization at low temperatures, J. Electroanal. Chem. Interfacial Electrochem. 280 (1990) 341–357. doi:10.1016/0022-0728(90)87008-8.

[316] M. Nakamura, N. Ikemiya, A. Iwasaki, Y. Suzuki, M. Ito, Surface structures at the initial stages in passive film formation on Ni(111) electrodes in acidic electrolytes, J. Electroanal. Chem. 566 (2004) 385–391. doi:10.1016/j.jelechem.2003.11.050.

[317] A. Seyeux, V. Maurice, L.H. Klein, P. Marcus, In situ scanning tunnelling microscopic study of the initial stages of growth and of the structure of the passive film on Ni(111) in 1 mM NaOH(aq), J. Solid State Electrochem. 9 (2005) 337–346. doi:10.1007/s10008-004-0627-5.

[318] B.E. Conway, B. Barnett, H. Angerstein-Kozlowska, B. V. Tilak, A surface-electrochemical basis for the direct logarithmic growth law for initial stages of extension of anodic oxide films formed at noble metals, J. Chem. Phys. 93 (1990) 8361–8373. doi:10.1063/1.459319.

[319] C.. D'Alkaine, M.. Santanna, The passivating films on nickel in alkaline solutions I. General aspects of the Ni (II) region, J. Electroanal. Chem. 457 (1998) 5–12. doi:10.1016/S0022-0728(98)00228-9.

[320] M. Keddam, Transpassive Dissolution of Ni in Acidic Sulfate Media: A Kinetic Model, J. Electrochem. Soc. 132 (1985) 2561–2566. doi:10.1149/1.2113624.

[321] P. Zoltowski, The capacity of monocrystalline nickel electrode in potassium hydroxide solution at low hydrogen overpotentials, Electrochim. Acta. 38 (1993) 2129–2133. doi:10.1016/0013-4686(93)80351-Y.

[322] D. Floner, C. Lamy, J.M. Leger, Electrocatalytic oxidation of hydrogen on polycrystal and single-crystal nickel electrodes, Surf. Sci. 234 (1990) 87–97. doi:10.1016/0039-6028(90)90668-X.

[323] D. Esau, F.M. Schuett, K.L. Varvaris, J. Björk, T. Jacob, G. Jerkiewicz, Controlled-Atmosphere Flame Fusion Growth of Nickel Poly-oriented Spherical Single Crystals—Unraveling Decades of Impossibility, Electrocatalysis. 11 (2020) 1–13.

doi:10.1007/s12678-019-00575-w.

[324] B. Beden, D. Floner, J.M. Léger, C. Lamy, A voltammetric study of the formation on hydroxides and oxyhydroxides on nickel single crystal electrodes in contact with an alkaline solution, Surf. Sci. 162 (1985) 822–829. doi:10.1016/0039-6028(85)90985-9.

[325] A. Mohsenzadeh, T. Richards, K. Bolton, DFT study of the water gas shift reaction on Ni(111), Ni(100) and Ni(110) surfaces, Surf. Sci. 644 (2016) 53–63. doi:10.1016/j.susc.2015.09.014.

[326] G. Kresse, J. Hafner, First-principles study of the adsorption of atomic H on Ni (111), (100) and (110), Surf. Sci. 459 (2000) 287–302. doi:10.1016/S0039-6028(00)00457-X.

[327] W. Visscher, E. Barendrecht, Anodic oxide films of nickel in alkaline electrolyte, Surf. Sci. 135 (1983) 436–452. doi:10.1016/0039-6028(83)90235-2.

[328] M. Grdeń, K. Klimek, EQCM studies on oxidation of metallic nickel electrode in basic solutions, J. Electroanal. Chem. 581 (2005) 122–131. doi:10.1016/j.jelechem.2005.04.026.

[329] S.L.L. Medway, C.A.A. Lucas, A. Kowal, R.J.J. Nichols, D. Johnson, In situ studies of the oxidation of nickel electrodes in alkaline solution, J. Electroanal. Chem. 587 (2006) 172–181. doi:10.1016/j.jelechem.2005.11.013.

[330] B. Beden, A. Bewick, The anodic layer on nickel in alkaline solution: an investigation using in situ IR spectroscopy, Electrochim. Acta. 33 (1988) 1695–1698. doi:10.1016/0013-4686(88)80245-7.

[331] H.-W. Hoppe, H.-H. Strehblow, XPS and UPS examinations of the formation of passive layers on Ni in 1 M sodium hydroxide and 0.5 M sulphuric acid, Surf. Interface Anal. 14 (1989) 121–131. doi:10.1002/sia.740140305.

[332] B. Beverskog, I. Puigdomenech, Revised Pourbaix diagrams for nickel at 25-300 °C, Corros. Sci. 39 (1997) 969–980. doi:10.1016/S0010-938X(97)00002-4.

[333] C.-C. Hu, T.-C. Wen, Effects of the nickel oxide on the hydrogen evolution and para-nitroaniline reduction at Ni-deposited graphite electrodes in NaOH, Electrochim. Acta. 43 (1998) 1747–1756. doi:10.1016/S0013-4686(97)00312-5.

[334] A.G. Pshenichnikov, Electrocatalytic properties of nickel and nickel-based alloys, Mater. Chem. Phys. 22 (1989) 121–148. doi:10.1016/0254-0584(89)90034-5.

[335] L.D. Burke, T.A.M. Twomey, Voltammetric behaviour of nickel in base with particular reference to thick oxide growth, J. Electroanal. Chem. Interfacial Electrochem. 162 (1984) 101–119. doi:10.1016/S0022-0728(84)80158-8.

[336] W. Visscher, E. Barendrecht, The anodic oxidation of nickel in alkaline solution, Electrochim. Acta. 25 (1980) 651–655. doi:10.1016/0013-4686(80)87072-1.

[337] W. Visscher, E. Barendrecht, Absorption of hydrogen in reduced nickel oxide, J. Appl. Electrochem. 10 (1980) 269–274.

[338] N.A. Shumilova, V.S. Bagotzky, Oxygen ionization on nickel in alkaline solutions, Electrochim. Acta. 13 (1968) 285–293. doi:10.1016/0013-4686(68)87001-X.

[339] R. Karimi Shervedani, A. Lasia, Evaluation of the surface roughness of microporous Ni-Zn-P electrodes by in situ methods, J. Appl. Electrochem. 29 (1999) 979–986. doi:10.1023/A:1003577631897.

[340] G. Jerkiewicz, Hydrogen sorption at/in electrodes, Prog. Surf. Sci. 57 (1998) 137–186. doi:10.1016/S0079-6816(98)00015-X.

[341] N.M. Markovic, P.N. Ross Jr., Surface science studies of model fuel cell electrocatalysts, Surf. Sci. Rep. 45 (2002) 117–229. doi:10.1016/S0167-5729(01)00022-X.

[342] P. Quaino, F. Juarez, E. Santos, W. Schmickler, Volcano plots in hydrogen electrocatalysis - uses and abuses., Beilstein J. Nanotechnol. 5 (2014) 846–854. doi:10.3762/bjnano.5.96.

[343] Y. Choquette, L. Brossard, A. Lasia, H. Ménard, Investigation of hydrogen evolution on Raney-Nickel composite-coated electrodes, Electrochim. Acta. 35 (1990) 1251–1256. doi:10.1016/0013-4686(90)90058-8.

[344] G. Kreysa, B. Hakansson, P. Ekdunge, Kinetic and thermodynamic analysis of hydrogen evolution at nickel electrodes, Electrochim. Acta. 33 (1988) 1351–1357. doi:10.1016/0013-4686(88)80125-7.

[345] J. Katić, M. Metikoš-Huković, R. Peter, M. Petravić, The electronic structure of the α-$Ni(OH)_2$ films: Influence on the production of the high-performance Ni-catalyst surface, J. Power Sources. 282 (2015) 421–428. doi:10.1016/j.jpowsour.2015.02.063.

[346] F. Juarez, D. Salmazo, E.R. Savinova, P. Quaino, G. Belletti, E. Santos, W. Schmickler, The initial stage of OH adsorption on Ni(111), J. Electroanal. Chem. 832 (2019) 137–141. doi:10.1016/j.jelechem.2018.10.047.

[347] Y. Bai, D. Kirvassilis, L. Xu, M. Mavrikakis, Atomic and molecular adsorption on Ni(111), Surf. Sci. 679 (2019) 240–253. doi:10.1016/j.susc.2018.08.004.

[348] C. Taylor, R.G. Kelly, M. Neurock, Theoretical Analysis of the Nature of Hydrogen at the Electrochemical Interface Between Water and a Ni(111) Single-Crystal Electrode, J. Electrochem. Soc. 154 (2007) F55–F64. doi:10.1149/1.2431326.

[349] J. Greeley, M. Mavrikakis, A first-principles study of surface and subsurface H on and in Ni(111): Diffusional properties and coverage-dependent behavior, Surf. Sci. 540 (2003) 215–229. doi:10.1016/S0039-6028(03)00790-8.

[350] Y. Dong, J. Dang, W. Wang, S. Yin, Y. Wang, First-Principles Determination of Active Sites of Ni Metal-Based Electrocatalysts for Hydrogen Evolution Reaction, ACS Appl. Mater. Interfaces. 10 (2018) 39624–39630. doi:10.1021/acsami.8b12573.

[351] S. Liu, T. Ishimoto, M. Koyama, First-principles study of oxygen coverage effect on hydrogen oxidation on Ni(1 1 1) surface, Appl. Surf. Sci. 333 (2015) 86–91. doi:10.1016/j.apsusc.2015.01.238.

[352] M.J. Janik, I.T. McCrum, M.T.M. Koper, On the presence of surface bound hydroxyl species on polycrystalline Pt electrodes in the "hydrogen potential region" (0–0.4 V-RHE), J. Catal. 367 (2018) 332–337. doi:10.1016/j.jcat.2018.09.031.

[353] J. Desilvestro, Characterization of Redox States of Nickel Hydroxide Film

Electrodes by In Situ Surface Raman Spectroscopy, J. Electrochem. Soc. 135 (1988) 885. doi:10.1149/1.2095818.

[354] V.S. Bagotzky, N.A. Shumilova, G.P. Samoilov, E.I. Khrushcheva, Electrochemical oxygen reduction on nickel electrodes in alkaline solutions—II, Electrochim. Acta. 17 (1972) 1625–1635. doi:10.1016/0013-4686(72)85053-9.

[355] M.-S. Kim, K.-B. Kim, A Study on the Phase Transformation of Electrochemically Precipitated Nickel Hydroxides Using an Electrochemical Quartz Crystal Microbalance, J. Electrochem. Soc. 145 (1998) 507. doi:10.1149/1.1838294.

[356] R.S.S. Guzmán, J.R. Vilche, A.J. Arvía, Non-equilibrium effects in the nickel hydroxide electrode, J. Appl. Electrochem. 9 (1979) 183–189. doi:10.1007/BF00616088.

[357] R.L. Doyle, I.J. Godwin, M.P. Brandon, M.E.G. Lyons, Redox and electrochemical water splitting catalytic properties of hydrated metal oxide modified electrodes, Phys. Chem. Chem. Phys. 15 (2013) 13737–13783. doi:10.1039/c3cp51213d.

[358] C. Johnston, P.R. Graves, In situ Raman spectroscopy study of the nickel oxyhydroxide electrode (NOE) system, Appl. Spectrosc. 44 (1990) 105–115. doi:10.1366/0003702904085769.

[359] L.J. Oblonsky, Surface Enhanced Raman Spectra from the Films Formed on Nickel in the Passive and Transpassive Regions, J. Electrochem. Soc. 142 (1995) 3677–3682. doi:10.1149/1.2048398.

[360] B.S. Yeo, A.T. Bell, In situ raman study of nickel oxide and gold-supported nickel oxide catalysts for the electrochemical evolution of oxygen, J. Phys. Chem. C. 116 (2012) 8394–8400. doi:10.1021/jp3007415.

[361] F. El Gabaly, K.F. McCarty, H. Bluhm, A.H. McDaniel, Oxidation stages of Ni electrodes in solid oxide fuel cell environments, Phys. Chem. Chem. Phys. 15 (2013) 8334–8341. doi:10.1039/c3cp50366f.

[362] H. Ali-Löytty, M.W. Louie, M.R. Singh, L. Li, H.G. Sanchez Casalongue, H. Ogasawara, E.J. Crumlin, Z. Liu, A.T. Bell, A. Nilsson, D. Friebel, Ambient-Pressure XPS Study of a Ni–Fe Electrocatalyst for the Oxygen Evolution Reaction, J. Phys. Chem. C. 120 (2016) 2247–2253. doi:10.1021/acs.jpcc.5b10931.

[363] S.H. Ahn, S.J. Hwang, S.J. Yoo, I. Choi, H.-J.J. Kim, J.H. Jang, S.W. Nam, T.-H.T.H. Lim, T.-H.T.H. Lim, S.-K.K. Kim, J.J. Kim, Electrodeposited Ni dendrites with high activity and durability for hydrogen evolution reaction in alkaline water electrolysis, J. Mater. Chem. 22 (2012) 15153–15159. doi:10.1039/c2jm31439h.

[364] J.-Y. Huot, Hydrogen Evolution and Interface Phenomena on a Nickel Cathode in 30 w/o KOH, J. Electrochem. Soc. 136 (1989) 1933. doi:10.1149/1.2097088.

[365] A.C. Makrides, Hydrogen Overpotential on Nickel in Alkaline Solution, J. Electrochem. Soc. 109 (1962) 977–984. doi:10.1149/1.2425216.

[366] M.A. McArthur, L. Jorge, S. Coulombe, S. Omanovic, Synthesis and characterization of 3D Ni nanoparticle/carbon nanotube cathodes for hydrogen evolution in alkaline electrolyte, J. Power Sources. 266 (2014) 365–373. doi:10.1016/j.jpowsour.2014.05.036.

[367] M. Gong, D.Y. Wang, C.C. Chen, B.J. Hwang, H. Dai, A mini review on nickel-based electrocatalysts for alkaline hydrogen evolution reaction, Nano Res. 9 (2016) 28–46. doi:10.1007/s12274-015-0965-x.

[368] N. Danilovic, R. Subbaraman, D. Strmcnik, K.C. Chang, A.P. Paulikas, V.R. Stamenkovic, N.M. Markovic, Enhancing the alkaline hydrogen evolution reaction activity through the bifunctionality of $Ni(OH)_2$/metal catalysts, Angew. Chemie - Int. Ed. 51 (2012) 12495–12498. doi:10.1002/anie.201204842.

[369] W. Sheng, M. Myint, J.G. Chen, Y. Yan, Correlating the hydrogen evolution reaction activity in alkaline electrolytes with the hydrogen binding energy on monometallic surfaces, Energy Environ. Sci. 6 (2013) 1509–1512. doi:10.1039/c3ee00045a.

[370] J. Greeley, T.F. Jaramillo, J. Bonde, I. Chorkendorff, J.K. Nørskov, Computational high-throughput screening of electrocatalytic materials for hydrogen evolution, Nat. Mater. 5 (2006) 909–913. doi:10.1038/nmat1752.

[371] J.P. Elder, A. Hickling, Anodic behaviour of the borohydride ion, Trans. Faraday Soc. 58 (1962) 1852–1864. doi:10.1039/tf9625801852.

[372] S. Li, C. Shu, Y. Chen, L. Wang, A new application of nickel-boron amorphous alloy nanoparticles: anode-catalyzed direct borohydride fuel cell, Ionics (Kiel). 24 (2018) 201–209. doi:10.1007/s11581-017-2180-0.

[373] D. Zhang, G. Wang, Y. Yuan, Y. Li, S. Jiang, Y. Wang, K. Ye, D. Cao, P. Yan, K. Cheng, Three-dimensional functionalized graphene networks modified Ni foam based gold electrode for sodium borohydride electrooxidation, Int. J. Hydrogen Energy. 41 (2016) 11593–11598. https://www.sciencedirect.com/science/article/pii/S0360319915307758 (accessed April 20, 2019).

[374] X. Geng, H. Zhang, W. Ye, Y. Ma, H. Zhong, Ni-Pt/C as anode electrocatalyst for a direct borohydride fuel cell, J. Power Sources. 185 (2008) 627–632. doi:10.1016/j.jpowsour.2008.09.010.

[375] D.M.F. Santos, B. Šljukić, L. Amaral, D. Macciò, A. Saccone, C.A.C. Sequeira, B. ljuki , L. Amaral, D. Maccio, A. Saccone, C.A.C. Sequeira, Nickel and Nickel-Cerium Alloy Anodes for Direct Borohydride Fuel Cells, J. Electrochem. Soc. 161 (2014) F594–F599. doi:10.1149/2.023405jes.

[376] D. Zhang, K. Cheng, N. Shi, F. Guo, G. Wang, D. Cao, Nickel particles supported on multi-walled carbon nanotubes modified sponge for sodium borohydride electrooxidation, Electrochem. Commun. 35 (2013) 128–130. https://www.sciencedirect.com/science/article/pii/S1388248113003214 (accessed April 20, 2019).

[377] M.G. Hosseini, N. Rashidi, R. Mahmoodi, M. Omer, Preparation of Pt/G and PtNi/G nanocatalysts with high electrocatalytic activity for borohydride oxidation and investigation of different operation condition on the performance of direct borohydride-hydrogen peroxide fuel cell, Mater. Chem. Phys. 208 (2018) 207–219. doi:10.1016/j.matchemphys.2018.01.018.

[378] B. Šljukić, J. Milikić, D.M.F. Santos, C.A.C. Sequeira, Carbon-supported Pt0.75M0.25 (M = Ni or Co) electrocatalysts for borohydride oxidation,

Electrochim. Acta. 107 (2013) 577–583. doi:10.1016/j.electacta.2013.06.040.

[379] M. Lefèvre, E. Proietti, F. Jaouen, J.P. Dodelet, Iron-Based catalysts with improved oxygen reduction activity in polymer electrolyte fuel cells, Science (80-.). 324 (2009) 71–74. doi:10.1126/science.1170051.

[380] E.S. Davydova, S. Mukerjee, F. Jaouen, D.R. Dekel, Electrocatalysts for Hydrogen Oxidation Reaction in Alkaline Electrolytes, ACS Catal. 8 (2018) 6665–6690. doi:10.1021/acscatal.8b00689.

[381] D. Xia, F. Tang, X. Yao, Y. Wei, Y. Cui, M. Dou, L. Gan, F. Kang, Seeded growth of branched iron–nitrogen-doped carbon nanotubes as a high performance and durable non-precious fuel cell cathode, Carbon N. Y. 162 (2020) 300–307. doi:10.1016/j.carbon.2020.02.046.

[382] R. Sgarbi, E.A. Ticianelli, F. Maillard, F. Jaouen, M. Chatenet, Oxygen Reduction Reaction on Metal and Nitrogen–Doped Carbon Electrocatalysts in the Presence of Sodium Borohydride, Electrocatalysis. (2020). doi:10.1007/s12678-020-00602-1.

[383] A.I. Yanson, P. Rodriguez, N. Garcia-Araez, R. V. Mom, F.D. Tichelaar, M.T.M. Koper, Cathodic Corrosion: A Quick, Clean, and Versatile Method for the Synthesis of Metallic Nanoparticles, Angew. Chemie Int. Ed. 50 (2011) 6346–6350. doi:10.1002/anie.201100471.

[384] A.I. Yanson, P. V. Antonov, P. Rodriguez, M.T.M. Koper, Influence of the electrolyte concentration on the size and shape of platinum nanoparticles synthesized by cathodic corrosion, Electrochim. Acta. 112 (2013) 913–918. doi:10.1016/j.electacta.2013.01.056.

[385] L. Ring, B.G. Pollet, M. Chatenet, S. Abbou, K. Küpper, M. Schmidt, M. Huck, A. Gries, M. Steinhart, H. Schäfer, From Bad Electrochemical Practices to an Environmental and Waste Reducing Approach for the Generation of Active Hydrogen Evolving Electrodes, Angew. Chemie Int. Ed. 58 (2019) 17383–17392. doi:10.1002/anie.201908649.

[386] K.S. Freitas, B.M. Concha, E.A. Ticianelli, M. Chatenet, Mass transport effects in the borohydride oxidation reaction - Influence of the residence time on the reaction onset and faradaic efficiency, Catal. Today. 170 (2011) 110–119. doi:10.1016/j.cattod.2011.01.051.

[387] Z. Jusys, H/D substitution effect on formaldehyde oxidation rate at a copper anode in alkaline medium studied by differential electrochemical mass spectrometry, J. Electroanal. Chem. 375 (1994) 257–262. doi:10.1016/0022-0728(94)03390-0.

[388] M.C.S. Escaño, Borohydride electro-oxidation on metal electrodes: Structure, composition and solvent effects from DFT, SPR Electrochem. 14 (2017) 1–22. doi:10.1039/9781782622727-00001.

[389] P. Ferrin, S. Kandoi, A.U. Nilekar, M. Mavrikakis, Hydrogen adsorption, absorption and diffusion on and in transition metal surfaces: A DFT study, Surf. Sci. 606 (2012) 679–689. doi:10.1016/j.susc.2011.12.017.

[390] S.-C. Huang, C.-H. Lin, J.-H. Wang, Trends of Water Gas Shift Reaction on Close-Packed Transition Metal Surfaces, J. Phys. Chem. C. 114 (2010) 9826–9834. doi:10.1021/jp1005814.

[391] G. Braesch, A.G. Oshchepkov, A. Bonnefont, F. Asonkeng, T. Maurer, G. Maranzana, E.R. Savinova, M. Chatenet, Nickel 3D Structures Enhanced by Electrodeposition of Nickel Nanoparticles as High Performance Anodes for Direct Borohydride Fuel Cells, ChemElectroChem. 7 (2020) 1789–1799. doi:10.1002/celc.202000254.

[392] A. Thompson, D. Attwood, E. Gullikson, M. Howells, K.-J. Kim, J. Kirz, J. Kortright, I. Lindau, Y. Liu, P. Pianetta, A. Robinson, J. Scofield, J. Underwood, G. Williams, H. Winick, Center for X-Ray Optics and Advanced Light Source - XRray Data Booklet, Lawrence Berkeley Natl. Lab. (2009) 176.

[393] J. Jia, X. Li, H. Qin, Y. He, H. Ni, H. Chi, CoO nanorods/C as a high performance cathode catalyst in direct borohydride fuel cell, J. Alloys Compd. 820 (2020) 153065. doi:10.1016/j.jallcom.2019.153065.

[394] Y. Kiros, S. Schwartz, Long-term hydrogen oxidation catalysts in alkaline fuel cells, J. Power Sources. 87 (2000) 101–105. doi:10.1016/S0378-7753(99)00436-X.

[395] M. Liu, J. Chang, J. Sun, L. Gao, Synthesis of porous NiO using NaBH4 dissolved in ethylene glycol as precipitant for high-performance supercapacitor, Electrochim. Acta. 107 (2013) 9–15. doi:10.1016/j.electacta.2013.05.122.

[396] B. Zhao, X.K. Ke, J.H. Bao, C.L. Wang, L. Dong, Y.W. Chen, H.L. Chen, Synthesis of flower-like NiO and effects of morphology on its catalytic properties, J. Phys. Chem. C. 113 (2009) 14440–14447. doi:10.1021/jp904186k.

[397] S.I. Kim, J.S. Lee, H.J. Ahn, H.K. Song, J.H. Jang, Facile route to an efficient nio supercapacitor with a three-dimensional nanonetwork morphology, ACS Appl. Mater. Interfaces. 5 (2013) 1596–1603. doi:10.1021/am3021894.

[398] X.H. Huang, J.P. Tu, X.H. Xia, X.L. Wang, J.Y. Xiang, L. Zhang, Y. Zhou, Morphology effect on the electrochemical performance of NiO films as anodes for lithium ion batteries, J. Power Sources. 188 (2009) 588–591. doi:10.1016/j.jpowsour.2008.11.111.

[399] P. Walker, W.H. Tarn, CRC Handbook of Metal Etchants, CRC Press, 1991.

[400] K. Asazawa, K. Yamada, H. Tanaka, A. Oka, M. Taniguchi, T. Kobayashi, A platinum-free zero-carbon-emission easy fuelling direct hydrazine fuel cell for vehicles, Angew. Chemie - Int. Ed. 46 (2007) 8024–8027. doi:10.1002/anie.200701334.

[401] N. Duteanu, G. Vlachogiannopoulos, M.R. Shivhare, E.H. Yu, K. Scott, A parametric study of a platinum ruthenium anode in a direct borohydride fuel cell, J. Appl. Electrochem. 37 (2007) 1085–1091. doi:10.1007/s10800-007-9360-y.

[402] J.R. Varcoe, P. Atanassov, D.R. Dekel, A.M. Herring, M.A. Hickner, P.A. Kohl, A.R. Kucernak, W.E. Mustain, K. Nijmeijer, K. Scott, T. Xu, L. Zhuang, Anion-exchange membranes in electrochemical energy systems, Energy Environ. Sci. 7 (2014) 3135–3191. doi:10.1039/C4EE01303D.

[403] L. Wang, M. Bellini, H.A. Miller, J.R. Varcoe, A high conductivity ultrathin anion-exchange membrane with 500+ h alkali stability for use in alkaline membrane fuel cells that can achieve 2 W cm-2 at 80 °c, J. Mater. Chem. A. 6 (2018) 15404–15412. doi:10.1039/c8ta04783a.

[404] G. Maranzana, A. Lamibrac, J. Dillet, S. Abbou, S. Didierjean, O. Lottin, Startup (and Shutdown) Model for Polymer Electrolyte Membrane Fuel Cells, J. Electrochem. Soc. 162 (2015) F694–F706. doi:10.1149/2.0451507jes.

[405] E. Proietti, F. Jaouen, M. Lefèvre, N. Larouche, J. Tian, J. Herranz, J.P. Dodelet, Iron-based cathode catalyst with enhanced power density in polymer electrolyte membrane fuel cells, Nat. Commun. 2 (2011). doi:10.1038/ncomms1427.

[406] F. Jaouen, E. Proietti, M. Lefèvre, R. Chenitz, J.P. Dodelet, G. Wu, H.T. Chung, C.M. Johnston, P. Zelenay, Recent advances in non-precious metal catalysis for oxygen-reduction reaction in polymer electrolyte fuel cells, Energy Environ. Sci. 4 (2011) 114–130. doi:10.1039/c0ee00011f.

List of Figures

Résumé

La pile à combustible directe à borohydrure (DBFC en anglais) est une technologie de pile à combustible prometteuse pour les applications portables et mobiles. L'utilisation de borohydrure de sodium ($NaBH_4$) sous forme de poudre comme substitut à l'hydrogène gazeux (dans une PEMFC) présente des avantages pour le stockage du combustible et la sécurité du système. Une fois dilué dans une solution alcaline, une importante quantité d'énergie peut être obtenue *via* la réaction d'oxydation des borohydrures (BOR). Cependant, cette réaction est très complexe et met en jeu de nombreux intermédiaires et chemins réactionnels en fonction de l'électrocatalyseur utilisé. De plus, elle est très peu connue et est le plus souvent étudiée sur des électrocatalyseurs à base de métaux nobles : les métaux du Groupe du platine (PGM). Puisque le combustible est utilisé en milieu alcalin, il est possible de remplacer ces PGMs par des métaux non-nobles pour catalyser la réaction. Les objectifs principaux de cette thèse, qui s'inscrit dans le cadre du projet MobiDiC financé par l'Agence Nationale de Recherche (ANR), sont multiples. (i) Etudier les mécanismes de la BOR sur des électrocatalyseurs PGMs, en particulier dans des conditions de fonctionnement de DBFC (grande concentrations de borohydrures) : une attention particulière est apportée au palladium car le mécanisme de la réaction est très peu connu sur ce métal. (ii) Trouver un métal non-noble actif pour la BOR. (iii) Développer des anodes de DBFC peu couteuses avec une architecture optimisée pour maximiser leur efficacité pour le BOR.

Les résultats regroupés dans ce manuscrit mettent en évidence l'empoisonnent de la surface des électrocatalyseurs PGM par des espèces réactionnelles intermédiaires, ce qui diminue grandement l'efficacité de la réaction, notamment à cause de cinétiques de transfert de charge plus lentes. La formation d'hydrures de palladium est manifeste en présence de borohydrures et modifie le chemin réactionnel de la BOR. Dans un second temps, des nanoparticules de nickel, obtenues par électrodéposition, ont démontré des performances très intéressantes pour la BOR ; cependant leur état d'oxydation doit être très précisément contrôlé et maintenu métallique. Des anodes de DBFC utilisant ces électrocatalyseurs non-nobles ont été développées ; sur support carbone, elles présentent des performances comparables à celles d'une anode à base de Pt. Dans le but d'optimiser leur activité, le support en carbone de ces anodes a finalement été remplacé par une structure 3D de Ni, qui permet d'obtenir des performances meilleures encore.

Mots clés : DBFC, Borohydrures, PGM, Non-noble, Nickel

Abstract

Direct Borohydride Fuel Cell (DBFC) is a promising alkaline fuel cell technology for portable and mobile applications. The use of solid sodium borohydride powder ($NaBH_4$) as a substitute fuel to gaseous hydrogen (in a PEMFC) is advantageous in terms of storage and safety concerns. Once diluted in a strong alkaline solution, it is possible to electro-oxidize it through the Borohydride Oxidation Reaction (BOR) which presents interesting properties in terms of energy generation. However, this anodic reaction is really complex and involves several intermediate species and reaction pathways. Moreover, in the pas it has been mainly investigated in laboratory conditions and using Platinum Group Metals (PGM) electrocatalysts. Meanwhile, since the BOR occurs in alkaline media it is possible to use non-noble materials to catalyse this reaction. The main objectives of this PhD, falling within the MobiDiC project funded by the French National Research Agency (ANR), are therefore (i) to explore the effect of the borohydride concentration on the reaction kinetics on the noble catalysts and particularly on palladium (since the mechanism of the BOR is poorly known on this metal), (ii) to find a non-noble material active towards the BOR and (iii) to develop low-cost DBFC anode with an optimized architecture to maximize its efficiency towards the BOR.

The results presented in this manuscript highlight the important poisoning of the PGM catalysts surface by intermediate species, which results in significant BOR efficiency loss mainly owing to slower charge transfer kinetics. Palladium hydrides were demonstrated to form in presence of borohydride, modifying the pathway of the reaction. In a second time, nickel nanoparticles, obtained by electrodeposition, were proven as performing non-noble catalysts only if their state of surface is precisely controlled and maintained metallic. DBFC performance matching the one using Pt-based anode was obtained with this Ni-based electrocatalysts supported on carbon paper. From this point, the anode support was replaced by Ni 3D structure and optimized to reach higher performance.

Keywords: DBFC, Borohydride, PGM, Non-noble, Nickel